CHIRAL CONFIGURATIONS FROM ACHIRAL LYOTROPIC CHROMONIC LIQUID CRYSTALS UNDER CONFINEMENTS

A Dissertation
Presented to
The Academic Faculty

by

Rui Chang

In Partial Fulfillment
of the Requirements for the Degree
Doctor of Philosophy in the
School of Chemical and Biomolecular Engineering

Georgia Institute of Technology
August, 2018

CHIRAL CONFIGURATIONS FROM ACHIRAL LYOTROPIC CHROMONIC LIQUID CRYSTALS UNDER CONFINEMENT

Approved by:

Dr. Mohan Srinivasarao, Advisor
School of Materials Science and Engineering
Georgia Institute of Technology

Dr. Alberto Fernandez-Nieves
School of Physics
Georgia Institute of Technology

Dr. Elsa Reichmanis, Advisor
School of Chemical and Biomolecular Engineering
Georgia Institute of Technology

Dr. J. Carson Meredith
School of Chemical and Biomolecular Engineering
Georgia Institute of Technology

Dr. Jung Ok Park
School of Materials Science and Engineering
Georgia Institute of Technology

Dr. Sven Holger Behrens
School of Chemical and Biomolecular Engineering
Georgia Institute of Technology

Date Approved: June 22nd, 2018

To my parents, grandparents, and friends

ACKNOWLEDGEMENTS

I would sincerely thank my thesis advisor, Dr. Mohan Srinivasarao, for his invaluable guidance in my research. He constantly encouraged me to think independently and deeply about scientific problems, and to read widely on other research topics and understand the big picture of the background. Moreover, he patiently trained me on efficient communication with others and provided plenty of opportunities to attend conferences. What I have learnt from him will be life-long assets in my career.

I truly appreciate the guidance from my co-advisor, Dr. Elsa Reichmanis. Her patience and support is a constant encouragement for me to overcome any difficulty during my research. She kindly provided resources and advice to improve my research and presentation skills. The research interests in her group also expand my knowledge in the field of polymer materials and organic electronics.

Then I want to thank Dr. Jung Ok Park for her help with my presentations and writing documents. I greatly valued her advice and time to improve my talks, posters, proposal, manuscripts, and thesis. Her critical and thorough attitude toward research has a far-reaching beneficial impact on me. I also thank Dr. Alberto Fernandez-Nieves, who impressed me with the beauty of soft matter physics in the early stage of my research. Attending his group meetings and taking his classes is a wonderful experience to learn how to think about soft matter materials from physics perspective. I thank Dr. J. Carson Meredith and Dr. Sven Holger Behrens for taking time to be in my committee. Their discussions during my proposal, pre-doctoral review, and defense were greatly appreciated.

I would like to thank Dr. Karthik Nayani, who was a graduate student in Dr. Srinivasarao's group. The collaboration with him was fruitful and significantly improved my understanding of liquid crystals. He also efficiently trained me to generate insightful idea and conduct research independently. I want to express my appreciation to Dr. Jinxin Fu, who was a postdoc researcher in Dr. Srinivasarao's group. His help with the optical microscope and conoscopy is priceless to me. I want to thank Dr. Perry Ellis, who was a graduate student in Dr. Fernandez-Nieves' group, and Dr. Nils Persson, who was a graduate student in Dr. Reichmanis group. The discussions with them helped me to develop the numerical calculation methods and Jones matrix simulation for liquid crystals. I also thank all the group members and alumni of Srinivasarao, Reichmanis, and Fernandez-Nieves labs for their help, advice, and friendship.

The love and support from my parents cannot be more appreciated. Their belief in my ability is a constant motivation to me. I also thank my cousins and grandparents for their love and care. I greatly value the support and advice from my friends. They always generously helped me as much as they could when I came across any problems. I wish them all a bright and fulfilling future. I appreciate my internship experience in Alcon Laboratories, where I worked with my mentor, Dr. Alex Chiang, and colleagues in surface chemistry group, R&D. Their career advice from industry has a strong impact on me in the choice of my full-time career.

Finally, I acknowledge the financial support from US Department of Energy, National Science Foundation, School of Chemical and Biomolecular Engineering, and School of Material Science and Engineering in Georgia Tech. I acknowledge the travel funds from Student Government Association and College of Engineering in Georgia Tech.

TABLE OF CONTENTS

LIST OF TABLES

LIST OF FIGURES

LIST OF SYMBOLS AND ABBREVIATIONS

$\boldsymbol{n}$	Director of nematic liquid crystal
$\boldsymbol{L}$	Local director of nematic liquid crystal
a_l	Molecular length
s_1, s_2, t_1, t_2, b_1, b_2	Six components of curvature in local Cartesian coordinates
g	Free energy density
K_{11}, K_{22}, K_{33}, K_{24}, K_{13}	Elastic constants of the splay, twist, bend, saddle-splay, and splay-bend deformations
K	Elastic constant under the assumption of $K = 10K_{22} = K_{11} = K_{33}$.
D_0	Diameter of the cylindrical capillary
R_0	Radius of the cylindrical capillary
F	Total elastic free energy
F_{24}	Saddle-splay elastic free energy
$W_\perp$	Anchoring strength in homeotropic orientation
$W_\parallel$	Anchoring strength in axial planar orientation
$\theta_\perp$	Tilt angle of the director on the surface from homeotropic orientation
$\theta_\parallel$	Tilt angle of the director on the surface from axial orientation
κ_1, κ_2	Principal curvatures
n_1, n_2	Director components along the principal curvatures
Φ	Twist angle of the doubly-twisted director field from the center to the boundary of the cylindrical capillary.
α_0	Twist angle of the twisted-bipolar tactoidr
Γ	Phase retardation due to the birefringence of the material
λ	Wavelength of the light
d	Optical path length
n_e , n_o	Extraordinary and ordinary refractive indices
Δn	Birefringence of nematic liquid crystals, $\Delta n = n_e - n_o$
$n_\parallel, n_\perp$	Refractive indices parallel and perpendicular to the optical axis

φ	The angle between the optical axis and the polarization of light
λ_p	Persistence length of LCLCs aggregates
$\bar{L}$	Average aggregate length of LCLCs aggregates
L	The length of the nematic building units
$\emptyset$	Volume fraction of lyotropic liquid crystals
k_B	Boltzmann constant
T	Temperature
C_i	Concentration of component *i*.
M_{SSY}	Molar mass of SSY
E	Scission energy of SSY aggregates
ρ_w	Density of water
ρ_{sol}	Density of SSY solution
N	Number of molecules in an aggregate
X_N	The fraction of the aggregates with N molecules
D	Diameter of LCLC aggregates.
r, ϕ, z	Radial, azimuthal, and axial axes of cylindrical coordinates
x, y, z	Axes of Cartesian coordinates
α	The angle between director projection in r-ϕ plane and r axis in cylindrical coordinates
β	The angle between director and z axis in cylindrical coordinates
Γ_α and Γ_β	Relaxation rate factors
θ_r	Rotation angle of capillary axis from the horizontal direction
I	Transmitted intensity
I_{max}	Maximum transmitted intensity along the cross section of a cylindrical capillary
t	Time
$\mathcal{D}$	Diffusivity of SSY molecules from isotropic phase to nematic phase in the biphase region
$\mathcal{D}_{iso}$	Diffusivity of SSY molecules in the isotropic phase
T_{NB}	Transition temperature between nematic phase and biphase
T_{BI}	Transition temperature between biphase and isotropic phase

$T_{biphase}$	Temperature range of biphase region, $T_{biphase} = T_{BI} - T_{NB}$.
ΔT_{NB}	Shift in T_{NB} of SSY with the addition of monovalent salts. $\Delta T_{NB} = T_{NB}$ (salts) - T_{NB} (salts free)
ΔT_{BI}	Shift in T_{BI} of SSY with the addition of monovalent salts. $\Delta T_{BI} = T_{BI}$ (salts) - T_{BI} (salts free)
$\Delta T_{biphase}$	Shift in $T_{biphase}$ of SSY with the addition of monovalent salts. $\Delta T_{biphase} = T_{biphase}$ (salts) – $T_{biphase}$ (salts free)
T_{OB}	Observation temperature for SSY tactoids
S	Scalar order parameter
θ_m	The angle between the axis of mesogen units and director orientation
$\boldsymbol{\mu}$	Oscillating dipole moment induced by electric field of incident light
$\boldsymbol{p}$	Polarizability of nematics
$\boldsymbol{E}$	Oscillating electric field of incident light
p'_x, p'_y, p'_z	Components of differential polarizability for nematics
r	Differential polarizability ratio, $r = p'_x/p'_z$
$I_{\perp}$	Raman intensity with parallel polarizers
$I_{\parallel}$	Raman intensity with perpendicular polarizers
θ	The angle between director and incident polarization orientation.
$R(\theta)$	Depolarization ratio
$< P_2 >$	The 2nd order parameter of nematics
$< P_4 >$	The 4th order parameter of nematics
$< P_2 >_{T=T_{NB}}$	The 2nd order parameter of nematics at transition temperature T_{NB}
$< P_2 >^*$ and β_0	Parameters of the empirical formula describing the temperature dependence of $< P_2 >$
m	Topological charge of singular defects
α_f	Flexibility parameter of LCLC aggregates, $\alpha_f = \bar{L}/\lambda_p$
θ_0	Flow alignment angle of nematic fluids under the effect of shear force
α_i	Viscosity coefficients for nematics, $i = 1, \ldots, 6$
λ_t	Tumbling parameter
$\bar{\eta}$ and $L(a)$	Parameters in Kuzuu and Doi's dereivation
$\overline{D_r}$	Rotational diffusion coefficient

c	Number of molecules in unit volume
a	Aspect ratio of LCLC aggregates
DT	The doubly-twisted director configuration
ER	The escaped radial director configuration
TER	The twisted escaped radial director configuration
TP	The twisted polar director configuration
TB	The twisted bipolar director configuration
EC	The escaped concentric director configuration
N	Nematic phase
I	Isotropic phase
N + I	Biphase region wherein the nematic phase and isotropic phase co-exist
LCLCs	Lyotropic chromonic liquid crystals
5CB	4-Cyano-4'-pentylbiphenyl
SSY	Sunset Yellow FCF
DSCG	Disodium cromoglycate
PEG	Polyethylene glycol
PBG	Racemic polybenzyl glutamate
PBLG	Polybenzyl-L-glutamate
SANS	Small angle neutron scattering

SUMMARY

Chirality has fascinated scientists for the past two centuries from structural color[1] to origins of life[2,3]. Intuitively, chiral structures can result from the chirality of constituent molecules[4]. But achiral molecules may also lead to macroscopic chiral configurations[5,6]. In this study, we documented the emergence of chiral structures from achiral lyotropic chromonic liquid crystals (LCLCs) confined to curved geometries.

When LCLCs were confined to cylindrical capillaries with degenerate planar anchoring, we surprisingly found a highly twisted configuration that replaced the usual axial configuration with no deformation[7,8]. The stability of this chiral configuration was attributed to the saddle-splay elasticity which significantly lowers the elastic free energy. Additionally, the emergence of the chiral configuration enabled us to estimate of the saddle-splay elastic constant for LCLCs as a function of temperature and concentration. Due to the small twist elastic constant, two chiral configurations were observed for LCLCs in cylindrical capillaries with homeotropic anchoring[9,10]. The study of these chiral configurations revealed the roles of aggregation behavior and surface anchoring on the director field. Using lyotropic polymer liquid crystals, we further generalized the emergence of chirality to other achiral lyotropics confined to cylindrical geometry. We suggested that the spontaneous chirality should be a universal configurational behavior for various achiral lyotropic systems with small twist elastic constant, which is independent from their chemical components.

Moreover, besides the usual achiral bipolar configuration, we observed two chiral configurations with LCLCs confined to the tactoidal geometry[11], which is a natural

confinement of nematics formed during the phase transition. Remarkably, one of these chiral configurations has long been proposed theoretically[12], but for first time it was realized in our experiments. At different temperatures and concentrations, the configurational transformation of LCLC tactoids was rationalized by the shifts of the average aggregate length. By exploiting the configurations of tactoids, we then studied the aggregation behavior of LCLCs with the addition of neutral polymer and ionic salts additives. Finally, the effects of different monovalent salts were further investigated on the transition temperatures and the orientational order of LCLCs. Our study reveals the physical insights of the chiral configurations from achiral lyotropics, which changes the common expectations of nematic materials based on the studies of thermotropic liquid crystals. The spontaneous emergence of chirality from achiral liquid crystals improves the general understanding of the symmetry-breaking phenomena in nature.

CHAPTER 1. INTRODUCTION

1.1 Chirality

1.1.1 The emergence of chirality in nature

Chirality is an asymmetric property of a structure that cannot be superimposed with its mirror image. Human hands are perhaps the most universal example of chirality. The left hand cannot overlap with the right hand, no matter how the hands are translated or rotated. The emergence of chirality is widely involved in various phenomena in nature[6,13]. Most of the known life systems show preference to a particular handedness of the chiral structure rather than its counterpart, which is known as homochirality and recognized as a signature of life[2,3,14]. For instance, the chiral molecular structures of amino acids (Figure 1.1a) are usually left-handed in nature[15], but the coiled shells of snails (Figure 1.1b) often exhibit right handedness[16]. Another intriguing phenomenon ascribed to chirality is the structural color of beetles[1]. The exoskeleton of the beetle is decorated by hexagonal cells with chiral structures. The light reflected by the chiral structures in the cells are left circularly polarized, leading to the green color viewed by the left circular polarizer as illustrated in the left image of Figure 1.1c. In the right image, the green color is lost because the reflected light is blocked by right circular polarizer.

To better understand the chirality-related phenomena in nature, it is crucial to investigate the origins of chiral structures. Intuitively, macroscopic chiral structures can result from the chirality of the constituent molecules[4,13,17]. For instance, a tartaric acid molecule in Figure 1.2a has two asymmetric carbons bonded with four different groups.

These asymmetric carbons are called stereogenic centers, which is a signature of molecular chirality. As discovered by Pasteur's brilliant experiments[4], levorotatory and dextrorotary enantiomers of tartaric acid molecules can be isolated by the formation of left-handed and right-handed chiral crystals, respectively. There are also exceptions of chiral molecules without a stereogenic center[18]. For instance, a derivative of ferrocene molecule in Figure 1.2b has two asymmetric rings which cannot easily rotate along the axis of the connecting bond[19]. These chiral molecules lacking the stereogenic centers are referred as planar chiral molecules.

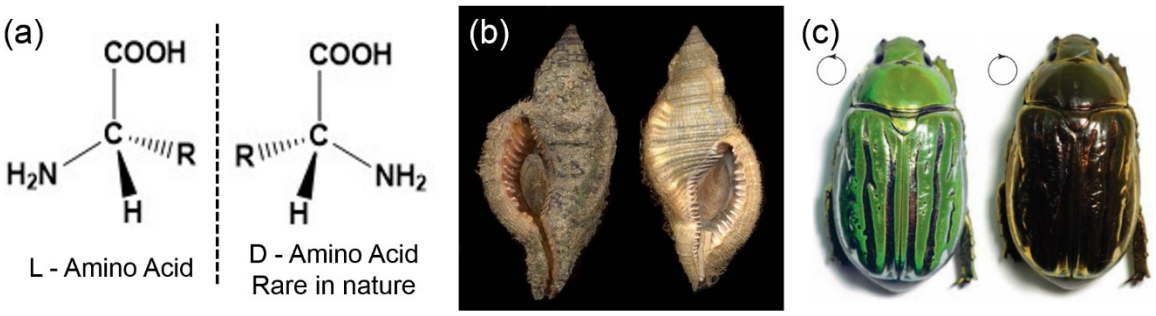

Figure 1.1 Chiral structures in nature. (a) The normal levorotatory (L-) and the rare dextrorotatory (D-) amino acid molecules. (b) A normal dextral specimen (right) and a rare sinistral specimen (left) of a snail species (*Cymatium pileare*)[16]. (c) The beetle, *C. gloriosa*, under the left-handed (left) and the right-handed (right) circularly polarized light[1].

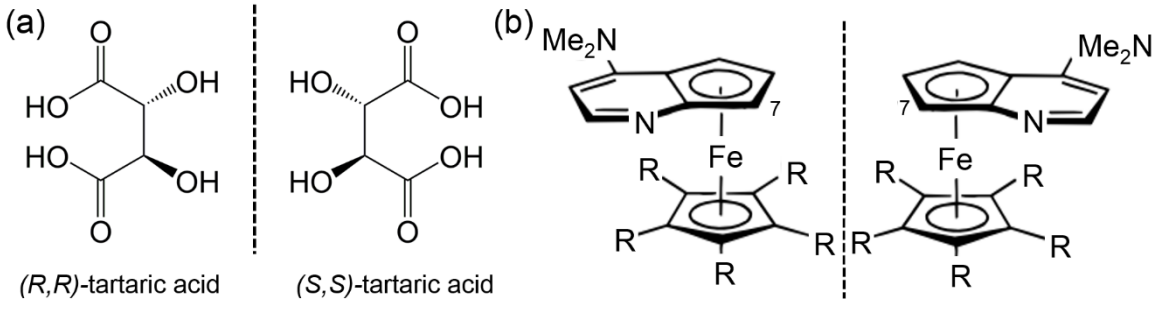

Figure 1.2 Examples of chiral molecules. (a) Tartaric acid enantiomers[4]. (b) The enantiomers of a derivative of ferrocene molecule with planar chirality[19].

Nevertheless, a more interesting finding is that molecular chirality is not an essential requirement for the formation of macroscopic chiral structures. Achiral molecules can also lead to macroscopic chirality[5,7,9,20-25]. As an example, the crystallization of sodium chlorate can occur in levo- or dextro- formats even though the ions are achiral[5,20]. But the mechanism of the symmetry-breaking crystal growth is still controversial. Another attractive group of achiral materials that can exhibit chiral structures is liquid crystals[7,9,21-25]. The chiral structures of achiral liquid crystals are the focus of this thesis and will be discussed intensively in the following chapters.

1.1.2 Chiral structures of achiral liquid crystals

Liquid crystal materials can be composed of either chiral or achiral molecules. With molecular chirality, the liquid crystal molecules adopt a twisting helical structure and exhibit cholesteric phase[26] as shown in Figure 1.3a. However, chiral structures can also emerge from achiral liquid crystal molecules[27-32]. In some situations, the emergence of chirality is attributed to unique structure of the achiral molecules[27,28]. In Figure 1.3c, the structure of a bent-core molecule has two branches making an angle with the core in the center[33,34]. The bent shape of the molecules results in the separation of chiral domains in the smectic liquid crystalline phase[35]. In other cases, the chiral structures can be induced by the confinement effect and the elastic properties from the usual rod-like achiral building blocks. This type of chiral configurations has been reported when the achiral liquid crystals were confined to droplets[27,28], tori[29,30], and microcavities[31,32]. For the chiral structure of a spherical droplet shown in Figure 1.3b[27], the orientations of the building blocks spontaneously break the mirror symmetry of the structure by forming a twist deformation. In this thesis, we will show our observations of the novel chiral configurations from achiral

liquid crystals in cylindrical[7-10] and tactoidal[11,36] geometries. By revealing the driving force of these chiral configurations, we provide significant physical insights to the fundamental understanding of the spontaneous chirality from achiral molecules.

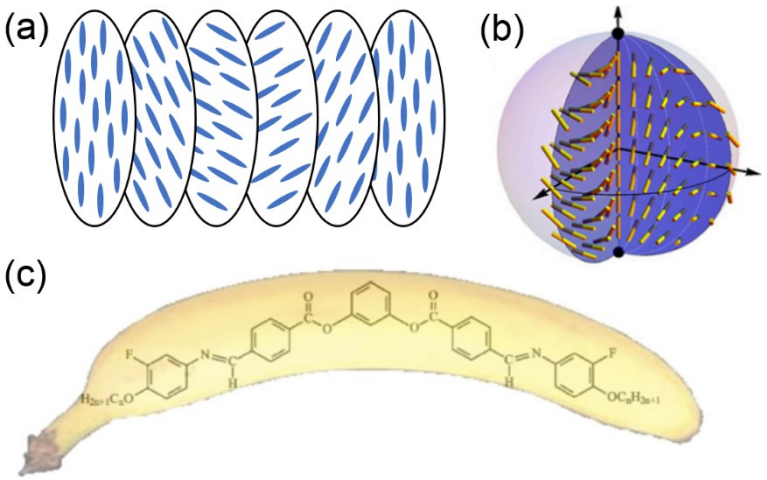

Figure 1.3 (a) Illustration of cholesteric liquid crystalline phase. (b) Chiral structure of achiral liquid crystal confined to a droplet[27]. (c) A bent-core molecule (also called banana-shaped molecule)[34].

Besides inspiring the origins of chirality in nature, investigating the chiral configurations of achiral liquid crystals is crucial to the development of opto-electronic devices[34,37-42]. The importance of chiral configurations of liquid crystals is distinguished in the display technology[37,40,43]. As illustrated in Figure 1.4, each pixel of liquid crystal display consists of a liquid crystal film between crossed polarizers. The molecules in the liquid crystal film adopt a twisted structure without any external fields (Figure 1.4a). The twist deformation rotates the polarization of incident light due to the wave-guiding phenomenon (will be discussed in Chapter 2.3.2)[37], leading to brightness of this pixel. When the electric voltage is applied (Figure 1.4b), the pixel becomes dark because liquid crystal molecules align parallel with the electric field and lose the twist deformation in the director structure. The light is completely blocked by the crossed polarizers because the

polarization is not shifted by the director field. Hence, the switch of the pixel is controlled by the external electric field, which changes the interaction between the director configuration and polarized light. Other applications of liquid crystals have also been explored in literature including optical components[44,45], sensors[11,46], organic electronics[47,48], and the precursors for carbon fabrication[49,50]. As will be discussed in this thesis, the chiral configurations we observed with achiral liquid crystals in different geometries may open new possibilities for the display and sensing applications.

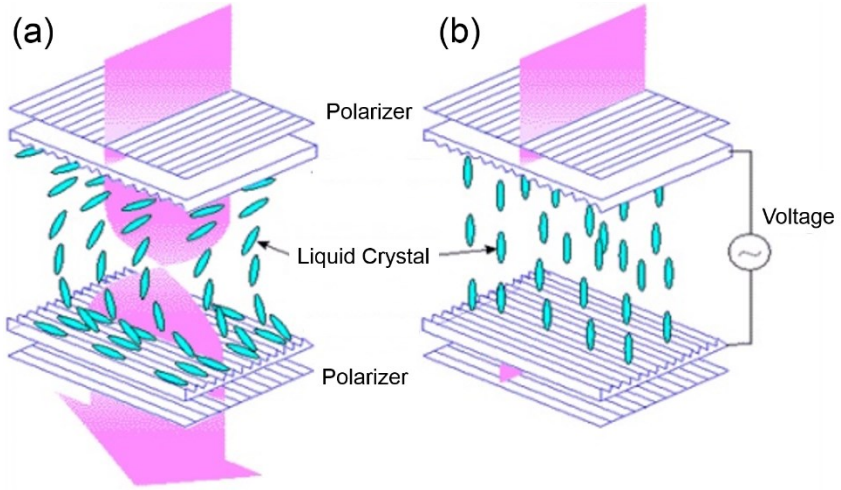

Figure 1.4 Optics of liquid crystal display. (a) No electric field. (b) Under the external electric field. Images are copied from website[51].

1.2 Nematic Liquid Crystals

1.2.1 Nematic liquid crystalline phase

Many materials exhibit multiple intermediate phase transitions from isotropic liquid to highly-ordered crystals. Considering rod-like building units in Figure 1.5, the material is in the isotropic liquid phase when the rods have random orientations and random positions. When the rods are densely packed as 3-D periodic cells with fixed orientations

and positions, the material exhibits anisotropic crystalline phase. Upon liquid phase to crystalline phase transition, the molecules lose the continuous rotational and translational symmetries, and gain both orientational and positional orders. Liquid crystalline phases have the symmetry and order between the liquid and the crystal. In the simplest liquid crystalline phase (nematic phase)[52], the rod-like mesogens are oriented in a particular direction, which is called the director of nematics and represented by a bivector, ***n***. But the mass centers of the rods are still random. Therefore, the nematic phase has partial orientational order but lacks positional order.

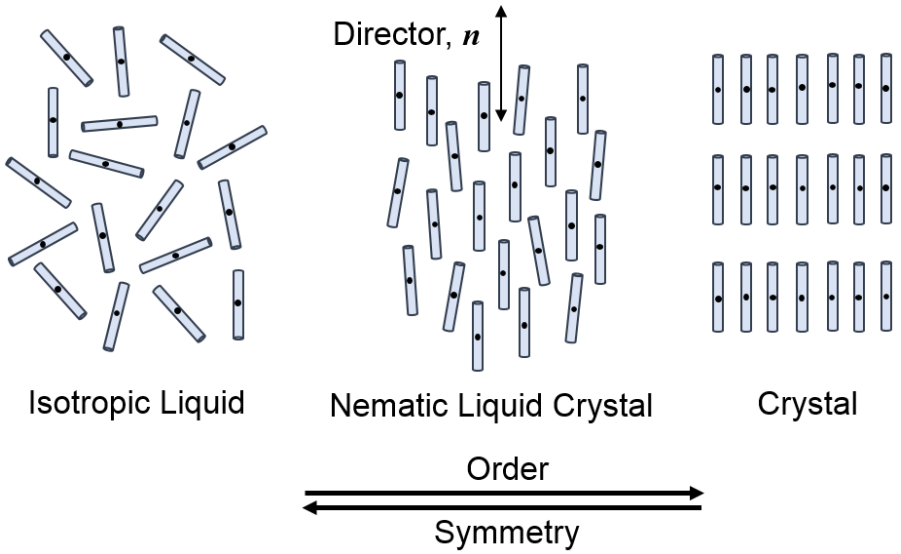

Figure 1.5 Phases of matter: liquid, nematic liquid crystal, and crystal.

Due to the intermediate symmetry and order, nematic phase exhibits rich phenomenology that arouse the interests of industrial applications[37,53,54] and fundamental research[55-60]. Mechanically nematic liquid crystals can flow like a liquid. But the long-range orientational order of nematics results in the anisotropic optical properties (birefringence), which leads to various optical effects. The interactions of liquid crystals with light have been widely integrated in industrial technologies, including display[37], bio-

sensing[53], and optical components[54]. The optical interactions are determined by the director configurations of nematics under confinement, which motivates the exploration of the configurational behavior and the underlying physics of nematic materials.

Besides nematic phase, there are other liquid crystalline phases with more complicated structures[61,62], such as cholesteric phase, smectic phases, columnar phase, blue phases, etc. For example, rather than aligning along a fixed director like nematic phase, the chiral mesogens in cholesteric phase form a helical structure in space as illustrated in Figure 1.3a[63]. In the smectic phases, both the orientational order and a small portion of positional order are present[58]. However, in this thesis, we will focus on the configurations and properties of nematic phase only.

1.2.2 Elasticity theory of liquid crystals

The director field of nematic phase naturally points towards a particular direction to avoid any deformations. This non-deformed uniform structure is expected to be the ground state when the nematic phase is perfectly aligned between flat surfaces with either planar anchoring (the director is parallel with the surface) or homeotropic anchoring (the director is perpendicular to the surface). However, confinements with curved surfaces result in much richer director configurations. The director field defers to the anchoring conditions on the curved surfaces at the expense of the elastic deformations of different modes. The deformations of the director field contribute to the elastic free energy, which can be described by the elastic continuum theory.

The elasticity theory of liquid crystals was firstly derived by Oseen[64] from the molecular level and later developed by Frank[65] in a phenomenological approach. Frank's

approach considers a local distortion of director represented by a unit bivector, $\boldsymbol{L}$. The variation of the director field is assumed to be slow on the molecular scale ($a_l \nabla \boldsymbol{L} \ll 1$, where a_l is the length of the molecules). The local Cartesian coordinates, *x, y, z*, are introduced with *z* axis parallel with $\boldsymbol{L}$ at the origin. Then the three local distortions, splay, twist, and bend, are the six components of curvatures as illustrated in Figure 1.6 [65].

$$\begin{aligned} &"Splay": \ s_1 = \partial L_x/\partial x, \ \ s_2 = \partial L_y/\partial y \\ &"Twist": \ t_1 = -\partial L_y/\partial x, \ \ t_2 = \partial L_x/\partial y \\ &"Bend": \ b_1 = \partial L_x/\partial z, \ \ b_2 = \partial L_y/\partial z \end{aligned} \tag{1.1}$$

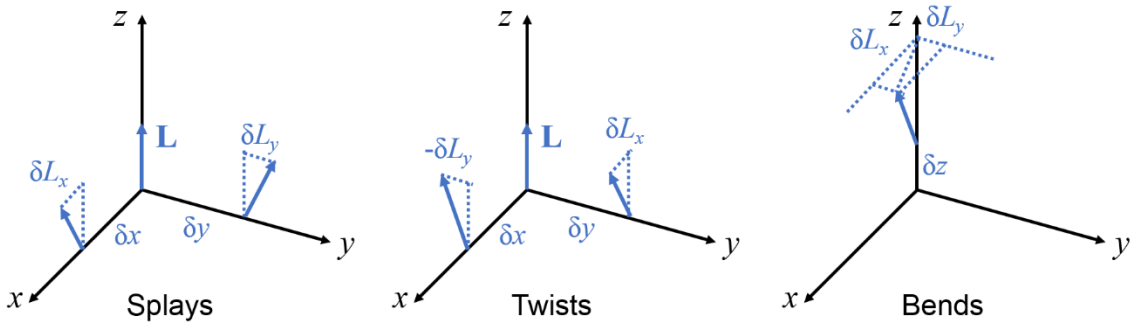

Figure 1.6 Six components of curvature in local Cartesian coordinates.

The bivector **L** can then be expressed by the six coefficients[65]:

$$\begin{aligned} L_x &= a_1 x + a_2 y + a_3 z + O(r^2) \\ L_y &= a_4 x + a_5 y + a_6 z + O(r^2) \\ L_z &= 1 + O(r^2), (r^2 = x^2 + y^2 + z^2) \end{aligned} \tag{1.2}$$

where $s_1 = a_1, t_2 = a_2, b_1 = a_3, -t_1 = a_4, s_2 = a_5, b_2 = a_6$.

The free energy density, *g*, is the quadratic function of the six coefficients[65].

$$g = k_i a_i + \frac{1}{2} k_{ij} a_i a_j, (i, j = 1 \ldots 6, k_{ij} = k_{ji}) \tag{1.3}$$

This expression can be simplified by imposing restrictions from the symmetry of the system. It is noted that reversing the director does not make any difference to nematic phase ($\boldsymbol{L}$ = -$\boldsymbol{L}$). Most of the liquid crystal molecules are non-polar. For polar molecules, it is equally possible for the molecules to be oriented "upwards" or "downwards". Hence, nematic liquid crystal lacks polarity and the free energy density is an even function of $\boldsymbol{L}$. Moreover, changing the axes of the coordinates should not change the elastic free energy of the director field. After imposing all the restrictions, the final expression of the elastic free energy density only contains four terms, corresponding to the director deformations of splay, twist, bend, and saddle-splay modes[65]:

$$g = \frac{1}{2}k_{11}(s_1 + s_2)^2 + \frac{1}{2}k_{22}(t_1 + t_2)^2 + \frac{1}{2}k_{33}(b_1^2 + b_2^2) - (k_{22} + k_{24})(s_1 s_2 + t_1 t_2) \qquad (1.4)$$

It was later pointed out by Nehring and Saupe[66] that Frank missed another term, the splay-bend term, in the elastic free energy expression which originally existed in Oseen's description[64]. After some mathematical transformations, the complete expression of the total elastic free energy, *F*, is written as the volumetric integral of five energy density terms in equation 1.5 [57]:

$$F = \int g dV = \frac{1}{2}\int dV \left[K_{11}(\nabla \cdot \boldsymbol{n})^2 + K_{22}(\boldsymbol{n} \cdot \nabla \times \boldsymbol{n})^2 + K_{33}(\boldsymbol{n} \times \nabla \times \boldsymbol{n})^2 - \right.$$

$$\left.(K_{22} + K_{24})\nabla \cdot (\boldsymbol{n}(\nabla \cdot \boldsymbol{n}) + \boldsymbol{n} \times \nabla \times \boldsymbol{n}) + K_{13}\nabla \cdot \big(\boldsymbol{n}(\nabla \cdot \boldsymbol{n})\big)\right] \qquad (1.5)$$

where $\boldsymbol{n}$ is the vector of director field, the coefficients of each energy density terms, K_{11}, K_{22}, K_{33}, K_{24}, and K_{13} are the elastic constants of the director deformations modes, splay, twist, bend, saddle-splay, and splay-bend deformations, respectively.

1.2.3 Discussions about elasticity theory

The coefficients of the terms in equation 1.5 are the elastic constants of different deformation modes. K_{11}, K_{22}, and K_{33} represent three bulk deformations, splay, twist, and bend (Figure 1.7a). K_{24} and K_{13} represent the saddle-splay and splay-bend deformations, which describe splay&twist and splay&bend distortions, respectively. The saddle-splay deformation can be illustrated vividly by the spontaneous splay and twist distortions of the toothpicks in Figure 1.7b. In prior literature, the splay, twist, and bend elastic free energies were relatively well understood and the three elastic constants have been characterized for a lot of liquid crystalline materials[67-70]. However, the contributions of saddle-splay and splay-bend elastic free energy were often debatable[71-73] since these two deformation modes cannot be easily separated from other modes. Several studies neglected the saddle-splay and splay-bend terms[66,69,74] because the saddle-splay (F_{24}) and the splay-bend (F_{13}) elastic free energies are expressed as the divergence forms in the volumetric integrals, which can be transformed to the surface integrals by Gaussian theorem as shown in equation 1.6 [57].

$$F_{24} + F_{13} = -\frac{1}{2}(K_{22} + K_{24}) \int dV \left[\nabla \cdot (\boldsymbol{n}(\nabla \cdot \boldsymbol{n}) + \boldsymbol{n} \times \nabla \times \boldsymbol{n})\right] + \frac{1}{2} K_{13} \int dV \left[\nabla \cdot \left(\boldsymbol{n}(\nabla \cdot \boldsymbol{n})\right)\right] =$$
$$-\frac{1}{2}(K_{22} + K_{24}) \int dS \left[\boldsymbol{\nu} \cdot (\boldsymbol{n}(\nabla \cdot \boldsymbol{n}) + \boldsymbol{n} \times \nabla \times \boldsymbol{n})\right] + \frac{1}{2} K_{13} \int dS \left[(\boldsymbol{\nu} \cdot \boldsymbol{n})(\nabla \cdot \boldsymbol{n})\right] \tag{1.6}$$

where $\boldsymbol{\nu}$ is the unit vector pointing outward along the normal of the boundary surface. Therefore, the saddle-splay and splay-bend terms are also referred as divergence terms or surface terms in the literature. As a result, there is a common argument that the director distortions approaching to the surface (saddle-splay and splay-bend deformations) are negligible in comparison to the deformations in the bulk (splay, twist, and bend deformations)[66,74,75]. However, this statement can be misleading because the saddle-splay and splay-bend terms describe the director deformations in the bulk, even though they can

be calculated by surface integrals. Although very little is known about the splay-bend elasticity currently, the saddle-splay elasticity has been found to play an important role on the director configurations, especially under the confinement effects of curved geometries[29,76-78].

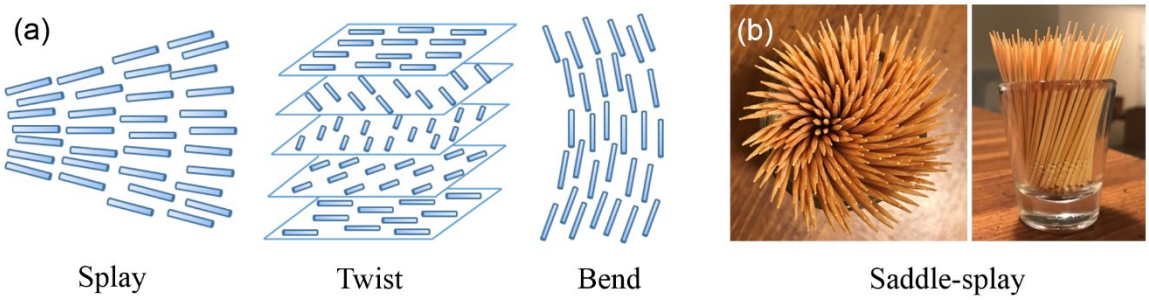

Figure 1.7 Illustrations of the director deformation modes. (a) The splay, twist, and bend director deformations. (b) The saddle-splay deformation illustrated by toothpicks in a glass.

The effects of confinement surfaces on the director configurations can be seen from the elastic free energy expression[65], which is a function of $(\nabla \boldsymbol{n})^2$. The effect of curvature is clearly shown in the saddle-splay and splay-bend elasticities[57] expressed as the second order derivatives of $\boldsymbol{n}$. Moreover, with planar anchoring, the saddle-splay elastic free energy can be transformed in term of principal curvatures, κ_1 and κ_2 [29]:

$$F_{24} = -\frac{1}{2}(K_{22} + K_{24}) \int dS \, (\kappa_1 n_1^2 + \kappa_2 n_2^2) \tag{1.7}$$

where n_1 and n_2 are director components along principal curvatures. Remarkably, we note that all the other elastic terms have a plus sign and increase the elastic free energy, but the saddle-splay deformation is the only term with a minus sign that can possibly reduce the elastic free energy. Hence, one would speculate that the stabilization of saddle-splay elasticity may lead to unexpected nematic configurations, especially under confinements

with curved surfaces. The saddle-splay effect on the director configurations has already been recognized in geometries with curvature, such as cylinders[79], tori[29,30], and droplets[80]. In this thesis, we will emphasize the importance of the saddle-splay term in Chapter 2 on the stabilization of the chiral configurations under cylindrical confinement.

1.2.4 Liquid crystal optics: polarized optical microscopy

Due to the long range orientational order, nematic liquid crystals exhibit birefringence with different refractive indices parallel ($n_{\parallel}$) and perpendicular ($n_{\perp}$) to the optical axis. When a nematic sample is placed between crossed polarizer and analyzer of a polarized optical microscope, the linearly polarized light passing through the sample can be decomposed to two rays, ordinary ray and extraordinary ray. The two rays experience different refractive indices of liquid crystal, which results in a phase retardation[37]: $\Gamma = \frac{2\pi}{\lambda}(n_e - n_o)d$, where λ is wavelength, d is sample thickness, n_e and n_o are the extraordinary and ordinary refractive indices related to $n_{\parallel}$ and $n_{\perp}37$ ($n_e = \frac{n_{\parallel}n_{\perp}}{\sqrt{n_{\parallel}^2 cos^2\varphi + n_{\perp}^2 cos^2\varphi}}$, $n_o = n_{\perp}$, where φ is the angle between optical axis and polarization of the light). Upon exiting the sample, the two rays with different phases recombine as an elliptical polarized light, which may transmit through the crossed analyzer. Hence, in our studies, we intensively used the birefringent textures under crossed polarizers to decipher the director configurations of nematic liquid crystals.

1.3 Lyotropic Chromonic Liquid Crystals (LCLCs)

1.3.1 Categories of liquid crystal materials

There are mainly two categories of liquid crystal materials, thermotropic liquid crystals and lyotropic liquid crystals[61]. Thermotropic materials exhibit liquid crystalline phases in a specific temperature range, free of solvents. They are used in most of the liquid crystal applications, hence their properties and behaviors are relatively well understood. The study of thermotropic liquid crystals has provided the basic knowledge and expectations for the behavior of conventional liquid crystalline materials. One of the most representative thermotropic molecules is 4-Cyano-4'-pentylbiphenyl, commonly called 5CB[40,81]. As shown in Figure 1.8a, individual 5CB molecule has a rod-like shape and serves as a building unit of nematic phase. 5CB undergoes a phase transition from crystalline to nematic phase at around 23 ^{o}C, and a phase transition from nematic to isotropic phase at around 35 ^{o}C [40,81].

Lyotropic liquid crystals exhibit liquid crystalline phases with the help of appropriate solvents[82]. The phase transition depends on both the concentration and the temperature. Historically, lyotropic liquid crystals refer to amphiphilic molecules[59,82] like surfactants, lipids, and proteins. Since many of these molecules exist in living organisms, the behaviors of lyotropics are crucial to understand the phenomenology in biological systems[83]. The interests in lyotropic liquid crystals have been growing as they exhibit intriguing configurational phenomena different from the conventional thermotropic liquid crystals[82,84-86]. Other lyotropic materials, such as polymer[87-89] liquid crystals and chromonic liquid crystals[90,91], have also been discovered and explored. In this thesis, we mainly focus on the lyotropic chromonic liquid crystals (LCLCs) to study their unusual chiral structures in curved geometries. We also use the thermotropic liquid crystal, 5CB,

as a comparison to show that the chiral configurations of LCLCs are distinctly different from the common expectations based on thermotropic liquid crystals.

1.3.2 Lyotropic Chromonic Liquid Crystals (LCLCs)

For conventional liquid crystals like 5CB, the constituent units of nematic phase are the individual rod-like molecules (Figure 1.8a). However, LCLCs depart from the conventional liquid crystals as their mesogens are self-assembled aggregates[90-92]. Figure 1.8b shows two typical achiral LCLC molecules, Sunset Yellow FCF (SSY) and disodium cromoglycate (DSCG). The plank-like molecules have a poly-aromatic core and two hydrophilic side groups. The molecules stack and form rod-like aggregates when they are dissolved in water. The aggregates are stabilized by the electrostatic interactions and hydrophilic-hydrophobic interactions between LCLC and water molecules. π-π interactions between hydrophobic poly-aromatic cores facilitate LCLC molecules to stack face to face. The ionic repulsions between hydrophilic side groups keep the distance between the adjacent LCLC aggregates. This self-assembly encloses the hydrophobic cores in the center of the aggregates and leaves hydrophilic side groups on the water-aggregate interface. At low concentrations or high temperatures, LCLC solutions exhibit isotropic phase with small aggregates oriented randomly. With the increase in concentration or the decrease in temperature, the aggregates grow longer and form the oriented nematic phase. The aggregation behavior is the molecular basis to understand the elastic properties and the configurational behavior of LCLCs.

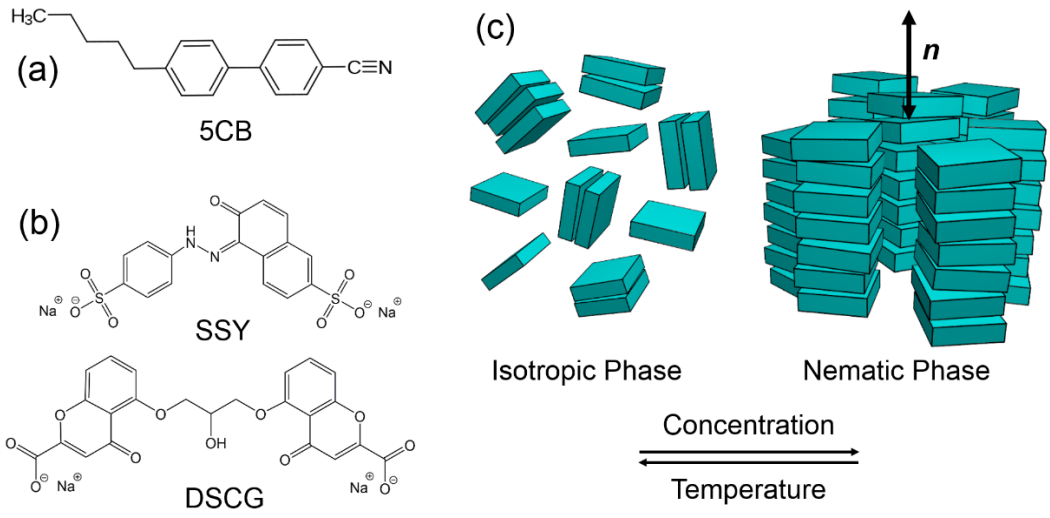

Figure 1.8 (a) Molecular structure of a thermotropic liquid crystal, 5CB. (b) Molecular structures of two LCLCs, SSY and DSCG. (c) Illustration of LCLC aggregates in isotropic phase and nematic phase.

Previous studies have demonstrated the significant elastic anisotropy of LCLCs, which is different from the properties of conventional liquid crystals. Elastic constants measurements of SSY and DSCG show that the splay and bend elastic constants are roughly in the same order, but the twist elastic constant is one order of magnitude smaller[93-95]. However, the three bulk elastic constants for thermotropic liquid crystals are usually in the same order of magnitude[52]. The small twist elastic constant of LCLCs indicates that the director field takes little energy to form a twist deformation (which is a signature of chiral configurations) rather than the splay and bend deformations. Moreover, the dependence of elastic constants of LCLCs on temperature and concentration does not agree with the phenomenological Landau-de Gennes model[93-95], which usually explains the elasticity of thermotropics[52]. Instead, the elastic behavior of LCLCs matches with the model for polymer liquid crystal considering the semi-flexibility of the rods[88]. Additionally, the traditional Onsager theory[96] fails to predict the phase transition of LCLCs. The product of volume fraction (ϕ) and the length-over-diameter ratio (L/D) for LCLCs ($\phi L/D$ = 0.3~1.5

[97]) is too small to meet Onsager's criterion for nematic order[98] ($\phi L/D > 4$). All these unusual phenomena intrigue us to study the configurations, elastic properties, and the aggregation behavior of LCLCs.

1.4 Thesis Outline

In the following chapters, we will show the surprising chiral structures from achiral LCLCs in curved geometries, which are not commonly expected for thermotropic liquid crystals. In Chapter 2, we report the chiral configurations of LCLCs rather than a deformation-free director configuration in cylindrical capillaries with degenerate planar anchoring[7,8]. Besides ascribing the formation of chirality to the small K_{22} of LCLCs, we highlight the key role of the saddle-splay elastic free energy on the stability of the chiral configuration. Remarkably, we, for the first time, exploited the chiral configuration to investigate K_{24} as a function of temperature and concentration. In Chapter 3, we report the results when we changed the boundary condition of the cylindrical capillaries. Two chiral configurations were observed for LCLCs with homeotropic anchoring on the surface[9,10]. Due to the small K_{22} of LCLCs[93-95], the director field initially exhibited a twisted and escaped radial configuration, which was then replaced by another chiral configuration with twisting line defects. The birefringent texture of the twisted and escaped radial configuration was studied as temperature and concentration were varied. The shifts of the birefringent texture were intrinsically determined by the aggregation behavior of LCLCs and the subsequent effects on the elastic constants. With high concentrations, we observed a novel configurational behavior of LCLCs, where the domains with different chiral configurations co-exist in the same cylindrical capillary. Since all the chiral configurations are driven by the small K_{22} of LCLCs, we expect that the emergence of chirality should be

widely present for different lyotropic liquid crystal materials because their K_{22} are commonly much smaller than K_{11} and K_{33}, which is independent from their chemical components. We validated this expectation in Chapter 4 using a lyotropic polymer liquid crystal, wherein the molecular structure is notably different from LCLCs. But rather remarkably, the racemic solutions of the lyotropic polymer liquid crystals exhibit the same chiral configurations as LCLCs in the cylindrical capillaries.

The configurations of LCLCs were then explored in another curved geometry, tactoids, which is a natural confinement of nematics during the phase transition. Besides the usual achiral bipolar structure[99,100] at high concentrations and temperatures, two chiral configurations of LCLC tactoids emerged at low concentrations and temperatures[11]. One of the chiral configurations, called escaped-concentric structure, has long been proposed theoretically[12], but for the first time it was observed in our experiments. We find that the configurational transformation of LCLC tactoids probes the change of average aggregate length as temperature and concentration are varied. Using the configurations of LCLC tactoids, we further studied the effects of external additives (neutral polymer and monovalent salts) on the aggregation behavior of LCLCs in Chapter 5 and 6. Moreover, the effects of monovalent salts on the LCLC tactoids exhibit intriguing dependence on LCLC concentration, salt concentration, and salt cation, which motivated us to further investigate the salts effects on the transition temperatures and order parameters of LCLCs in Chapter 7. A plausible mechanism of salts effects on LCLCs aggregates was also proposed based on the screening of electrostatic repulsion. Chapter 8 summarizes our findings and suggests future works.

CHAPTER 2. CHIRAL CONFIGURATION OF LCLCS UNDER CYLINDRICAL CONFINEMENT WITH PLANAR ANCHORING

2.1 Introduction

As a simple geometry with curvature, cylindrical geometry was intensively used in literature to study the confinement effect on the director configurations of nematic liquid crystals[77,101-105]. Notably, the principal curvatures of cylindrical geometry are different in the axial and the azimuthal directions, imposing significant impact on the saddle-splay contribution to the elastic free energy[29]. Most of the prior studies focus on the director configurations in cylindrical confinement with homeotropic anchoring (the director is anchored perpendicular to the surface)[77,79,103,106,107], which will be discussed in Chapter 3. The study of cylindrical confinement with planar anchoring (the director is anchored parallel with the surface) is rare because there exists an axial configuration free of any deformation as illustrated in Figure 2.1a. This configuration is adopted by the conventional thermotropic liquid crystals like 5CB in a borosilicate cylindrical capillary with degenerate planar anchoring. As shown in Figure 2.1b, 5CB looks completely dark under crossed polarizers when the capillary axis is parallel with or perpendicular to the polarizer. The transmitted intensity emerges when the capillary is rotated by 45^{o} as shown in Figure 2.1c. This birefringent pattern indicates that the director everywhere is along the axial orientation of the cylinder. The axial configuration is commonly expected as the ground state of nematics in cylindrical confinement with planar anchoring since the director field has no deformation that may cost elastic free energy. However, we found a different chiral configuration for LCLCs confined to borosilicate cylindrical capillaries with degenerate planar anchoring. Rather surprisingly, this chiral configuration with a large twist distortion replaces the non-deformed axial configuration as the ground state of LCLCs.

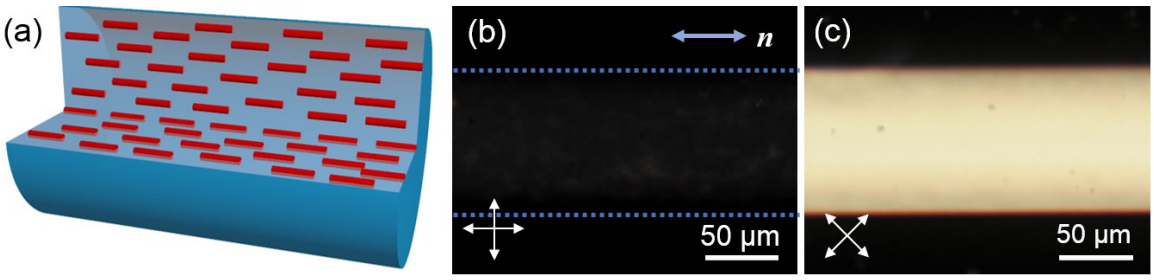

Figure 2.1 (a) Director field of the axial configuration. Red rods represent the director of nematic liquid crystal. (b, c) Polarized optical microscopy image of 5CB with the axial configuration under crossed polarizers. The blue dot lines indicate the inner boundary of the cylindrical capillary. The orientations of polarizer and analyzer are indicated by the double-headed white arrows. The director orientation is indicated by the double-headed blue arrow.

2.2 The doubly-twisted (DT) configuration of LCLCs[7,8]

The discussion in section 2.2 is based on the collaboration with Dr. Karthik Nayani, Dr. Jinxin Fu, and Dr. Perry Ellis.

2.2.1 Polarized optical microscopy observations

Departing from 5CB, the LCLC material, DSCG, in a borosilicate cylindrical capillary exhibits a different birefringent texture (the materials and sample preparations are described in Appendix A.7.1 and A.7.2). As shown in Figure 2.2a and 2.2b, multiple domains exist in a single cylinder separated by domain walls. Individual domain shows transmitted intensity even though the polarization is parallel to the long axis of the capillary. The transmitted intensity under crossed polarizers is an indication of twisted director field, which guides the polarization and enables the light to pass through the crossed polarizers[37]. We use a doubly-twisted (DT) director configuration illustrated in Figure 2.2g to explain the observed texture. The director is along the axial orientation in the center of the cylinder and progressively twists from the center to the boundary.

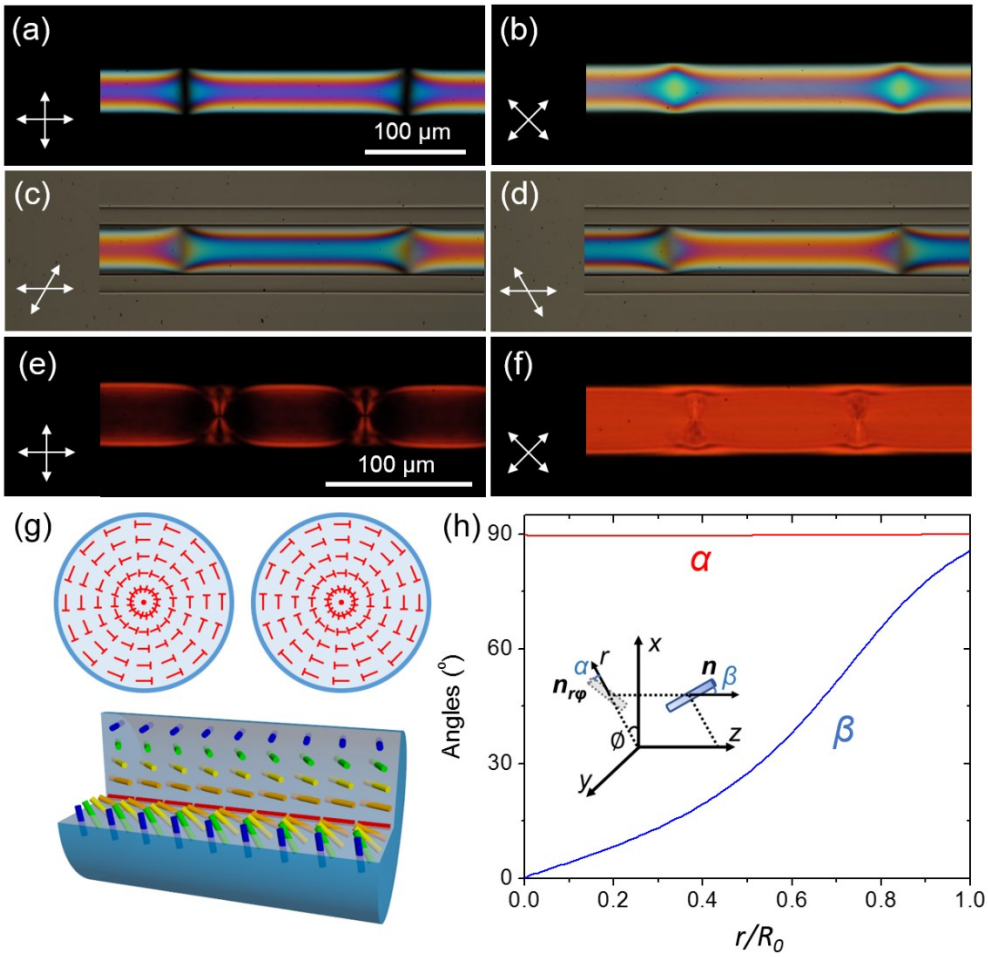

Figure 2.2 (a-d) Polarized optical microscopy images of DSCG in a borosilicate cylindrical capillary. (a) Under crossed polarizers, the polarizer is parallel with the capillary axis. (b) Under crossed polarizers, the polarizer makes an angle of 45° with the capillary axis. (c, d) The polarizer and analyzer make an angle of 60°. (e, f) Polarized optical microscopy images of SSY in a borosilicate cylindrical capillary under crossed polarizers. (e) The polarizer is parallel with the capillary axis. (f) The polarizer makes an angle of 45° with the capillary axis. The orientations of polarizer and analyzer are indicated by the double headed white arrows. (g) Illustrations of the DT director field. In the cross sections, the nail head indicates that this side of the director points into the viewing plane. (h) Calculated director field of the DT configuration. The inset shows the definitions of characteristic angles, α and β.

For achiral DSCG molecules, the left-handed and right-handed twist deformations are energetically equivalent. Hence, both left-handed and right-handed DT domains are equally expected to emerge in the cylindrical capillary. In Figure 2.2c and 2.2d, the color changes when polarizer and analyzer make an angle of 60° clearly show that the director

fields in the adjacent domains twist with opposite handedness. In Figure 2.2e and 2.2f, the DT director configuration was also observed using another LCLC material, SSY. The domains with opposite twist handedness are separated by point defects.

2.2.2 The role of saddle-splay elastic free energy

After discussing the director configuration, we noticed that it is unusual for the DT chiral structure to be the ground state of LCLCs when there exists an axial director configuration with no deformation, since the twist deformation in the chiral configuration costs elastic free energy and destabilizes the chiral configuration. To explain the stability of the DT configuration, we looked into the morphology of the inner surface of the borosilicate cylindrical capillary in Appendix A.1.1 Figure A.1. But we did not observe any visible patterns that may align the director on the surface. Here we rationalize the emergence of the DT configuration by considering the role of saddle-splay term in the elastic free energy expression. As mentioned in section 1.2.3, for degenerate planar anchoring, the saddle-splay elastic free energy can be expressed in terms of two principal curvatures of the geometry, κ_1 and κ_2[29]: $F_{24} = -\frac{1}{2}(K_{22} + K_{24}) \int dS\,(\kappa_1 n_1^2 + \kappa_2 n_2^2)$. In cylindrical confinement, κ_1 in axial orientation is 0 and κ_2 in azimuthal orientation is $1/R_0$ (R_0 is the inner radius of the cylindrical capillaries). The saddle-splay term reduces the elastic free energy by aligning the director on the surface along larger principal curvature[29,30] in the azimuthal orientation, which is in favor of the DT configuration. In this situation, the splay, twist, and bend deformations are screened by the contribution of saddle-splay elasticity, which drives the total elastic free energy of the DT configuration lower than the non-deformed axial structure.

We performed numerical minimization of the elastic free energy to study the stable configurations of LCLCs in cylinders using the relaxation method[9,108,109]. In cylindrical coordinates, the director $\boldsymbol{n} = (n_r, n_\emptyset, n_z)$ can be described by two characteristic angles, α and β, as illustrated in the inset of Figure 2.2h. α is the angle between the projection of director in r-ϕ plane and r axis. β is the angle between director and z axis. Hence, the director is expressed as $\boldsymbol{n} = (cos\alpha sin\beta, sin\alpha sin\beta, cos\beta)$. Using the relaxation method, α and β converge to the solution of Euler-Lagrange equations by solving the partial differential equations[9,107,108]: $\frac{\partial \alpha}{\partial t} = -\Gamma_\alpha \frac{\delta F}{\delta \alpha}$, $\frac{\partial \beta}{\partial t} = -\Gamma_\beta \frac{\delta F}{\delta \beta}$, where Γ_α and Γ_β are the relaxation rate factors, t is the time coordinate introduced in relaxation method, F is the elastic free energy. The value of t increases in the iterations as α and β converge to the solution. The elastic free energy was calculated with the consideration of the saddle-splay elasticity using the expression: $F = \frac{1}{2}\int dV\,[K_{11}(\nabla \cdot \boldsymbol{n})^2 + K_{22}(\boldsymbol{n} \cdot \nabla \times \boldsymbol{n})^2 + K_{33}(\boldsymbol{n} \times \nabla \times \boldsymbol{n})^2 - (K_{22} + K_{24})\nabla \cdot (\boldsymbol{n}(\nabla \cdot \boldsymbol{n}) + \boldsymbol{n} \times \nabla \times \boldsymbol{n})]$. The numerical minimization was programmed and performed in MATLAB.

The director field converges to the DT configuration when $K_{24} > K_{22}$. As shown in Figure 2.2h, the angle $\alpha = 90^o$ does not vary with radial position (r/R_0). The increase of angle β from the center ($r/R_0 = 0$) to the boundary ($r/R_0 = 1$) indicates the twist angle through the radius of the cylinder. The requirement for the emergence of the DT configuration, $K_{24} > K_{22}$, can easily be satisfied by LCLCs since they have an extremely small K_{22} (We estimated that K_{24}/K_{22} for SSY is around 60[8], and K_{24}/K_{22} for DSCG is 10~20[7]. The estimation of K_{24} will be discussed in Chapter 2.3). As a comparison, K_{24}/K_{22} of 5CB is only 1.2[78], which explains the absence of the DT configuration.

At about the same time, the DT configuration of LCLCs was also independently observed by Z. S. Davidson et al[8]. The conclusions of their study are consistent with our results. Additionally, they analyzed the stability of the point defects (present in SSY samples, Figure 2.2e,f) and the domain wall structures (present in DSCG samples, Figure 2.2a-d) that separate the domains with opposite twist directions. Based on their work[8], the point defects are stable for SSY solutions since their K_{24}/K_{33} is larger than 4. But DSCG solutions exhibit domain walls due to a small K_{24}/K_{33}. (We estimated that K_{24}/K_{33} for SSY is around 6[8], and K_{24}/K_{33} for DSCG is around 0.8[7]. The estimation of K_{24} will be discussed in Chapter 2.3)

2.3 Temperature and concentration dependence of the saddle-splay elastic constant

The director configurations of confined nematics are determined by the elastic deformation modes represented by the elastic constants. The bulk elastic constants can be measured by the director distortions under the effects of external field[110] (Freedericksz transition[111]) and light scattering[70,112]. However, the measurement of the saddle-splay elastic constant is often a challenging task because this deformation mode is hard to be individually excited and visualized. Previously, deuterium nuclear-magnetic-resonance (NMR) techniques have been used to measure K_{24} with samples confined to sub-micrometer cavities[113]. Another method requires the comparison of observed polarized optical textures with the simulated textures[78]. These methods may involve large error and cannot separate the saddle-splay deformation from other deformation modes and the effect of surface anchoring. In this section, we introduce a new method to measure K_{24} based on the director field of the DT configuration and for the first time (at the best of our knowledge) investigate the dependence of K_{24} on the concentration and the temperature.

2.3.1 *Theoretical calculation of the twist angle with different elastic constants*

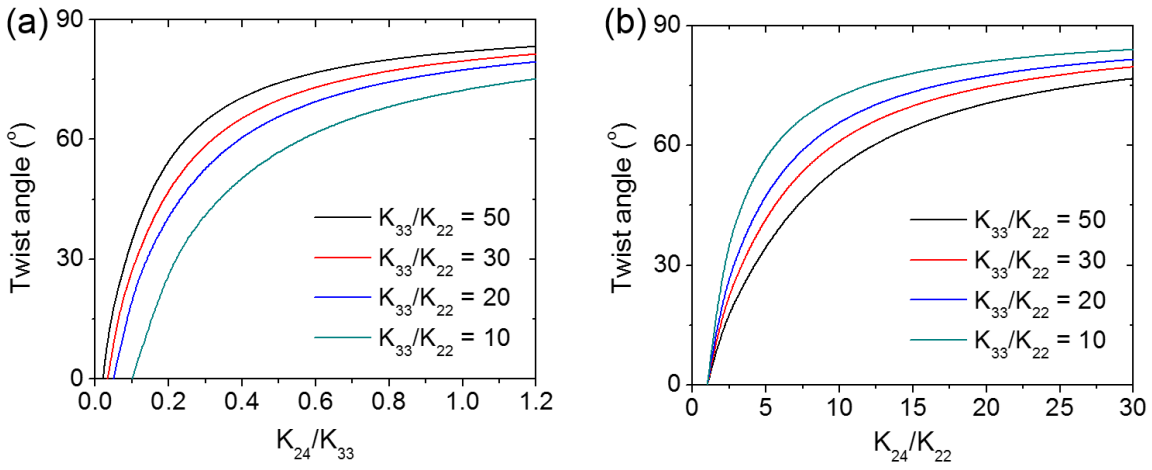

Figure 2.3 Calculated twist angle of the DT director field from the center to the boundary of the cylinder. (a) Twist angle as a function of K_{24}/K_{33}. (b) Twist angle as a function of K_{24}/K_{22}.

In the DT configuration, the twist angle of the director from the center to the boundary of the cylinder is an important feature determined by the bulk and the saddle-splay elastic constants. With the help of numerical calculation, we obtained the twist angles as the elastic constants were varied by the numerical minimization of elastic free energy as aforementioned in section 2.2.2. The splay deformation is not involved in the DT director field. The twist angle is a function of K_{22}, K_{33}, and K_{24}. As shown in Figure 2.3, the calculated twist angle of the director field cannot be larger than 90° because the saddle-splay elasticity aligns the director on the surface towards the azimuthal direction. A 90° twist corresponds to the largest twist angle that can stabilize the DT configuration. In Figure 2.3a, for a fixed K_{33}/K_{22}, the twist angle of the DT director field increases with a rise of K_{24}/K_{33}. When K_{24}/K_{33} is fixed, larger K_{33}/K_{22} results in a larger twist angle of the director field. When plotted as a function of K_{24}/K_{22} in Figure 2.3b, the twist angle increases with a rise of K_{24}/K_{22} for the same K_{33}/K_{22}. However, for fixed K_{24}/K_{22}, the twist angle is

reduced by an increase in K_{33}/K_{22}. Since K_{22} and K_{33} of LCLCs have been characterized in literature[93-95], the value of K_{24} can be extracted with the measurement of the twist angle. The DT configuration serves as a novel platform to study K_{24} as a function of the temperature and the concentration.

2.3.2 Twist angle measurement at different temperatures and concentrations

The twist angle of the DT director field can be measured by the wave-guiding experiment. When the Mauguin limit is satisfied[114] (the total twist angle through the cylinder, 2Φ, is much smaller than the retardation of polarized light due to the birefringence of nematics, $2\Phi \ll |\Gamma| = \left|\frac{2\pi}{\lambda}(n_e - n_o)d\right|$), the polarization of the light is guided by the twisted director field if the polarizer matches the director orientation on the entrance plane[37]. In this situation, the polarization of the light transmitted out of the sample is parallel with the director on the exiting plane. Therefore, the transmitted intensity of the DT domains can be driven to extinction by uncrossing the polarizers. The combination of the polarizer and analyzer corresponding to the extinction of transmitted intensity shows the twist angle of the director field. The details of the wave-guiding experiments are described in Appendix A.1.2, Figure A.2.

Different twist angles of the DT director field were observed as the concentration and temperature were varied for DSCG solutions. As shown in Figure 2.4a, the twist angle is reduced with the increase in concentration. For a fixed concentration, the twist angle has a maximum as a function of the temperature. When plotted with reduced temperature, T/T_{NB} (T_{NB} is the transition temperature between nematic phase and biphasic region, wherein the nematic phase and isotropic phase co-exist), the maximum twist angles of different

concentrations correspond to the same T/T_{NB} (Figure 2.4b). With a high DSCG concentration of 17 wt%, the birefringent pattern in Figure 2.4c still shows transmitted intensity due to a twisted director field. But we couldn't find a well-aligned DT domain to measure the twist angle. Further increasing the concentration to 18 wt% results in no transmitted intensity under crossed polarizers as shown in Figure 2.4d, indicating an axial configuration with zero twist angle.

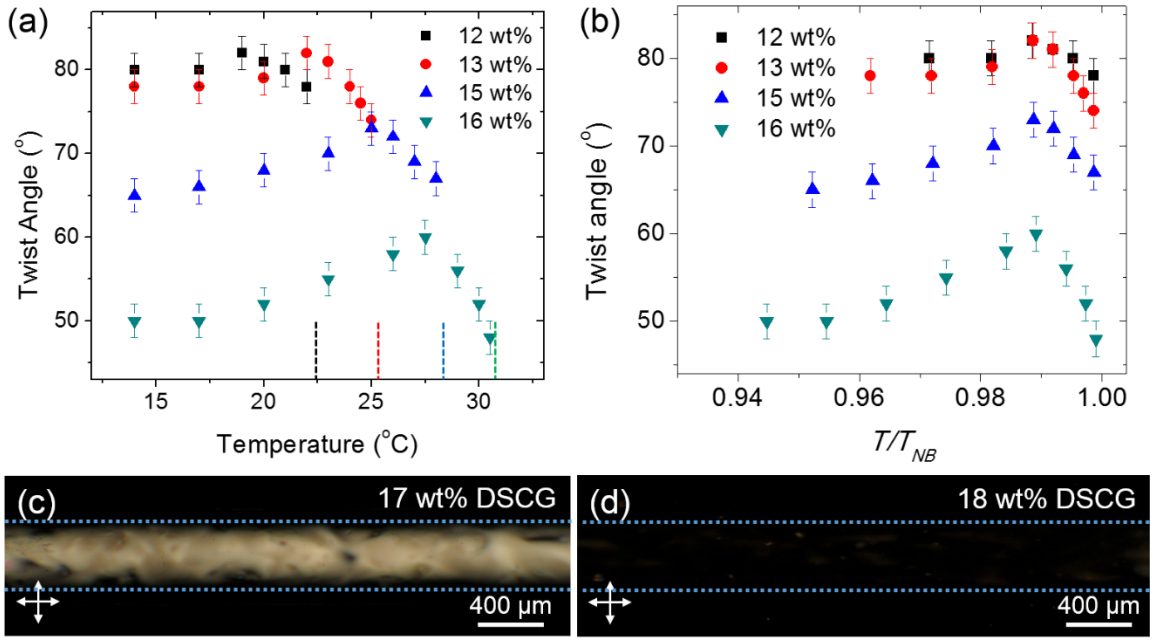

Figure 2.4 (a) Twist angles of the DT director field of DSCG as a function of the temperature and the concentration measured from wave-guiding experiments. The dashed lines indicate phase transition temperature, T_{NB}. (b) Plotting of the twist angles as a function of reduced temperature, T/T_{NB}. (c, d) Polarized optical microscopy images of 17 wt% and 18 wt% DSCG under crossed polarizers. The dashed blue lines indicate the inner surfaces of the cylindrical capillaries.

The twist angle of the DT configuration was also measured with SSY for different concentrations and temperatures. But all the samples exhibited a similar twist angle of 87° ±5°. We note that in Figure 2.3, when K_{24} is much larger than K_{33} and K_{22}, the twist angle is close to 90° and has little dependence on the elastic constants. In this situation, the twist

angle of 90^{o} enables the maximum contribution of the saddle-splay elasticity to stabilize the DT configuration. Based on a twist angle of 87^{o}, SSY has a large saddle-splay elastic constant, $K_{24}/K_{33} \sim 6$ [7,8] (will be discussed in section 2.3.3). Therefore, the twist angle of SSY loses its sensitivity to the variation of the temperature and the concentration.

2.3.3 Extraction of the saddle-splay elastic constant

Besides the twist angle of the DT director field, the ratio of bend/twist elastic constants, K_{33}/K_{22}, is also required to extract the value of K_{24}. We use the K_{33}/K_{22} data of 15 wt% DSCG measured by Nastishin et al. as plotted in Appendix A.1.3, Figure A.3[93]. The ratio K_{33}/K_{22} decreases with the increase in the temperature, which is consistent with the elastic constants model for semi-flexible rods system[88,115,116]. In the elastic constants model, K_{33}/K_{22} is expressed in terms of the volume fraction (ϕ) and the persistence length of the aggregates (λ_p)[88,115], $K_{33}/K_{22} \sim (\phi\lambda_p)^{2/3}$. The persistence length becomes smaller as temperature rises, leading to the decrease of K_{33}/K_{22} in Figure A.3. The model for bulk elastic constants will be discussed in detail in section 2.4.1.

Using the K_{33}/K_{22} values in Figure A.3, K_{24}/K_{33} and K_{24}/K_{22} of 15 wt% DSCG were extracted and presented in Figure 2.5a. K_{24} values were also plotted in Figure 2.5b. The ratios show that K_{24} of DSCG is much larger than K_{22}, but in the same order of magnitude with K_{33}. With an extremely small K_{22} ($K_{24}/K_{22} = 10 \sim 20$ as shown in Figure 2.5a), DSCG meets the requirement for the formation of the DT configuration, $K_{24} > K_{22}$, as revealed by the numerical calculation. The small K_{22} is the decisive property of LCLCs for the emergence of the chiral structure in cylinder with degenerate planar anchoring under the stabilization of the saddle-splay elasticity. We then note that K_{24}/K_{33} and K_{24}/K_{22} have

contrasting scaling with the temperature. With the increase in the temperature, K_{24}/K_{33} becomes larger, but K_{24}/K_{22} becomes smaller. As aforementioned, K_{33}/K_{22} decreases as the temperature increases[93], leading to smaller theoretical twist angle with fixed K_{24}/K_{33} as predicted in Figure 2.3a. However, the measured twist angle has a maximum as a function of temperature, suggesting that K_{24}/K_{33} should increase with an increase in temperature. With fixed K_{24}/K_{22}, the decrease of K_{33}/K_{22} results in the rise of theoretical twist angle as predicted in Figure 2.3b. Therefore, K_{24}/K_{22} should decreases with an increase in temperature to rationalize the maximum twist angle as a function of temperature presented in Figure 2.4a.

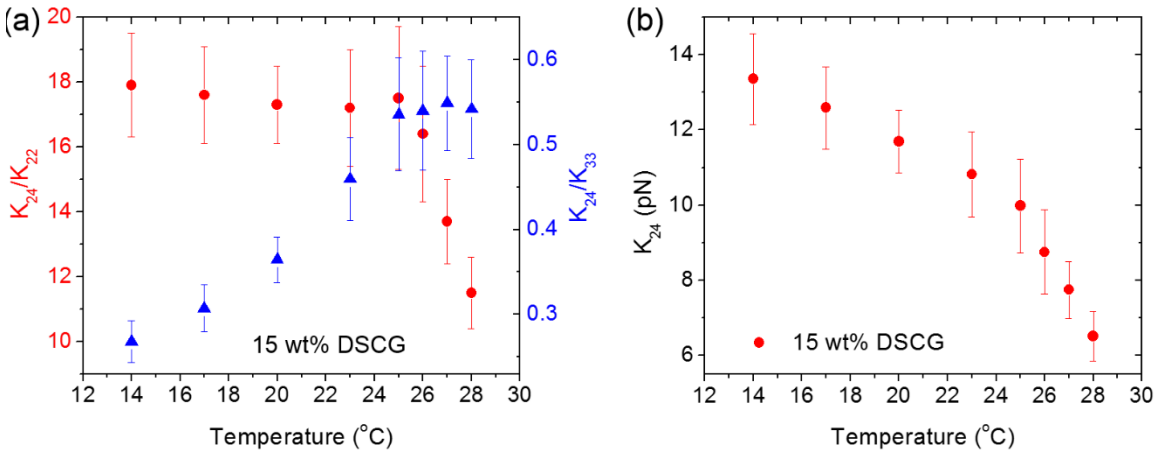

Figure 2.5 (a) K_{24}/K_{22} and K_{24}/K_{33} of 15 wt% DSCG as a function of temperature. (b) K_{24} values of 15 wt% DSCG as a function of temperature.

The values of K_{24} at other DSCG concentrations cannot be obtained due to the lack of K_{33}/K_{22} values in the literature. But we can infer the concentration dependence of K_{24} from the change of twist angle and theoretical calculation. As the concentration rises, the volume fraction increases and K_{33}/K_{22} becomes larger, leading to larger theoretical twist angle with fixed K_{24}/K_{33} as predicted in Figure 2.3a. However, the measured twist angle in

Figure 2.4 decreases with an increase in concentration, which can be only rationalized by a decrease of K_{24}/K_{33}.

2.4 Theoretical discussions of elastic constants

The elastic constants of nematics are intrinsically determined by their building units. For LCLCs, the splay, twist, and bend elastic constants are correlated with the aggregation behavior at different temperatures and concentrations in the theoretical model[88,115,116]. However, the relationship of the saddle-splay elastic constant with the aggregates is not clear due to the lack of theoretical understanding and experimental measurements. In this section, we firstly consider the models of the three bulk elastic constants for LCLCs[88,115,116], and then discuss the model for the saddle-splay elastic constant based on our measurements.

2.4.1 Models for bulk elastic constants

Conventional approach to describe bulk elastic constants is based on the excluded volume mechanism in Onsager model[96]. Under the assumption of long rigid rods, the bulk elastic constants are expressed as a function of the volume fraction ($\emptyset$) and the aspect ratio ($\frac{L}{D}$) [96]: $K_{11} = \frac{7}{8\pi}\frac{k_B T}{D}\emptyset\frac{L}{D}$, $K_{22} = K_{11}/3$, $K_{33} = \frac{4}{3\pi^2}\frac{k_B T}{D}\emptyset^3\left(\frac{L}{D}\right)^3$, where k_B is Boltzmann constant, T is temperature, L and D are the length and diameter of the building units. However, this model fails to describe the elastic constants of LCLCs[93-95]. For instance, K_{11}/K_{22} for DSCG can be as high as 30 [95], which is much larger than 3 predicted by the conventional model[96].

The conventional theoretical model can be improved by considering the flexibility of LCLCs aggregates (characterized by the persistence length, λ_p), since the molecules in the aggregates are connected by weak non-covalent bonds. For semi-flexible aggregates, the bend deformation is no longer limited by the aggregate length[88,116]. The semi-flexible aggregates can relieve bending energy by conforming to the deformed orientation. Instead, the bend elastic constant can be expressed as a function of persistence length[88], $K_{33} = \frac{4}{\pi}\frac{k_BT}{D}\emptyset\frac{\lambda_p}{D}$. The twist elastic constant for semi-flexible rods is also a function of persistence length[85,115]: $K_{22} = \frac{k_BT}{D}\emptyset^{1/3}\left(\frac{\lambda_p}{D}\right)^{1/3}$. However, the flexibility of the aggregates does not affect the splay elastic constant. Since splay deformation changes the density of aggregate ends, long aggregates limit the number of aggregate ends to adjust the density difference, which cannot be relieved by the flexibility[88]. Hence, the splay elastic constant is expressed as[117]: $K_{11} = \frac{4}{\pi}\frac{k_BT}{D}\emptyset\frac{\bar{L}}{D}$, where $\bar{L}$ is the average length of LCLC aggregates with a poly-disperse length distribution. This model has been widely used in the literature to explain the elastic behaviors of semi-flexible rod-like liquid crystalline systems such as LCLCs[93-95] and lyotropic polymer liquid crystals[118].

2.4.2 Discussions of the saddle-splay elastic constant

Unlike the splay, twist, and bend elastic constants, the measurements of K_{24} are rare in literature[78,113,119,120] and the model of K_{24} with the nematic building blocks is not established yet. The DT configuration of LCLCs serves as a convenient platform to measure K_{24} as a function of the temperature and the concentration, which enables us to propose a plausible model for the scaling of K_{24} with the aggregation behavior of LCLCs.

From the theoretical model of the splay, twist, and bend elastic constants, one would speculate that the average contour length ($\bar{L}$) and the persistence length (λ_p) of the LCLC aggregates may play a significant role on the value of K_{24}. The average length of LCLC aggregates is strongly dependent on the temperature and the concentration (an exponential function)[121], whereas the persistence length is a property of the aggregates and only has a weak dependence on temperature ($\lambda_p \sim 1/T$)[122]. By assuming $K_{24} \sim \bar{L}$, the dependence of K_{24}/K_{33} ($K_{24}/K_{33} \sim \bar{L}/\lambda_p$) and K_{24}/K_{22} ($K_{24}/K_{22} \sim \bar{L}/\lambda_p{}^{1/3}$) on the temperature should be dominated by the average aggregate length, since the temperature dependence of the average aggregate length is more dramatic than that of the persistence length. However, this expectation cannot explain the rise of K_{24}/K_{33} as the temperature increases in Figure 2.5a. Moreover, the scaling of K_{24} with average aggregate length also contradicts with the twist angle of SSY upon adding poly-ethylene glycol (PEG). As aforementioned, the twist angle of PEG-free SSY is 87°±5°, which corresponds to $K_{24}/K_{33} \sim 6$. As a condensing agent, PEG molecules elongate SSY aggregates via excluded volume mechanism (will be discussed in Chapter 5.1)[123-125]. Under the assumption of $K_{24} \sim \bar{L}$, the addition of PEG is expected to increase K_{24}/K_{33}, leading to an increase of twist angle in the DT director field. In Table 2.1, however, 1.0 M (34.8 wt%) SSY + 0.5 wt% PEG exhibits a smaller twist angle than that of 1.0 M SSY free of any additives. Additionally, in Chapter 4, we will discuss the estimation of K_{24} for a lyotropic polymer liquid crystal, poly-benzyl glutamate (PBG). The molecular length of PBG (100 ~ 200 nm [118,126]) is much longer than the average aggregate length of SSY (5 ~ 20 nm [97]). But PBG has a smaller twist angle (50°) and a smaller K_{24}/K_{33} (0.24) as shown in Table 2.1. These inconsistencies indicate that K_{24} does not scale with the average aggregate length.

After ruling out the effect of average aggregate length, we then consider the relationship of K_{24} with the persistence length of LCLC aggregates. We note again that in Figure 2.5a, the rise of temperature leads to an increase in K_{24}/K_{33} and a decrease in K_{24}/K_{22}. When K_{24} scales with the persistence length, the power of the persistence length should be smaller than 1 and larger than 1/3 to be consistent with the temperature dependences of K_{24}/K_{33} and K_{24}/K_{22} ($K_{24}/K_{33} \sim 1/\lambda_p{}^{(1-x)}$, $K_{24}/K_{22} \sim \lambda_p{}^{(x-1/3)}$, $1/3 < x < 1$). Moreover, the scaling of K_{24} with the persistence length rationalizes the small K_{24}/K_{33} and the small twist angle of PBG solutions (the estimation of K_{24} for PBG will be discussed in detail in Chapter 4). The persistence length of PBG molecules (70-140 nm[126,127]) is much longer than that of LCLC aggregates (~ 10 nm, estimated based on the values of K_{11}/K_{33} in literature[94,95], $K_{11}/K_{33} \sim \bar{L}/\lambda_p$). Therefore, K_{24}/K_{33} value and the corresponding twist angle of the DT director field for PBG should be smaller than those for LCLC solutions. Additionally, the relationship of K_{24} with persistence length is supported by the twist angle of DSCG with the addition of NaCl. Prior literature showed that LCLC aggregates are more flexible with smaller persistence length under higher ionic strength[123,128]. As shown in Figure 2.6c, 18 wt% DSCG free of any NaCl exhibits no transmitted intensity in a borosilicate cylindrical capillary under crossed polarizers, indicating that the director is in the axial orientation with no twist deformation. With the NaCl concentration of 1.7 wt%, the twist deformation evolves in the director field with some transmitted intensity under crossed polarizers as shown in Figure 2.6d. As the persistence length is reduced by NaCl, the large K_{24}/K_{33} of the DSCG + NaCl solution drives the formation of the DT configuration to replace the axial configuration of the NaCl-free DSCG. The twist angles of the DT director field and K_{24}/K_{33} values of different solutions are listed in Table 2.1.

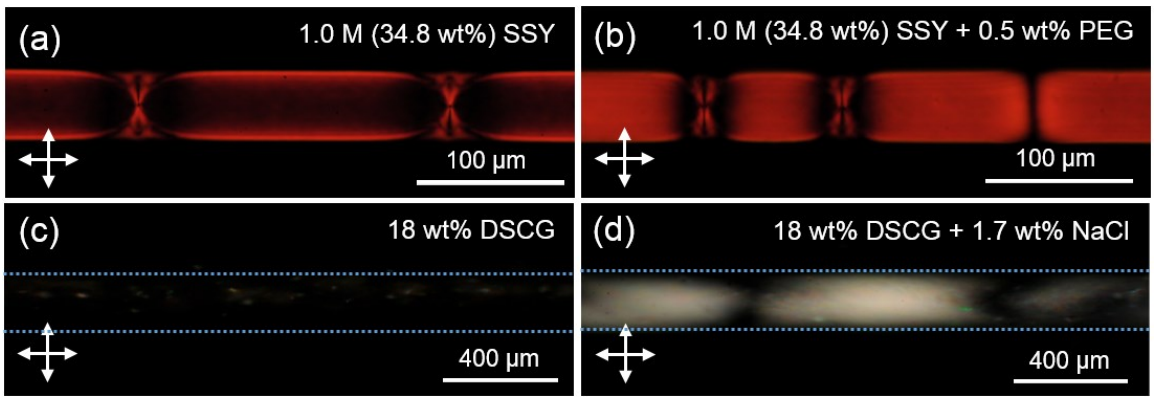

Figure 2.6 Polarized optical microscopy images of (a) 1.0 M (34.8 wt%) SSY, (b) 1.0 M (34.8 wt%) SSY + 0.5 wt% PEG, (c) 18 wt% DSCG, and (d) 18 wt% DSCG + 1.7 wt% NaCl. The dotted blue lines in (c) and (d) indicate the inner surface of the cylindrical capillaries.

Table 2.1 The twist angles and K_{24}/K_{33} values of different solutions.

Solution	Twist angle	K_{24}/K_{33}
1.0 M (34.8 wt%) SSY	87°	6 [94]
1.0 M (34.8 wt%) SSY + 0.5 wt% PEG	65°	0.85
14 wt% DSCG	75°	0.83 [95]
12 wt% PBG	50°	0.24 [118]
18 wt% DSCG	0°	0.05 [95]
18 wt% DSCG + 1.7 wt% NaCl	20°	0.40

Note: The twist angles were measured by wave-guiding experiments. The K_{24}/K_{33} values were calculated by numerical minimization based on the twist angle measurements and the K_{33}/K_{22} values in the citations. The K_{33}/K_{22} values for SSY + PEG solution and DSCG + NaCl solution are assumed the same as those of additive-free SSY and DSCG solutions.

2.5 Conclusions

In this chapter, we reported a doubly-twisted (DT) chiral configuration of achiral LCLCs in cylindrical capillaries with degenerate planar anchoring. Rather surprisingly, this

chiral configuration is the ground state of LCLCs in cylindrical confinement when there exists an axial configuration free of any deformation. The stability of the DT configuration was attributed to the role of saddle-splay elasticity, which lowers the elastic free energy of the DT configuration below that of the axial configuration. The presence of the DT configuration indicates that the most stable state with the lowest possible elastic free energy is not necessarily be the non-deformed uniform director field. The chiral configuration with large twist deformation can even have a lower elastic free energy thanks to the contribution of the saddle-splay elasticity.

By measuring the twist angle of the DT director field, we extracted the saddle-splay elastic constant, K_{24}, of LCLCs at different temperatures and concentrations. For the first time, the dependence of K_{24} on the temperature and the concentration was investigated and correlated to the aggregation behavior of LCLCs. We proposed that K_{24} is determined by the persistence length of LCLC aggregates rather than the contour length. The verification of this plausible relationship requires the measurements of the persistence length as the temperature and the concentration are varied, which will be an interesting future work to better understand LCLC self-assembling mechanism.

CHAPTER 3. CHIRAL CONFIGURATIONS OF LCLCS UNDER CYLINDRICAL CONFINEMENT WITH HOMEOTROPIC ANCHORING

3.1 Introduction

The configurations of nematic liquid crystals in cylindrical confinement with homeotropic anchoring (the director is anchored perpendicular to the surface) has attracted considerable interests[107,129-132] because the confinement shape leads to the frustration between uniform director field and radial boundary condition. Intuitively, the frustration can be solved by a planar radial configuration[129] as illustrated in Figure 3.1a. The director everywhere is along the radial direction, which creates pure splay deformation and a singular line defect along the center of the cylinder[129]. As shown in Figure 3.1b, the energy-costly line defect can be avoided by allowing the director to escape in the "third dimension" along the axial orientation[130,132]. This configuration, namely, the escape radial (ER) configuration, has been intensively studied in experimental observations and theoretical analysis as the ground state of conventional thermotropic liquid crystals with similar splay, twist, and bend elastic constants[107,131]. In the ER configuration, the director field adopts the bend deformation to remove the singular line defect in the center and partially reduce the energy contribution of the splay deformation. Moreover, the ER director field can escape along either positive or negative axial orientation. The different escape directions of the ER director field result in the alternating point defects with topological charges of +1 and -1 as shown in Figure 3.1c[107,131,133].

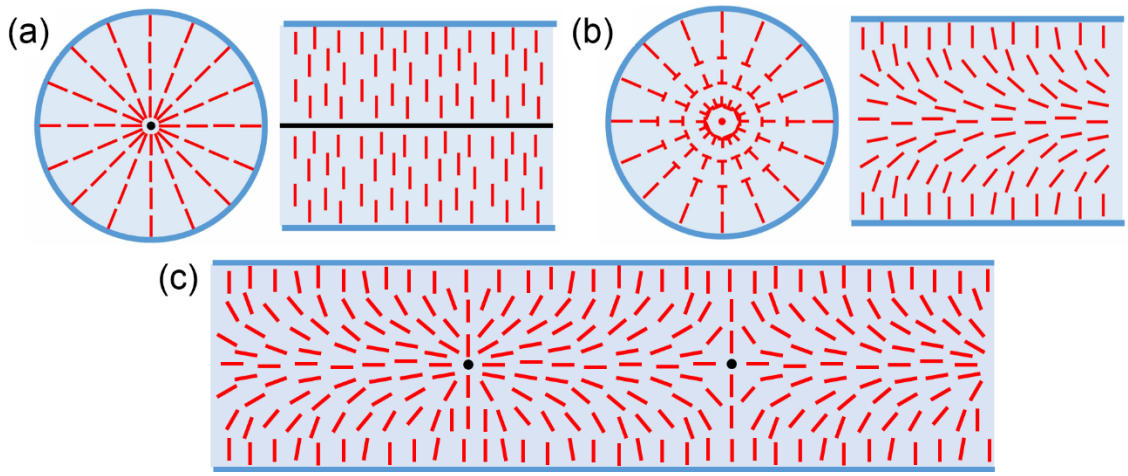

Figure 3.1 The cross section (left) and side view (right) illustrations of (a) the planar radial director configuration and (b) the escape radial (ER) director configuration. Red rods represent the nematic director. The nail head in (b) indicates that this side of the director points out of page. The black dot and black line in (a) represent a singular line defect. (c) Side view illustration of the ER director configuration with point defects. The point defects with the topological charges of +1 (left) and -1 (right) are represented by the black dots.

In this chapter, we report our studies on the nematic configurations in cylindrical capillaries with homeotropic anchoring using LCLCs, which have an exceptionally small twist elastic constant[93-95]. In section 3.2, departing from the usual achiral ER configuration, we introduce the two chiral configurations of LCLCs in cylindrical capillaries with homeotropic anchoring, the twisted escaped radial (TER) configuration and the twisted polar (TP) configuration. Here, we note that these two chiral configurations of LCLCs were firstly published by Jeong et al[9]. However, at the same time, we independently observed the same configurational behaviors of LCLCs and reported our results in APS march meeting (2015)[10]. Then in section 3.3, we further discuss the birefringent textures of the TER configuration at different temperatures and concentrations, which reveal the aggregation behavior of LCLCs and the subsequent effects on the elastic constants. Moreover, at high LCLC concentrations, we report a novel configurational behavior in section 3.4, the co-existence of the TER and the DT chiral configurations. The emergence

of the DT domains enables the estimations of the anchoring strengths for SSY on the surface of the parylene-N film.

3.2 The twisted escape radial (TER) and the twisted polar (TP) configurations of LCLCs

3.2.1 The twisted escape radial (TER) configuration

As shown in Figure 3.2a, the director field of the conventional achiral ER configuration (realized by a thermotropic liquid crystal, 5CB) exhibits the birefringent texture of alternating dark and bright stripes under crossed polarizers[79,107,131]. The pattern shows no transmitted light at the boundary of the capillary since the director is in the radial orientation conforming to the homeotropic anchoring on surface. The bright stripes emerge when the director escapes from the radial orientation, which makes an angle δ ($0^o < \delta < 90^o$) with the polarizers. In the central region of the capillary, the texture exhibits no transmitted intensity as the director is along the cylindrical axis parallel with the polarizer. When SSY solutions were wicked into cylindrical capillaries, homeotropic anchoring was induced by the parylene-N film coated on the inner surface of cylindrical capillaries by chemical vapor deposition[134] (The CVD coating method is described in Appendix A.7.2). In Figure 3.2b, the center of the capillary in the birefringent texture exhibits prominent transmitted intensity, which is the signature of twist deformation. The twisted director field changes the polarization of the light, resulting an increase of transmitted intensity under the crossed polarizers, in particular at the center of the cylinder. The director field spontaneously develops a twist deformation in addition to the splay and bend deformations

which prevail in the ER structure. Hence, this chiral structure is referred as the twisted escape radial (TER) configuration as illustrated in Figure 3.2d.

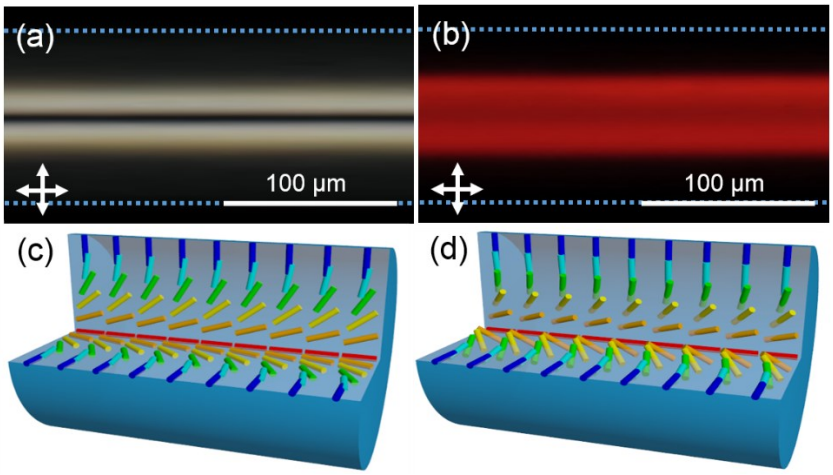

Figure 3.2 The polarized optical microscopy images of (a) the ER configuration of 5CB and (b) the TER configuration of SSY. The director field illustrations of (c) the ER configuration and (d) the TER configuration.

Similar to the ER configuration[107,131,133], the director field of the TER configuration is energetically equivalent to escape in either positive or negative direction along capillary axis. The TER domains with opposite escape directions are separated by alternating point defects with topological charges of +1 and -1 as observed in Figure 3.3a. For achiral SSY molecules, it is also equally possible for the twist deformation of the TER configuration to be either left-handed or right-handed. In Figure 3.3b, multiple TER domains with different twist handedness were observed in a single cylindrical capillary. The adjacent domains are separated by the non-twisted ER wall structures, since the central regions of the walls show extinction of transmitted intensity. When the polarizer and analyzer are decrossed (Figure 3.3c and 3.3d), the different twist handedness of the adjacent domains were indicated by the different birefringent patterns. The TER configuration was also observed with DSCG solution as shown in Figure 3.3e-g. The opposite twist directions of the adjacent domains

are clearly shown by the patterns when the polarizer and analyzer makes an angle of 20° in Figure 3.3f and 3.3g.

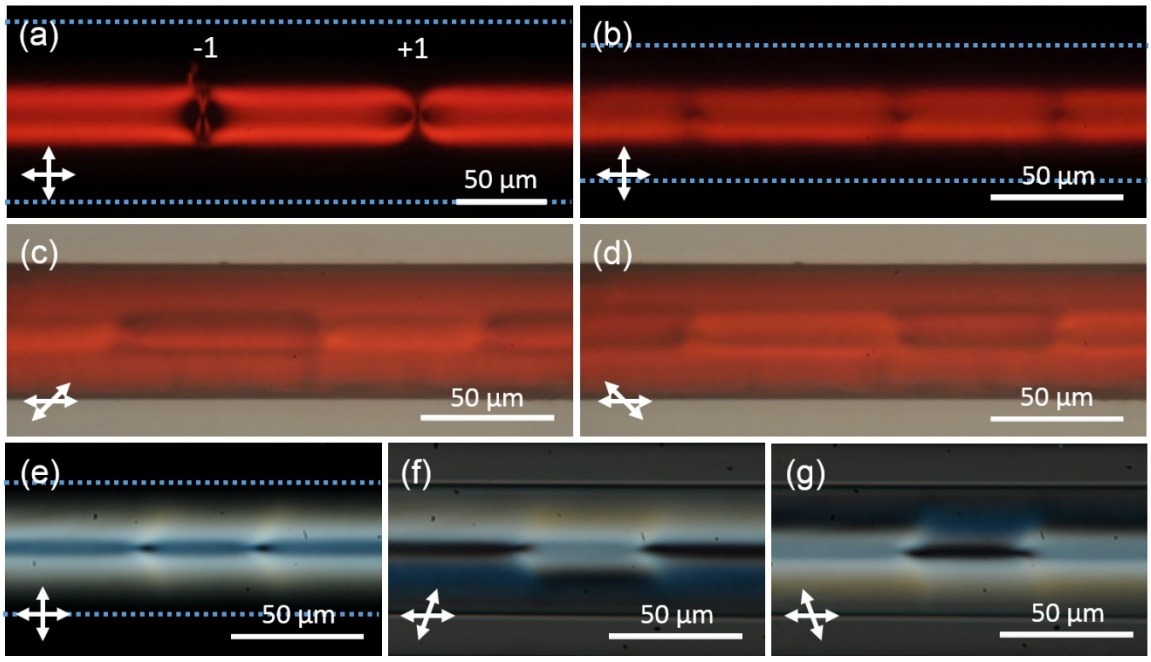

Figure 3.3 (a) Polarized optical microscopy image of the TER configuration for SSY with +1 (right) and -1 (left) point defects under crossed polarizers. (b-d) Polarized optical microscopy images of the TER domains for SSY with different twist handedness. (b) The polarizer and analyzer are crossed. (c, d) The polarizer and analyzer make an angle of 45°. The polarizer and analyzer orientations are indicated by the double-headed white arrows. The blue dotted lines indicate the inner surface of cylindrical capillaries. (e-g) Polarized optical microscopy images of the TER domains for DSCG with different twist handedness. (e) The polarizer and analyzer are crossed. (f, g) The polarizer and analyzer make an angle of 70°.

The stability of the chiral TER configuration can be rationalized by the exceptionally small K_{22} of LCLCs. In the TER configurations, the director field develops twist deformation to partially relieve the energy contributions of the splay and bend deformations prevalent in the ER configuration. Therefore, the total elastic free energy of the chiral TER configuration is lower than that of the non-twisted ER configuration. As aforementioned, at about the same time, the emergence of the TER configuration for

LCLCs was also observed by Jeong et al[9]. Their study showed the same driving force (the small K_{22} of LCLCs) for the formation of the TER configuration by numerical minimization of the elastic free energy. Additionally, they provided energy analysis of the walls between the adjacent domains with different twist directions and the point defects between adjacent domains with different escape directions.

3.2.2 The twisted polar (TP) configuration

To our surprise, while the temperature and the concentration remained unchanged, the TER configuration of LCLCs was replaced by another chiral configuration after aging for one day. The new chiral configuration is stable for around one month until the phase transition happens due to the slow water evaporation from the ends of the capillaries. This configurational transformation was observed for both SSY and DSCG as shown in Figure 3.4a-f. The transformation can occur anywhere in the cylindrical capillaries, but often at the ends of the capillaries or the defects of the TER structure. The spontaneous transition of the director configuration indicates that the TER configuration is just a transient state of LCLCs in cylindrical capillaries with homeotropic anchoring, whereas the new chiral structure that emerges in the aging process has a lower energy. While replacing the TER configuration, two line defects formed in the new chiral structure twisting helically along the axis of the cylinder (Figure 3.4a). The transition process took one to two days until the whole capillary exhibited the new chiral configuration (Figure 3.4b). The defect lines are singular since they are visible under bright field[135] as shown in Figure 3.4c. For SSY (Figure 3.4a-d), the distance between the two lines is around 0.8 times of cylindrical diameter, and the half pitch of the helix is around 3.4 times of cylindrical diameter. For DSCG (Figure 3.4e,f), the distance between the two lines and the half pitch of the helix are

smaller, around 0.6 and 1.4 times of cylindrical diameter, respectively. For the diameters of the cylindrical capillaries from 50 μm to 400 μm, the distance between line defects normalized by the diameter of the cylinder does not vary with the size of the capillary. However, the pitch varies considerably along the cylindrical capillaries, especially in the proximity to defects and domain walls. Due to the achiral nature of LCLC molecules, the double-helical twist of the line defects can form left-handed and right-handed domains, which are separated by the domain walls as shown in Figure 3.4e and f.

The director field of this novel chiral configuration was discussed first by Jeong et al[9] based on the planar polar configuration. In cylinder with homeotropic anchoring, the planar polar configuration was predicted theoretically as the stable structure for materials with weak homeotropic anchoring on the cylindrical surface[79]. But this configuration was never observed before in any experiments. As illustrated in Figure 3.4g, there are two defects in the cross-sectional director field with the topological charges of +1/2. When the cross section is twisted along the axial orientation, the two +1/2 defect lines emerge and conform to a double helical structure as shown in Figure 3.4h. In this twisted planar polar configuration, the director in the central region of each half pitch is perpendicular to the viewing plane. Hence, the central regions exhibit no transmitted intensity when the capillaries are rotated by 0^o and 45^o under crossed polarizers as shown in Figure 3.4b,d,e,f. Moreover, when the polarization is parallel with the long axis of the capillary, the birefringent texture of the twisted planar polar configuration is expected to show no transmitted light since the director field has no component out of the cross section. However, both SSY and DSCG textures show some transmitted intensity under crossed polarizers (Figure 3.4b,e). As a result, Dietrich et al.[23] further argued that the director field

has a transverse twist deformation out of the cross-sectional plane as approaching to the defect lines. The configuration with transverse twist was then referred as the twisted polar (TP) configuration as illustrated in Figure 3.4i. It is noted that the director field around +1/2 defects is dominated by the splay and the bend distortions. The twist deformation out of the cross-sectional plane stabilizes the line defects for LCLCs with a small twist elastic constant.

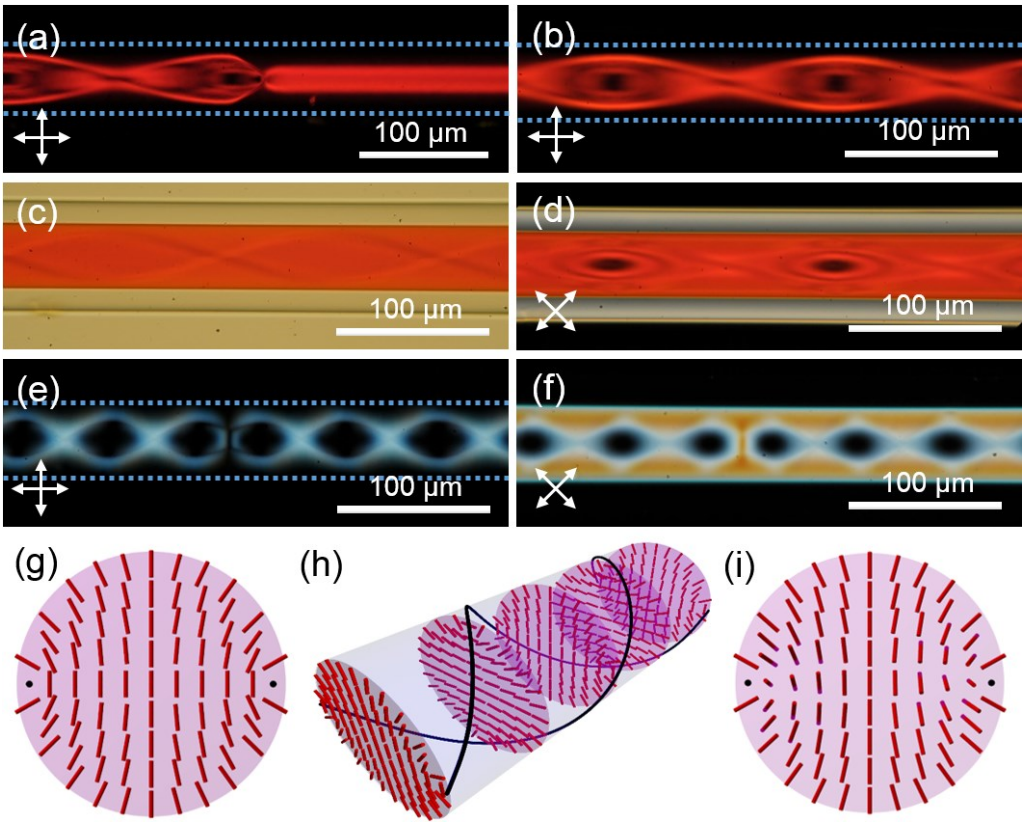

Figure 3.4 (a) The transition from the TER configuration to the twisted planar (TP) configuration for SSY. (b-d) Polarized optical images of the TP configuration for SSY (b) under crossed polarizers when the cylindrical axis is along the polarizer (c) with bright field. (d) under crossed polarizers when the cylindrical axis is at 45° with the polarizer. (e, f) Polarized optical images of the TP configuration for DSCG under crossed polarizers when the polarizer is at 0° and 45° with capillary axis, respectively. The blue dotted lines represent the inner walls of the cylindrical capillaries. The orientations of the polarizer and analyser are indicated by the double-headed white arrows. (g) The cross-sectional director field of the planar polar configuration. (h) The director field of the twisted planar polar configuration. (i) The cross-sectional director field of the TP configuration. The red rods represent nematic director. The black dots and lines represent the singular defects.

3.3 Birefringent texture of the TER configuration at different temperatures and concentrations

Based on the observations of chiral configurations, we studied the birefringent patterns of the TER configurations at different temperatures and concentrations for SSY solutions in cylindrical capillaries. We found that the evolution of the birefringent texture is an indirect measurement of SSY aggregation behavior. The average length of the aggregates has contrasting effects on the splay and bend deformation modes, leading to the temperature and concentration dependence of the birefringent texture.

3.3.1 Polarized optical microscopy observations

In Figure 3.5a and 3.5b, we plotted the transmitted intensity profiles of SSY along the cross section of the cylinder to quantitively compare the birefringent patterns of the TER configuration for different temperatures and concentrations. In the birefringent texture of the TER configuration (Figure 3.2b), the boundary of the cylinder exhibits extinction of transmitted light due to the homeotropic anchoring on the surface. Accordingly, the profiles show no transmitted intensity at the normalized position $r/R_0 = \pm 1$ (r is the radial position and R_0 is the radius of the cylinder). The two bright stripes arise in the birefringent texture as the director escapes and twists from the boundary to the center, which lead to the two peaks in the intensity profiles. Since the polarization of the light is guided by the twist deformation of the director field, the central region of the cylinder shows prominent transmitted intensity. In the intensity profiles, the intensity at the center ($r/R_0 = 0$) is only slightly lower than the maximum intensity of the peaks: $I(r/R_0 = 0) = (0.7\sim0.8)\ I_{max}$.

Figure 3.5a compares the intensity profiles for the SSY solutions of different concentrations at fixed temperature of 39 ^{o}C. The distance between the two peaks is larger with a higher concentration. At the fixed concentration of 1.04 M, the intensity profiles at different temperatures are shown in Figure 3.5b. Higher temperature results in a smaller distance between the two peaks. The insets of Figure 3.5a and 3.5b amplify the two peaks of the intensity profiles to clearly illustrate the temperature and concentration dependence. For various temperatures and concentrations, the normalized distances between the two peaks (normalized by the diameter of the cylinder) are plotted in Figure 3.5c. The normalized width between the bright stripes increases with an increase in the concentration and a decrease in the temperature. The rescaling of the normalized width as a function of reduced temperature (T/T_{NB}, T_{NB} is the transition temperature between nematic phase and biphasic region in which both nematic and isotropic phases are present) separates the role of the temperature and the concentration. In figure 3.5d, the normalized width decreases significantly as T/T_{NB} increases, but exhibits no dependence on concentration.

The width between the bright stripes in the birefringent pattern reveals the contributions of various deformation modes to the director field. For the ER configuration with no twist (Figure 3.2a,c), the birefringent texture is sensitive to the balance of the splay and bend deformations, which has been utilized to measure the ratio of elastic constants, K_{11}/K_{33} [136,137]. With the consideration of the twist deformation in the TER configuration, we calculated the stable director fields with different K_{11}/K_{33} values by numerical minimization of the elastic free energy (described in Chapter 2). The elastic free energy is expressed as $F = \int dV \left\{\frac{1}{2}[K_{11}(\nabla \cdot \boldsymbol{n})^2 + K_{22}(\boldsymbol{n} \cdot \nabla \times \boldsymbol{n})^2 + K_{33}(\boldsymbol{n} \times \nabla \times \boldsymbol{n})^2]\right\}$ without the saddle-splay term because the saddle-splay contribution to the elastic free energy does

not vary with different K_{11}/K_{33}. K_{22}/K_{33} = 0.1 is fixed in the calculation based on the measurements in literature[94].

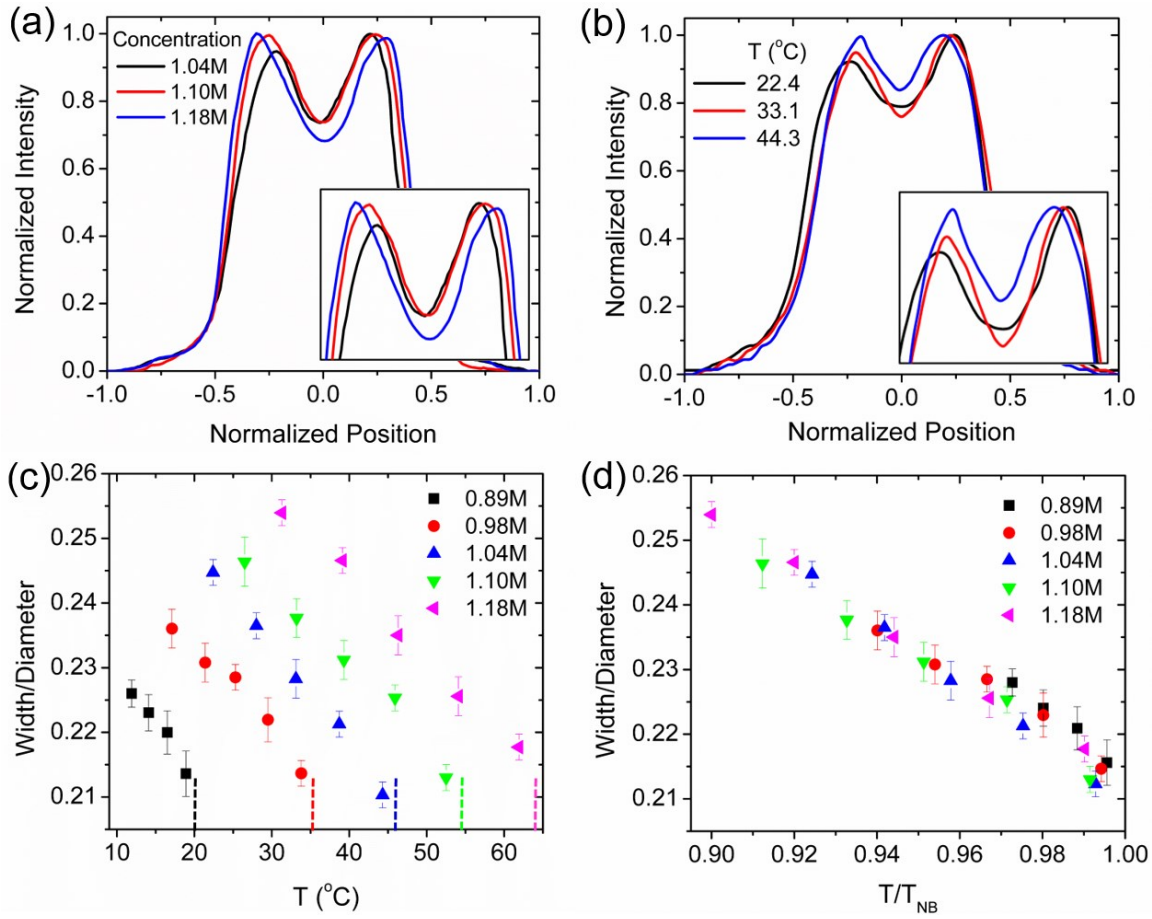

Figure 3.5 (a) Cross-sectional intensity profiles of the birefringent patterns for the TER configuration at different concentrations. The corresponding temperature of SSY is fixed at 39 °C. The inset shows the enlarged region of the two peaks. (b) Cross-sectional intensity profiles of the birefringent patterns for the TER configuration at different temperatures. The corresponding concentration is fixed at 1.04 M. The inset shows the enlarged region of the two peaks. (c) The temperature and concentration dependence of the width between two bright stripes. The width is normalized by the diameter of the cylinder. The dashed lines indicate the transition temperature between nematic and biphasic region (T_{NB}). (d) The width between two bright stripes as a function of reduced temperature (T/T_{NB}).

In cylindrical coordinates, the director $\boldsymbol{n} = (n_r, n_\phi, n_z)$ is described by two characteristic angles, α and β. α is the angle between the projection of director in r-ϕ plane and r axis. β is the angle between director and z axis. As shown in Figure 3.6a, in the

calculated director field of the TER configuration, $\beta(r/R = 1) = 90^o$ corresponds to the homeotropic anchoring at the boundary and $\beta(r/R = 0) = 0^o$ shows the escape of director field along cylindrical axis at the center. The twist deformation is shown by the increase of α from 0^o at the boundary to around 60^o at the center. With the increasing value of K_{11}/K_{33}, the bend deformation is energetically favorable in comparison to the cost of splay deformation. As a result, the decrease of $\beta(r/R)$ from the boundary to the center is faster. The corresponding birefringent texture is expected to exhibit larger width between the bright stripes, since the bright stripes result from the bending of the director away from the radial orientation ($\beta(r/R)$ deviates from 90^o). Additionally, with the increasing values of K_{11}/K_{33}, the increase of $\alpha(r/R)$ from the boundary to the center is also faster. The twist distortion of the director field (represented by the angle α) changes the polarization of the light and leads to the increase in the transmitted intensity of the birefringent texture, which also contributes to the larger width between the bright stripes. Using Jones matrix method (please see descriptions in Appendix A.7.5)[37], we simulated the birefringent textures of the TER configuration with various K_{11}/K_{33} values as shown in Figure 3.6b. The distance between the bright stripes in the simulated textures increases with the rise of K_{11}/K_{33}, which is consistent with our expectations.

Since the mesogens of LCLCs are semi-flexible aggregates, the scaling behaviors of different elastic constants have contrasting dependence on the aggregate length distribution[88,115]. As described in Chapter 2.4, the splay elastic constant scales linearly with volume fraction and average aggregate length[117] ($K_{11} \sim \phi\bar{L}$). On the contrary, the bend elastic constant is dependent only on the persistence length[88], λ_p ($K_{33} \sim \phi\lambda_p$). The average aggregate length of LCLCs has a strong dependence on the temperature and the

concentration[121], whereas persistence length is a molecular property, which is only a weak function of temperature[122]. Consequently, the dependence of the TER birefringent texture on the temperature and the concentration can be rationalized by the aggregation behavior of LCLCs and the subsequent effects on the elastic constants.

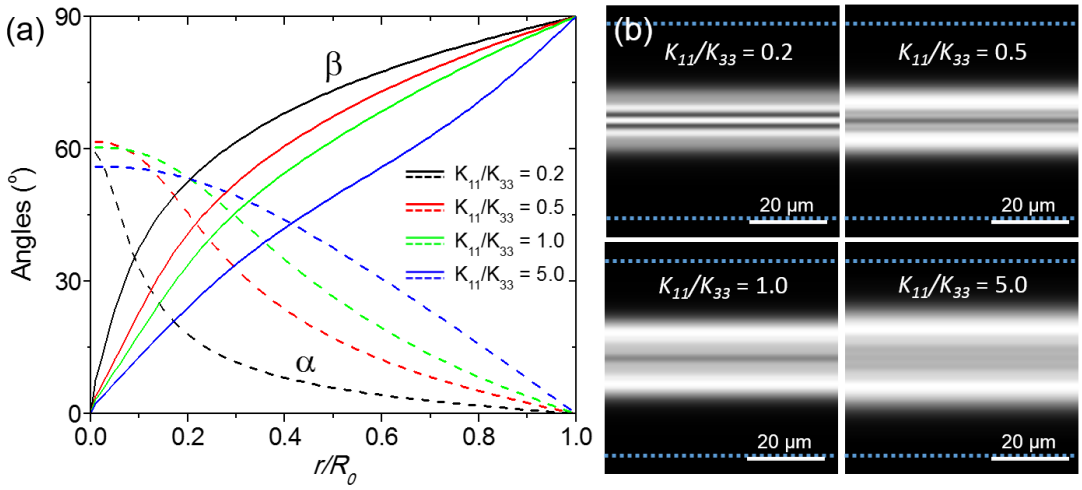

Figure 3.6 (a) Director fields of the TER configuration with different K_{11}/K_{33} from numerical calculation. Dashed lines are the angle α. Solid lines are the angle β. (b) Calculated patterns of the TER configurations from Jones matrix simulation under crossed polarizers with different K_{11}/K_{33}. The diameter of the cylinders in the simulation is 50 μm. The dotted blue lines indicate the surface of the cylindrical geometry.

3.3.2 Theoretical explanations: length distribution of SSY aggregates

The poly-dispersed length distribution of SSY aggregates was calculated using a 1-D self-assembling model for semi-flexible rod-like system[121]. Previously, this model has been used to explain the aggregation behavior[138], elastic properties, and configurations of tactoids[11] in LCLCs. The relative volume fraction, X_N, of aggregates with N constituent molecules is calculated by[121]: $X_N = N(X_1\exp(E/k_BT))^N\exp(-E/k_BT)$. Here, the relative volume fraction of individual molecule, X_1, is expressed as a function of volume fraction $\emptyset$ and temperature T [121]: $X_1 = \frac{(1+2\emptyset\exp(E/k_BT))-\sqrt{1+4\emptyset\exp(E/k_BT)}}{2\emptyset\exp(2E/k_BT)}$, where E is the

scission energy required to break an aggregate. This model assumes the isodesmic aggregation process, wherein E is a constant independent of the aggregate length. We use a commonly accepted value from literature in our calculation[11,94,123], namely, $E = 7.25k_BT$, where k_B is the Boltzmann constant. The volume fraction of SSY, $\emptyset$, can be calculated by the molar concentration, C_{SSY}, and molar mass, M_{SSY} [94]: $\emptyset = 1 - (\rho_{sol} - C_{SSY}M_{SSY})\frac{1}{\rho_w}$, where $\rho_w = 1.0\ \mathrm{g/cm^3}$ is the density of water, ρ_{sol} is the density of SSY solutions as measured in Appendix A.2.1, Figure A.4.

Using this model, the aggregate length distributions at a given temperature (T = 25 ^{o}C) for different concentrations are presented in Figure 3.7a. The peak position of the unimodal length distribution represents the aggregates with N constituent molecules which occupy the largest relative volume fraction (X_N). With the increase of concentration, the peak position shifts to larger number of molecules in an aggregate and the relative volume fraction of long aggregates ($N > 40$) increases. Figure 3.7b shows the length distributions of SSY aggregates for different temperatures at a fixed concentration (1.04 M). With a decrease in temperature, the peak position shifts to larger number of molecules in an aggregate and the relative volume fraction of long aggregates increases. These characters of the length distribution indicate that the aggregates have longer length in average at lower temperatures and higher concentrations.

The shifts in the aggregate length distribution are reflected in the intensity profiles of the birefringent patterns of the TER configuration as the temperature and the concentration are varied. The long aggregates at low temperatures and high concentrations result in large K_{11}/K_{33} ($K_{11}/K_{33} \sim \bar{L}/\lambda_p$). In this situation, the energy density of the splay

deformation is large in the center of the cylinder, which can be relieved by enhancing the bend deformation. As a result, for high concentrations and low temperatures, the large K_{11}/K_{33} leads to the large width between bright stripes in the birefringent pattern of the TER configuration. The shifts of average aggregate length alter the ratio of elastic constants, which rationalize the changes observed in the TER birefringent texture at different temperatures and concentrations.

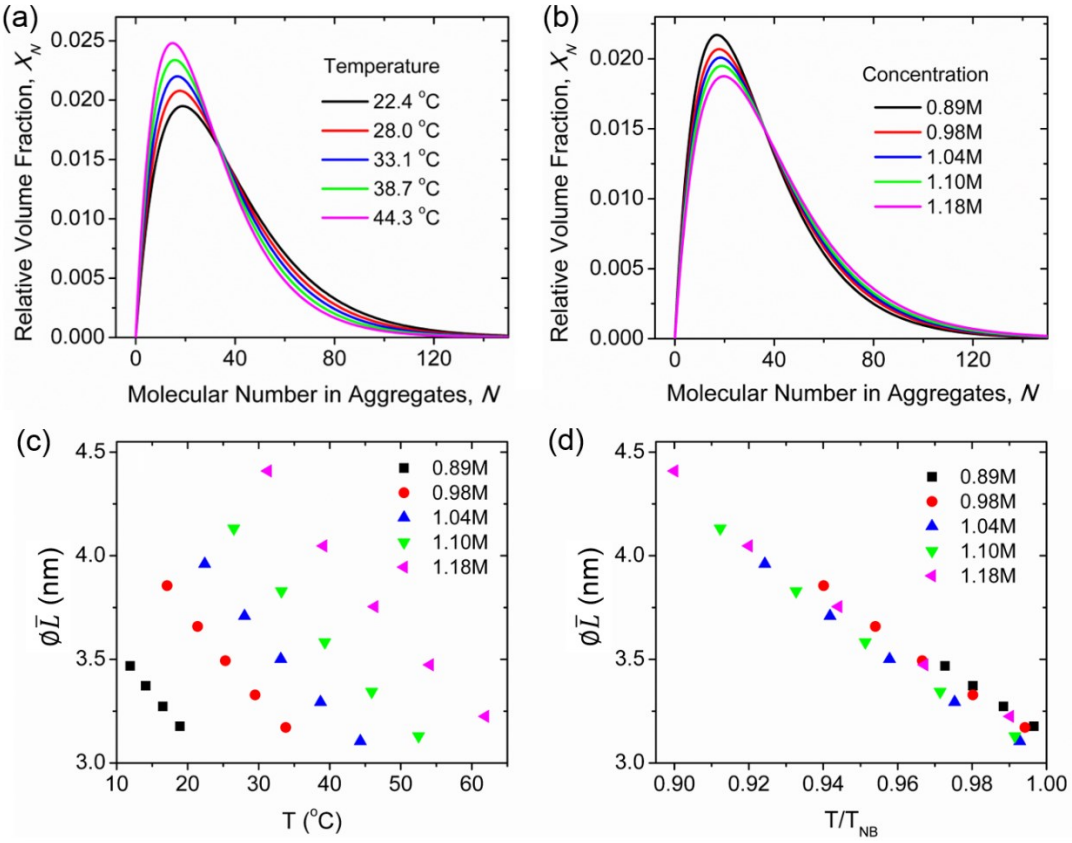

Figure 3.7 (a) The calculated length distributions of aggregates for different concentrations at the fixed temperature of 25 ºC. (b) The calculated length distributions of aggregates at different temperatures for the same concentration of 1.04 M. (c) The temperature and concentration dependence of the product of volume fraction and average aggregate length ($\emptyset\bar{L}$). (d) $\emptyset\bar{L}$ as a function of reduced temperature, T/T_{NB}, with a range of concentrations.

We note that when replotted with reduced temperature, T/T_{NB}, the width between bright stripes is independent of SSY concentration as shown in Figure 3.5d. This

dependence of birefringent texture on the temperature and the concentration shows similarity with that of 2nd and 4th order parameters. As reported by Nayani et al., the order parameters of SSY is only a function of T/T_{NB}, which do not vary with the change of the concentration[11]. The shifts in birefringent intensity profiles of the TER configuration are captured by the order parameters as the temperature and the concentration are varied. According to Onsager's theory, the order parameters are determined by the volume fraction ($\emptyset$) and aspect ratio ($\bar{L}/D$) of the aggregates[96]. Here, we plotted $\emptyset\bar{L}$ calculated by the self-assembling model for different temperatures and concentrations in Figure 3.7c, which shows remarkable consistency with the width between bright stripes in Figure 3.5c. As shown in Figure 3.7d, $\emptyset\bar{L}$ as a function of T/T_{NB} is independent of SSY concentration. We do note that in general, Onsager theory fails to predict the phase transition of LCLCs[139,140]. But $\emptyset\bar{L}/D$ still reveals the nature of the order parameters and well explains the changes of birefringent texture for different temperatures and concentrations.

3.4 Anchoring violation with high LCLC concentrations

At high SSY concentrations (> 1.15 M), we observed an unreported co-existence of domains with the TER configuration and the doubly-twisted (DT) configuration. The presence of the DT domains indicates the violation of the homeotropic anchoring, which enables us to estimate the homeotropic anchoring strength of SSY on the parylene-N surface with the help of numerical calculation.

3.4.1 Polarized optical microscopy observations with high concentrations

As aforementioned, we found that the TER configuration is the stable state for SSY in cylindrical capillaries coated with parylene-N film when the concentration is lower than

1.15 M. The Appendix A.2.2 has further explanation that the stability of the TER configuration is not related to transient effects from filling the capillary. However, a disparate configurational behavior was observed with high concentrations ($C_{SSY} > 1.15$ M). Although the TER configuration was exhibited when the capillaries were initially filled with nematic solutions, a different configuration, in co-existence with the TER configuration, was observed upon heating to isotropic phase and cooling back to nematic phase. As shown in Figure 3.8a, a birefringent texture clearly distinct from the TER configuration can be clearly visualized. For this texture, we note that there is transmitted light intensity (under cross-polarized illumination) at the edges of the capillary as well, indicating that the director at the boundary is not in the radial direction. Moreover, as shown in Figure 3.8e, these domains always have some transmitted intensity (under cross-polarized illumination) irrespective of the angle between the long axis of the capillary and the polarizers, which is a feature of a twisted director configurations. This birefringent pattern emerging for high SSY concentrations in parylene-N coated cylindrical capillaries agrees with the DT structure as illustrated in Figure 3.8f, which was described in Chapter 2 as the ground state of SSY in cylinder with degenerate planar anchoring (free of any coating). Due to the achiral nature of SSY molecules, both left-handed and right-handed twisted domains were expected and observed in the experiments separated by defect structures as shown in Figure 3.8b. The DT configuration is further confirmed by the wave-guiding phenomena described in Chapter 2.3. In Figure 3.8c and 3.8d, the right-handed and left-handed domains exhibit extinction of transmitted intensity respectively when the polarizer and analyzer make an angle of 50^o. With this polarizer and analyzer combination, the twist angle of the sample in Figure 3.8 was measured as $70^o \pm 15^o$. The error bar shows

the variations of the twist angle from the measurements of multiple samples. The data of the waveguiding experiment is present in Appendix A.2.3 Figure A.5.

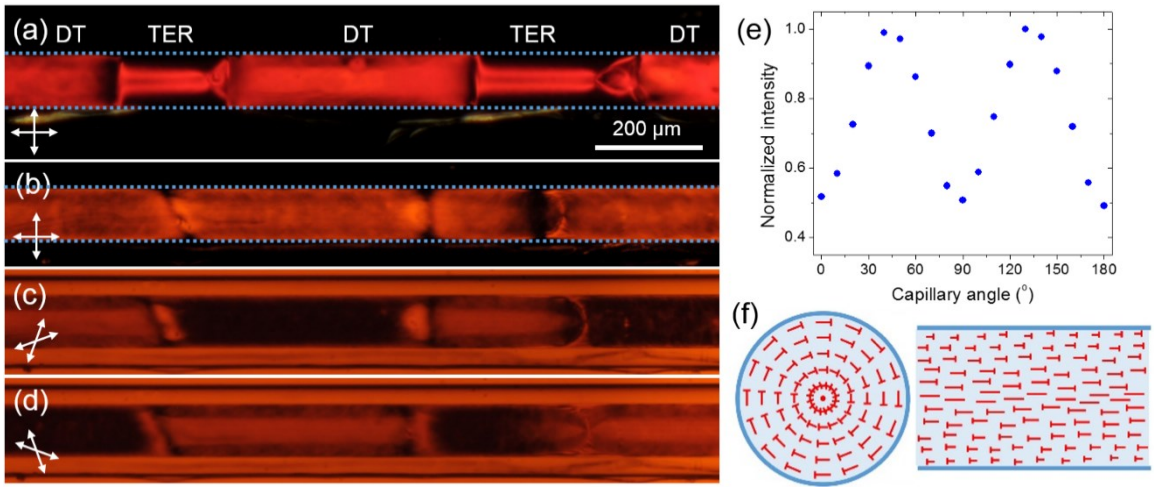

Figure 3.8 Polarized optical microscopy images of 1.18 M SSY after heating to isotropic phase and quenching back to nematic phase. (a) The co-existence of the TER domains and the DT domains under crossed polarizers. The blue dotted lines indicate the inner surface of the cylindrical capillary. (b) The DT domains with opposite twisted handedness separated by defects. (c) and (d) show the extinction of transmitted intensity for right-handed and left-handed domains when the polarizers make an angle of 50°. (e) The transmitted intensity of a DT domain as the capillary is rotated under the crossed polarizers. (b)-(e) were observed and measured with monochromatic illumination (589 nm). (f) Director field illustration of the cross section and the side view of the DT configuration. The heads of the nails indicate that the director inclines out of the page.

3.4.2 The estimation of the homeotropic anchoring strength

The director of the DT domains on the boundary is parallel with the cylindrical surface, which violates the homeotropic anchoring induced by the parylene-N alignment film. While it is possible that the emergence of the DT configuration results from the non-uniform deposition of parylene-N alignment film, we provide evidence in the Appendix A.2.2 that the non-uniformity of the deposition is not an important parameter. The emergence of the DT domains indicates finite homeotropic anchoring on the surface of the parylene-N. Here, we address the stability of the DT domains in co-existence with the TER

domains by considering the anchoring strength in the expression of the elastic free energy. Moreover, the saddle-splay elastic free energy is also included since this term plays an important role on the stability of the DT configuration[65] as discussed in Chapter 2. Therefore, the elastic free energy is expressed as equation 3.1 [65,141]:

$$F = \int dV \left\{\frac{1}{2}[K_{11}(\nabla \cdot \boldsymbol{n})^2 + K_{22}(\boldsymbol{n} \cdot \nabla \times \boldsymbol{n})^2 + K_{33}(\boldsymbol{n} \times \nabla \times \boldsymbol{n})^2]\right\} -$$

$$\int dV \frac{1}{2}(K_{22} + K_{24})\nabla \cdot [\boldsymbol{n}(\nabla \cdot \boldsymbol{n}) + \boldsymbol{n} \times \nabla \times \boldsymbol{n}]] + \int \frac{1}{2} W_{\perp} sin^2\theta_{\perp} dS \qquad (3.1)$$

where $\boldsymbol{n}$ is the nematic director, $W_{\perp}$ is the homeotropic anchoring strength, $\theta_{\perp}$ is the tilt angle of the director from the normal of the cylindrical surface.

The director field corresponding to the minimum of elastic free energy was calculated by numerically solving Euler-Lagrange equations using relaxation method as described in Chapter 2. The bulk elastic constants in the calculation are $K_{11} = K_{33} = 10K_{22} = K$ based on the measurements in the literature[94]. The saddle-splay elastic constant of SSY, $K_{24}/K = 6$, is used in our calculation from the twist angle measurement of the DT configuration in Chapter 2. In the cylindrical coordinates, the director is expressed in terms of two angles, α and β. α is the angle between the projection of director in r-ϕ plane and the r axis. β is the angle between director and axial axis. The definitions of α and β are shown in the inset of Figure 3.9a.

As expected, the numerical minimization converges to the TER configuration with infinite strong anchoring ($W_{\perp} = \infty$). Nevertheless, when $W_{\perp} < 1.24\times10^{-5}$ J/m^2, the calculation converges to different configurations with different initial conditions. The TER configuration is the stable state with the initial director field of $\alpha(r, t = 0) =$

$0, \beta(r, t = 0) = \frac{\pi}{2R} r$. But the DT configuration is converged in the calculation with the initial director field of $\alpha(r, t = 0) = \pi/2, \beta(r, t = 0) = \frac{\pi}{2R} r$. With $W_\perp$ = 1.2×10^{-5} J/m^2, the converged director fields of the two configurations are plotted in Figure 3.9a. In the director field of the TER configuration, $\beta(r/R_0 = 1) = 90^o$ corresponds to the homeotropic anchoring at the boundary and $\beta(r/R_0 = 0) = 0^o$ shows the escape of director field along cylindrical axis as approaching to the center. The twist deformation is indicated by the increase of α from 0^o on the boundary ($r/R_0 = 0$) to around 60^o in the center ($r/R_0 = 1$). The DT configuration is recognized by the invariance of α with the radial position ($\alpha(r/R_0) = 90^o$). The twist angle of the DT configuration increases from the center ($r/R_0 = 0$) to the boundary ($r/R_0 = 1$) of the cylinder as shown by the angle β. Despite that the TER configuration has a lower elastic free energy in the calculation, the DT configuration exists as a metastable state corresponding to a local minimum. The two local-minima observed in the solution of the Euler-Lagrange equations rationalize the co-existence of the two chiral configurations.

The phase diagram in Figure 3.9b presents the stable regions of the TER and the DT configurations in terms of the dimensionless variables $R_0W_\perp/K$ (R_0 is the radius of the cylinder) and K_{24}/K. The stable regions were calculated by the numerical minimization of equation 3.1 with the elastic constants of $K_{11} = K_{33} = 10K_{22} = K$ [94] (described in Chapter 2.2). The co-existence of the TER and the DT domains is stable with small $W_\perp$ ($R_0W_\perp/K <$ 60) and large K_{24} ($K_{24}/K > 2$). In this region, the small energy cost of the anchoring violation is overcome by the stabilization of the saddle-splay elastic free energy. Since the elastic constant, K, increases with the concentration, higher concentration has a smaller dimensionless variable $R_0 W_\perp /K$, which is in favor of the co-existence of the two

configurations. This explains that the DT domains were only observed with concentrated SSY solutions (> 1.15 M). With K_{24}/K = 6 and K = 14 pN for 1.15 M SSY[94], the homeotropic anchoring strength of SSY on parylene-N film coated in cylindrical capillaries with the inner diameter of 100 μm is estimated as $W_{\perp} = 1.2\times10^{-5}$ J/m^2. Typically, the anchoring strength of nematics reported in the literature varies broadly[142], $10^{-7} \sim 10^{-2}$ J/m^2. Our estimation is in the weak anchoring regime of conventional nematics. The weak homeotropic anchoring may promote the transition from the TER configuration to the TP configuration during the aging process as suggested by Jeong et al[9] and Crawford et al[79]. The weak anchoring allows the deviation of the director from the radial orientation on the boundary and facilitates the formation of line defects in the TP configuration. However, we note that this anchoring strength of SSY is relatively strong comparing with the values reported for lyotropic liquid crystals[143-145], which are usually $10^{-7} \sim 10^{-5}$ J/m^2. For instance, our estimation of the homeotropic anchoring strength for SSY on parylene-N film is stronger than that for DSCG induced by *N, N*-dimethyl-*N*-octadecyl-3-aminopropyl trimethoxysilyl chloride (DMOAP). V.G. Nazarenko et al.[143] estimated the homeotropic anchoring strength of DSCG on DMOAP coated glass slide, $W_{\perp}$(DSCG) = 10^{-6} J/m^2. The weak anchoring facilitates the anchoring transition of DSCG from homeotropic to planar anchoring after aging for 20 hours. Whereas the homeotropic anchoring of SSY in parylene-N coated capillaries remains for weeks until the phase transition occurs due to the slow water evaporation.

Moreover, the phase diagram suggests that the co-existence of the TER and the DT configurations is more likely to exist in small capillaries with small $R_0W_{\perp}/K$. But the experimental observations show the opposite tendency. Comparing with the cylindrical

capillaries mentioned above (inner diameter is 100 μm), the DT domains were exhibited in larger capillaries (inner diameter is 200 μm) with a lower concentration (C_{SSY} > 0.96 M) but were not observed in smaller capillaries (inner diameter is 50 μm). The inconsistency of calculation and observation indicates that the homeotropic anchoring strength is weaker in larger capillaries. With K = 6 pN [94] for 0.96 M SSY, the anchoring strength in capillaries with inner diameter of 200 μm is estimated to be $W_{\perp} = 2.7\times10^{-6}$ J/m^2. Since the anchoring strength is greatly affected by the surface morphology of the alignment film, we suggest that the difference of anchoring strength may result from the chemical vapor deposition process of parylene-N. The diffusion of the parylene precursor into larger capillaries is faster, causing a faster deposition speed on the inner capillary wall. The roughness of coated film should increase with the increase of deposition speed, which may reduce the homeotropic anchoring strength.

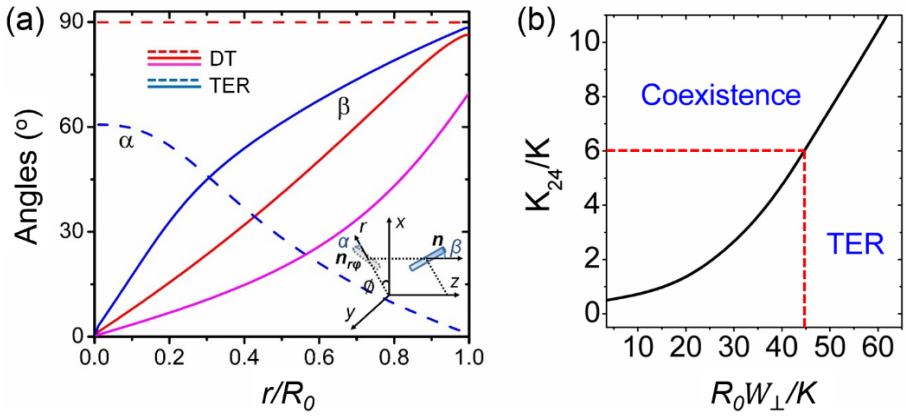

Figure 3.9 (a) The converged director fields of the DT configuration (red lines: $W_{\parallel} = 0$; magenta line: $W_{\parallel} = 1.4\times10^{-6}$ J/m^2) and the TER configuration (blue lines). Dashed lines are α and solid lines are β. The inset shows the definitions of the angles α and β in cylindrical coordinates. The homeotropic anchoring is fixed as $W_{\perp} = 1.2\times10^{-5}$ J/m^2. The two director configurations are converged with different initial conditions. (b) The calculated stable regions of the TER configuration and the co-existence of the TER domains and the DT domains.

3.4.3 The estimation of the axial planar anchoring strength

Furthermore, we notice that the twist angle of the DT domains in parylene-N coated cylindrical capillaries is smaller than that in uncoated cylindrical capillaries with degenerate planar anchoring. The twist angle of the DT domains from the center to the boundary in parylene-N coated cylindrical capillaries is $70^{o} \pm 15^{o}$ for 1.18 M SSY solution at room temperature of 22 ^{o}C (Appendix A.2.3, Figure A.5). Whereas, the twist angle in uncoated cylindrical capillaries was measured to be around 90^{o} with the same concentration and temperature (Appendix A.2.3, Figure A.6). As aforementioned, the DT configuration is stabilized by the saddle-splay contribution to the elastic free energy, which aligns director on the surface to the azimuthal direction with larger principal curvature. Therefore, a 90^{o} twist angle corresponds to the largest contribution of the saddle-splay elasticity to stabilize the DT configuration. The homeotropic anchoring violation in parylene-N coated cylinders is not expected to reduce the twist angle, but only adds a constant value to the total elastic free energy.

We suggest that the small twist angle of the DT domains in parylene-N coated capillaries is driven by the non-degenerate planar anchoring of SSY aggregates on parylene-N film. The director on the surface is weakly aligned in the axial orientation by parylene-N film. The axial planar anchoring can be inferred from the long-range orientational order of the parylene-N molecules coated on the wall of the cylindrical capillaries. In Figure 3.10a and 3.10b, the wall of an uncoated cylindrical capillary exhibits no light transmission under crossed polarizers since the borosilicate glass does not have birefringence. In Figure 3.10c, the capillary wall coated with parylene-N looks dark when the polarizer is parallel with the capillary axis. The transmitted intensity arises when the

capillary is rotated by 45° (Figure 3.10d). The transmitted intensity as a function of rotation angle (θ_r) is plotted in Figure 3.10g, which can be well fitted by the theoretical intensity profile of the axial alignment, $I/I_{max} = sin^2(\theta_r/2)$. The colors emerging with a λ-plate in Figure 3.10e and 3.10f also support the axial orientation of the parylene-N fibers. The lower-order yellow color in Figure 3.10e indicates a reduced retardation by the λ-plate when the orientation of the parylene-N molecules (the slow axis of the molecules[146]) is parallel with the fast axis of the λ-plate along the long axis of the capillary. When the orientation of the parylene-N molecules is perpendicular with the fast axis of λ-plate, the additive retardation results in the higher-order blue color as shown in Figure 3.10f.

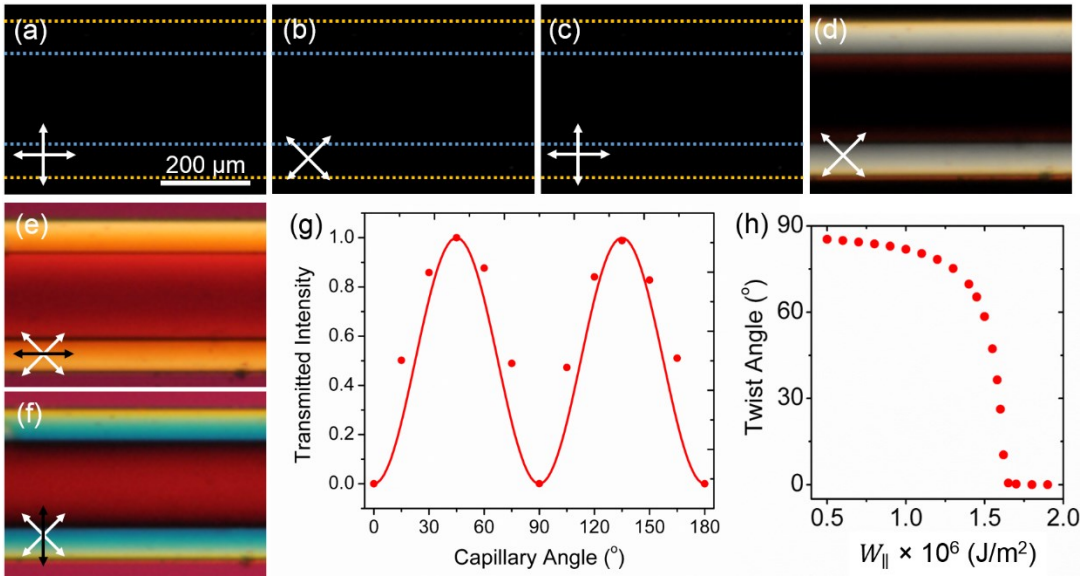

Figure 3.10 Polarized optical microscopy images of cylindrical capillaries under crossed polarizers. (a, b) An uncoated cylindrical capillary. (c, d) A parylene-N coated cylindrical capillary. The dotted blue and yellow lines indicate the inner and outer surfaces of the cylindrical capillaries, respectively. (e, f) A parylene-N coated capillary with a λ-plate inserting at 45° between the crossed polarizers. The black double-headed arrows indicate the fast axis of λ-plate. The white double-headed arrows indicate the orientations of polarizers. All the capillaries were filled with isotropic SSY solution (C_{SSY} = 0.80 M). (g) The transmitted intensity of the capillary wall when the capillary was rotated under crossed polarizers (dots). The data is fitted with the theoretical intensity function of the axial alignment (line, $I/I_{max} = sin^2(\frac{\theta_r}{2})$). (h) The calculated twist angle of the DT configuration as a function of the axial planar anchoring strength.

The axial planar anchoring induced by the long-range order of parylene-N molecules adds a planar anchoring term in the elastic free energy equation[141], $F_{\parallel} = \int \frac{1}{2} W_{\parallel} sin^2\theta_{\parallel} dS$, where $\theta_{\parallel}$ is the deviation angle of the director on the surface from the axial orientation, $W_{\parallel}$ is the axial planar anchoring strength. By minimizing the elastic free energy of the DT director field (described in Chapter 2.2), the twist angle as a function of $W_{\parallel}$ is plotted in Figure 3.10h calculated with the elastic constants of $K_{11} = K_{33} = 10K_{22} = K$ [94] and $K_{24}/K = 6$ [7]. The calculated twist angle is close to 90° when $W_{\parallel} < 10^{-6}\ \mathrm{J}/m^2$, but decreases dramatically with the increase of $W_{\parallel}$. When $W_{\parallel} > 1.65 \times 10^{-6}\ \mathrm{J}/m^2$, the director field exhibits the axial configuration with a twist angle of zero. Based on the measured twist angle of 70° ± 15°, the axial planar anchoring strength of SSY on parylene-N film is estimated to be $W_{\parallel} = 1.0 \sim 1.5 \times 10^{-6}\ \mathrm{J}/m^2$. This axial planar anchoring strength is weak comparing with that of conventional nematics in literature ($10^{-2} \sim 10^{-7}$ J/m^2), but stronger than that of LCLCs aligned by rubbed polymer films (10^{-7} J/m^2)[147,148].

3.5 Conclusions

In this chapter, we report the chiral configurations of achiral LCLCs in cylindrical capillaries with homeotropic anchoring. Shortly after filling the capillary, LCLCs director field departs from the usual ER configuration by developing a twist deformation (the TER configuration). Due to the small K_{22}, the twist deformation stabilizes the chiral TER configuration by partially relieving the energy of the splay and the bend deformations in the ER configuration. After aging for one day, the TER configuration was replaced by another chiral configuration featured by two twisting line defects, which is described as the twisted polar (TP) configuration.

By exploring the TER birefringent texture, we demonstrated that the width between bright stripes is an indirect measurement of LCLCs aggregation behavior as the temperature and the concentration are varied. Low temperatures and high concentrations lead to large widths between the bright stripes due to the elongation of the average aggregate length and the contrasting effects on the elastic constants of LCLCs. When plotted as a function of T/T_{NB}, the dependence of the width between bright stripes on reduced temperature is independent of concentration. The roles of temperature and concentration on the birefringent texture of LCLCs shows similarity as the roles on the order parameters.

As a novel configurational phenomenon, the co-existence of the TER and the DT domains was observed for high concentrations of LCLCs, indicating a violation of the homeotropic anchoring on the surface. With the help of numerical calculation, we addressed that the energy cost of the anchoring violation in the DT domains is overcome by the stabilization of the saddle-splay elasticity. Additionally, the smaller twist angle of the DT domains in the parylene-N coated cylindrical capillaries indicates an alignment effect in axial orientation, which is likely induced by the long-range orientational order of parylene-N molecules. Our estimations of the homeotropic anchoring strength and the axial planar anchoring strength provide important information to understand the confinement effects on the emergence of chirality. Particularly, we expect that the formation of the TP configuration is facilitated by the weak homeotropic anchoring of LCLCs. At this stage, we are not able to provide further understanding of the configurational transition between the TER and the TP structures. More theoretical works are required to describe the director field and analyze the energy of the TP configuration.

CHAPTER 4. EMERGENCE OF CHIRALITY FOR OTHER ACHIRAL LYOTROPICS: CHIRAL CONFIGURATIONS OF RACEMIC LYOTROPIC POLYMER LIQUID CRYSTALS UNDER CYLINDRICAL CONFINEMENT

4.1 Introduction

As mentioned in previous chapters, the chiral configurations of achiral LCLCs are driven by the small K_{22} and the curvature of the confinement surfaces. Based on this understanding, we may reasonably expect the same chiral configurations in cylindrical geometries for other nematics with K_{22} much smaller than K_{11} and K_{33}. As shown by early literature[117,118], the small K_{22} is not a special property for LCLCs, but seems to be a common feature for various lyotropic liquid crystals composed of semi-flexible building blocks. For instance, polymer molecules having rigid, rod-like backbones can be oriented in solutions and form the nematic phase[149,150]. K_{22} of lyotropic polymer nematics is also one order of magnitude smaller than K_{11} and K_{33} [118,151]. Studies have discovered that the high degree of elastic anisotropy leads to unexpected configurational transition in the thin film of lyotropic polymer nematics when a sufficiently high magnetic field is applied (Freedericksz transition)[152]. Under such conditions, rather than a uniform splay deformation, a periodic splay-twist distortion was observed for the nematic lyotropic polymer liquid crystals[152]. The splay-twist distortion has a lower critical field simply because the energy cost of the pure-splay director deformation is relieved by the relatively inexpensive twist distortion. Consequently, we speculate that the emergence of chirality

should be present in cylindrical confinements for achiral lyotropic polymer liquid crystals due to their small K_{22}, even though polymer molecules are notably different from the LCLCs aggregates.

In this chapter, we report our investigations of the director configurations in cylindrical capillaries using racemic poly-benzyl glutamate (PBG) solutions. PBG is a synthetic chiral polypeptide[153,154]. With individual enantiomers, PBG solutions exhibit cholesteric liquid crystalline phase[155,156] in which the director field adopts a twisted helical structure (Figure 1.3a)[61]. The interference of the helical pitches results in the fingerprint texture under crossed polarizers as shown in Figure 4.1a. The nematic phase forms when equal amounts of levorotatory and dextrorotatory enantiomers are mixed and dissolved in a mixed solvent of 18% 1,4-dioxane, 82% dichloromethane, and a few drops of N,N-dimethylformamide[118]. Under crossed polarizers, schlieren texture of nematic phase is exhibited free of any fingerprints as shown in Figure 4.1b, indicating that the two PBG enantiomers are thoroughly mixed as a racemic solution with no phase separation. (The materials and sample preparations are described in Appendix A.7.1 and A.7.2.)

Nematic PBG solutions were then confined in cylindrical geometries with planar and homeotropic anchorings. Remarkably, the chiral configurations observed for racemic PBG solutions are identical to those observed for LCLCs in cylindrical capillaries. Our observations provide a solid example to support the universal existence of the chiral configurations for different achiral lyotropic liquid crystals in cylindrical confinements. The emergence of chirality is completely elastic-driven, which is irrespective to the chemical components of the lyotropic nematics. This general symmetry-breaking

configurational behavior distinguishes lyotropic liquid crystals from the conventional thermotropic liquid crystals, which usually exhibit achiral configurations under cylindrical confinements[130-132].

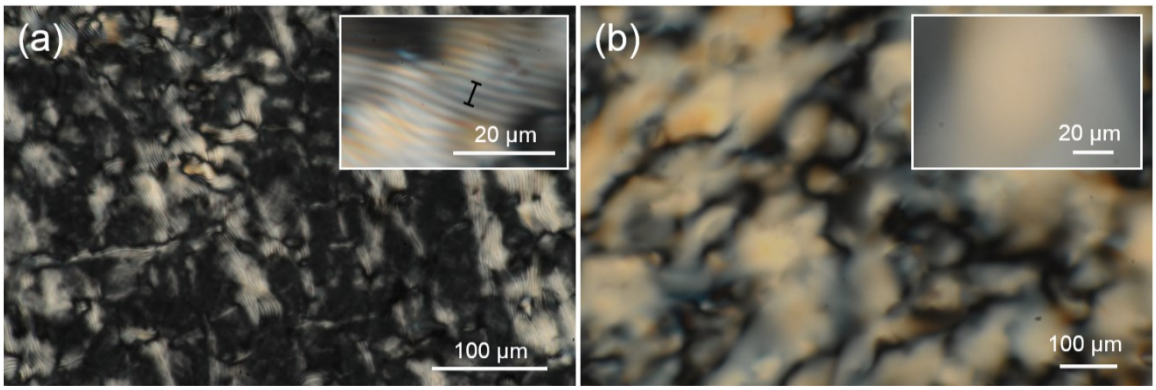

Figure 4.1 Polarized optical microscopy images of (a) levorotatory PBG enantiomer (PBLG) and (b) racemic PBG under crossed polarizers. The solutions were sandwiched between two flat glass slides with a thickness of 70 μm. The concentration is 12 wt% for both samples. The amplified image in the inset of (a) shows the fingerprint texture of cholesteric phase with a pitch of 4 μm as indicated by the black line. The amplified image in the inset of (b) shows a schlieren texture of nematic phase with no fingerprints.

4.2 Chiral configuration of racemic lyotropic polymer liquid crystals in cylindrical capillaries with planar anchoring

4.2.1 Polarized optical microscopy observations

Nematic PBG solution in a parylene-N coated cylindrical capillary conforms to planar anchoring on the surface. The director is aligned parallel with the capillary wall due to the interactions between the phenyl rings on PBG side chains and the phenyl rings on parylene-N backbones. Under crossed polarizers, racemic PBG solution exhibits multiple domains in a parylene-N coated cylindrical capillary as shown in Figure 4.2a and 4.2b. The adjacent domains are separated by defect structures. Individual domain does not show

complete extinction of light as the capillary is rotated under crossed polarizers. This pattern was observed around 12 hours after filling the capillary and remained stable for at least 5 days until the sample does not exhibit nematic phase due to solvent evaporation.

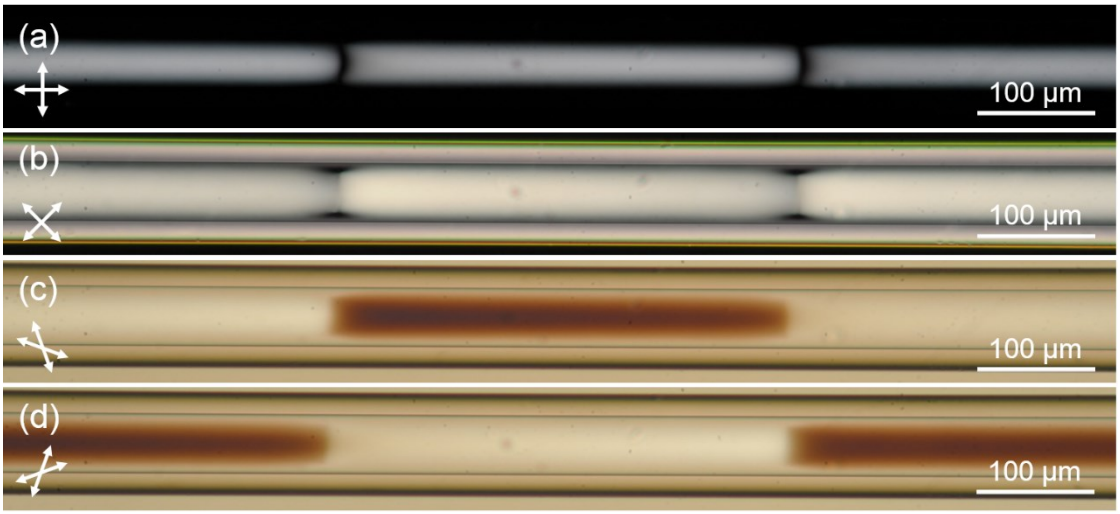

Figure 4.2 (a, b) Birefringent patterns of the DT domains for racemic PBG under crossed polarizer when the cylinder axis is at 0° and 45° with the polarizer. (c, d) Birefringent patterns of the DT domains for racemic PBG when the angle between polarizer and analyzer is 50°. The orientations of polarizer and analyzer are indicated by the double-headed white arrows. The solutions were filled in parylene-N coated cylindrical capillaries with a concentration of 12 wt%.

For individual domain, the transmitted intensity of the birefringent pattern under crossed polarizers is a signature of twist deformation in the director field. The twisted director field rotates the polarization of incident light, which enables the light to pass through the crossed analyzer[37]. This birefringent pattern can be explained by the doubly-twisted (DT) director field, which is identical to the chiral configuration of LCLCs in Chapter 2. In the DT configuration, the director is axial along the center of the cylinder and twists progressively from the center to the boundary (Figure 2.2g). Since the PBG solution is racemic with no preference of either chirality, both right-handed and left-handed twists of the director field have equal probability to emerge in the cylinder. This expectation

agrees with our observation of multiple domains in a single capillary, wherein the director fields in the adjacent domains twist with opposite handedness. The opposite twist directions are clearly revealed by the colors in Figure 4.2c and 4.2d when the polarizer and analyzer are decrossed.

4.2.2 Twist angle measurement and the estimation of saddle-splay elastic constant

As mentioned in Chapter 2, the emergence of the DT configuration from achiral nematics is rationalized by the stabilization due to the saddle-splay contribution to the elastic free energy. We developed a method to estimate the value of K_{24} for LCLCs by measuring the twist angle of the DT director field. Here, we follow the method established in Chapter 2 to extract the K_{24} value of racemic PBG solution, which is the first estimation of K_{24} for lyotropic polymer liquid crystals at the best of our knowledge. In Appendix A.3.1, Figure A.7, we provide the AFM images of the parylene-N film coated on the glass substrate. The surface of the parylene-N does not have any micropatterns that may align the director of nematics. Therefore, we estimated the value to K_{24} under the assumption of degenerate planar anchoring condition.

The twist angle of the DT director field can be measured from the optical rotation of polarized light[37]. As aforementioned, the wave-guiding requirement (Mauguin limit) is satisfied when the total twist angle, 2Φ, is much smaller than the phase retardation (Γ) due to the birefringence of nematics[37], $2\Phi \ll |\Gamma| = \left|\frac{2\pi}{\lambda}(n_e - n_o)d\right|$. However, the small birefringence of PBG ($\Delta n = 0.005$)[157] cannot satisfy the waveguiding requirement with the path length of 50 μm (the inner diameter of the cylindrical capillary). However, we failed to observe a good DT domain in cylindrical capillaries with the inner diameter of 100 μm

or larger. Therefore, the twist angle of the director field cannot be directly measured by the wave-guiding experiments.

With comparable twist angle and phase retardation, we used Jones matrix simulation (please see Appendix A.7.5) to find the twist angle by fitting the measured transmitted intensities with the calculation for different DT director fields. Firstly, the transmitted intensities with different polarizer and analyzer angles were measured with monochromatic illumination of 486 nm. The polarizer is rotated every 10^o from 0^o to 180^o (horizontal direction). For each polarizer angle, the analyzer is also rotated every 10^o from -90^o to 90^o (vertical direction). The maximum and minimum transmitted intensity at every polarizer angle is plotted in Figure 4.3a. The transmittance reaches the lowest value with the polarizer angle of 20^o. Figure 4.3b presents the transmitted intensity as a function of analyzer angle when the polarizer is fixed at 20^o. The DT domain exhibits the lowest intensity with the analyzer at 70^o.

Next, the transmitted intensities with different polarizer and analyzer angles were numerically simulated by the Jones matrix method (see the description in the Appendix A.7.5). The DT director fields used in the simulation were calculated by minimizing elastic free energy as K_{24} is varied (as described in Chapter 2.2). The elastic constants and the birefringence used in the calculation are $K_{11} : K_{22} : K_{33} = 1 : 0.055 : 0.67$ and $\Delta n = 0.005$ as reported in literature[118,157]. The simulated transmitted intensity curves with a twist angle of 60^o are plotted in Figure 4.3c and 4.3d. With a twist angle of 60^o, the simulated curves best fit with the measured curves in the experiment (Figure 4.3a and 4.3b). The corresponding saddle-splay elastic constant of PBG is $K_{24}/K_{11} = 0.16 \pm 0.03$. Based on this

estimation, K_{24} is about 6 times larger than K_{22} (K_{24}/K_{22} = 6.5 ± 1.2). The large K_{24} is consistent with the theoretical requirement for the emergence of the DT configuration, $K_{24} > K_{22}$. The transmitted intensities were also measured using monochromatic 656 nm illumination as presented in Figure 4.4a and 4.4b. The polarizer angle of the lowest transmitted intensity for 656 nm illumination is about 10° different from that for 486 nm illumination. Using the same K_{24}/K_{11} (K_{24}/K_{11} = 0.16), the measured transmitted intensities of 656 nm illumination can also be well fitted by the calculated intensities as shown in Figure 4.4c and 4.4d.

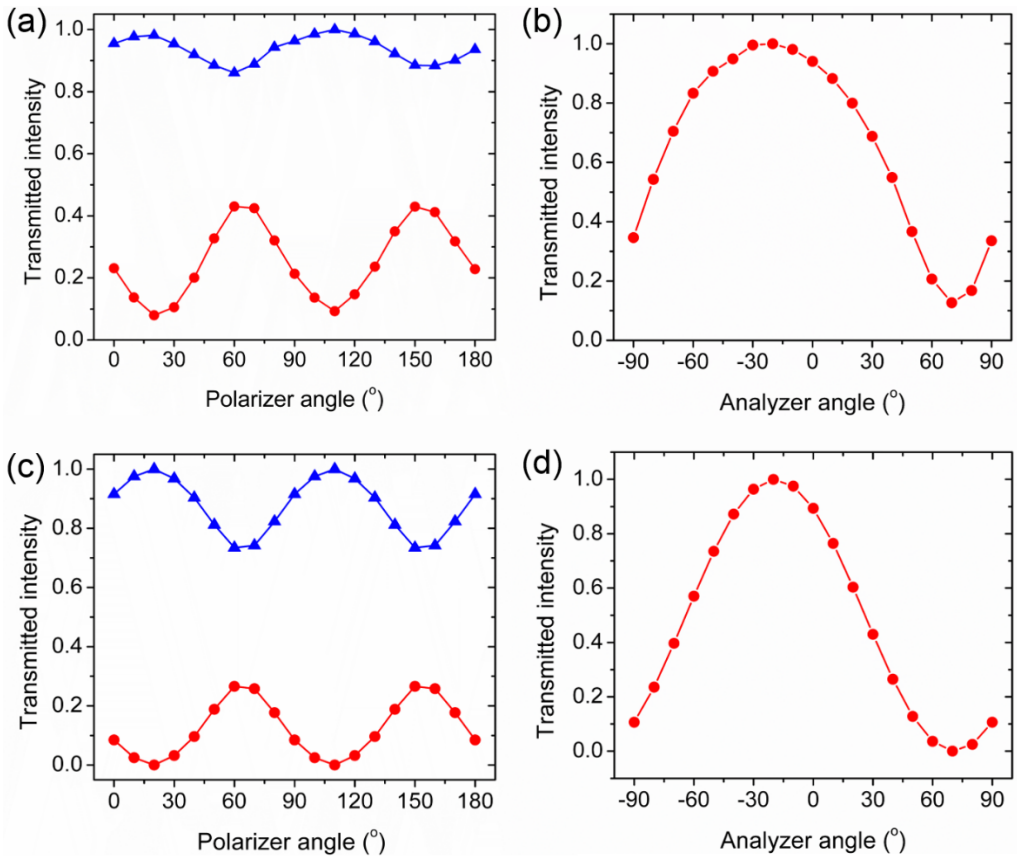

Figure 4.3 Twist angle measurement of the DT director field under 486 nm monochromatic illumination. (a, c) The maximum (blue triangles) and minimum (red circles) transmitted intensities at different polarizer angles when the analyzer is rotated through -90° to 90°. (a) is measured from experiments and (c) is calculated by Jones matrix simulation. (b, d) The transmitted intensities at different analyzer angles when the polarizer is fixed at 20°. (b) is measured from experiments and (d) is calculated by Jones matrix simulation.

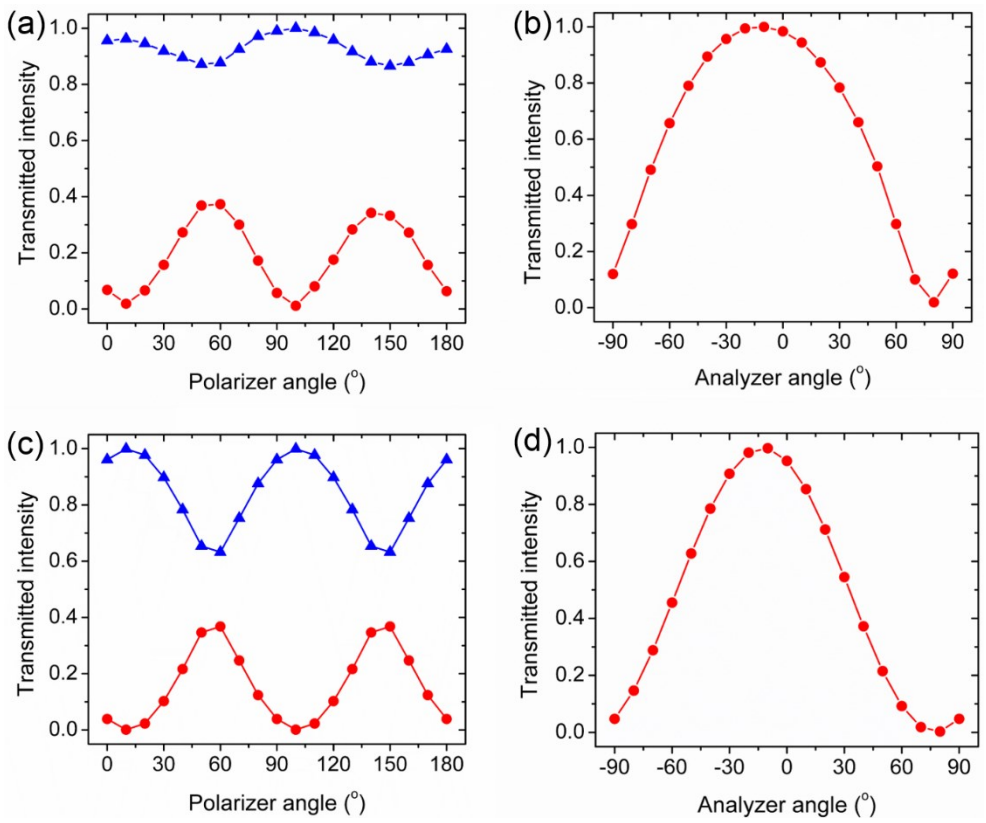

Figure 4.4 Twist angle measurement of the DT director field under 656 nm monochromatic illumination. (a, c) The maximum (blue triangles) and minimum (red circles) transmitted intensities at every polarizer angle when the analyzer is rotated through -90° to 90°. (a) is measured from experiments and (c) is calculated from Jones matrix simulation. (b, d) The transmitted intensities at every analyzer angle when the polarizer is fixed at 10°. (b) is measured from experiments and (d) is calculated from Jones matrix simulation.

It is noted that although the length of PBG molecules (100 ~ 200 nm [118,126]) is much longer than that of LCLC aggregates (5~20 nm [97]), the relative K_{24} of PBG (K_{24}/K_{11} = 0.16 ± 0.03) is smaller than that of LCLCs (SSY: K_{24}/K_{11} = 6. DSCG: K_{24}/K_{11} = 1.2). Since K_{11} is linear with the length of the building blocks[96] ($K_{11} \sim \emptyset \frac{L}{D}$), we infer that K_{11} of PBG with a longer average length of molecules should be larger than that of LCLCs. As reported in literature, K_{11} of PBG is about 20 pN [118], whereas K_{11} of both SSY and DSCG are about 5~10 pN [93-95]. The larger K_{11} of PBG leads to a smaller K_{24}/K_{11} value, indicating that K_{24} does not scale linearly with the average length of the building blocks as K_{11}. This indication

is consistent with our discussion of K_{24} for PBG and LCLCs in Chapter 2.4, where we suggested the dependence of K_{24} on the persistence length rather than the contour length of the building units.

4.3 Chiral configuration of racemic lyotropic polymer liquid crystal in cylindrical capillaries with homeotropic anchoring

4.3.1 Polarized optical microscopy observations

In this section, we report the configurations of racemic PBG in borosilicate cylindrical capillaries in absence of alignment film. Around 30 min after filling the capillary, the birefringent pattern of PBG exhibits a dark stripe at the central region and two bright stripes close to the boundary (Figure 4.5a). The orientation of the director can be surmised from the color with a λ-plate inserted at 45° between crossed polarizers as shown in Figure 4.5b. When the fast axis of the sample is superimposed over the fast axis of λ-plate, the additive retardation results in higher order blue color. Otherwise if the fast axis of the sample is parallel with the slow axis of λ-plate, the reduced retardation leads to a lower order yellow color. With the birefringence of PBG[157], Δn = 0.005, the director orientation is the slow axis for linear polarized light. The two bright stripes of the birefringent pattern in Figure 4.5a exhibit blue and yellow colors in Figure 4.5b with a λ-plate, indicating that the director escapes and deviates from the radial orientation. The magenta color in the central region shows that the director is along the axial orientation in the center of the cylinder. This director field of PBG agrees with the features of the ER configuration as illustrated in Figure 3.1b. As shown in Figure 4.5c, the typical birefringent pattern of the ER configuration for 5CB exhibits no transmitted intensity on the boundary

and two bright stripes emerge as the director approaches to the center. In the birefringent texture of PBG, however, the bright stripes are very close to the boundary of the capillary and the boundary still displays some transmitted intensity. These features of PBG birefringent textures suggest that the director on the surface is tilted from the radial orientation under finite homeotropic anchoring.

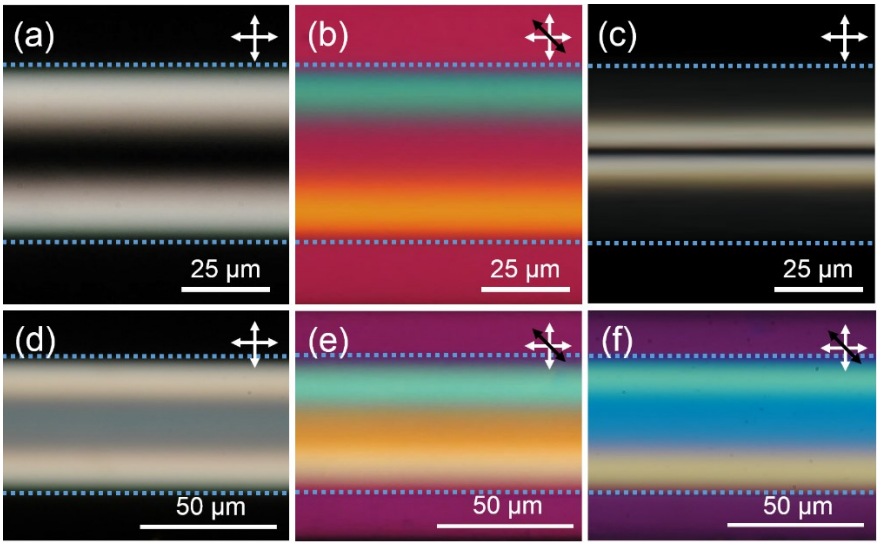

Figure 4.5 (a, b) Birefringent texture of PBG under crossed polarizers captured 30 min after filling the capillary. The polarizer and analyzer orientations are indicated by the double-headed white arrows. The dashed blue lines indicate the inner surface of the cylindrical capillaries. (b) was captured with a λ-plate inserted at an angle of 45° with crossed polarizers. The fast axis of λ-plate is indicated by the double-headed black arrows. (c) Typical ER birefringent pattern of 5CB in cylindrical capillary with homeotropic anchoring. (d-f) Birefringent texture of PBG under crossed polarizers captured around 24 hours after filling the capillary. (e, f) were captured with a λ-plate inserted at an angle of 45° with crossed polarizers.

After aging for 24 hours, the transmitted intensity of the PBG birefringent pattern increases in the central region of the cylinder as shown in Figure 4.5d, indicating that the twist deformation evolves in the director field. This director field corresponds to the TER configuration as illustrated in Figure 3.2d. Due to the small K_{22} of PBG[118], the TER configuration is stabilized since the relatively "cheap" twist deformation partially relieves

the energy contributions of splay and bend deformations in the ER director field. The twist deformation increases the director component in the azimuthal orientation, resulting the yellow and blue colors in the central region observed with a λ-plate under crossed polarizers (Figure 4.5e and 4.5f). The yellow and blue colors correspond to right-handed and left-handed twisted domains, respectively.

Due to the racemic nature of the PBG solution, multiple TER domains with alternating left-handed and right-handed twist directions are expected in a cylindrical capillary. While the domains with different twist directions were observed in different cylindrical capillaries, both twist domains were not apparent in a single capillary. A possible explanation to rationalize the absence of the domains with opposite twist handedness is the chirality amplification due to small inequality of the two enantiomers. Literature has shown that the chiral configurations of confined achiral liquid crystals can easily exhibit homochirality due to tiny amount of external chiral dopants[158,159]. The concentration of chiral dopants can be as low as 0.1 wt% to effectively shift the handedness of twist direction. The homochirality observed for the TER configuration may result from a small excess of either PBG enantiomer. Additionally, it should be equivalent for the TER director field to escape towards either positive or negative axial orientation. When the domains with opposite escape directions meet, point defects should emerge with alternating topological charges of +1 and -1 as illustrated in Figure 3.1c. The TER configuration with point defects was observed for LCLCs in Figure 3.3a. However, point defects are absent in our observation with PBG for both the ER and the TER configurations. As shown in Figure 4.5, the birefringent pattern of PBG exhibits a wide stripe in the central region of the cylinder, indicating that director field has a wide escaped core. To create point defects,

plenty of director adjustments are required, consuming considerable elastic free energy. Hence, we could speculate that the instability of point defects favors the single escaped direction of the director field.

Roughly 70 hours after filling the capillaries, another chiral configuration with two twisting line defects (Figure 4.6a and 4.6b) were observed for PBG in replace of the TER configuration. This birefringent texture can be explained by the twisted polar (TP) configuration as illustrated in Figure 3.4i, which is the same as the chiral configuration of LCLCs in Chapter 3. The director field in the cross section of the cylinder shows two +1/2 defects on each side. The double helical structure of the line defects is exhibited when the cross-sectional director field twists along the axial orientation. The director also twists transversely out of the cross-sectional plane, resulting in the transmitted intensity in the birefringent texture when the polarizer is parallel with the capillary axis (Figure 4.6a). Due to the small K_{22} of PBG, the transverse twist can partially relieve the energy consumption of the splay and the bend deformations, and thus stabilizes the line defects.

For the TP configuration, the center between the two crossing points of the line defects is expected to exhibit extinction of transmitted light as the sample is rotated under the crossed polarizers, since the director is normal to the polarization plane. In Figure 4.6a, the center of two crossing points (indicated by the yellow arrow) shows no transmitted intensity when polarization is parallel with the capillary axis. However, the transmitted intensity arises when the sample is rotated by 45^{o} as shown in Figure 4.6b. The rise of transmitted intensity in the center of two crossing points is another indication of the anchoring violation on the capillary surface. When the director tilts from the radial

orientation of the cylinder, the director gains the component out of the radial orientation at the center of the two crossing points, which results in the transmitted intensity under crossed polarizers when the sample is rotated by 45°. In Figure 4.6c and 4.6d, both right- and left-handed twists of the line defects were observed in a single capillary. A defect structure is formed between the two domains with different twist directions as pointed by the blue arrows. The opposite twist handedness is clearly shown with a λ-plate inserted at 45° between crossed polarizers. In Figure 4.6d, the lines oriented parallel and perpendicular with the fast axis of the λ-plate exhibit yellow and blue colors, respectively. The yellow line is on top of the blue line for the domain on the left, whereas the blue line is on top of the yellow line for the domain on the right.

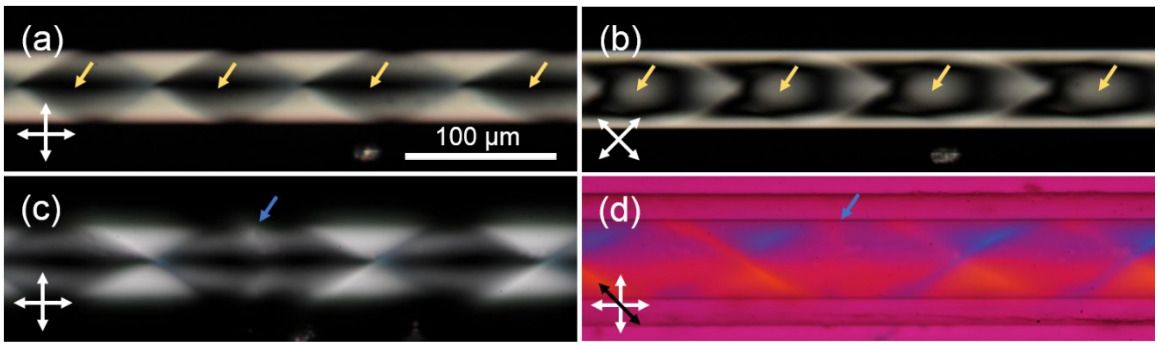

Figure 4.6 (a, b) Birefringent textures of PBG under crossed polarizers captured 70 hours after filling the capillaries (a) The cylindrical axis is parallel with the polarizer. (b) The cylindrical axis is rotated by 45° with the polarizer. The polarizer and analyzer orientations are indicated by the double-headed white arrows. The central regions between two crossing points are indicated by single-headed yellow arrows. (c, d) Images of two adjacent domains in which the line defects twist with opposite handedness. The two domains are separated by a defect structure as pointed by the single-headed blue arrows. (c) is observed under crossed polarizers. (d) is observed with a λ-plate at 45° with the crossed polarizers. The fast axis of λ-plate is indicated by the double-headed black arrow.

4.3.2 Anchoring violation on the surface

The TER birefringent textures of PBG are compared in Figure 4.7a in cylindrical capillaries with inner diameters of D_0 = 50 μm, 100 μm, and 200 μm. With an increase in the capillary size, the region close to the capillary wall is darker and the position of two bright stripes is closer to the center of the cylinder. These features of birefringent textures are apparent in the intensity profiles of the cross section in Figure 4.7c. The distance between the two bright peaks is smaller for larger diameter of the capillary. Moreover, the transmitted intensities close to the boundary of the capillaries (< 3 μm) were measured and plotted in Figure 4.7b as the cylinders were rotated under crossed polarizers. For D_0 = 200 μm, the boundary shows no transmitted intensity at rotation angles of 0° and 90° when the capillary axis is parallel with and perpendicular to the polarizer. The maximum transmittance occurs when the capillary axis and the polarizer are at 45°. This transmitted intensity suggests that the director on the boundary is perpendicular to the surface of the cylinder. However, for D_0 = 100 μm and 50 μm, the minimum transmitted intensities correspond to rotation angles of 85° and 80°, respectively. It suggests that the director on the boundary deviates from the normal orientation of the surface. The transmitted intensity curves are fitted with the theoretical transmittance of the uniform director field[37], $I = sin^2\left(\frac{\theta_r - \theta_\perp}{2}\right)$, where θ_r is the rotation angle of the capillary, $\theta_\perp$ is the tilt angle of director from the radial orientation. The fitting curves are presented as solid lines in Figure 4.7b. The tilt angles of the fitting curves are 0°, 5°, and 11° for capillaries with the inner diameters of D_0 = 200 μm, 100 μm, and 50 μm, respectively.

The director field of confined nematics is significantly affected by the anchoring strength on the surface of the confinement. With weak homeotropic anchoring, small confinements allow a tilt angle of the director on the surface to relieve the elastic free

energy of bulk director distortions. Whereas large confinements provide enough space for bulk deformations and suppress any anchoring violation of the director on the surface. Hence, with the help of numerical calculation, the tilt angle of the director on the surface of the small capillaries enables us to estimate the homeotropic anchoring strength of PBG on the interface of borosilicate capillaries[143,148,160]. In the numerical calculation, besides the splay, twist, bend, and saddle-splay terms, the homeotropic anchoring term is considered in the elastic free energy expression[141], $F_W = \int \frac{1}{2} W_\perp \sin^2\theta_\perp dS$, where $W_\perp$ is the homeotropic anchoring strength and $\theta_\perp$ is the tilt angle of the director on the surface from the radial orientation. The ratio of the elastic constants used in the energy minimization is $K_{11} : K_{22} : K_{33} : K_{24} = 1 : 0.055 : 1.5 : 0.16$ as reported in literature[118]. The calculation method of the energy minimization is the same as that described in Chapter 2.2.2.

As shown in Figure 4.8, the director field converges to the TER configuration at the minimum elastic free energy. The angle α indicates the twist deformation of the director field, which increases from 0° to about 60° from the boundary ($r/R_0 = 1$) to the center ($r/R_0 = 0$). The angle β on the boundary ($r/R_0 = 1$) shows the tilt angle of director from the radial orientation. With $W_\perp = 4\times10^{-6}$ J/m^2, the calculated tilt angles on the surface are 2°, 4°, and 10° for capillaries with inner diameter of D_0 = 200 μm, 100 μm, and 50 μm, respectively. These calculated tilt angles best match with the tilt angles measured in the experiments (0°, 5°, and 11° for D_0 = 200 μm, 100 μm, and 50 μm, respectively). The anchoring strength of nematics reported in literature has large variations[142,144,161] of 10^{-7}~10^{-2} J/m^2. Our estimated homeotropic anchoring strength of PBG, $W_\perp = 4\times10^{-6}$ J/m^2, is in the weak anchoring regime for conventional nematics. With the calculated director fields, Jones matrix simulation was performed (see Appendix A.7.5) and the corresponding cross-sectional

intensity profiles are presented in Figure 4.7d. The simulated intensity profiles capture the features of birefringent patterns in cylinders of different sizes. For larger capillaries, the transmitted intensity in proximity of the surface is lower and the bright peaks are closer to the center of the cylinders.

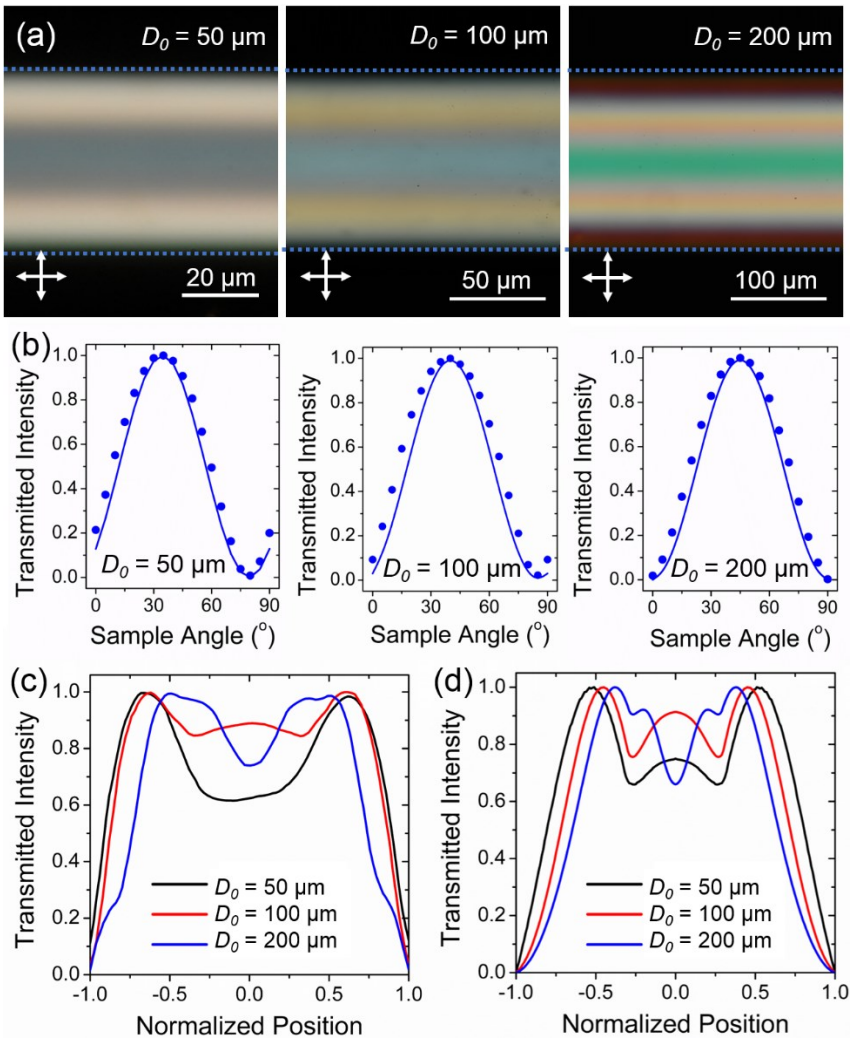

Figure 4.7 (a) The TER birefringent patterns of PBG under crossed polarizers in cylindrical capillaries with inner diameters (D_0) of 50 μm, 100 μm, and 200 μm. The polarizer and analyzer orientations are indicated by the double-headed white arrows. The dashed blue lines indicate the inner surface of the cylindrical capillaries. (b) The transmitted intensities as a function of rotation angle in the region close to the boundary of the cylinders (< 3 μm). The circles are experimental data. The lines are the fitting curves of theoretical transmittance of the uniform director field. (c) and (d) are the transmitted intensity profiles of the cross section measured from experiments and calculated from Jones Matrix simulation, respectively.

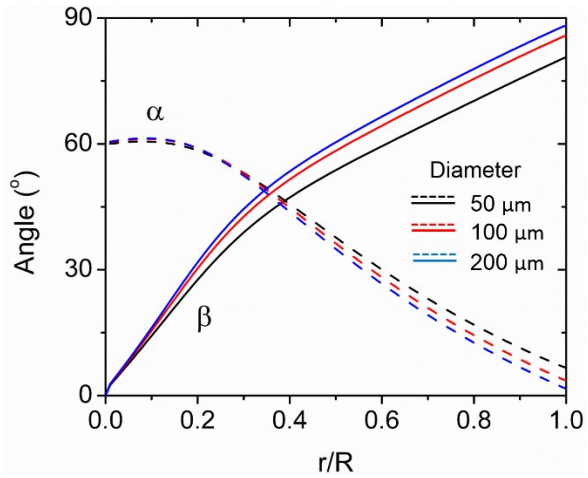

Figure 4.8 The calculated TER director fields in cylinders with finite homeotropic anchoring strength, $W_{\perp} = 4\times10^{-6}$ J/m^2.

4.4 Discussions and conclusions

In this chapter, we summarized our work on a racemic lyotropic polymer liquid crystal (PBG) confined in cylindrical capillaries, where the chiral configurations observed for PBG are the same as those for achiral LCLCs. A DT configuration was exhibited with degenerate planar anchoring, which enabled the first estimation of the saddle-splay elastic constant for lyotropic polymer liquid crystals. With homeotropic anchoring, the ER, TER, and TP configurations were observed in sequence during the aging process. The director on the surface was tilted from the normal orientation in small cylindrical capillaries, from which we estimated the homeotropic anchoring strength of PBG on the surface.

Remarkably, even though nematic phase of polymer and LCLCs are composed of different building units, they exhibit similar chiral structures in cylindrical capillaries driven by the common property of small twist elastic constant. Our work indicates that the emergence of chirality might be a universal behavior for achiral lyotropics, independent from the molecular compositions of the materials. Another supportive observation is the

chiral configurations of achiral lyotropic micellar liquid crystals in cylindrical capillaries reported recently by Dietrich et al[23]. Above a certain concentration, surfactant molecules self-assemble as disk-like micelles[82,162]. The principal axes of the supramolecular micelles are oriented and form nematic phase. Dietrich et al.[23] studied the configurations of nematic lyotropic micelles in cylindrical capillaries with homeotropic anchoring. Despite the difference in the self-assembling mechanism, micelles exhibit the same chiral TER configuration as LCLCs and polymers. The TP configuration was also observed with micelles under the effect of magnetic field. The similarities of the chiral configurations for different achiral lyotropics are truly remarkable, which implies that the emergence of chirality is a general configurational behavior for lyotropic liquid crystals since their twist elastic constants are commonly much smaller than the splay and bend elastic constants. This symmetry-breaking phenomenon is fully elasticity-driven, which does not depend on the molecular chirality. The chiral configurations and the large elastic anisotropy distinguish lyotropic liquid crystals from the conventional thermotropic liquid crystals. The theoretical explanation of the small twist elastic constant for lyotropics is a fundamental question that needs to be further studied.

The differences of the chiral structures for various lyotropic systems are also worth noting. For instance, LCLCs and polymer liquid crystals spontaneously exhibit the TP configuration in cylindrical capillaries after aging. The configurational transition was attributed to the weak homeotropic anchoring on the surface of the cylindrical confinement. But for micellar liquid crystals, the TP configuration only emerges under the effect of external magnetic field[23]. In this situation, the magnetic field alignment squeezes the escaped director field and destabilizes the ER configuration. The measurements of

anchoring strength for micellar liquid crystals will help to understand the stability of the TP configuration. Additionally, the features of the TP configuration also reveal the information of the elastic properties for different lyotropic materials. In Table 4.1, we compared the distance between the line defects and the half pitch of the double helical twist for PBG, SSY, DSCG, and micelles[23]. We speculate that due to the small K_{22} of lyotropics, the double helical twist of the line defects may lower the elastic free energy of the director field by relieving the energy costs of the splay and bend deformations close to the lines. Hence, the pitch of the line defects is determined by the ratio of the elastic constant K/K_{22} (assuming $K = K_{11} = K_{33}$). As shown in Table 4.1, K/K_{22} of SSY is much smaller than that of PBG and DSCG. As a result, the TP configuration of SSY has a larger pitch in the director field than that of PBG and DSCG. The distance between the line defects may depend on the effects of saddle-splay elasticity and the anchoring strength. A complete description of the TP configuration still requires future work of experimental observation, theoretical analysis, and characterization of elastic properties.

Table 4.1 The features of the twisted polar (TP) configurations for PBG, SSY, DSCG, and micelles

Materials	Distance/Diameter	Half Pitch/Diameter	K/K_{22}
PBG	1	2.1	30 [54]
SSY	0.8	3.4	8 [55]
DSCG	0.6	1.4	35 [70]
Micelles		2.5 [23]	

Note: Distance/Diameter is the distance between two line defects normalized by the diameter of the cylindrical capillaries. Half Pitch/Diameter is the half pitch of the double helical twist of the line defects normalized by the diameter of the cylindrical capillaries. Distance/Diameter and Half Pitch/Diameter data of PBG, SSY, and DSCG were measured from the birefringent patterns of the TP configurations shown in Chapter 4.3.1 and Chapter 3.2.2. Half Pitch/Diameter data of micelles and K/K_{22} data are from the references.

CHAPTER 5. CHIRAL CONFIGURATIONS OF LCLC TACTOIDS AND THE EFFECT OF A NEUTRAL POLYMER ADDITIVE

5.1 Introduction

LCLCs are distinguished from conventional liquid crystals since the building units of nematic phase are self-assembled rod-like aggregates rather than individual molecules[84]. The interactions between adjacent LCLC molecules in the aggregates are rather weak, which is only several times of k_BT [11,94,123]. The poly-disperse length distribution of the aggregates is sensitive to temperature, concentration, and external impurities. As a result, there exists a large biphase temperature range in the phase diagram of LCLCs (Figure 5.1a), where the isotropic phase and nematic phase co-exist. Upon cooling from the isotropic phase, the isolated nematic domains emerge in the continuous isotropic phase when the temperature is just below the phase transition temperature between isotropic phase and biphase region (T_{BI}). These nematic domains, referred as tactoids, are the natural confinements to study nematics in curved geometries. As shown in Figure 5.1b, the nematic domains of typical SSY tactoids exhibit a symmetric pattern of the conventional bipolar structure (which will be discussed in section 5.2)[99,100,163]. The tactoids are surrounded by isotropic phase, which looks dark under crossed polarizers. Upon further cooling the sample, the nematic domains will expand to be continuous and the isotropic phase will be isolated as individual domains. Finally, the isotropic domains disappear and the entire sample exhibits nematic phase when the temperature reaches T_{NB}, the phase transition temperature between nematic phase and biphase region.

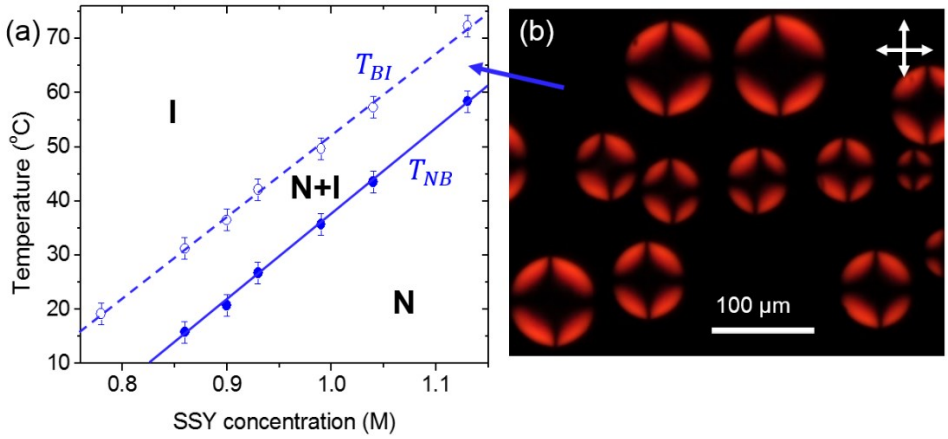

Figure 5.1 (a) The phase diagram of SSY. I: isotropic phase. N: nematic phase. N+I: biphase region where the nematic phase and isotropic phase co-exist. (b) SSY bipolar tactoids under crossed polarizers.

The configurations of tactoids attract considerable interests of scientists[74,164-167] since they serve as a convenient setting to study confined nematics coupled with the effect of curvature. The tactoidal configurations reveal the dedicate interplay of the elastic deformation modes and the nematic-isotropic interface. In this chapter, we begin the discussion on the observation of SSY tactoids at different temperatures and concentrations. Besides the usual bipolar tactoids at high concentrations and temperatures, we found two chiral configurations of SSY tactoids at low concentrations and temperatures. Remarkably, one of the chiral configuration, the escape-concentric (EC) configuration, was realized in our experiments for the first time[11]. The configurational transformation of tactoids probes the changes of aggregate length distribution, which enables us to study the effect of a neutral polymer additive on the aggregation behavior of SSY.

5.2 Configurations of LCLCs tactoids[11]

The discussion in section 5.2 was based on the collaboration with Dr. Karthik Nayani and Dr. Jinxin Fu.

5.2.1 Polarized optical microscopy observations

To observe the SSY tactoids, the SSY solutions were filled in rectangular capillaries with the cross-sectional inner dimension of 100 μm × 1000 μm (see Appendix A.7 for materials and sample preparation). Upon cooling from isotropic phase, the tactoids nucleate on the flat top and bottom surfaces of the capillary wall at the temperature below T_{BI}. The reduced temperature of all the observations were fixed at T/T_{BI} = 0.99. For high SSY concentrations, tactoids in Figure 5.2a exhibit a symmetric pattern corresponding to the conventional bipolar configuration. As illustrated in Figure 5.2c, the bipolar tactoid has a singular point defect on each side of the surface (boojums). The director aligns parallel with the surface and connects the two boojums. As the typical structure of tactoids, the bipolar configuration has been observed with a lot of lyotropic liquid crystals such as tobacco mosaic virus[150] and vanadium pentoxide[86,168]. The bipolar director field is dominated by the splay deformation close to the two boojums[27]. The shape of the bipolar tactoids is controlled by the surface energy and the elastic energy of nematic phase[99,163]. For SSY, the bipolar tactoids exhibit a hemi-spherical shape since the effect of surface tension is dominant and the contact angle is around 90^o (will be discussed in section 5.3.3, Figure 5.9d). But generally, the shape of the bipolar tactoids is elongated when the surface energy and elastic energy are comparable.

At low concentrations and temperatures, tactoids exhibit notably different birefringent textures as shown in Figure 5.2b. One of the patterns still has a bipolar axis with two boojums on the sides. But the center of the tactoids shows transmitted intensity with multiple fringes, which is distinct from the dark central region of the bipolar tactoids when the polarizer is parallel with or perpendicular to the bipolar axes. The transmitted

intensity in the center of the birefringent pattern is an indication of the twist deformation and chiral structure. As illustrated in Figure 5.2d, the director field evolves the twist distortion to relieve the splay deformation close to the boojums due to the small twist elastic constant of LCLCs. This chiral configuration of tactoids, namely the twisted-bipolar (TB) tactoids, were observed previously with SSY crowded by polyethylene glycol (PEG)[36]. But we used a different experiment to realize the TB tactoids with additive-free SSY at low concentrations and temperatures.

Another type of tactoids in Figure 5.2b exhibits a pattern with radial symmetry under crossed polarizers. We deciphered the director field of these tactoids from the linear dichroism images as shown in Figure 5.3c and 5.3d. When the light is polarized in the vertical direction (Figure 5.3c), the left and right sides of the tactoid are brighter than the top and bottom sides. It indicates that the director on the left and right of the tactoid is along the vertical direction with the molecular planes perpendicular with the polarizer. The top and bottom sides of the tactoid are brighter than the left and right sides when the light is polarized in horizontal direction (Figure 5.3d), indicating that the director on top and bottom are along horizontal direction. Hence, we infer from the dichroism images that the director field close to the boundary of the tactoid is aligned concentrically. From the boundary to the center, the director twists and escapes along the normal axis of the concentric planes to avoid a singular line defect in the center of the tactoid. The twist deformation is clearly shown by the swirling patterns in the dichroism images. This director field is consistent with the escaped-concentric (EC) configuration as illustrated in Figure 5.2e, which has long been proposed theoretically in literature[12] but never been observed before. Due to the small twist elastic constant of LCLCs, the director field of the EC

configuration conforms to the bend and the twist deformations to minimize the splay deformation in the bipolar and TB tactoids. Notably, there was an argument in the literature that the EC configuration is identical to the TB director field with a twist angle of 90° [169]. However, we suggest that the EC configuration is a different novel chiral structure for tactoids. The differences between the two configurations are the presence of the boojums and the director field around them. As shown in Figure 5.3b, the bright field image of the EC tactoid does not exhibit any singular boojums. We speculate that to minimize the splay deformation, the director field of the EC configuration avoids the formation of boojums by violating the planar anchoring on the surface in the small central region of the tactoids (Figure 5.2e).

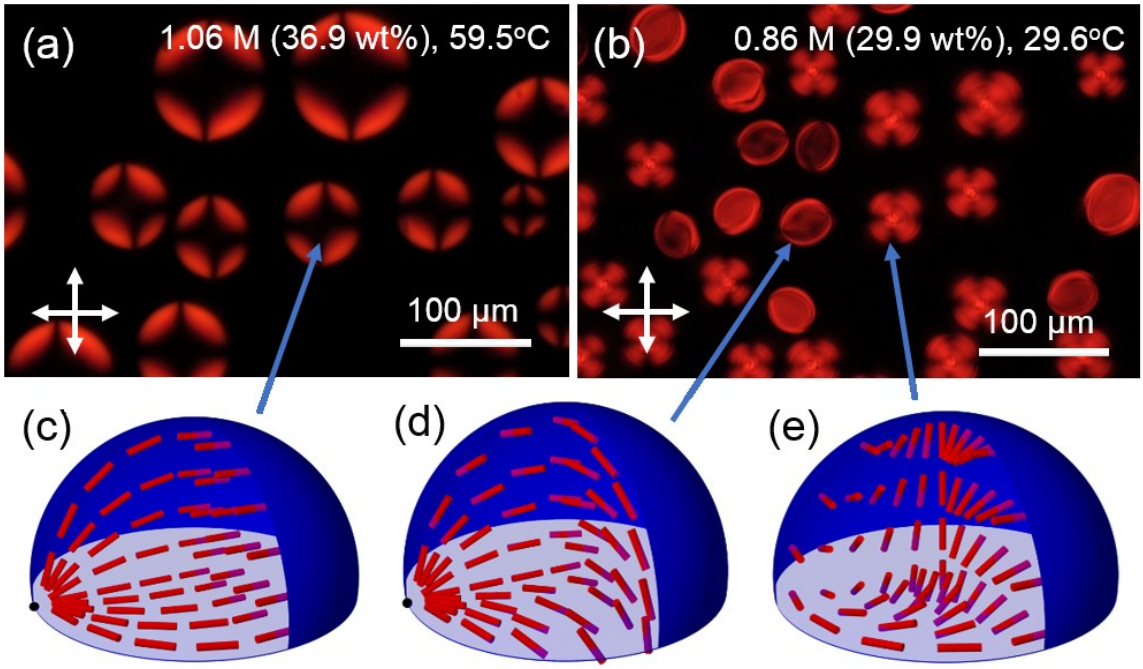

Figure 5.2 Polarized optical microscopy images of SSY tactoids with the concentrations and the temperatures of (a) 1.06 M (36.9 wt%), 59.5 °C and (b) 0.86 M (29.9 wt%), 29.6 °C. Director fields illustrations of (c) the bipolar configuration, (d) the twisted-bipolar (TB) configuration, and (e) the escaped-concentric (EC) configuration. The tactoids are attached on the flat surface of the rectangular capillaries and exhibit a hemi-spherical shape. Red rods represent the director of nematic phase. Black dots represent the singular point defects on the surface.

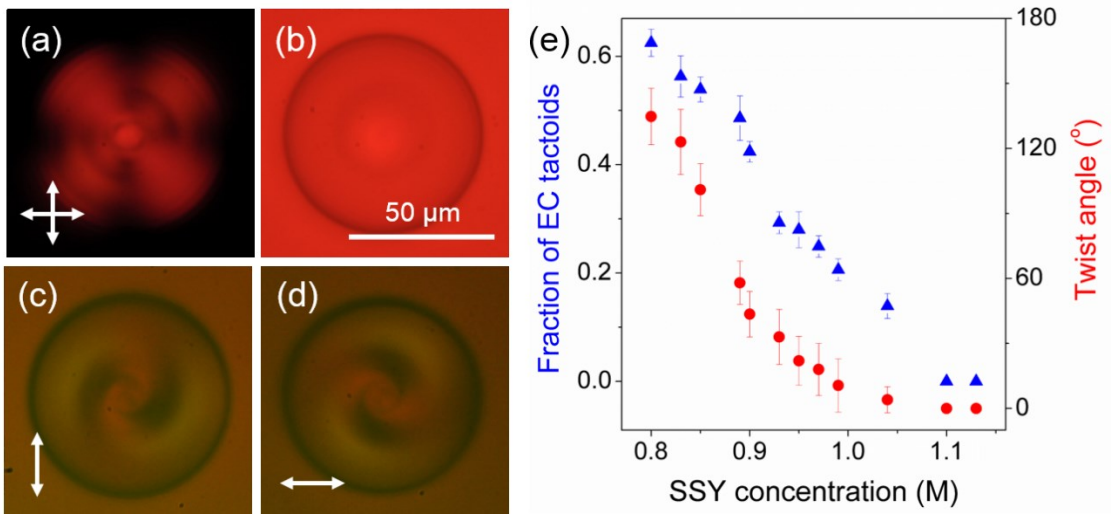

Figure 5.3 Polarized optical microscopy images of an EC tactoid (a) under crossed polarizers, (b) under bright field, (c) under polarizer only in vertical direction, (d) under polarizer only in horizontal direction. (c) and (d) are captured with monochromatic illumination of 551 nm. (e) The fraction of tactoids with the EC configuration (blue triangles) and the twist angle of the TB configuration (red circles) as a function of SSY concentration.

For different SSY concentrations, we counted the fraction of the EC tactoids and measured the twist angle of the TB tactoids by wave-guiding method (see Appendix A.4.1, Figure A.8). As shown in Figure 5.3e, the fraction of the EC tactoids and the twist angle of the TB tactoids decrease with the rise of SSY concentration. In the next section, we rationalize the configurational transformation of tactoids at different temperatures and concentrations by the aggregation behavior and its contrasting effects on the elastic constants of LCLCs.

5.2.2 Using tactoids to probe the aggregation behavior of LCLCs

Using the self-assembling model[121] described in section 3.3.2, we calculated the length distributions of SSY aggregates at the observation temperatures for various concentrations. As shown in Figure 5.4, for low concentrations at low temperatures, the

peak position corresponds to a large number of molecules in an aggregate and the volume fraction of long aggregates ($N > 40$) is large. The aggregates have long average length in the tactoids with low concentrations. The shifts in the average aggregate length have contrasting effects on the elastic constants of LCLCs. As mentioned in section 2.4.1, the splay elastic constant, K_{11}, is proportional to the average aggregate length, $\bar{L}$, which is expressed as[117] $K_{11} = \frac{4}{\pi}\frac{k_B T}{D}\emptyset\frac{\bar{L}}{D}$. The average aggregate length of LCLCs is strongly affected by temperature and concentration[121]. Nevertheless, the twist and bend elastic constants are the functions of persistence length[85,115], λ_p ($K_{22} = \frac{k_B T}{D}\emptyset^{1/3}\left(\frac{\lambda_p}{D}\right)^{1/3}$, $K_{33} = \frac{4}{\pi}\frac{k_B T}{D}\emptyset\frac{\lambda_p}{D}$), which is a molecular property with only a weak dependence on the temperature[122]. As a consequence, for high concentrations and high temperatures, the aggregates have a short average length and the splay elastic constant is small. The bipolar configuration of tactoids is stable since the elastic free energy of this configuration is dominated by the cheap splay deformation close to the boojums. As concentration is lowered, the aggregates grow longer and the splay deformation becomes expensive. Due to the small twist elastic constant of SSY, the director field of the TB tactoids adopts the twist deformation to partially reduce the splay energy close to the boojums. Other tactoids exhibit the EC configuration using the twist and the bend deformations to minimize the splay distortion.

We note that the emergence of the TB configuration in replace of the achiral bipolar configuration for SSY is consistent with the stability criterion proposed by R. D. Williams[170], which is $K_{11} \geq K_{22} + 0.431K_{33}$. Based on Zhou et al.'s measurements[94], at the temperatures of nematic phase, $K_{22} + 0.431K_{33}$ for SSY solutions is typically 2.4 ~ 4.7 pN

and K_{11} is around 5.5 ~ 8.5 pN. Additionally, the EC configuration is usually considered as the stable state for nematic droplets when the bend elastic constant is smaller than the splay elastic constant ($K_{11}/K_{33} > 1$)[12]. There is one report of the EC configurations for 5CB droplets with $K_{11}/K_{33} < 1$ only under the effect of shear force[171]. But this criterion is not fulfilled for SSY according to Zhou et al.'s measurements[94] (in nematic temperature range, K_{11}/K_{33} for SSY is typically 0.6 ~ 1). Nevertheless, we note that the elastic constants of SSY were measured in the nematic temperature range ($T < T_{NB}$)[94]. But the temperatures of tactoids are close to the transition temperature between biphase and isotropic phase (T/T_{BI} = 0.99), which are higher than T_{NB}. Upon heating the solutions, the value of K_{11} may further decrease due to the shorter length of the aggregates[117], whereas the values of K_{33} do not change significantly as a function of temperature[84,115]. Hence, the value of K_{33} for nematic tactoids in the biphase temperature region may be larger than the value of K_{11}, which can possibly rationalize the formation of the EC configuration.

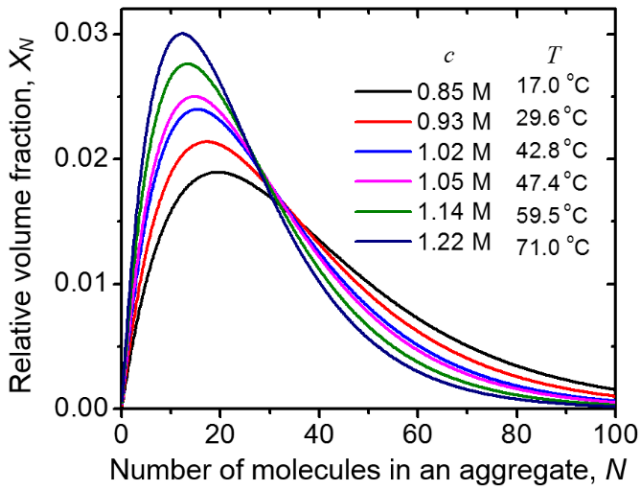

Figure 5.4 The distributions of the number of molecules in an aggregate for different concentrations and temperatures calculated by the self-assembling model discussed in Chapter 3.3.2 [121]. The temperatures used in the calculation are the observation temperatures of tactoids, T/T_{BI} = 0.99. The concentrations used in the calculation are the concentrations of tactoids extrapolated from the phase diagram.

5.3 The effect of neutral polymer on configurations of tactoids

As shown in Chapter 5.2, the configurations of LCLC tactoids probe the shifts in the average aggregate length at different concentrations and temperatures. Hence, the configurational transformation of tactoids can be utilized to study the aggregation behavior of LCLCs, which can also be easily affected by different types of impurities such as neutral polymers[123,124] and ionic salts[139,172]. In this section, we report the results of the configurations of LCLC tactoids crowded by a neutral polymer, poly-ethylene glycol (PEG). LCLC solutions with the addition of ionic monovalent salts are discussed later in Chapter 6, which exhibit intriguing changes in the configurations of tactoids and the phase transition temperatures.

5.3.1 Excluded volume effect

PEG is known as a condensing agent for lyotropic systems[123-125]. The condensing effect is understood by the excluded volume mechanism[173-175]. As illustrated in Figure 5.5, PEG molecules (M_w = 1500) exist as large coils in solutions at low concentrations (The gyration diameter of PEG coils is around 2.5 nm[258], larger than the gap between LCLC aggregates of around 1.5 nm[189]). In the biphase region, the coils are expelled from LCLC aggregates and accumulate in isotropic phase to achieve the maximum available volume[123]. The concentration difference of PEG molecules between LCLC-rich nematic domains and PEG-rich isotropic domains applies osmotic pressure on the LCLC aggregates[124]. The equilibrium is reached when the osmotic pressure due to the excluded volume effect is in balance with the repulsion between LCLC aggregates. Since the constituent units of LCLCs are self-assembled aggregates rather than individual molecules, the excluded volume effect

would increase the aggregate length and enhance the side-by-side packing of the aggregates[123]. As a result, we expect that the condensing effect of PEG has a significant impact on the configurations of tactoids by changing the aggregation behavior of LCLCs. With the addition of PEG, the elongation of the LCLC aggregates results in a large splay elastic constant (as discussed in Chapter 5.2.2 and Chapter 2.4.1)[117], which induces the formation of the chiral TB and EC tactoids to minimize the splay deformation in the director field.

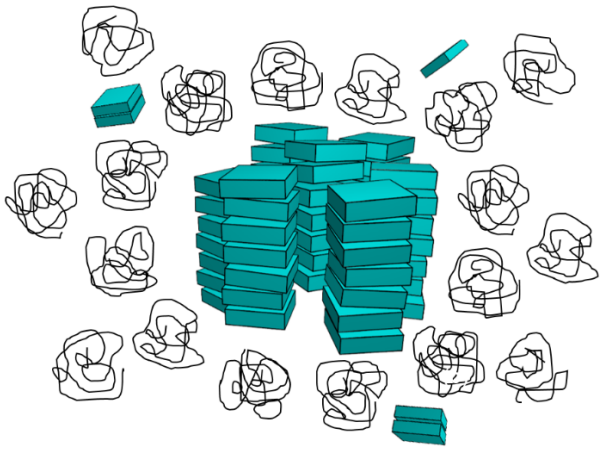

Figure 5.5 Excluded volume effect of PEG on SSY aggregates.

5.3.2 Polarized optical microscopy observations

In Figure 5.6a, the tactoids of PEG-free SSY with a high concentration (1.05 M, 36.5 wt%) exhibit the conventional bipolar configuration. The TB and EC chiral tactoids emerge with the addition of PEG as shown in Figure 5.6b and 5.6c, which is consistent with our expectation. Since the splay elastic constant is linear with the average length of the aggregates (as discussed in Chapter 2.4.1)[117], the elongation of the LCLC aggregates under the effect of PEG results in a larger K_{11}. As a consequence, the director fields of tactoids minimize the expensive splay deformation by forming the TB and EC chiral

configurations with twist and bend deformations. The fraction of the EC tactoids and the twist angle of the TB tactoids are plotted in Figure 5.6d and 5.6e. For all SSY concentrations, the fraction and the twist angle increase with the increase of PEG concentration. The increase in the fraction and the twist angle with the addition of PEG is more dramatic for higher SSY concentrations. The depletion attraction of the excluded volume effect occurs when the gyration radius of PEG coils is much larger than the distance between SSY aggregates. In tactoids, higher SSY concentrations have shorter aggregates but a larger number of them. The aggregates pack tightly with a smaller separation distance. Hence, tactoids for high SSY concentrations experience stronger depletion attraction and show larger increase in the fraction and the twist angle with the addition of PEG.

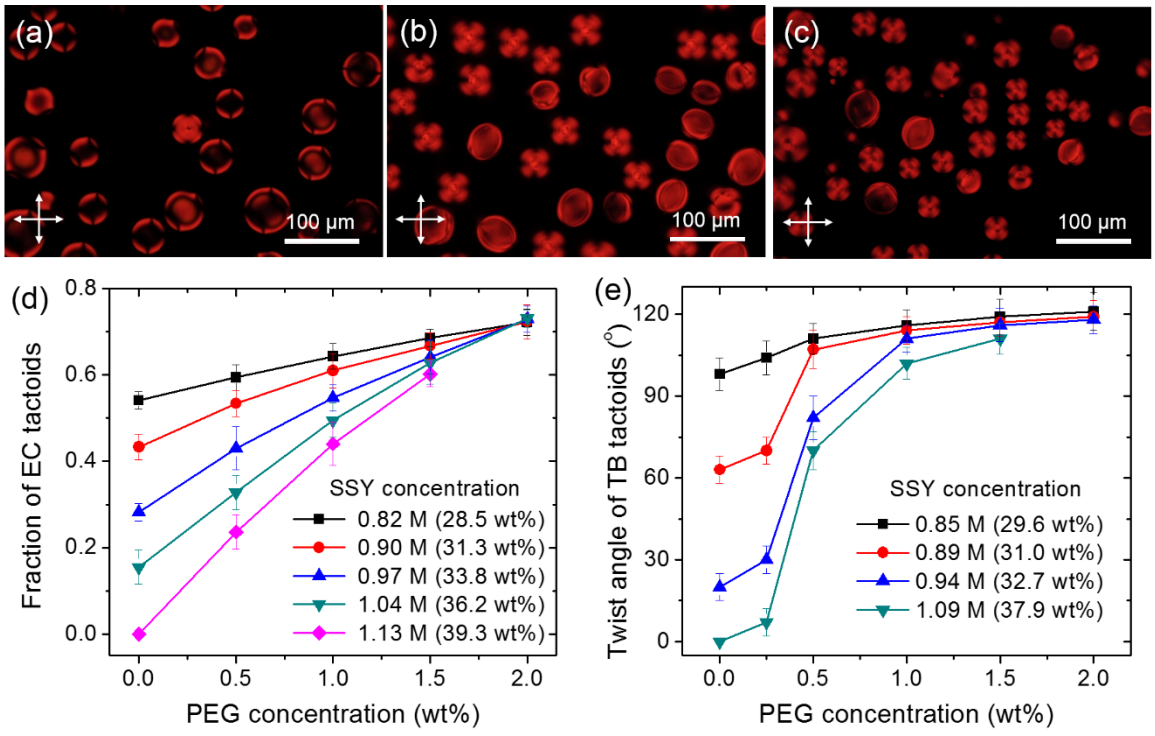

Figure 5.6 Polarized optical microscopy images of tactoids with SSY concentration of 1.09 M (37.9 wt%) and PEG concentration of (a) 0 wt%, (b) 1.0 wt%, and (c) 2.0 wt%. (d) The fraction of the EC tactoids with various SSY and PEG concentrations. (e) The twist angle of the TB tactoids with various SSY and PEG concentrations.

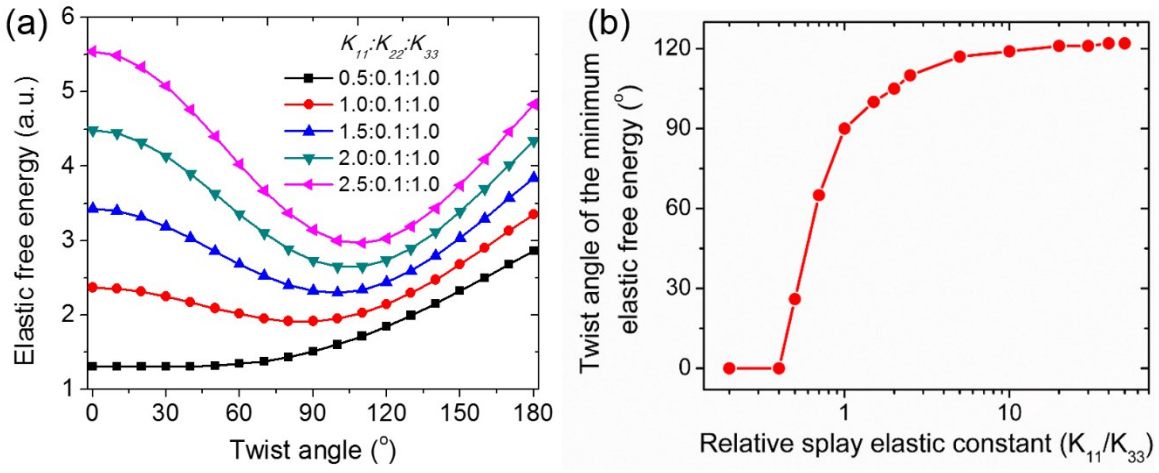

Figure 5.7 (a) The elastic free energy of a TB tactoid as a function of twist angle. (b) The twist angle of the minimum elastic free energy as a function of K_{11}/K_{33}.

It is noted that in Figure 5.6e, the twist angle of the TB tactoids reaches the plateau of 125° with high PEG concentrations ($C_{PEG} \geq 1.5$ wt%). Adding more PEG does not further increase the twist angle but drives the tactoids to columnar phase (see Appendix A.4.2, Figure A.9). The upper bound is set by the maximum twist angle that can relieve the splay elastic free energy close to the boojums of the tactoids. To understand the plateau of the twist angle, we performed the numerical calculation of the elastic free energy of the TB droplet following prior studies[11,27,28,176,177]. The director field of the TB droplet is shown in Appendix A.4.1, equation A.1. In the calculation, the ratio of the twist/bend elastic constants (K_{22}/K_{33}) is fixed at 0.1 because K_{22} for LCLCs is an order of magnitude smaller than K_{33} and K_{11}. The relative splay elastic constant (K_{11}/K_{33}) varies from 0.2 to 50. As shown in Figure 5.7a, the twist angle corresponding to the minimum elastic free energy increases with the increase of K_{11}/K_{33}. In Figure 5.7b, we note that the twist angle cannot be larger than 125° even with an unreasonably large K_{11}/K_{33}. Beyond this limit, the elastic free energy of the TB configuration cannot be reduced by the formation of the twist deformation in the director field. Rather than increasing the twist angle, the tactoids

transform to the EC configuration to minimize the splay deformation and avoid the formation of singular boojums.

5.3.3 Configurational transformation of tactoids in the aging process

The images and the measurements in Figure 5.6 were obtained within 5 min after the formation of the tactoids at the reduced temperature T/T_{BI} = 0.99. Nevertheless, the configurations of tactoids surrounded by PEG continue to transform for hours during the aging process at a fixed temperature (T/T_{BI} = 0.99). As shown in Figure 5.8a, all the tactoids grow larger as time goes and the TB tactoids gradually transform to the EC configuration. All the tactoids exhibit the EC configuration after 5 hrs. Eventually after 17 hours, the tactoids coalesce into a single nematic domain and stops growing at least for the next 24 hours. Based on the excluded volume mechanism, the high concentration of PEG molecules in the isotropic phase applies osmotic pressure on SSY aggregates in the tactoids. The equilibrium is reached when the osmotic pressure is in balance with the electrostatic repulsion between SSY aggregates. Before reaching the balance, SSY molecules diffuse from the isotropic phase to the nematic domains under the effect of osmotic pressure, causing the growth in the size of tactoids. In the meantime, SSY aggregates are elongated by the depletion attraction effect. As the length of the aggregates grows, the increase of the splay elastic constant results in the configurational transformation of tactoids from the TB to the EC structure. The time required to reach the equilibrium is controlled by the diffusivity of SSY molecules from the isotropic to the nematic phase ($\mathcal{D}$). The diffusion of SSY molecules is described by the second Fick's law[178,179]: $\frac{\partial C_{SSY}}{\partial t} = \mathcal{D}\frac{\partial^2 C_{SSY}}{\partial x^2}$, where C_{SSY} is the SSY concentration, t is the time, x is the

characteristic length, which is the radius of the tactoids (R_0). Using scaling argument, the equilibrium time scale is a function of tactoidal radius and diffusivity: $t \sim \frac{R_0^2}{\mathcal{D}}$. With $R_0 =$ 80 μm and $t = 17$ hrs, we estimated that the diffusivity of SSY molecules in biphase solution is in the order of 10^{-13} m^2/s. Prior study by Renshaw and Day measured the diffusivity of diluted SSY solution in the isotropic phase by NMR experiments[180], $\mathcal{D}_{iso} = 10^{-11}$ m^2/s. The value of our estimation is expected to be smaller than theirs because the diffusion is suppressed by the orientational order of the nematic phase and the interface of the tactoids.

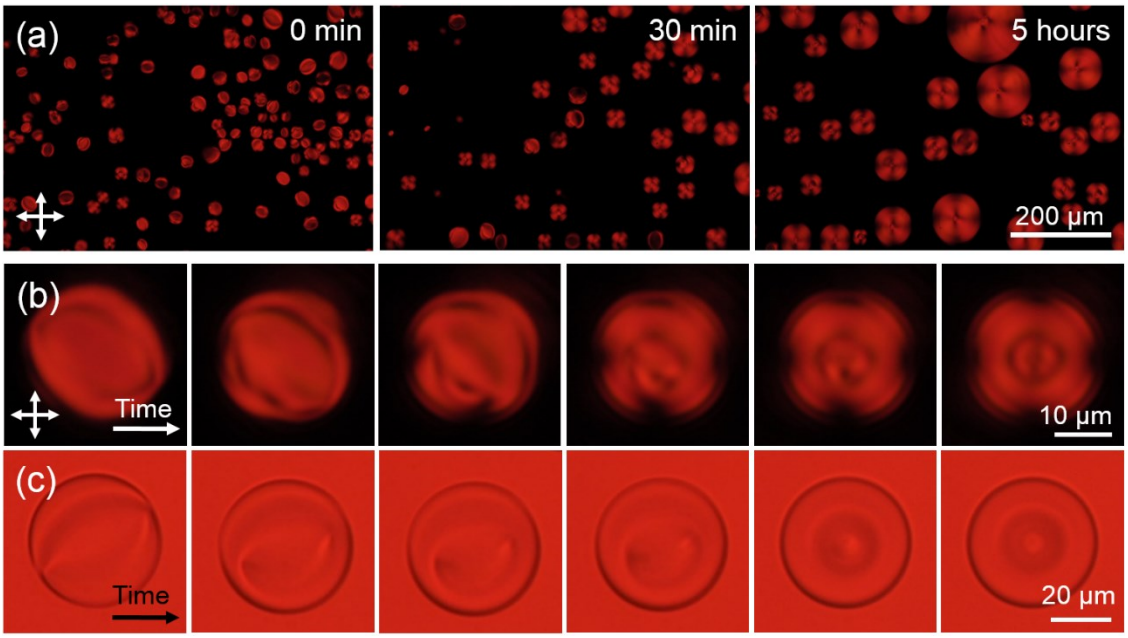

Figure 5.8 (a) Polarized optical microscopy images of tactoids with SSY concentration of 1.05 M (36.5 wt%) and PEG concentration of 0.5 wt%. From the left to the right, the images were captured at 0 min, 30 min, and 5 hours after the formation of tactoids, respectively. The temperature is fixed at T/T_{NB} = 0.99 (54 ºC). (b, c) Time evolution of tactoids during aging process under crossed polarizers and bright field. The pattern transfers from the TB texture to the EC texture. The solution is 0.98 M SSY + 0.5 wt% PEG aged at 39 ºC.

During the transition from the TB to the EC configurations, the snapshots of a tactoid under crossed polarizers and bright field are presented in Figure 5.8b and 5.8c,

respectively. From the top view, the two boojums of a TB tactoid move closer as time goes. They eventually vanish when the director field conforms to the EC configuration. The bipolar axis can rotate around the normal axis of the focal plane. The rotation speed varies considerably from 10 s/round to 30 min/round and can be either in clockwise or anticlockwise directions. The time required for each tactoid to complete the transformation also has large variation from 1 min to 2.5 hrs. Typically larger tactoids take longer time to transform.

However, we note that it is unusual for the boojums to move closer. Since the two boojums of a TB tactoid repel each other, they naturally locate at the two poles to keep the largest distance. To understand the defect motion, we observed the tactoids with the intermediate structure during the transition on different focal planes. In the left images of Figure 5.9a and 5.9b, the focal plane is moved upward from the boundary of the tactoid. One of the boojums is sharply focused as pointed by the blue arrow. But when the focal plane is lower than the boundary of the tactoids, the other boojum is in focus as shown in the right images of Figure 5.9a and 5.9b. It indicates that during the transformation, the two boojums are on different heights and the bipolar axis is tilted from the horizontal plane. The tilt of the bipolar axis still enables the two boojums to keep the largest distance. In Figure 5.9c, we observed the side-view of the tactoids nucleating on the side wall of a square capillary. Two SSY tactoids crowded with PEG exhibit a large contact angle of 150^{o}. The boojums can move on the spherical tactoidal surface while keeping the largest distance of the diameter. Viewing from the top view, the projections of the two boojums on the horizontal plane look closer when the bipolar axis tilts from the horizontal plane. However, when one of the boojums moves onto the flat surface of the capillary wall, the

distance between the two boojums is reduced due to the attachment on the surface and the TB structure is no longer stable. In this situation, transformation occurs from the TB to the EC configuration. For PEG-free SSY solutions, the tactoids have a hemi-spherical shape with a contact angle of 92° (Figure 5.9d). The freedom of the boojum axis is limited by the small contact angle and hence the defect motion was not observed.

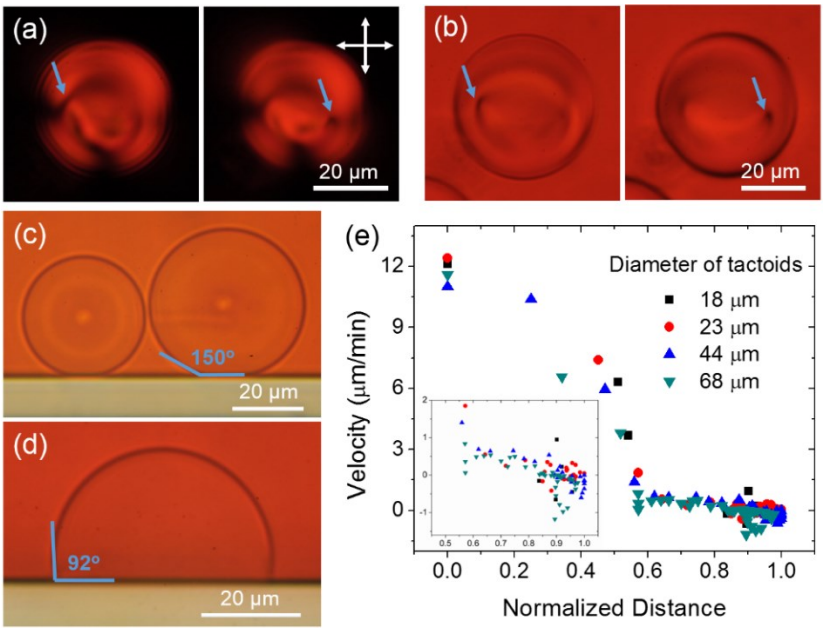

Figure 5.9 (a, b) Polarized optical microscopy images of a tactoid with the intermediate structure from the TB to the EC configurations during the configurational transition. The image of (a) is under crossed polarizers and the image of (b) is under bright field. The focal planes of the left and right images are different by 10 μm. The boojums on the left side and the right side are on focus respectively as pointed by the blue arrow. (c, d) The tactoids nucleating on the side wall of a square capillary under bright field. The solution of (c) is SSY + PEG. The contact angle is measured as 150°. The solution of (d) is PEG-free SSY with a contact angle of 92°. (e) The velocity of defect motion as a function of the normalized distance between the two defects. The inset is the enlarged image when the normalized distance is larger than 0.57. The velocity was measured from the top view. The distance between the defects was normalized by the diameters of the tactoids.

Furthermore, we measured the distance between the boojums from the top view as a function of time and calculated the speed of defect motion. Figure 5.9e presents defect velocity as a function of the normalized distance (the distance between the boojums in the

top view normalized by the diameter of the tactoids). Positive sign means that the defects are moving towards each other from the top-view, and negative sign means getting away from each other. Despite the difference in the size of tactoids, defects move slowly with the speed less than 1 μm/min when the normalized distance is larger than 0.57. In this region, the defects can either move towards or away from each other since the velocity can have either positive or negative sign. It supports our explanation that the boojum axis can rotate in any directions on the spherical surface of the tactoids. When the normalized distance is less than 0.57, the speed increases rapidly and the transformation is completed within 2 min. The critical normalized distance for configurational transformation does not depend on the size of the tactoids. It is the position where one of the boojums moves onto the flat surface of the capillary wall. This normalized distance of 0.57 corresponds to 55^{o} tilt angle of bipolar axis and 145^{o} contact angle of tactoids, which is very close to the measured contact angle of 150^{o}.

5.4 Conclusions

Tactoids has been interesting objects for scientists as a natural subject of confinement with curved surface for nematics during the phase transition[99,165-167,181]. In this chapter, we summarize our observations of SSY tactoids at different concentrations and temperatures. Besides the conventional achiral bipolar configuration with high concentrations, SSY tactoids exhibited two chiral structures, the TB and the EC configurations, as the concentration was lowered. The TB tactoids were reported previously for SSY crowded by PEG molecules[36]. But our experiments realize the TB tactoids with additive-free SSY solutions for low concentrations and temperatures. Remarkably, the EC configuration of tactoids was observed for the first time in our experiments, which has been predicted

theoretically in prior literature[12] but has not been reported in any experiments. We showed that the EC structure differs from the TB configuration with a twist angle of 90° since the EC director field is free of any singular defects.

Using a self-assembling model[121], we found that the configurations of tactoids can be used to probe the aggregation behavior of SSY. For high concentrations, SSY aggregates are short and the splay elastic constant is small. In this situation, the bipolar configuration dominated by the splay deformation is the stable structure for tactoids. As the concentration is lowered, the aggregates are elongated and the splay deformation becomes expensive. The director field develops the twist and the bend deformations to relieve the splay energy, conforming to the chiral TB and EC configurations. With this understanding, we expect that a neutral polymer additive, PEG, would have an impact on the configurations of tactoids since PEG molecules elongate the LCLC aggregates by the excluded volume effect. Upon adding PEG, we observed the transformation of tactoids from the achiral bipolar structure to the chiral TB and EC structures as discussed in section 5.3. During the aging process, the configurational transition from the TB to the EC structures were also observed and investigated for SSY + PEG solutions.

By exploring SSY tactoids, we find the relationship of the macroscopic director configurations, elastic properties, and molecular aggregation, which provides significant physical insights to understand the behavior of LCLCs. However, more theoretical work is still needed to describe the director field of the novel EC configuration. Besides the fundamental importance, we also suggest that the sensitivity of tactoidal configurations to aggregation behavior could be used in optical sensing application to detect neutral polymers and other chemical impurities in the aqueous LCLCs solutions.

CHAPTER 6. THE EFFECTS OF MONOVALENT SALTS ON THE CHIRAL CONFIGURATIONS OF LCLC TACTOIDS

6.1 Introduction

The nematic phase of LCLCs is composed of self-assembled rod-like aggregates as the building units[84]. The molecular stacking of LCLCs is reversible since the molecules in the individual aggregate are bonded by weak non-covalent interactions[97]. The exploration of the aggregation behavior is essential in understanding the elastic properties and configurational behavior of LCLCs, which brings plenty of fundamental questions to scientists: how do the interactions between LCLC molecules and solvents stabilize the aggregates system? What effects can be imposed on LCLC aggregates when the external impurities are added into the solution? For charged LCLC aggregates, the addition of ionic salts would be strongly involved in the self-assembling mechanism of LCLCs by influencing the electrostatic forces. Prior literature found that the monovalent salts promote the formation of nematic phase for low LCLC concentrations but destroy the nematic phase for high LCLC concentrations[123,139,172,182-184]. Many plausible explanations were proposed including the screening of Coulomb repulsions[139], salts effects on hydrogen bonds[184], the contrasting changes of contour length and persistence length of the aggregates[123], and the formation of complex aggregate structures[172]. However, none of them can well describe the concentration dependence of salts effects on LCLC phase diagram. A systematic exploration of different salts concentrations and LCLC concentrations is still absent.

For the work discussed in this chapter, we utilized SSY tactoids to explore the effects of sodium chloride (NaCl) on the aggregation behavior in the biphase region. Using the self-assembling model[121] in Chapter 3.3.2, the calculated average aggregate length is shifted by NaCl via the change of phase transition temperatures. Furthermore, we investigated the change of phase transition temperatures by monovalent salts with different cations and anions. A plausible mechanism of salts effects on LCLC aggregates was proposed based on the electrostatic interactions between LCLC molecules and salt ions.

6.2 The effect of sodium chloride on the configurations of tactoids

6.2.1 Polarized optical microscopy observations

The SSY tactoids with different concentrations of NaCl were observed under crossed polarizers in Figure 6.1. For low SSY concentration (0.86 M), NaCl-free tactoids in Figure 6.1a1 exhibit the chiral EC and TB configurations. The fraction of the EC tactoids is reduced by NaCl for the NaCl concentration of 1.16 M as shown in Figure 6.1a2. However, in Figure 6.1a3, a higher NaCl concentration of 1.74 M increases the fraction of the EC tactoids. NaCl concentration higher than 1.74 M destroys nematic phase and leads to coagulation of the aggregates. For high SSY concentration (1.14 M), NaCl-free tactoids in the Figure 6.1b1 exhibit the bipolar configuration with no twist. The addition of NaCl drives the tactoids to the chiral EC and TB configurations as shown in Figure 6.1b2 (C_{NaCl} = 1.16 M). The fraction of the EC tactoids is plotted in Figure 6.1c with various SSY and NaCl concentrations. When SSY concentration is low (C_{SSY} < 1.00 M), the fraction of the EC tactoids is reduced by low NaCl concentrations (C_{NaCl} < 1.16 M) but raised by high

NaCl concentration (C_{NaCl} > 1.16 M). With high SSY concentration (C_{SSY} > 1.00 M), adding more NaCl always results in an increase in the fraction of the EC tactoids.

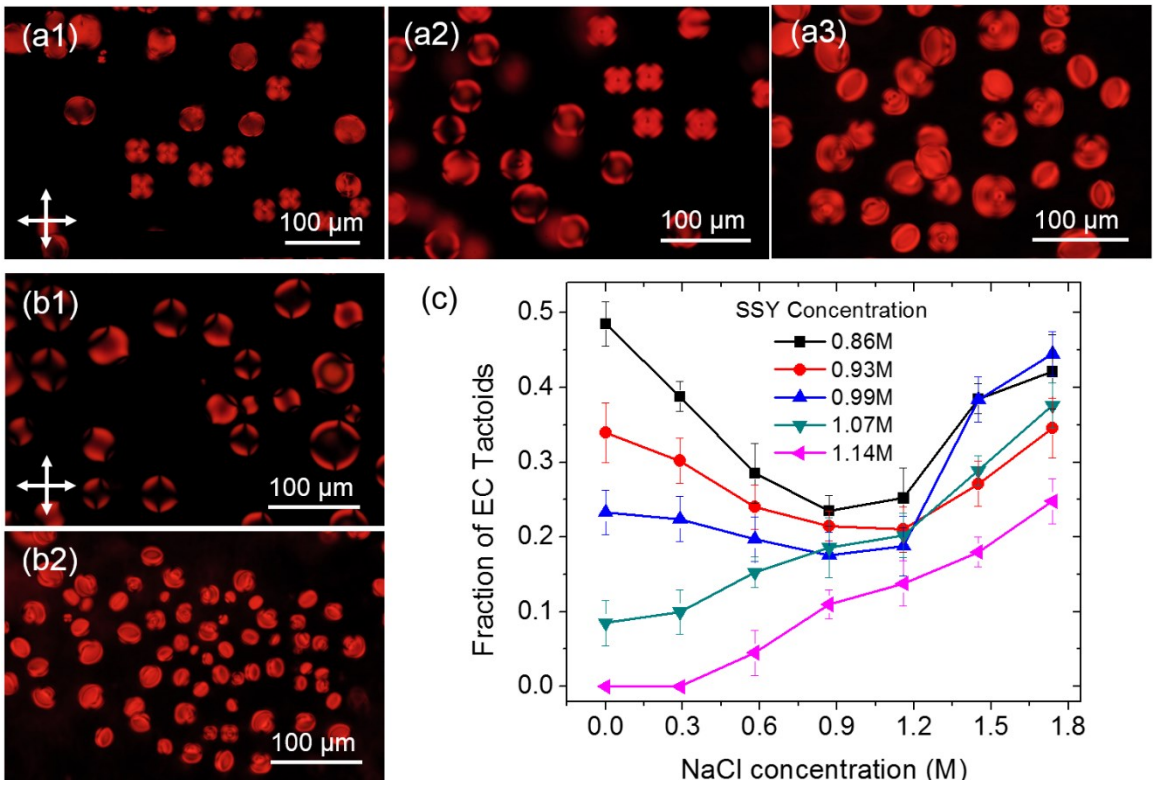

Figure 6.1 Polarized optical microscopy images of SSY tactoids with the addition of NaCl. SSY concentration for (a) is C_{SSY} = 0.86 M. NaCl concentrations are C_{NaCl} = 0, 1.16, and 1.74 M for (a1), (a2), and (a3), respectively. SSY concentration for (b) is C_{SSY} = 1.14 M. NaCl concentrations are C_{NaCl} = 0 and 1.16 M for (b1) and (b2), respectively. (c) The fraction the EC tactoids with different concentrations of SSY and NaCl.

6.2.2 Aggregation behavior of LCLCs with the addition of sodium chloride

As shown in Chapter 5, the configurations of tactoids are intrinsically controlled by the average length of SSY aggregates. After showing the dependence of tactoidal configurations on SSY concentration and NaCl concentration, we noticed that the addition of NaCl shifts the phase transition temperatures of SSY solutions, which significantly changes the average aggregate length in the tactoids. We then measured the phase diagram

of SSY + NaCl solutions to understand the NaCl effect on the configurations of tactoids. The change of transition temperature between biphase and isotropic phase, T_{BI}, is plotted in Figure 6.2a. With low SSY concentrations (C_{SSY} < 1.03 M), T_{BI} is raised by the increase of NaCl concentration when NaCl concentration is less than 1.00 M. But increasing NaCl concentration to 1.45 and 1.74 M reduces T_{BI}. With high SSY concentrations (C_{SSY} > 1.03 M), the addition of NaCl always suppresses the nematic phase by reducing T_{BI}.

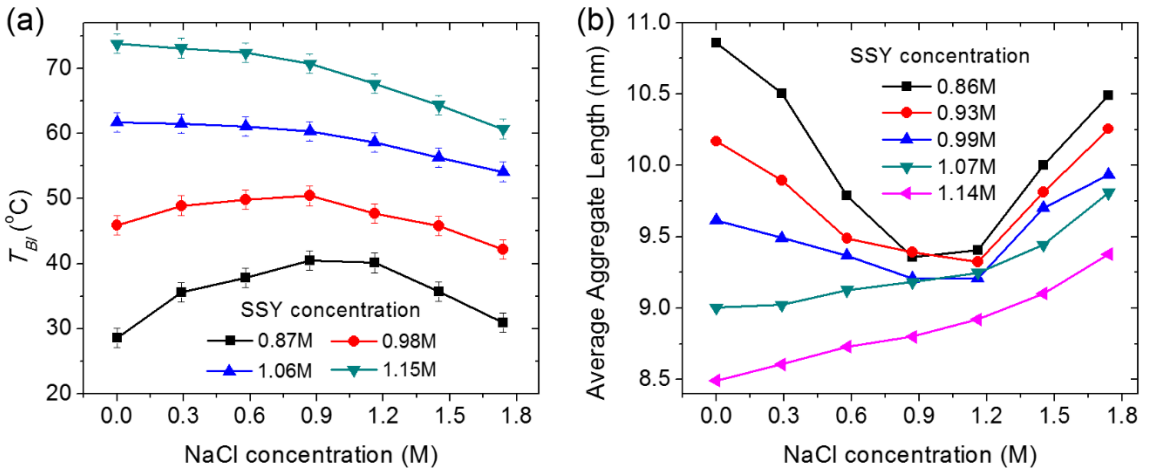

Figure 6.2 (a) Phase transition temperature, T_{BI}, of SSY with the addition of NaCl for different concentrations of SSY and NaCl. The error bar shows the difference of T_{BI} measured by heating the solution from biphase region to isotropic phase and cooling the solution from isotropic phase to biphase region. (b) The average aggregate length of SSY with the addition of NaCl calculated by a self-assembling model.

In our experiments, we fixed the reduced observation temperature (T_{OB}) at T_{OB}/T_{BI} = 0.99 to observe tactoids. When the transition temperature is shifted by NaCl, the aggregate length distribution of SSY tactoids is altered as the consequence. Using the self-assembling model[121] in section 3.3.2, we calculated the average aggregate length at T_{OB} for different NaCl and SSY concentrations as shown in Figure 6.2b. The calculated average aggregate length (Figure 6.2b) shows similar dependence on the concentrations of SSY and NaCl as the fraction of the EC tactoids (Figure 6.1c). For low SSY concentrations (C_{SSY} < 1.03 M),

the rise of T_{BI} by low concentrations of NaCl (C_{NaCl} < 1.00 M) leads to an increase in T_{OB}, corresponding to shorter average length of the aggregates. The splay deformation is cheap in the bipolar and the TB structures. As a result, the fraction of the EC tactoids is reduced. However, with higher NaCl concentrations (C_{NaCl} > 1.00 M), T_{BI} becomes smaller and the aggregates are longer. Consequently, more tactoids exhibit the EC configuration with high NaCl concentrations to minimize the expensive splay deformation in the director field. For high SSY concentrations (C_{SSY} > 1.03 M), adding NaCl always reduces T_{OB} and elongates aggregates. Therefore, the splay deformation becomes expensive and more tactoids exhibit the EC configuration.

6.3 Shifts in the transition temperatures of LCLCs with the addition of different monovalent salts

6.3.1 Transition temperatures measurements

We have addressed that NaCl affects the configurations of SSY tactoids by changing the phase transition temperatures. The contrasting tendencies of salts effects on the phase diagram for high and low SSY concentrations have driven considerable interests in prior studies[123,139,172,182-184]. But the mechanism of the interactions between salt ions and LCLC aggregates is still unclear. It was widely suggested that monovalent salts increase the scission energy (the energy required to break one aggregate) and promote longer aggregates thanks to the screening of electrostatic repulsion between SSY molecules[123,139,185,186]. The elongation of the aggregates explains the increase of transition temperatures with low SSY and NaCl concentrations. However, the explanations are disputable for the destabilization of the nematic phase with high SSY or high NaCl

concentrations. Moreover, cation size of monovalent salts was found decisive to the stability of LCLC nematics[172]. Small cations such as Na^+ and Li^+ promote the nematic order but large cations such as Et_4N^+ and Bu_4N^+ suppress the nematic order.

Inspired by these suggestions, we explored the transition temperatures of SSY + NaCl with different SSY and NaCl concentrations. The transition temperature between biphase and isotropic phase, T_{BI}, has been shown in Figure 6.2a. In Figure 6.3a, we plot the transition temperature between nematic phase and biphase region, T_{NB}, with different concentrations of SSY and NaCl. The shift in T_{NB} with the addition of NaCl exhibits the same tendency as that in T_{BI}, which depends on both concentrations of NaCl and SSY. However, the temperature range of the biphase region ($T_{biphase} = T_{BI} - T_{NB}$) is expanded by NaCl as shown in Figure 6.3b. This expansion is particularly significant when NaCl concentration is higher than 1.25 M. Moreover, the effect of the salt with smaller cation, LiCl, on the transition temperature of SSY, T_{NB}, is shown in Figure 6.3c. T_{NB} has a maximum value as a function of LiCl concentration for all the concentrations of SSY. But when we use the salt with larger cation such as KCl, T_{NB} is reduced by the addition of KCl for all the concentrations of SSY and KCl as shown in Figure 6.3d. The other transition temperature, T_{BI}, shows similar tendencies with the addition of LiCl and KCl, which are shown in Appendix A.5.1 Figure A.10.

To study the effects of different cations and anions, we systematically compared the transition temperatures of SSY with the addition of LiCl, NaCl, KCl, LiBr, NaBr, and KBr in Figure 6.4. In Figure 6.4a, the difference of SSY transition temperature, $\Delta T_{NB} = T_{NB}(\text{salt}) - T_{NB}(\text{salt-free})$, is present with fixed salts concentration of 0.58 M. The salts with smaller cations increase the transition temperatures and stabilize nematic phase more

efficiently. For the same SSY concentration, ΔT_{NB} of LiCl/LiBr is larger than that of NaCl/NaBr and KCl/KBr. However, changing anion from Cl^- to Br^- does not make any difference on the transition temperatures. Additionally, salts with larger cations expand the biphase temperature region ($\Delta T_{biphase} = T_{biphase}$(salt) - $T_{biphase}$(salt-free)) more effectively as shown in Figure 6.4b. For all the SSY concentrations, $\Delta T_{biphase}$ of KCl/KBr is larger than that of NaCl/NaBr and LiCl/LiBr. For other salt concentrations, the shifts in T_{NB} and $T_{biphase}$, show the same tendencies as those in Figure 6.4, which are present in Appendix A.5.2 Figure A.11.

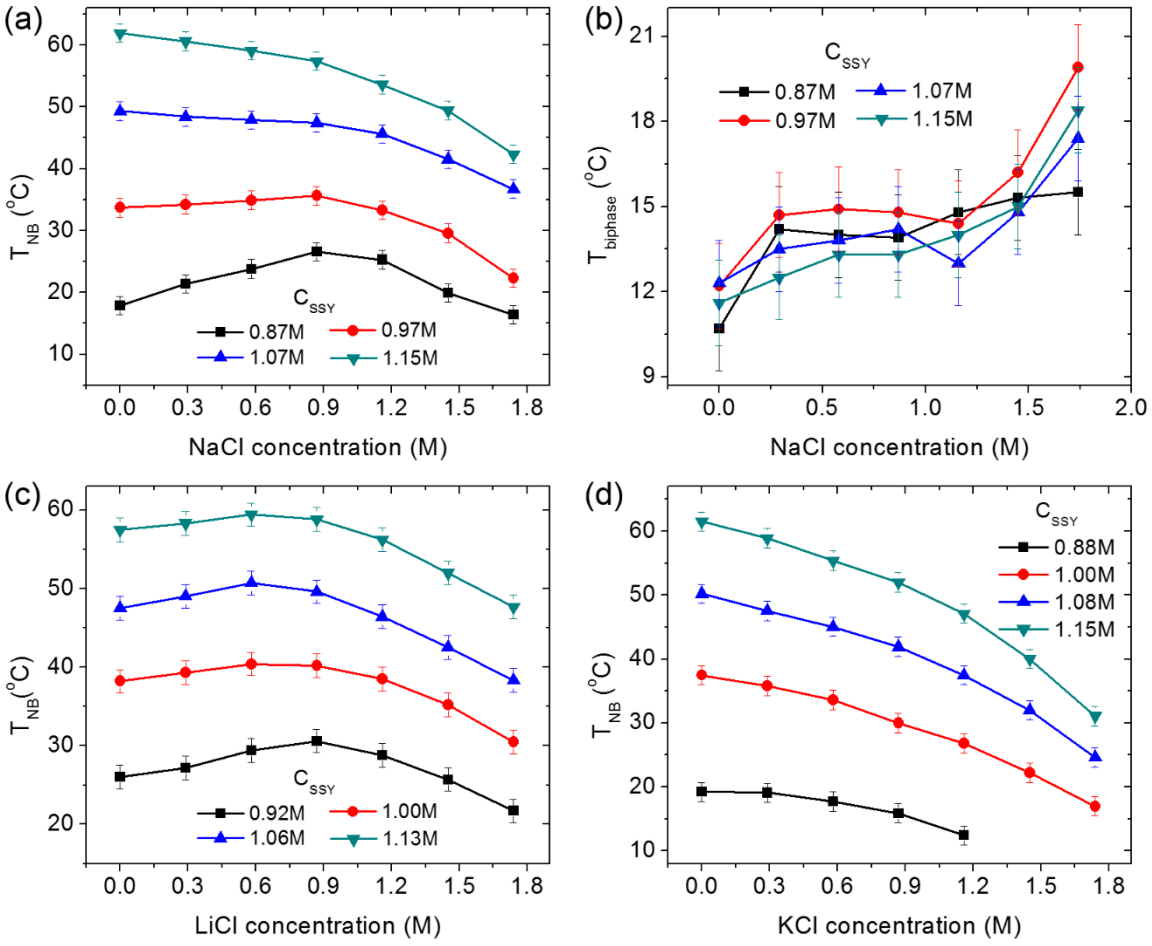

Figure 6.3 (a, c, d) The dependence of T_{NB} on the concentrations of SSY and monovalent salts. The monovalent salts are (a) NaCl, (c) LiCl, and (d) KCl. (b) The dependence of the biphase temperature range ($T_{biphase}$) on the concentrations of SSY and NaCl.

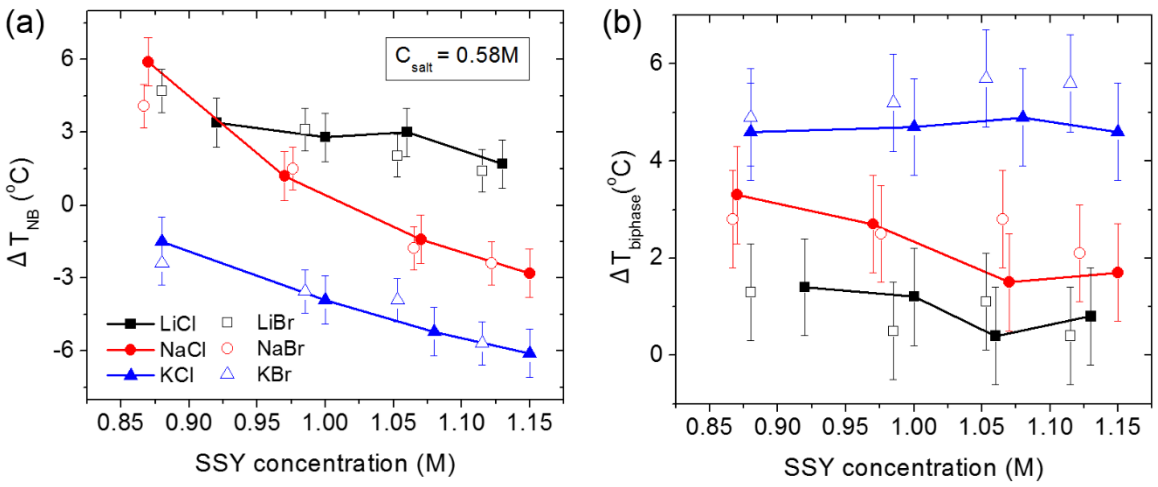

Figure 6.4 The dependence of (a) ΔT_{NB} and (b) $\Delta T_{biphase}$ on SSY concentration and monovalent salts with different cations and anions. The salts concentrations are fixed at 0.58 M.

6.3.2 Plausible salt mechanism on the aggregation behavior

Having shown the shifts in the transition temperatures with the addition of monovalent salts, we now raise a fundamental question about the mechanism of salts effects on the aggregation behavior of LCLCs. What is the interaction between SSY aggregates and monovalent salts which intrinsically changes the phase transition temperatures?

Consider the simple 1-D rod-like structure of the aggregates in Figure 6.5. Plank SSY molecules stack into columns by the π-π interactions of the aromatic cores, keeping a periodic distance of 0.34 nm[187,188] because of the Coulomb repulsion between the SO_3^- groups on the sides of the molecules. The aggregates are surrounded by the Na^+ ions due to the attraction force between the Na^+ ions and the SO_3^- groups. Two side-by-side aggregates keep a center-to-center distance of about 3 nm[189] due to the repulsion between the Na^+ layers.

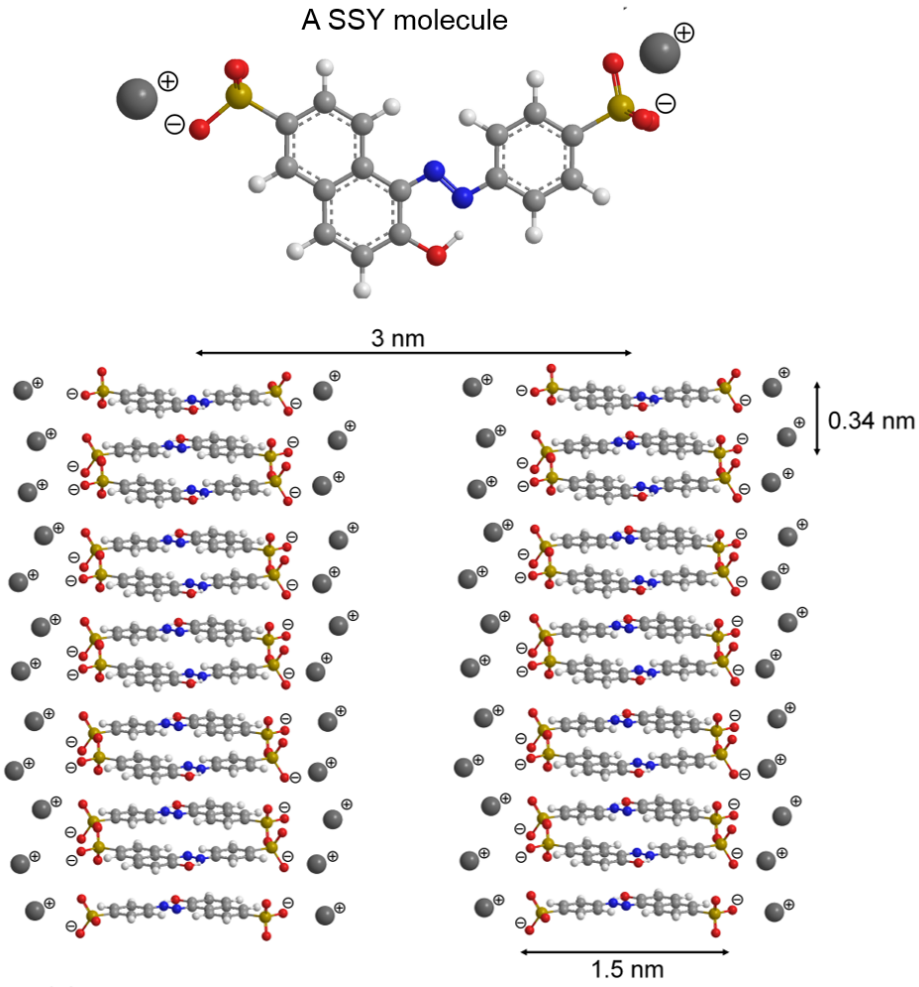

Figure 6.5 Illustration of two side-by-side SSY aggregates.

When a low concentration of ionic salts is added into the system (C_{salt} < 1.00 M), the anions fill the gaps between the aggregates and screen the repulsion between Na^+ as shown in Figure 6.6a. When the electrostatic screening is more significant than the steric effect of the anions, the aggregates would pack more closely with a smaller center-to-center distance. This screening of inter-aggregate repulsion is expected to stabilize the nematic phase and increase the phase transition temperatures. As shown in Table 6.1, the gap between SSY aggregates (~ 1.5 nm[189]) is much larger than the diameter of the anions (0.4 ~ 0.8 nm[190-192]). Hence, the size of the anions should not influence SSY phase diagram,

which is consistent with the experimental measurements with the addition of Br^- and Cl^- salts. For the effects of cations, small cations of salts can penetrate the individual aggregates and screen the repulsion between the adjacent SSY molecules. This intra-aggregate screening increases the scission energy and elongates the aggregates. Thus Na^+ and Li^+ salts promote the nematic order and raise the transition temperatures for $C_{salt} < 1.00$ M and $C_{SSY} < 1.03$ M (Figure 6.6a). However, when the diameter of cation is close to the stacking distance between SSY molecules (0.34 nm[187]), the steric effect prohibits the intra-aggregate screening of the electrostatic repulsion (Figure 6.6b). Moreover, the inter-aggregate screening of the electrostatic repulsion is also interrupted because the large cations locate between the aggregates. This model describes the situation of K^+ salts, which significantly reduce the transition temperatures of SSY (Figure 6.6b). In case of large salt concentrations ($C_{salt} > 1.00$ M), sufficient ions form double electric layers between the aggregates. The size of several cations and anions layers is comparable to the gap between the aggregates (1.5 nm[189]). In this situation, the steric effect plays a major role to destroy the nematic phase and all kinds of salts reduce the transition temperatures of SSY.

We note again that for the same amount of salts, the rise of transition temperatures is suppressed (or the drop of transition temperatures is enhanced) by an increase in SSY concentration. This fascinating dependence of the transition temperatures on SSY concentration is a challenge for the current mechanisms of salt effect. We suggest that close to the transition temperatures, the average aggregate length for higher SSY concentration should be shorter but there should be a larger number of aggregates in the solution. Fewer aggregates are placed side by side. Consequently, salts additives cannot effectively screen the Coulomb repulsion between the aggregates but exist as impurities to suppress the

nematic order. A more comprehensive theory should consider the electrostatic interaction between misplaced aggregates in addition to our model. Furthermore, the expansion of the biphase temperature range by salts cannot be explained by our simple mechanism. The expansion may indicate the change of aggregate length distribution and the formation of complex aggregate structures.

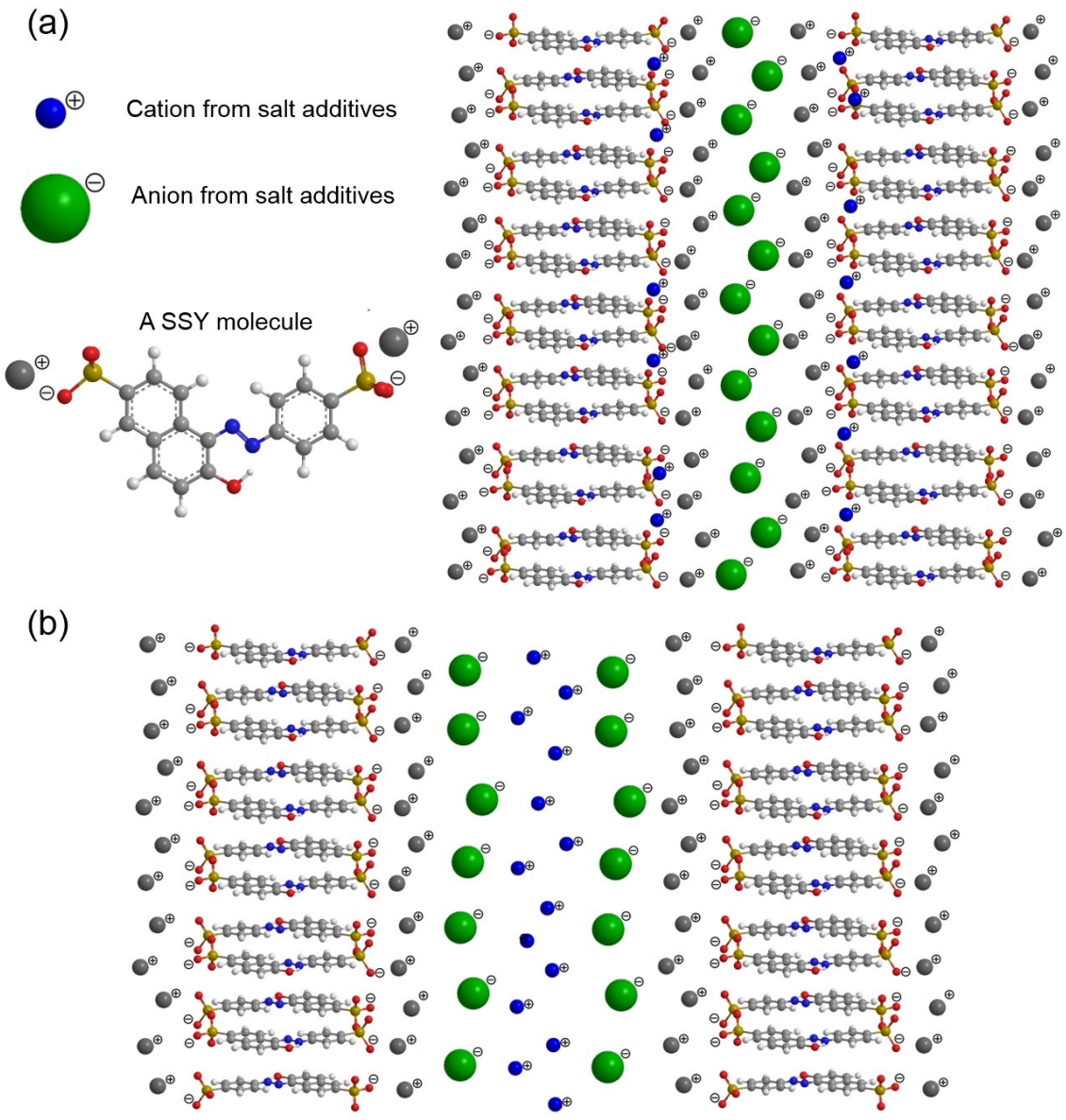

Figure 6.6 Illustrations of SSY aggregates surrounded by monovalent salts. (a) SSY aggregates doped with slow concentration of salts (C_{salt} < 1.00 M) with small cation (Na^+ or Li^+). (c) SSY aggregates doped with monovalent salts with large cations (K^+).

Table 6.1 Ionic diameters of the cations and the anions used in the experiments[190-192]

Ions	K^+	Na^+	Li^+	Br^-	Cl^-
Ionic Diameter	0.30 nm	0.23 nm	0.15 nm	0.78 nm	0.44 nm

6.4 Conclusions and future work

For decades, researchers used different additives to study the aggregation behavior of LCLCs, but the mechanisms of the additive effects are still not clear. In this study, we took the advantage of tactoids to investigate the roles of monovalent salts on the aggregation of LCLCs. We demonstrated in Chapter 5 that tactoids present as an optical probe to detect the average length of LCLC aggregates. The bipolar tactoids prevail when the aggregates are short. Two chiral structures, the TB and the EC configurations, emerge when the aggregates are elongated. As discussed in this chapter, the configurational transformation of tactoids indicates the complicated shifts in the aggregate length distribution and the phase transition temperatures of LCLCs with the addition of monovalent salts.

The mechanism of salts effects on the phase transition temperatures was then explored systematically using the monovalent salts with different cations (Li^+, Na^+, K^+) and anions (Cl^-, Br^-). The shifts in the transition temperatures depend on SSY concentration, salt concentration, and the cation size. We proposed a simple mechanism based on the screening of intra- and inter-aggregate electrostatic repulsion. For future work, we suggest the characterization of the structural parameters of SSY aggregates with the addition of salts using small angle neutron scattering (SANS)[193-196]. Moreover, molecular modelling and simulations are also necessary to understand the interactions between LCLCs and salts.

CHAPTER 7. THE EFFECTS OF MONOVALENT SALTS ON THE ORIENTATIONAL ORDER OF LCLCS

7.1 Introduction

Nematic liquid crystalline phase differs from the isotropic liquids by having the long range orientational order of the rod-like building units[52]. The orientation of the nematic director fluctuates spontaneously. The average of the orientations for many building units at a given time should be equivalent to the average of the orientations for a given building unit at many moments. The degree of the orientational order for nematic liquid crystals can be comprehensively described by a tensor order parameter[52,57]. For simple rod-like systems, the order parameters are defined based on the average of Legendre polynomial[52]. Since reversing the orientation of nematic director does not make any difference ($\boldsymbol{n} = \boldsymbol{-n}$)[52], only the even orders of Legendre polynomials make sense for the order parameters of nematic liquid crystals. The scalar order parameter (S), which is the 2nd order Legendre polynomial, is usually used to describe the orientational order. S is expressed as $S = \langle\frac{3cos^2\theta_m-1}{2}\rangle$, where θ_m is the angle between the axis of the mesogen units and the director orientation, the brackets indicate temporal and spatial average. The value of S ranges from 0 (for isotropic liquid) to 1 (for perfectly aligned mesogens with no fluctuation). S for typical liquid crystals is 0.3 ~ 0.9, which decreases with the increase in temperature[61].

The value of order parameters can be measured using various methods, such as birefringence measurement[197,198], nuclear magnetic resonance[188,199,200], and Raman scattering[201-204]. For the work discussed in this chapter, we used depolarized Raman

scattering to measure the 2nd and 4th order parameters of SSY with the addition of monovalent salts. In Chapter 6, we have shown that the monovalent salts significantly alter the phase diagram and the configurations of tactoids by changing the aggregation behavior of SSY. The measurements of order parameters will help to understand the salts effects on the aggregation behavior from the changes of orientational order.

7.2 Raman Spectroscopy

7.2.1 Introduction to Raman spectroscopy

When the light interacts with a molecule, the oscillating electric field of the light ($\boldsymbol{E}$) induces an oscillating dipole moment ($\boldsymbol{\mu}$) in the molecule, which is proportional to its polarizability ($\boldsymbol{p}$): $\boldsymbol{\mu} = \boldsymbol{pE}$. The oscillating dipole moment can absorb and emit lights by the transition between different energy levels. For the usual elastic transition, the energy of scattered photons is equal to the energy of absorbed photons, which is called "Rayleigh scattering" (elastic scattering)[205]. A very small amount of photons are scattered with the energy different from the incident photons, which is referred as "Raman scattering"[206] (inelastic scattering).

The intensity of Raman scattering (I) is proportional to the square of differential polarization with respect to the distortion coordinates (q_k)[207-209]: $I \propto \left[\left(\frac{\partial p}{\partial q_k}\right)_{q_k=0}\right]^2$. The vibrations of many bonds, such as C-C stretching of phenyl rings, are Raman active when they have large differential polarizability, even if their polarizability is small. On the other hand, water molecules have a large polarizability, but their differential polarizability is small. Therefore, water does not have much influence on Raman intensity, which makes it

suitable to characterize SSY aqueous solutions. For liquid crystal materials with large anisotropy, the differential polarizability is a tensor with three components: $\left(\frac{\partial p}{\partial q_k}\right)_{q_k=0} = \begin{bmatrix} p'_x & & \\ & p'_y & \\ & & p'_z \end{bmatrix}$. Hence, the degree of long-range order can be extracted from the angular dependence of Raman intensity.

7.2.2 Using depolarized Raman spectroscopy to measure order parameters

For depolarized Raman spectroscopy, the scattered intensity is measured with the polarization parallel with ($I_{\parallel}$) and perpendicular to ($I_{\perp}$) the incident laser[203]. The ratio of the perpendicular and parallel intensities, $R(\theta) = \frac{I_{\perp}}{I_{\parallel}}$, is called depolarization ratio. The depolarization ratio can be expressed in terms of the angle between the polarization of the incident light and the orientation of the vibrating bond (θ), the 2nd and 4th order parameters ($< P_2 >$ and $< P_4 >$), and the differential polarizability ratio ($r = p'_x/p'_z$)[202,204,210].

$$R(\theta) = \frac{I_{\perp}(\theta)}{I_{\parallel}(\theta)} = \frac{(-1+r)^2\left(-56-40\langle P_2\rangle-9\langle P_4\rangle+105\langle P_4\rangle cos(4\theta)\right)}{-56(3+4r+8r^2)+40\langle P_2\rangle(-1+r)(3+4r)\left(1+3cos(2\theta)\right)-3\langle P_4\rangle(-1+r)^2\left(9+20cos(2\theta)+35cos(4\theta)\right)} \quad (7.1)$$

By measuring Raman intensities with different orientations of the sample, the values of $< P_2 >$, $< P_4 >$, and r can be extracted from fitting the depolarization ratio as a function of θ.

To measure the Raman intensities of SSY at different orientations, we need a sample of monodomain where the director everywhere is along the same direction. This monodomain can be achieved using a rectangular capillary with degenerate planar anchoring. The configurations of SSY in rectangular capillaries have been investigated comprehensively in recent literature[211-215]. Here, we briefly describe the formation of the monodomain used in the Raman experiments. As shown in Figure 7.1, under crossed

polarizers, the birefringent pattern of SSY confined in the rectangular capillary exhibits the extinction of the light when the polarizer is parallel with (or perpendicular to) the long axis of the capillary. Only the region close to the capillary wall shows transmitted intensity since the director deviates from the uniform orientation due to the planar anchoring on the surface. The monodomain shows linear dichroism with monochromatic illumination of 551 nm as shown in Figure 7.1b and 7.1c. The sample exhibits lower transmitted intensity with more light absorption when the polarizer and capillary axis have the same orientation (Figure 7.1b). In this situation, the polarizer is parallel with the molecular plane of SSY and perpendicular to the director. Therefore, the director of the sample is aligned perpendicular to the capillary axis. In Figure 7.1c, the polarizer is perpendicular to the planes of SSY molecules and parallel with the director, resulting less light absorption and more transmitted intensity.

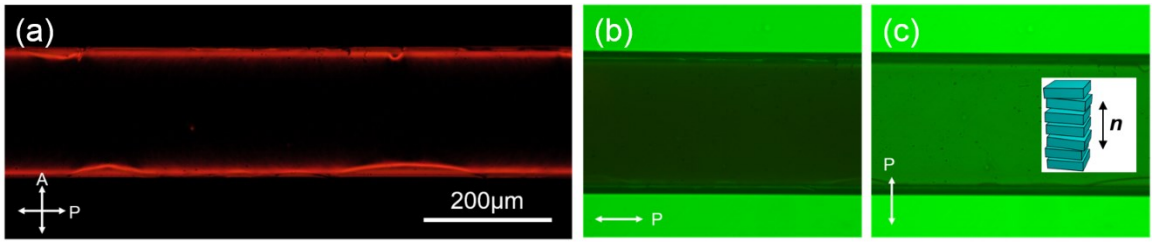

Figure 7.1 (a) Polarized optical microscopy image of SSY solution in a rectangular capillary under crossed polarizers. (b, c) SSY solution in a rectangular capillary with the polarizer parallel with and perpendicular to the capillary axis, respectively. The inset in (c) shows that the director of SSY in the capillary is perpendicular to the capillary axis. P and A represent the orientations of polarizer and analyzer.

The typical Raman spectra of SSY are present in Figure 7.2a with different polarizer and analyzer combinations (see Appendix A.7.4 for the Raman spectroscopy system). The peak positions and relative intensities does not have much difference upon adding salts as shown in Figure 7.2b. The strongest peak at the wave number of 1597 cm^{-1}

results from the C-C stretching of phenyl rings, which is frequently used in literature to extract the 2nd and 4th order parameters[204,212]. The fact that the phenyl C-C stretching peak is stronger than any peaks between 1463-1380 cm^{-1} also reveals that the NH hydrazone structure (Figure 1.7b) of SSY molecules is dominant rather than the N=N azo structure[204].

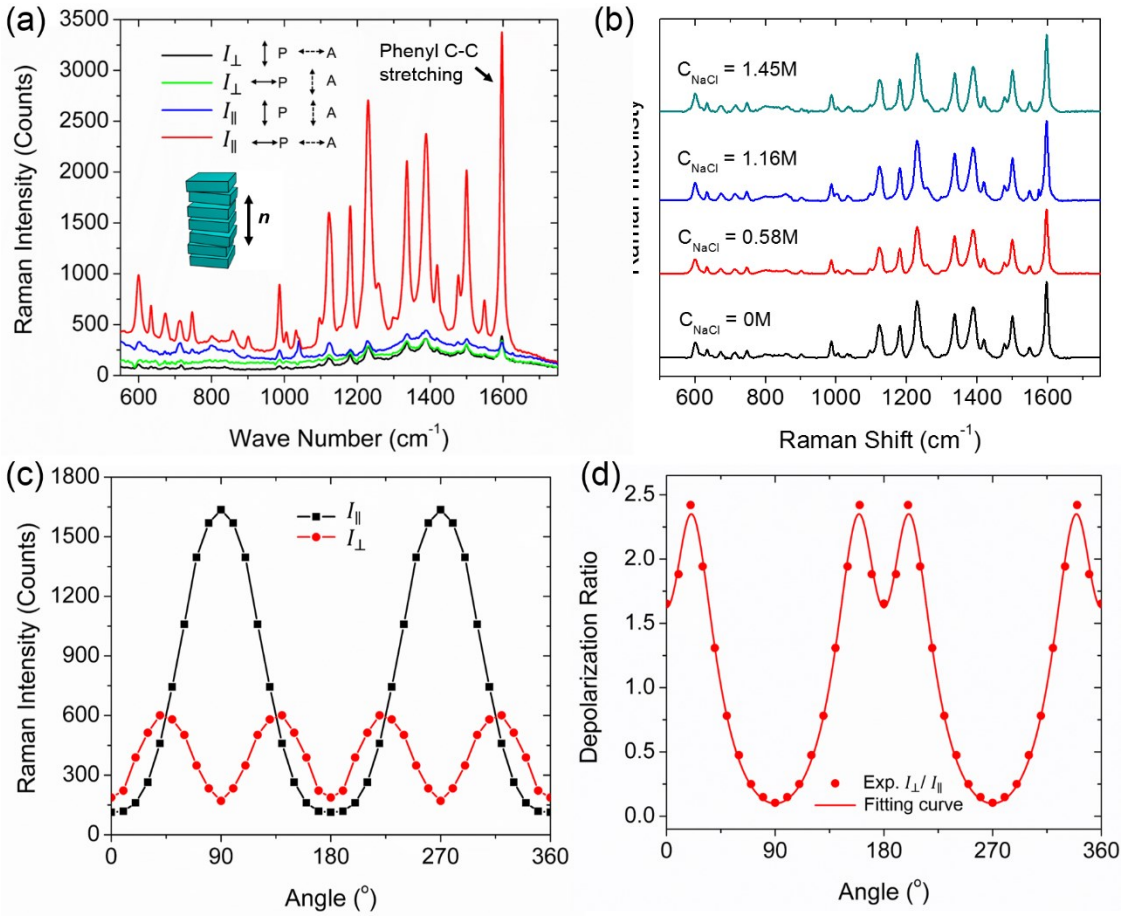

Figure 7.2 (a) Raman spectra of SSY solution with different polarizer and analyzer combinations. The director is oriented along the vertical direction. The orientations of polarizer (P) and analyzer (A) are indicated in the insets. (b) Raman spectra of SSY solutions with different concentrations of NaCl. (c) Intensities of phenyl C-C stretching peak as a function of rotation angle with the polarizer parallel with ($I_{\parallel}$) and perpendicular to ($I_{\perp}$) the analyzer. (d) Experimental dots and fitting curve of depolarized ratio ($I_{\parallel}/I_{\perp}$) as a function of rotation angle.

In Figure 7.2a, the peaks of SSY solution have different intensities with different combinations of polarizer and analyzer. When the polarization of the incident light is

parallel with the planes of SSY molecules (the polarizer is parallel with the capillary axis), the light induces larger differential polarizability and stronger Raman intensity (green and red spectra). On the contrary, the Raman intensity is weak (black and blue spectra) when the polarization of the incident light is perpendicular to the molecular planes (the polarizer is perpendicular to the capillary axis). Moreover, the Raman intensity is usually stronger when the polarizer and analyzer are parallel (blue and red spectra) rather than perpendicular (black and green spectra). When the sample is rotated from 0^o to 360^o, the intensity of phenyl C-C stretching peak as a function of rotational angle is plotted in Figure 7.2c. The intensities when the polarizer and analyzer are parallel and perpendicular ($I_{\parallel}$ and $I_{\perp}$) exhibit two-fold symmetry and four-fold symmetry, respectively. The depolarized ratio ($I_{\parallel}/I_{\perp}$) is calculated and fitted with equation 7.1 as shown in Figure 7.2d to obtain the 2^{nd} and 4^{th} order parameters ($< P_2 >$ and $< P_4 >$).

For the work in the following sections, we used depolarized Raman spectroscopy to measure the order parameters of SSY solution free of any additives. Then we explored the effects of monovalent salts with different cations (LiCl, NaCl, and KCl) on SSY order parameters.

7.3 Order parameters of Sunset Yellow (SSY) under the effects of monovalent salts

7.3.1 Order parameters of additive-free SSY

The order parameters of additive-free SSY solutions for different concentrations and temperatures are presented in Figure 7.3. $< P_2 >$ and $< P_4 >$ decrease with the increase in the temperature and the decrease in the concentration as shown in Figure 7.3a and 7.3b. However, when rescaled with reduced temperature, T/T_{NB}, the order parameters in Figure

7.3c and 7.3d are only functions of the reduced temperatures, which are independent of the concentration. The role of the concentration is only to change the transition temperatures, whereas the reduced temperature determines the degree of orientational order. This temperature and concentration dependence of order parameters is consistent with previous measurements by my collaborators, Dr. Karthik Nayani and Dr. Jinxin Fu[11], which was rationalized by Onsager theory of phase transition[96]. In Onsager theory, the order parameter at the phase transition temperature is determined by the product of volume fraction (ϕ) and average aggregate length ($\bar{L}$)[96]. As estimated by the self-assembling model for LCLCs, the values of $\phi\bar{L}$ at the phase transition temperature are independent from SSY concentration[11].

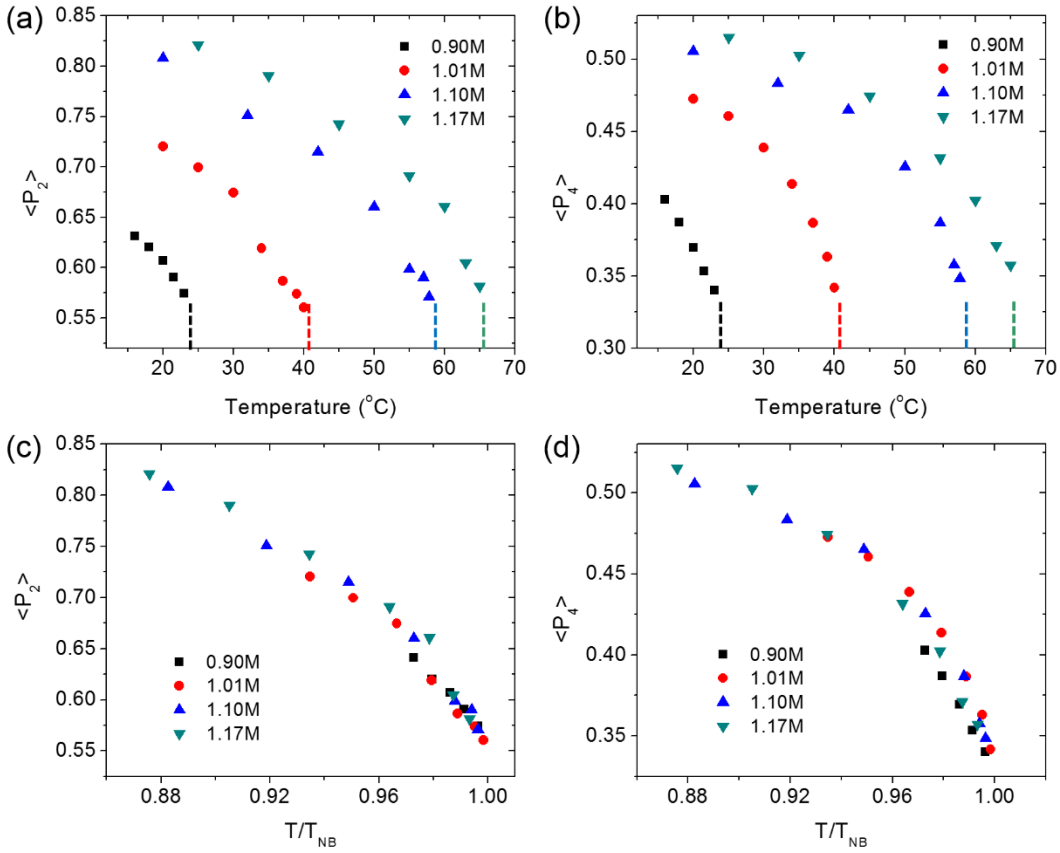

Figure 7.3 (a, b) The 2nd and 4th order parameters of SSY solutions with different concentrations as a function of temperature. The dashed lines represent the transition temperature, T_{NB}, for different SSY concentrations. (c, d) The 2nd and 4th order parameters of SSY solutions with different concentrations as a function of reduced temperature, T/T_{NB}.

7.3.2 Order parameters of SSY with the addition of LiCl, NaCl, and KCl

In this study, we discuss the order parameters of SSY with the addition of LiCl, NaCl, and KCl. In Figure 7.4, the order parameters of 0.92 M SSY + LiCl solutions are present as an example. The data of SSY + NaCl and SSY + KCl can be found in the Appendix A.6.1, Figure A.12 - Figure A.14. In Chapter 6.3, we have shown that the monovalent salts effects on the transition temperatures of SSY depend on salt concentration, SSY concentration, and the cations. In Figure 7.4, the transition temperatures of SSY + LiCl solutions, (T_{NB}) are indicated by the dashed lines and the order parameters are measured from 16 ºC to T_{NB}. As shown in Figure 7.4a and 7.4b, at the same temperature, $< P_2 >$ and $< P_4 >$ of SSY + LiCl solutions can be either larger or smaller than those of LiCl-free SSY solutions. But the order parameters close to T_{NB} are reduced significantly by LiCl. Moreover, $< P_2 >$ and $< P_4 >$ are replotted in Figure 7.4c and 7.4d as a function of T/T_{NB}. For the fixed SSY concentration, the order parameters of SSY + LiCl are smaller than those of LiCl-free SSY solutions at the same T/T_{NB}. But different LiCl concentrations do not change the order parameters as a function of T/T_{NB}. For different SSY concentrations, the order parameters of SSY with fixed LiCl concentration are compared in Figure 7.4e and 7.4f as a function of T/T_{NB}. The order parameters are independent of SSY concentration, which is the same as behavior of salt-free SSY solutions (Figure 7.3c and 7.3d). The effects of NaCl and KCl on the order parameters of SSY are similar as those of LiCl, which are presented in Appendix A.6.1, Figure A.13 and Figure A.14. For salts with different cations, the values of order parameters close to T_{NB} and the range of order parameters from room temperature to T_{NB} are compared in Table 7.1. Both the values close to T_{NB} and the ranges of $< P_2 >$ and $< P_4 >$ are reduced by all the monovalent

salts. But the salts effects on order parameters are independent of cation size, which notably depart from the salts effects on the transition temperatures.

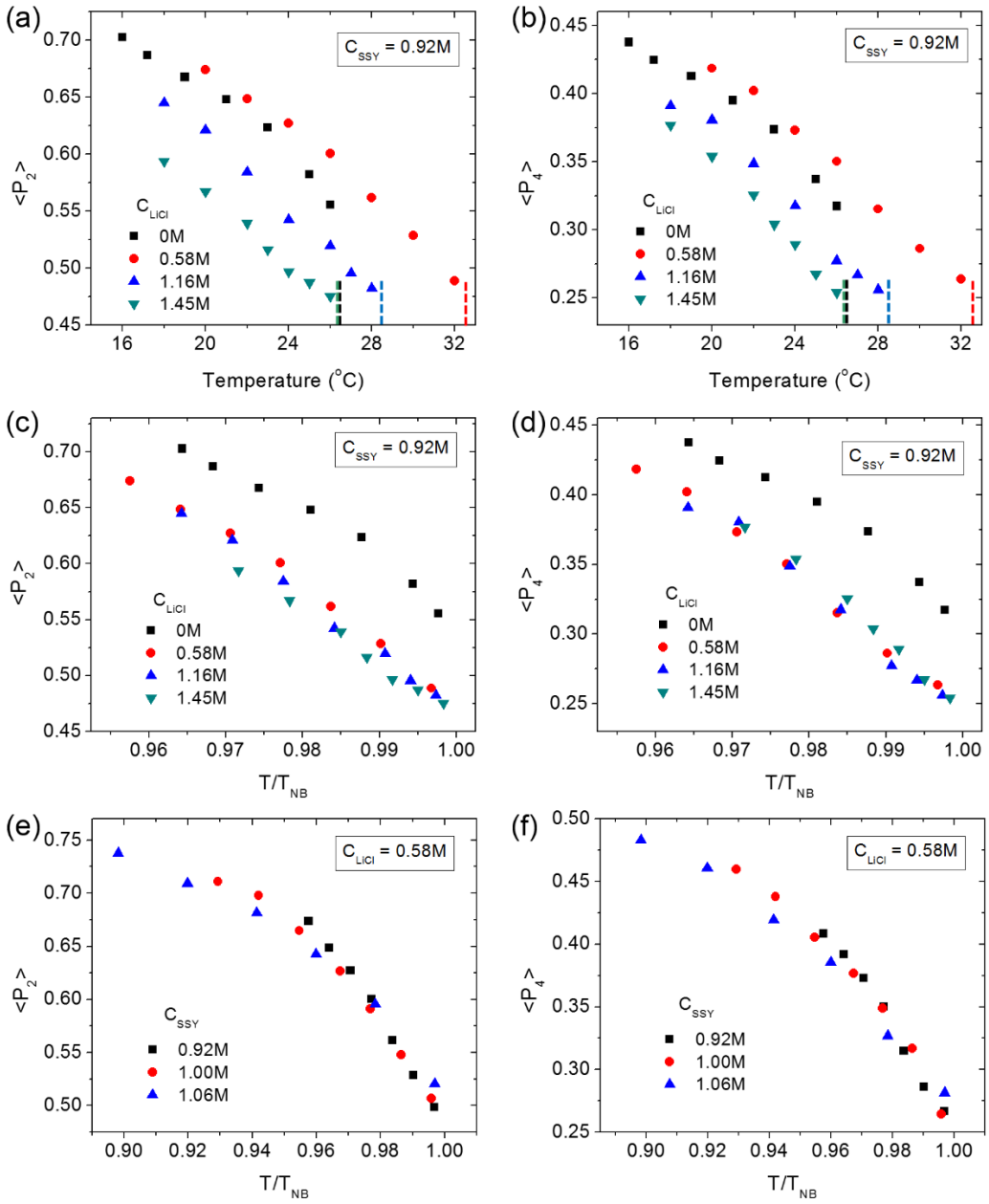

Figure 7.4 (a, b) The 2nd and 4th order parameters of SSY + LiCl solutions for different LiCl concentrations as a function of temperature. The SSY concentration is fixed at 0.92 M. The dashed lines represent the transition temperature, T_{NB}. (c, d) The 2nd and 4th order parameters of SSY + LiCl solutions for different LiCl concentrations as a function of reduced temperature, T/T_{NB}. The SSY concentration is fixed at 0.92 M. (e, f) The 2nd and 4th order parameters of SSY + LiCl solutions for different SSY concentrations as a function of reduced temperature, T/T_{NB}. The LiCl concentration is fixed at 0.58 M.

Table 7.1 The values of $< P_2 >$ and $< P_4 >$ close to T_{NB} and the ranges of $< P_2 >$ and $< P_4 >$ for SSY with the addition of LiCl, NaCl, and KCl.

	SSY	SSY + LiCl	SSY + NaCl	SSY + KCl
$< P_2 >$ close to T_{NB}	0.55	0.48	0.49	0.51
$< P_4 >$ close to T_{NB}	0.32	0.25	0.25	0.25
Range of $< P_2 >$	0.55 ~ 0.85	0.48 ~ 0.74	0.49 ~ 0.75	0.51 ~ 0.77
Range of $< P_4 >$	0.32 ~ 0.55	0.25 ~ 0.49	0.25 ~ 0.47	0.25 ~ 0.50

7.3.3 Theoretical analysis

As shown in section 7.3.2, we noticed that the order parameters close to T_{NB} are significantly reduced by the addition of monovalent salts. $< P_2 >$ at transition temperature is a crucial parameter for the emergence of nematic phase during the phase transition, which was theoretically predicted by the Onsager model[96]. Based on the assumption of rigid rods, the model finds that the $< P_2 >_{T=T_{NB}}$ is a constant, 0.79 [85,216], which is much larger than our measurements (0.48 ~ 0.55) and the data for other nematics reported in literature (0.3 ~ 0.7)[52,217,218]. Moreover, $< P_2 >$ at T_{NB} of SSY + salts solutions cannot be rationalized by the product of $\phi\bar{L}$ as described by Onsager model. For the same SSY concentration, the volume fraction of SSY aggregates (ϕ) is fixed. But for different salts concentrations, the average aggregate length, $\bar{L}$, is different at different transition temperatures based on the self-assembling model[121]. Hence, the value of $\phi\bar{L}$ is not a constant at T_{NB} for SSY with different salt concentrations, which can be either larger or smaller than the $\phi\bar{L}$ of salt-free SSY solutions. But the order parameters at T_{NB} for all the SSY + salts solutions are smaller than those of salt-free SSY solutions, which is inconsistent with the shifts of $\phi\bar{L}$.

Based on Onsager's initial work for rigid rods, scientists improved the phase transition theory by considering the flexibility of the rods[219-222]. The flexibility is included in the theory by the parameter, $\alpha_f = \frac{\bar{L}}{\lambda_p}$, where λ_p is the persistence length of the building mesogens. The theory of semi-flexible rods was first derived by Khokhlov and Semenov[219] and later improved by Z. Y. Chen[220-222]. Figure 7.5a shows the theoretical prediction of $< P_2 >_{T=T_{NB}}$ by Z. Y. Chen[221] as a function of α_f. When α_f is smaller than 0.6, the increase of aggregates flexibility (larger α_f) leads to a smaller $< P_2 >_{T=T_{NB}}$. With sufficient flexibility of the aggregates (α_f > 0.6), $< P_2 >_{T=T_{NB}}$ becomes less dependent on α_f with a value of 0.45.

According to the elastic constants model[87,115,116] in Chapter 2.4.1, α_f for SSY can be estimated by the ratio of splay and bend elastic constants[94], $\alpha_f = \frac{\bar{L}}{\lambda_p} \sim \frac{K_{11}}{K_{33}} \sim 0.5$. This value of α_f is in the region where $< P_2 >_{T=T_{NB}}$ strongly depends on the flexibility of the aggregates. With the addition of salts, SSY aggregates are more flexible[123,128] with smaller λ_p and larger α_f. Thus $< P_2 >_{T=T_{NB}}$ should be reduced by salts, which is consistent with our experimental measurements. Since the salt effect on the persistence length of the aggregates is only a function of ionic strength[123,128], cation size theoretically does not make any difference to $< P_2 >_{T=T_{NB}}$. This theoretical conclusion rationalizes our order parameters measurements of SSY + LiCl, NaCl, and KCl solutions. SSY solutions adding salts with different cations have the same order parameters close to T_{NB}. Moreover, the increase in salts concentrations (0.58 M ~ 1.45 M) results in larger α_f. But for α_f > 0.6, theoretically, the flexibility of the aggregates does not affect the value of $< P_2 >_{T=T_{NB}}$. It

rationalizes the independence of the order parameters close to T_{NB} on salts concentrations as measured in our experiments.

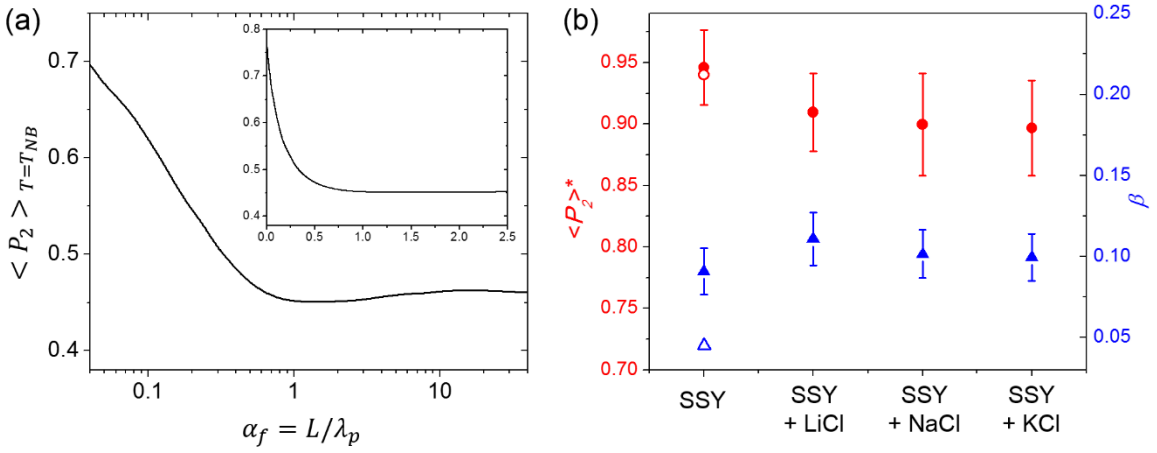

Figure 7.5 (a) Theoretical dependence of $< P_2 >$ at T_{NB} on the flexibility of the aggregates. The inset enlarges the region of α_f = 0 ~ 2.5. (b) The fitting parameters of the empirical equation for the 2nd order parameter of SSY with the addition of different monovalent salts. The solid circles and triangles are extracted from the fitting of our data. The open circles and triangles are from the literature[204].

Additionally, the temperature dependence of $< P_2 >$ for salt-free SSY, SSY + LiCl, SSY + NaCl, and SSY + KCl were fitted with the empirical formula based on the mean field theory[223,224]: $< P_2 > = < P_2 >^* (1 - T/T_{NB})^{\beta_0}$, where $< P_2 >^*$ is the intrinsic 2nd order parameter of the material when the temperature is absolute zero; β_0 is the parameter that represents the temperature dependence of the 2nd order parameter. In section 7.3.2, we have shown that $< P_2 >$ is independent of the concentrations of SSY and salts when plotted as a function of T/T_{NB}. Hence, the data of all the SSY and salts concentrations were used in the fitting. The confidential interval is represented by the error bar as shown in Figure 7.5b. For salt-free SSY, $< P_2 >^*$ is calculated to be about 0.95 and β_0 is about 0.09 as indicated by the solid circles and triangles in Figure 7.5b. Our calculated $< P_2 >^*$ is comparable but β_0 is larger than the values in the literature[204] (the open circle and triangle

in Figure 7.5b). Larger β_0 indicates that the order parameter has a stronger dependence on the temperature. With the addition of salts, $< P_2 >^*$ becomes smaller (about 0.90) and β_0 is slightly larger (about 0.10) than those of salt-free SSY solutions. The values of $< P_2 >^*$ and β_0 do not vary with cation size. And the error bar of $< P_2 >^*$ is larger with the addition of the salts, especially for NaCl and KCl.

7.4 Conclusions and future work

As shown in this chapter, we used depolarized Raman spectroscopy to measure the order parameters of SSY under the effects of monovalent salts, LiCl, NaCl, and KCl. We have demonstrated in Chapter 6 that the cation size of the monovalent salts makes a significant difference on the phase transition temperatures of SSY. But the order parameters of SSY are not affected by different cations. Additionally, the order parameters are independent of the concentrations of SSY and salts when plotted as a function of T/T_{NB}. The concentrations of SSY and salts only change the transition temperatures of the SSY solutions. T/T_{NB} is the key factor to determine the order parameters. However, although the order parameters for different salts concentrations (0.58 M ~ 1.45 M) are the same as a function of T/T_{NB}, the addition of salts reduce the order parameters, compared with salts-free SSY solutions. The small 2nd order parameter at T_{NB} with the addition of salts was rationalized by the theoretical phase transition model considering the flexibility of the aggregates[219-222].

As the future work, it is worth expanding the explorations of the transition temperatures and the order parameters of SSY when the salts with higher valences are added. Furthermore, based on our plausible salt mechanism (discussed in section 6.3.2), the anion

size should not make any difference on the transition temperatures since the sizes of Cl^- and Br^- is much smaller than the distance between SSY aggregates. Thus, the effect of anion could be observed using large anions with the sizes comparable with the aggregates distance. Additionally, it would also be interesting to exchange the Na^+ cations inf SSY molecules to Li^+ and K^+ to explore the role of ions interactions in the aggregating systems.

CHAPTER 8. CONCLUSIONS AND FUTURE WORK

8.1 Conclusions

Confined nematic liquid crystals exhibit rich configurational phenomena under the effects of curved surfaces and the anisotropy of elastic constants. In this thesis, we documented the novel chiral configurations from achiral LCLCs in cylindrical and tactoidal confinements, which spontaneously break the mirror symmetry of the director configurations. The emergence of chirality from achiral molecules distinguishes the configurational behavior of lyotropic liquid crystals from the usual expectations based on the conventional thermotropic liquid crystals. The underlying physics of the chiral configurations provides fundamental insights to understand the behaviors of liquid crystals and the general symmetry-breaking phenomena in nature.

The chiral configurations of achiral LCLCs confined in cylindrical geometry were summarized in Chapter 2-4. In Chapter 2, we reported the DT chiral configuration in replace of the usual axial configuration for LCLCs confined in cylindrical capillaries with degenerate planar anchoring[7,8]. Rather surprisingly, we found that the elastic free energy of the DT configuration with large twist distortion is lower than the non-deformed axial structure due to the stabilization of the saddle-splay elasticity. By characterizing the twist angle of the DT director field, we estimated the saddle-splay elastic constant for LCLCs as a function of temperature and concentration. In Chapter 3, we reported the two chiral configurations of LCLCs in cylindrical capillaries with homeotropic anchoring, the TER configuration and the TP configuration[9,10]. Due to the small twist elastic constant of LCLCs[93-95], the twist deformation spontaneously evolves in the director field to relieve the

energy contributions of the splay and bend deformations. The birefringent pattern of the TER configuration exhibits remarkable dependence on the aggregation behavior of LCLCs at different temperatures and concentrations. Furthermore, for high LCLC concentrations, we reported a novel co-existence of domains with the DT configuration and the TER configuration. The anchoring violation of the DT domains enabled us to estimate the anchoring strengths of LCLCs on the surface of the parylene-N alignment film.

Since the formation of the chiral configurations from achiral LCLCs was fully attributed to the elastic anisotropy coupling with the curvature of the surfaces, we reasonably expect similar chiral configurations for other lyotropic liquid crystalline materials with small twist elastic constants in cylindrical capillaries, regardless of their molecular structures. To validate this expectation, in Chapter 4, we showed the chiral configurations of a racemic lyotropic polymer liquid crystal confined in cylindrical capillaries, which has a small twist elastic constant[117,118] but a notably different molecular structure from LCLC aggregates. Remarkably, the racemic lyotropic polymer liquid crystal exhibits the same chiral configurations as those of LCLCs in cylindrical capillaries for both degenerate planar anchoring and homeotropic anchoring. Another supportive observation was recently reported by C. F. Dietrich et al[23], wherein the TER and the TP chiral configurations were observed with achiral lyotropic micellar liquid crystals in cylindrical capillaries with homeotropic anchoring. Our observations, together with the work of C. F. Dietrich et al.[23], indicate that the emergence of chiral configurations can be a universal phenomenon for various lyotropic systems, since it seems to be a common property of lyotropics to have an extremely small twist elastic constant[117,118]. This configurational

behavior of lyotropics is distinctly different from the usual achiral configurations of the conventional thermotropic liquid crystals.

Next, we explored the chiral configurations of LCLCs in tactoids, which is a natural confinement of nematics with curved surfaces formed during the phase transition. As shown in Chapter 5, we found that the configurations of tactoids can be used as the optical probe to detect the average aggregate length of LCLCs[11]. With short aggregates at high temperatures and high concentrations, the tactoids exhibit the conventional achiral bipolar configuration with a small K_{11}. As the aggregates are elongated at low temperatures and low concentrations, K_{11} of LCLCs increases significantly, which leads to the formation of tactoids with the chiral TB and EC configurations. It is worth noting that the EC configuration has been expected theoretically when K_{33}/K_{11} is small[12], but was realized for the first time in our experiments. This aggregation-elasticity-configuration relationship was further validated by the effects of a neutral polymer and ionic salts additives on the tactoidal structures. The neutral polymer (PEG) elongates LCLC aggregates by the excluded volume mechanism[123-125], which induces the transformation of tactoids from the achiral bipolar structure to the two chiral configurations. As shown in Chapter 6, the tactoidal configurations were changed by the addition of NaCl, which shifts the phase transition temperatures and the subsequent average aggregates length of LCLCs. Additionally, the salts effects on the transition temperatures of LCLCs were further explored with different cations and anions. Our results show that the salts effects have interesting dependence on the LCLC concentration, salts concentration, and the size of the cations, which can be explained by a plausible mechanism based on the electrostatic interactions between salts ions and LCLC aggregates.

In Chapter 7, we further discussed the salts effects on the order parameters of LCLCs using depolarized Raman spectroscopy. Monovalent salts significantly reduce the order parameters of LCLCs close to T_{NB}. The roles of the temperature, LCLC concentration, and salts concentration were separated when the order parameters were plotted as a function of reduced temperature, T/T_{NB}. The order parameters in terms of T/T_{NB} are independent of LCLC concentration, salts concentration, and cation size. Finally, we discussed the salts effects on the order parameters based on the phase transition theory considering the flexibility of the aggregates[219-222].

8.2 Future work

8.2.1 Chirality amplification of LCLCs configurations.

Due to the achiral nature of LCLC molecules, the chiral configurations in our experiments exhibit both right-handed and left-handed twist deformations in cylinders and tactoids. But when the solutions have a small excess of chiral molecules, the twist direction of the chiral structures can easily be altered by the molecular chirality of the chiral additives[17,158,159,225]. The chirality amplification of the chiral configurations from achiral liquid crystals was observed recently with the TB tactoids of LCLCs[158,159]. As shown in Figure 8.1. the tactoids of DSCG under the effect of PEG exhibit both right-handed and left-handed TB structures free of any chiral additives. The tactoids with opposite twist directions are distinguished by decrossing the polarizers as shown in Figure 8.1a. The numbers of tactoids with right-handed and left-handed twists are equal. Under the effects of R-limonene and S-limonene, the twist deformations of the TB tactoids become single-handed as shown in Figure 8.1b and 8.1c, repectively.

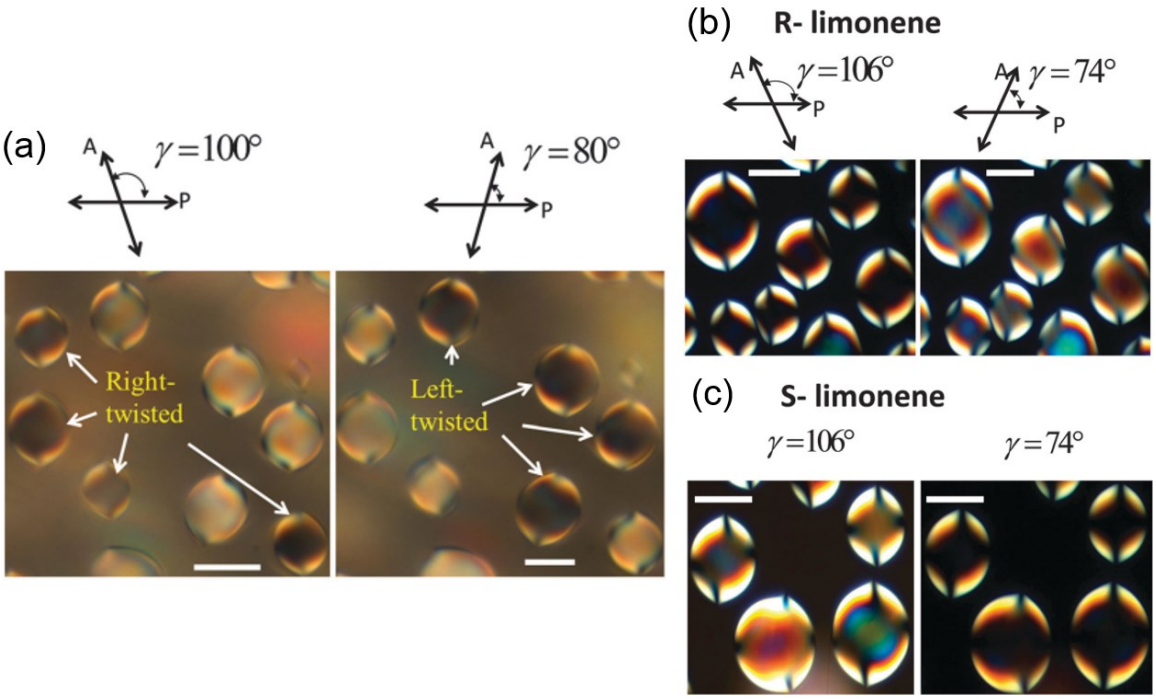

Figure 8.1 (a) Polarized optical microscopy textures of DSCG tactoids crowded by PEG molecules with no chiral additives. The tactoids with right-handed and left-handed twist deformations are different when viewed under decrossed polarizers. (b, c) Textures of DSCG tactoids crowded by PEG molecules with the addition of R-limonene and S-limonene, respectively. R-limonene and S-limonene additives induce homochirality of tactoids with right-handed and left-handed twists, respectively.[159]

The preliminary results in our group by Sujin Lee and Dr. Jinxin Fu showed the chiral amplification of the DT configuration for LCLCs in cylindrical capillaries with degenerate planar anchoring[226]. In Figure 8.2, the twist distortion in the DT configuration of DSCG is biased by L-alanine (or R-alanine) with the critical concentration of only 0.2 wt%. However, L-alanine (or R-alanine) cannot amplify the chirality in the DT configuration of SSY. The critical concentration to achieve homochirality for DSCG in cylindrical capillaries also varies considerably for different chiral dopants.

As a future work, it is necessary to explore the interactions between LCLC molecules and various chiral dopants to understand the mechanism of chiral amplification.

The chiral amplification of LCLCs is very inspiring for the origin of homochirality phenomenon in biological systems, which is recognized as a signature of life[2,3,14]. The small excess of chiral dopants might be the driving force for the preference of one handedness rather than the other for a lot of chiral biomolecules and biostructures in nature. Moreover, the chiral amplification may also be used as an optical sensor to detect chiral molecules. The detection of chiral molecules is an important technique in the biomedical industry[227], since different enantiomers of chiral molecules have different effects on human body[228]. The birefringent patterns of chiral configurations from achiral LCLCs have a quick and sensitive response to the presence and the handedness of the external chiral enantiomers[158,159]. Compared with the current chiral detection using circular dichroism[227,229], the chiral configurations of LCLCs in our study require simpler experimental setup (a glass capillary), shorter response time (< 1min), and less volume of samples (~μL) to effectively detect chiral enantiomers with low concentrations (~0.2 wt%).

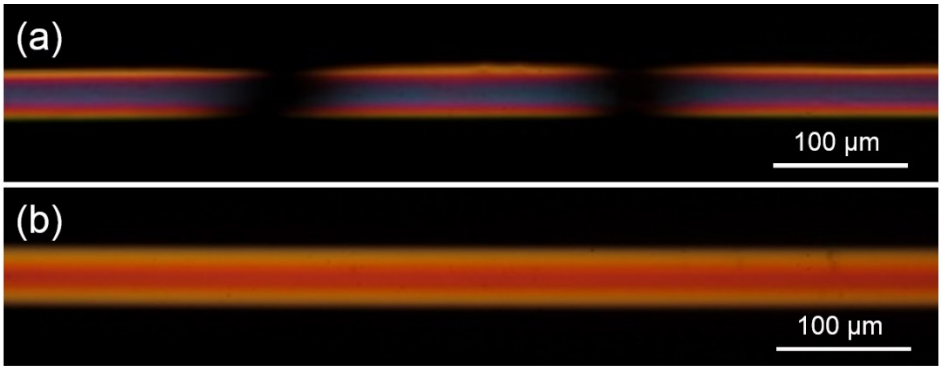

Figure 8.2 Polarized optical microscopy images of the DT configuration of DSCG in cylindrical capillaries with degenerate planar anchoring. (a) DSCG with no chiral dopant shows multiple domains with different handedness of twist distortions. (b) With the addition of 0.2 wt% L-alanine, the director of the DT configuration prefers left-handed twist deformation. The domains with right-handed twist are absent in the capillary. Images curtesy of collaborator, Sujin Lee.

8.2.2 The defects of LCLCs

For most of the situations in previous chapters, we restricted our analysis to continuous variation of the nematic director fields where Frank-Oseen elastic theory is applicable[64,65]. But there are situations where the director variation is not smooth and discontinuities exist as singular defects[55,230]. For instance, in cylindrical capillaries with degenerate planar anchoring, the adjacent domains of the DT configuration for SSY with opposite twist directions are separated by singular point defects (Figure 2.2e and 2.2f). In cylindrical capillaries with homeotropic anchoring, the TP configuration of LCLCs is featured by the two singular line defects twisting along the capillary axis (Figure 3.4). Discontinuity of the director field may also appear on the surface (boojum) as shown by the bipolar and the TB configurations of tactoids in Figure 5.2c and 5.2d.

Here we pay attention to the point defects observed with SSY upon heating the sample to the biphase region, wherein both nematic phase and isotropic phase are present. In Figure 8.3a, 1.0 M SSY solution was confined in a cylindrical capillary with homeotropic anchoring (coated with parylene-N) and the temperature of the sample was in the biphase temperature range close to the transition temperature, T_{BI} (T/T_{BI} = 0.995). The nematic domain of SSY exhibits multiple point defects with alternating topological charges (m) of +1 and -1 under the crossed polarizers. These point defects are visible in bright field as shown in Figure 8.3b, indicating the singularity of the defects[135]. The director fields surrounding the point defects are illustrated in Figure 8.3e. During the phase transition, the interface forms between the isotropic phase and nematic phase in the biphase temperature range. The isotropic phase emerges at the bottom and the nematic phase is on the top since the heat stage is placed under the cylindrical capillary. Alternating +1 and -1 point defects (boojums) locate on the interface between the two phases as illustrated in Figure 8.3e. It is

worth noting that in Figure 8.3a, the brushes of +1 boojums in the birefringent pattern are twisted but the brushes of -1 boojums are not. The twisted brushes indicate that the director field close to +1 boojums is chiral with the twist distortion to relieve the large energy contribution of the splay deformation. But the director field close to -1 boojums somehow refuses to twist. More interestingly, in a square capillary with homeotropic anchoring (Figure 8.3c), the boojums are pushed to the corners of the capillary, which indicates a response to the curvature of the geometry. We recommend performing theoretical energy analysis to understand the chirality around the point defects of LCLCs for future work. The saddle-splay elastic free energy should be considered in the analysis since it plays an essential role on the stability of topological defects[231-233].

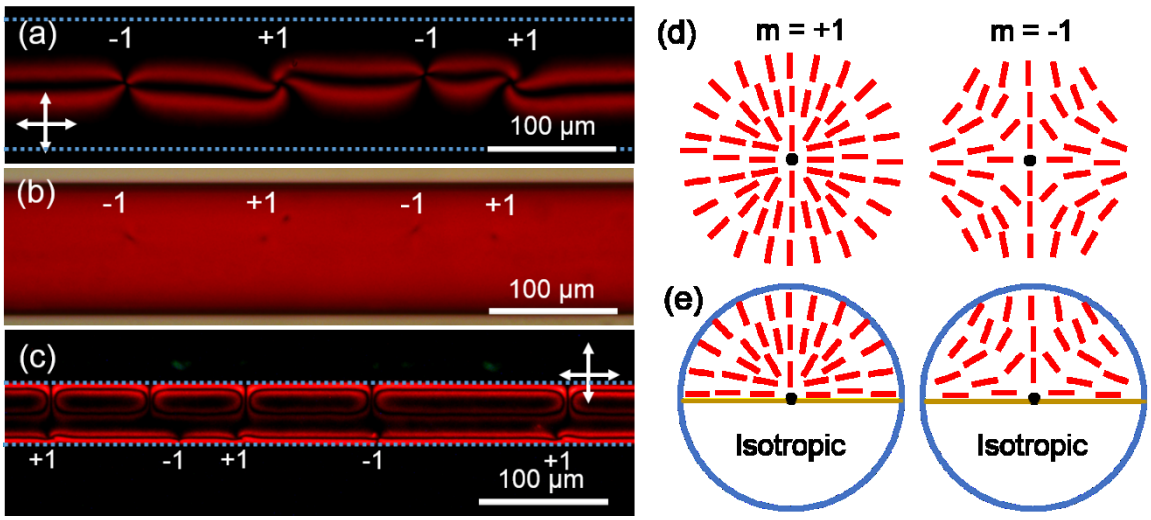

Figure 8.3 Polarized optical microscopy images of SSY in the biphase region in a cylindrical capillary with homeotropic anchoring. (a) is under crossed polarizers. (b) is under bright field. +1 and -1 show the boojums with alternating topological charges. (c) Polarized optical microscopy images of SSY in biphase region in a square capillary with homeotropic anchoring. The blue dotted lines in (a) and (c) indicate the inner surfaces of the capillaries. (d) Director fields illustrations of +1 and -1 point defects. The black dots represent singular point defects. The red rods represent nematic director. (e) Director fields illustrations of +1 and -1 boojums in biphase region in the cylindrical capillaries. The golden lines represent the interface between nematic and isotropic phases.

8.2.3 Characterization of the dimension and persistence length of LCLCs aggregates

The properties and macroscopic configurations of LCLCs are intrinsically determined by their aggregation behavior. As explained in Chapter 2, the temperature and concentration dependence of the saddle-splay elastic constants (K_{24}) suggests that K_{24} is related to the persistence length rather than the counter length of LCLC aggregates. The characterization of the persistence length for LCLC aggregates will be helpful to validate our expectations about the K_{24} model, which can be measured by small angle neutron scattering (SANS)[193,195]. Moreover, as discussed in Chapter 6 and Chapter 7, the monovalent salts may affect both the counter length and the persistence length of LCLCs aggregates[124,139,172] as indicated by the changes of transition temperatures and order parameters. SANS measurements of aggregates dimensions and persistence length can hopefully decipher the salts mechanism on the aggregation behaviour of LCLCs.

8.2.4 Rheology of LCLCs fluids under the effect of shear force

Isotropic fluids can have induced birefringence under the effect of shear force, which aligns the molecules at an angle between the velocity gradient and the direction of the flow (Figure 8.4a)[234]. Anisotropic uniaxial nematic fluids behave differently under the effect of shear force, which is described by Ericksen-Leslie theory[235-239]. The theory introduces six viscosity coefficients (α_i) to determine the hydrodynamics. But only two coefficients, α_2 and α_3, appear in the equation of the director under the shear flow[235-239]. The dependence of flow alignment angle (θ_0) on the coefficients can be expressed as a function of the tumbling parameter, λ_t [235-239]: $\theta_0 = 0.5cos^{-1}(1/\lambda_t)$, where $\lambda_t = \frac{\alpha_2 + \alpha_3}{\alpha_2 - \alpha_3}$.

The solution of θ_0 has three possibilities[240]: 1) $0 \geq \alpha_3 \geq \alpha_2$, $\lambda_t > 1$, flow aligned. 2) $\alpha_3 \geq 0 \geq \alpha_2$, $-1 < \lambda_t < 1$, tumbling. 3) $\alpha_3 \geq \alpha_2 \geq 0$, $\lambda_t < -1$, flow aligned.

The flow behavior of nematic fluids can be theoretically predicted based on Kuzuu and Doi's derivation[241-243] which correlates α_2 and α_3 with the aggregate dimension, the tumbling parameter, and the order parameters: $\alpha_2 = -\bar{\eta}L(a)(1+\frac{1}{\lambda_t}) < P_2 >$, $\alpha_3 = -\bar{\eta}L(a)(1-\frac{1}{\lambda_t}) < P_2 >$. Here, $\bar{\eta} = \frac{ck_BT}{2\overline{D_r}}$, where c is the number of molecules in unit volume, k_B is Boltzmann constant, T is the temperature, $\overline{D_r}$ is the rotational diffusion coefficient depending on the concentration, molecular weight, and temperature. Consequently, $\bar{\eta}$ is a positive parameter for nematics. $L(a) = \frac{a^2-1}{a^2+1}$, where a is the aspect ratio of the aggregates. $L(a)$ is also positive since a for nematics is larger than 1. λ can be expressed in terms of the 2nd and 4th order parameters[244]: $\lambda_t = L(a)\frac{5<P_2>+16<P_4>+14}{35<P_2>}$, which is also larger than zero since the order parameters of nematics are positive[245]. As a result, the sign of α_2 is negative for nematic fluids. Whether the fluids are flow aligning or non-flow aligning is determined by the sign of α_3.

The flow behavior of nematic polymer fluids has been investigated by the studies of Srinivasarao and Berry[246], Burghardt and Fuller[247], and Magda et al[248]. In Srinivasarao and Berry's experiments[246], polymer nematics were uniformly aligned between two glass slides, and the shear force was applied when one of the two glass slides was moved along the orientation of the director field (Figure 8.4a). The optical method has been developed to detect the director orientation induced by the shear force using the conoscopy patterns[249]. Normally in the orthoscopy mode of the optical microscope, when the sample is placed on

the front focal plane of the objective, the light transmitting through the sample is collected by the objective and then converted to the magnified virtual image by the eye piece[250]. In the conoscopy mode, the light collected by the objective is observed on the back focal plane using a Bertrand lens[114]. Due to the birefringence, the beams transmitting through the nematic sample from various angles exhibit interference pattern on the back focal plane of the objective[37], which reveals the changes of the director orientations under the effect of shear force. As shown in Figure 8.4b, when the director is perfectly aligned in the horizontal direction, the center of the interference pattern should be in the center of the back focal plane. But when the director is tilted under the effect of shear flow, the center of the interference pattern will move to the left side or the right side accordingly.

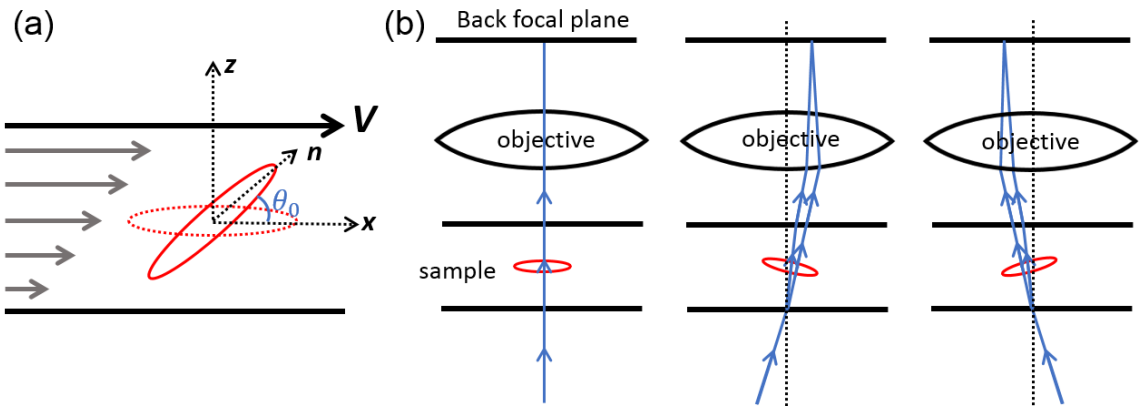

Figure 8.4 (a) Illustration of a rod-like molecule under the shear force. x is the direction of shear force. z is the direction of velocity gradient. $\boldsymbol{n}$ is the director. θ_0 is the flow alignment angle. (b) Schematics of conoscopy system of the microscope. The red rods represent the director orientations in the samples. The blue arrows represent the optical path of a light in the center of the conoscopy system. The left image shows that when the director is uniformly aligned perpendicular to the optical path, the center of the interference pattern is in the center of the back focal plane. The middle and right images show that when the director is tilted, the centers of the interference patterns are deviated to the right and left sides of the back focal plane.

With the order parameters of SSY measured by depolarized Raman spectroscopy, the theoretical predictions of the flow behavior have been performed by Xuxia Yao[212]. The

results suggest that 1.10 M and 1.25 M SSY solutions are not flow-aligning ($\alpha_3 \geq 0 \geq \alpha_2$, $-1 < \lambda_t < 1$)[212]. The shear-flow experiments need to be performed to validate these predictions. For preliminary explorations, we prepared the uniformly aligned 1.10 M SSY cells with the thickness of 190 μm by confining the solutions between glass slides rubbed with abrasive paper[94]. The sides of the SSY cells were sealed by silicon oil, which allows the glass slides to move while preventing the evaporation of water. As shown in Figure 8.5a and 8.5b, the uniformly aligned SSY sample exhibits extinction of transmitted light under crossed polarizers when the rubbing direction is parallel (or perpendicular) with the polarizers. The domain shows transmitted intensity when the polarizers are rotated by 45^o with the rubbing direction. The uniformly aligned SSY monodomain results in the conoscopy interference pattern in Figure 8.5c. When the top glass slide is moved along the director orientation with a velocity of 1.7 μm/s (automatically controlled by a syringe pump) to the right side, the center of the interference pattern moves to the right as shown in Figure 8.5d. (Here we note that the left and right sides of the conoscopy pattern are inverted by the lens system when directly observing the pattern from the eye piece with the Bertrand lens. However, the pattern is inverted again when captured by the camera in our experimental setup. Hence, the position of the center captured in the image is inverted twice back to the real position of the center in the conoscopy pattern.) This deviation of the center in the conoscopy pattern indicates that 1.10 M SSY solution is not flow aligning, which is consistent with the prediction by Yao[212].

As the future work, the rheology of SSY fluids needs to be explored with different SSY concentrations, temperatures, and shear velocities. It will also be interesting to study the flow behavior of DSCG and other LCLCs if the monodomains of these materials can

be prepared. Additionally, a better experimental setup should be designed to precisely align the orientation of shear force parallel with orientation of director field. The mismatch of the two orientations as small as 2° can lead to a twist in the conoscopy pattern or completely destroy the conoscopy pattern[249].

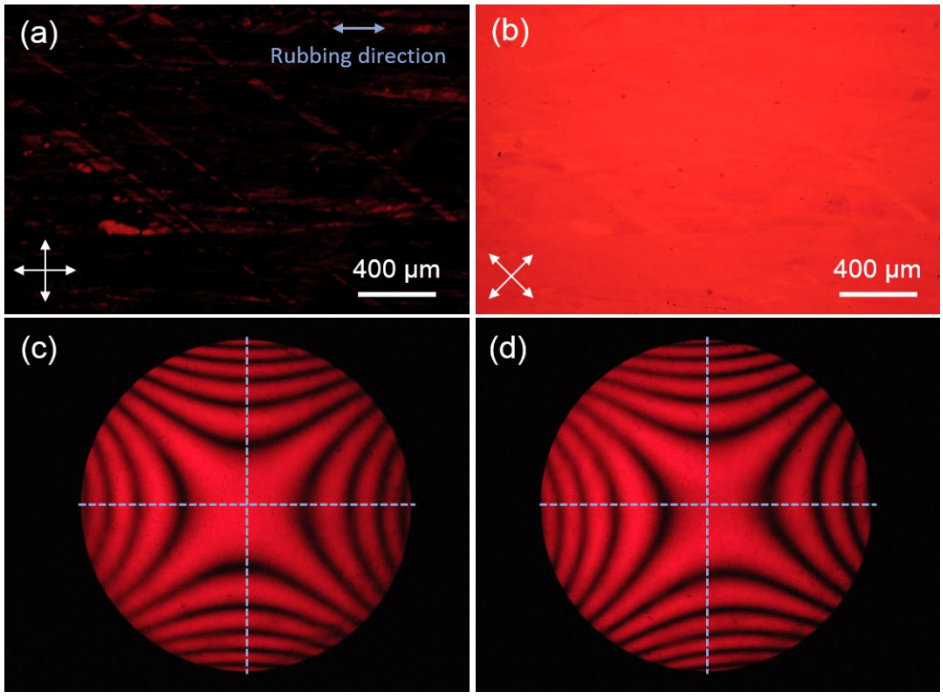

Figure 8.5 (a, b) Polarized optical microscopy images of SSY between two glass slides rubbed by abrasive paper. (a) The rubbing direction is parallel with the polarizer. (b) The rubbing direction is at 45° with the polarizer. (c) The conoscopy pattern of a uniformly aligned 1.10 M SSY with no shear force. The thickness of the cell is around 190 μm. The blue dashed lines indicate the horizontal and vertical diameters of the viewing circle. The crossing point of the blue dashed lines show the center of the viewing circle. (d) The conoscopy pattern of 1.10 M SSY under the effect of shear force.

APPENDIX A. SUPPORTING INFORMATION

A.1 Supporting information for Chapter 2

A.1.1 Morphology of inner surface of cylindrical capillaries

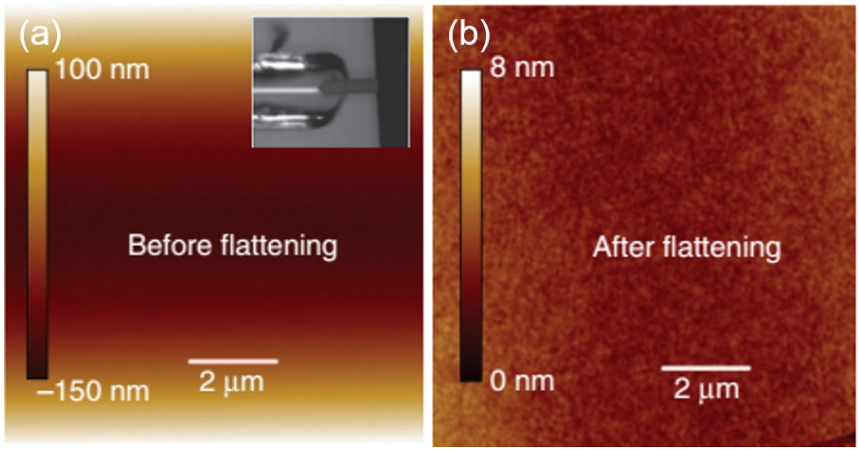

Figure A.1 Atomic force microscopy (NanoScope, BRUKER) images of the inner surface of a borosilicate cylindrical capillary. The images were obtained by directly scanning the inner surface of the capillary as shown by the inset of (a). After flattening the image, (b) shows no patterns on the surface that may align the director of nematic liquid crystals. Image curtesy of collaborators, Dr. Jinxin Fu, Dr. Nabil Kleinhenz, and Dr. Karthik Nayani[7].

A.1.2 Wave-guiding experiments to measure the twist angle of the doubly-twisted (DT) configuration

The twist angle of the DT configuration from the center to the boundary of the cylinder is measured by wave-guiding experiments. When the Mauguin limit is satisfied[114] (the total twist angle of the director field, 2Φ, is much smaller than the retardation of polarized light due to the birefringence of nematics, $2\Phi \ll \Gamma = \frac{2\pi}{\lambda}(n_e - n_o)d$), the polarization of the light follows the twist deformation in the director field if the incident

polarization matches the director orientation on the entrance surface. Hence the twist angle can be measured by the transmitted intensity at the center of the capillary with different polarizer and analyzer combinations. The transmitted intensity is measured by the polarized optical microscopy images under monochromatic illumination (486 nm). The polarizer is rotated every 5° from 0° through 180° (horizontal direction). At every polarizer angle, the analyzer is also rotated from -90° to 90° (vertical direction). For 14 wt% DSCG solution, the maximum and minimum transmitted intensities at every polarizer angle when the analyzer is rotated are plotted in Figure A.2a. The highest maximum and the lowest minimum transmitted intensities emerge when the polarizer angle is 75°, corresponding to the situation that the polarizer angle matches the director at the bottom surface of the cylinder. When the polarizer is fixed at 75°, the transmitted intensities of every analyzer angle are plotted in Figure A.2b. The extinction of transmitted light emerges when the analyzer angle is 15°, which is perpendicular with the director on the top surface of the cylinder. Hence, the twist angle from the center to the boundary is measured as 75° ± 5°.

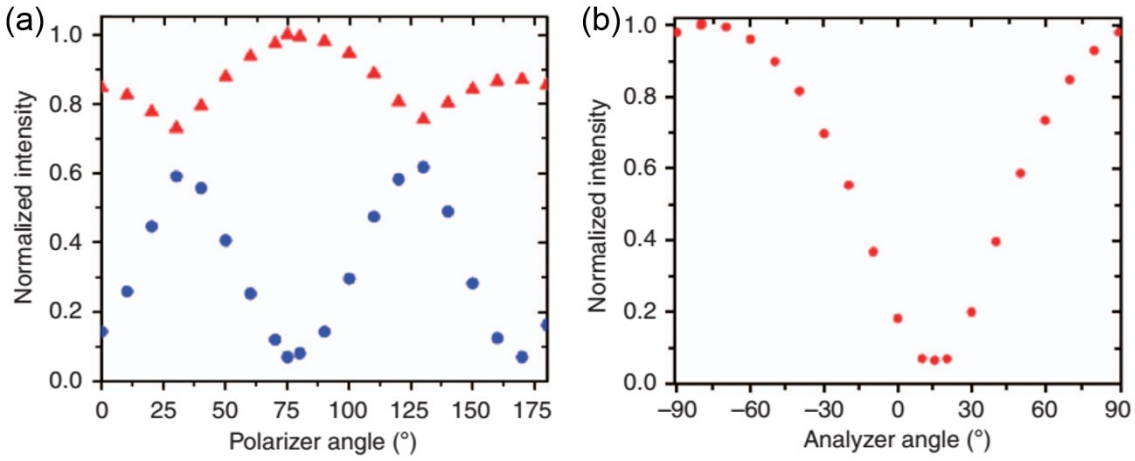

Figure A.2 (a) The maximum (red triangles) and minimum (blue circles) transmitted intensities at every polarizer angle. (b) The transmitted intensities at every analyzer angle when polarizer is fixed at 75°.[7]

Due to the small birefringence of DSCG[218] ($\Delta n = -0.02$), the twist angle was measured in cylinders with the inner diameters of 200 μm to 500 μm to meet the requirement of Mauguin limit[114]. With the birefringence of -0.02 for DSCG and cylinders inner diameter of 200 μm, the retardation is $\left|\frac{2\pi}{\lambda}\Delta nd\right| = \left|\frac{2\pi}{0.486\ \mu m}(-0.02) \times 200\ \mu m\right| = 51.5$ rad, which is much larger than the total twist angle through the capillary ($2 \times 75^o = 150^o = 2.6$ rad). For SSY solutions, the twist angle can be measured in cylinders with the inner diameters of 50 μm to 500 μm due to the large birefringence[251] ($\Delta n = -0.08$) The measured twist angle for both LCLC solutions does not show any dependence on the capillary size.

A.1.3 K_{33}/K_{22} of DSCG reported in literature[93]

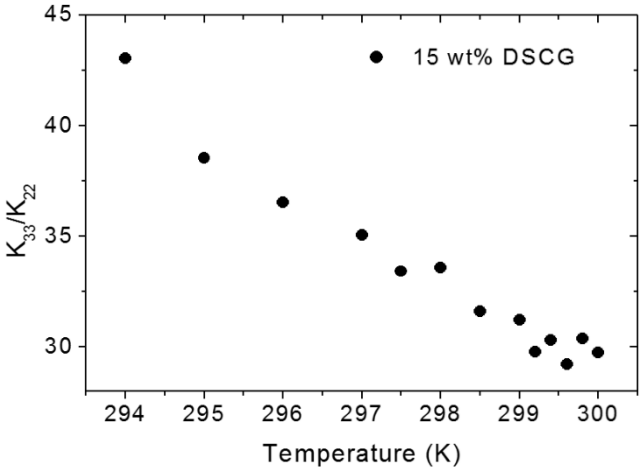

Figure A.3 *K_{33}/K_{22}* as a function of temperature for 15 wt% DSCG reported by Nastishin et al.[93].

A.2 Supporting information for Chapter 3

A.2.1 The density of SSY solutions

The densities of SSY solutions were measured at room temperature (22 °C) with different concentrations. The weights of 500 μL SSY solutions were measured and the densities were calculated as weight/volume.

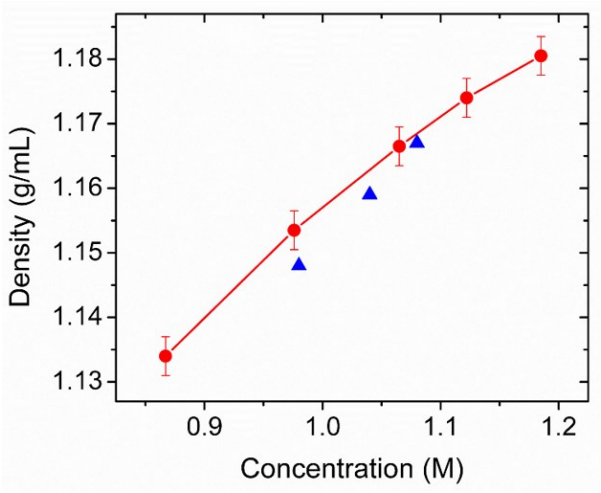

Figure A.4 The density of SSY solutions as a function of the concentration. The red circles are the data of our measurements at 22 °C. The blue triangles are the data from the literature[94].

A.2.2 Discussions about the stability of the doubly-twisted (DT) domains in parylene-N coated cylindrical capillaries with high SSY concentrations.

With high SSY concentrations (> 1.15 M), we observed both TER and DT domains co-existing in the parylene-N coated cylindrical capillaries after heating to isotropic phase and quenching back to nematic phase. Intuitively, the emergence of the DT domains can be attributed to the non-uniform deposition of parylene-N film on the inner surface of the capillaries. However, this explanation does not agree with our observations that when the capillary was filled with nematic SSY solution, the TER birefringent pattern was initially exhibited throughout the cylinder before heating to isotropic phase. After heating and quenching, the DT domains can randomly locate at any regions of the cylinder for high

concentrations. Moreover, the temperature range in our experiments is 10 to 100 ºC, which is not high enough to cause the degradation of parylene-N (the temperature required for parylene-N to degrade is higher than 270 ºC [146,252]). Additionally, the DT domains does not emerge for low SSY concentrations in parylene-N coated capillaries. Hence, we ruled out the possibility of the non-uniform parylene-N alignment film which may lead to the emergence of the DT domains.

Furthermore, the DT domains only emerges in parylene-N coated cylinders after heating to isotropic phase and quenching back to nematic phase, which might be due to the removal of capillary flow effects. Another possibility is the decrease of anchoring strength with the increase of temperature as explored with thermotropic nematics effects[253,254]. The temperature dependence of anchoring strength of LCLCs need to be investigated to validate this explanation, which is beyond the discussion of this work. Once the DT domains arise, cooling back to room temperature or aging the sample does not drive the DT domains back to the TER configuration, possibly due to the large energy barrier between the two configurations.

A.2.3 Twist angle measurements of the doubly-twisted configuration in parylene-N coated cylindrical capillaries and uncoated cylindrical capillaries.

The twist angle of the DT configuration of SSY was measured by the waveguiding experiments as described in Appendix A.1.2. For high SSY concentration (1.18 M), the transmitted intensities of a DT domain in a parylene-N coated cylindrical capillary (in co-existence with the TER domains) are plotted in Figure A.5 with different polarizer and analyzer combinations. The lowest transmitted intensity is exhibited with the polarizer

angle at 70° and analyzer angle at 20°, corresponding to the twist angle of 70° in the DT director field. Figure A.6 shows the birefringent pattern and the waveguiding experiment data of the DT configuration for 1.18 M SSY in an uncoated borosilicate cylindrical capillary. The lowest transmitted intensity is exhibited with the polarizer angle at 90° and analyzer angle at 0°, corresponding to the twist angle of 90° in the DT director field.

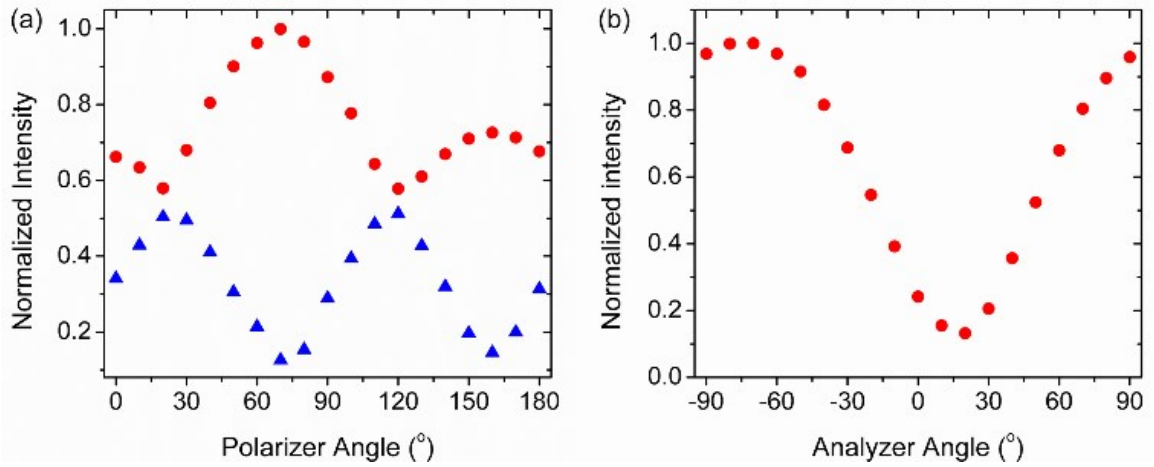

Figure A.5 Waveguiding experiment data of the DT domains in parylene-N coated cylindrical capillaries. The concentration of SSY is 1.18 M. (a) The maximum (red circles) and minimum (blue triangles) transmitted intensities at every polarizer angle. (b) The transmitted intensities at every analyzer angle when polarizer is fixed at 70°.

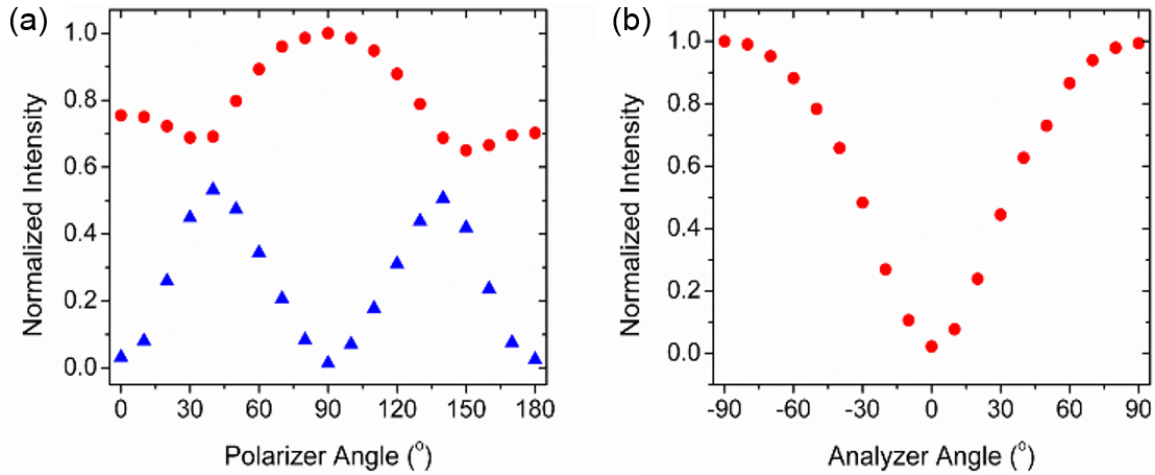

Figure A.6 Waveguiding experiment data of the DT domains in a borosilicate cylindrical capillary free of any coating. The concentration of SSY is 1.18 M. (a) The maximum (red circles) and minimum (blue triangles) transmitted intensities at every polarizer angle. (b) The transmitted intensities at every analyzer angle when polarizer is fixed at 90°.

A.3 Supporting information for Chapter 4

A.3.1 Surface morphology of parylene-N coating on the glass substrate

The director configurations can be affected if the surface of parylene-N coating on the inner capillary wall has micropatterns that may lead to the alignment of the director on the surface. We ruled out this possibility by characterizing surface morphology of parylene-N film using atomic force microscopy (AFM, NanoScope, BRUKER). The parylene-N surface coating on the inner wall of cylindrical capillaries cannot be characterized directly because breaking the capillaries would destroy the surface morphology. Hence, we examined the parylene-N film coated on a flat borosilicate glass slide by chemical vapor deposition under the same condition (see Appendix A.7.2). As shown in Figure A.7, the parylene-N film surface exhibits no visible features that might align the director on the surface. Both the height image and the phase image show a smooth surface with small roughness (2.7 nm and 1.3°, respectively)

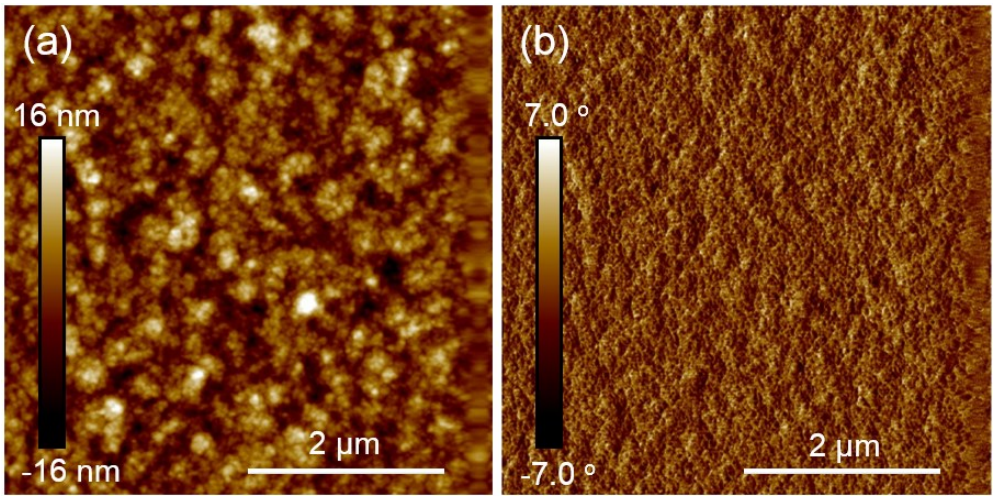

Figure A.7 (a) Height image and (b) phase image of a parylene-N film coated on a flat borosilicate substrate. Both height and phase images do not show visible patterns that may align the director on the surface. The roughness of the surface measured by the height and the phase images are 2.7 nm and 1.3°, respectively.

A.4 Supporting information for Chapter 5

A.4.1 Twist angle measurement of the twisted bipolar (TB) director field for SSY tactoids

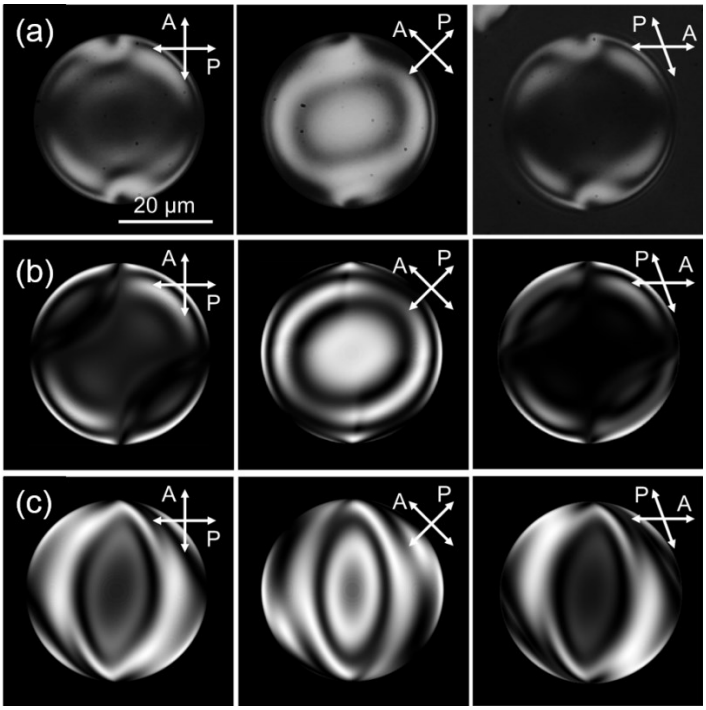

Figure A.8 (a) Polarized optical microscopy images of an additive-free twisted-bipolar (TB) tactoid. The left and middle images were captured between crossed polarizers. The right image shows the extinction of transmitted light at the center when the angle between polarizer and analyzer is 70°. (b) and (c) are the simulated images of a TB tactoid with the twist angle of 20° and 160°, respectively. The birefringence of -0.08 and the radius of 20 μm were used in the simulation. P and A indicate the orientations of polarizer and analyzer.

The twist angle of the TB tactoids is measured by wave-guiding experiments. As aforementioned, the wave-guiding requires that the retardation of polarized light is much larger than the twist angle of the director field[37]. For a typical SSY tactoid with the radius of 20 μm in Figure A.8, we used monochromatic illumination of 589 nm and took the birefringence value of $\Delta n =$ -0.08[138]. (For SSY, we cannot use monochromatic illumination of 486 nm for wave-guiding experiments as for DSCG, since SSY has strong absorption of light with the wavelength of 450 ~ 530 nm[138].) The shape of the additive-free

SSY tactoids is a hemisphere attached to the flat surface because the contact angle of tactoids is around 90° (Figure 5.9d). For SSY + PEG tactoids, the shape is approximated as a sphere when the contact angle is as large as 150° (Figure 5.9c). For an additive-free tactoid, the retardation is $|\Gamma| = \left|\frac{2\pi}{\lambda}\Delta nd\right| = \left|\frac{2\pi}{0.589\ \mu m}(-0.08) \times 20\ \mu m\right| = 17$ rad, which is much larger than the maximum twist angle through the tactoids ($\emptyset = 125^o = 2.2$ rad). In this situation, the polarization of incident light is guided by the twist deformation of the director field. Hence, the center of the TB tactoids exhibit transmitted intensity under crossed polarizers as shown in the left and middle images of Figure A.8a. The extinction of transmitted intensity occurs when the analyzer is horizontal and polarizer is oriented at 70° (the right image of Figure A.8a). This combination of polarizer and analyzer indicates that the director on the bottom tactoidal surface is parallel with the polarizer direction and the director on the top capillary wall is perpendicular to the analyzer direction. The corresponding twist angle can be either 20° or 160° for different twist directions. From the numerical calculation in Figure 5.7, a twist angle of 160° is not reasonable for the TB tactoids. We also performed Jones matrix simulation (see Appendix A.7.5) to determine the twist angle by the calculated birefringent pattern using the TB director field expressed as equation A.1[27].

$$n_{TB} = \left\{-\frac{zr\cos\left(\alpha_0\frac{r}{\sqrt{1-z^2}}\right)}{\sqrt{z^2r^2+(1-z^2)^2}}, sin\left(\alpha_0\frac{r}{\sqrt{1-z^2}}\right), \frac{(1-z^2)\cos\left(\alpha_0\frac{r}{\sqrt{1-z^2}}\right)}{\sqrt{z^2r^2+(1-z^2)^2}}\right\} \quad (A.1)$$

where r is the radial position in cylindrical coordinates, z axis is along the bipolar axis, α_0 is the twist angle. The simulated textures of the TB tactoids with the twist angles of 20° and 160° are present in Figure A.8b and A.8c, respectively. The textures of the TB tactoids

with the twist angle of 20° are similar as those observed in Figure A.8a. Hence, the twist angle of this tactoid is 20°.

A.4.2 Columnar SSY tactoids with the addition of PEG

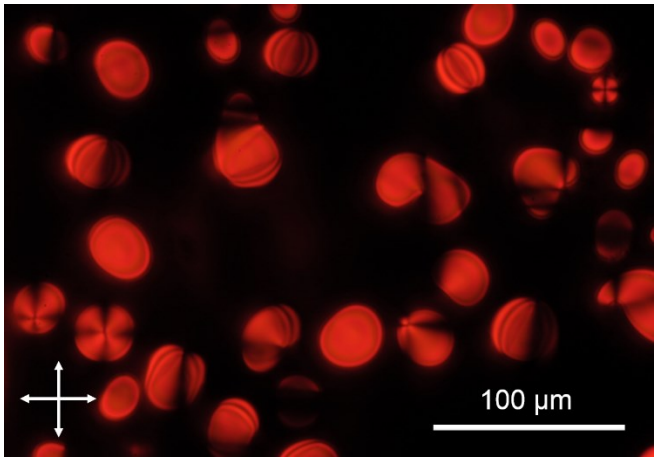

Figure A.9 Columnar SSY tactoids with the addition of PEG. The concentration of SSY is 1.09 M (37.9 wt%). The concentration of PEG is 2 wt%. The observation temperature is 38.6 °C.

A.5 Supporting information for Chapter 6

A.5.1 The effects of LiCl and KCl on transition temperatures (T_{BI} and $T_{biphase}$) of SSY.

Figure A.10 presents the transition temperature, T_{BI}, and the biphase temperature range, $T_{biphase}$, at different concentrations of SSY and monovalent salts (LiCl and KCl). The dependence of T_{BI} on the SSY concentration and salt concentration shows similar tendencies as the dependence of the other transition temperature, T_{NB} (Chapter 6.3.1, Figure 6.3). Like the effect of NaCl (Figure 6.3b), $T_{biphase}$ becomes larger under the effects of LiCl and KCl. The increase of $T_{biphase}$ is more significant by salts with larger cations.

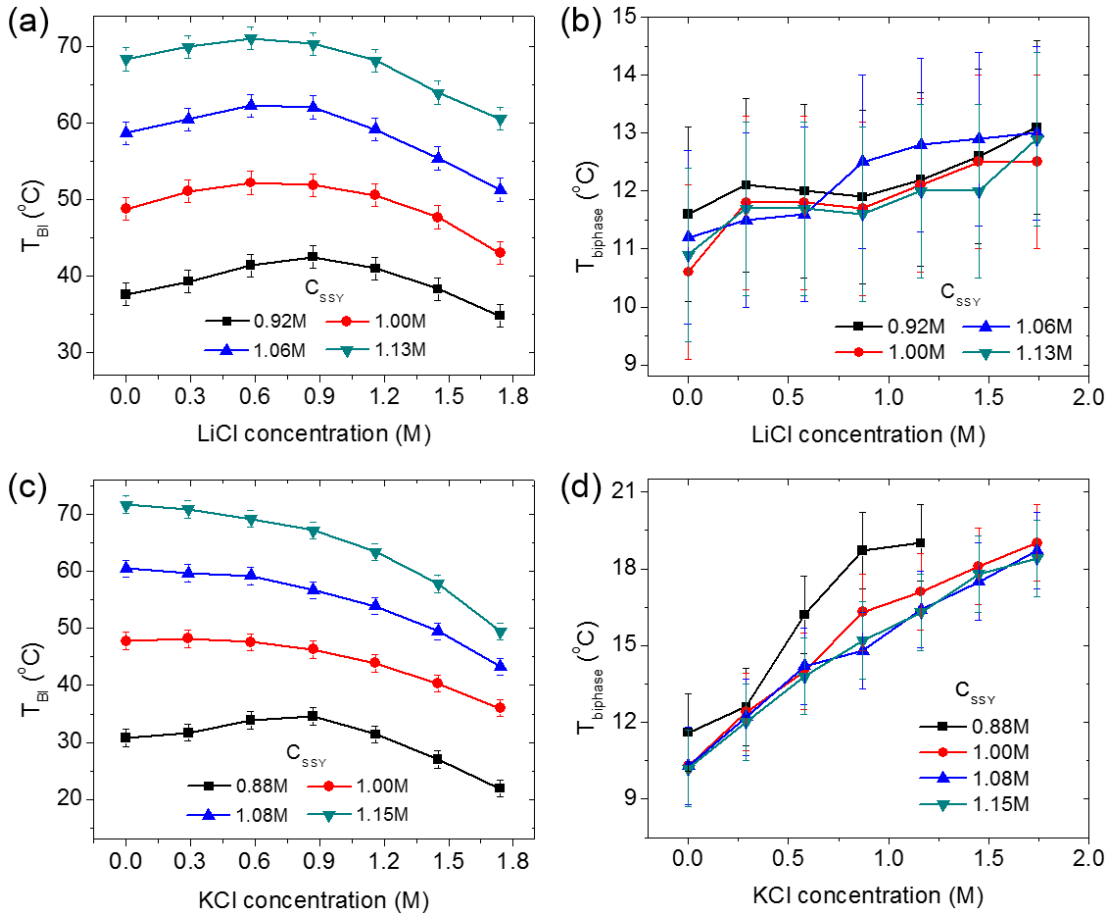

Figure A.10 The dependence of the transition temperature (T_{BI}) and the biphase temperature range ($T_{biphase}$) on the concentrations of SSY and monovalent salts. The monovalent salt of (a) and (b) is LiCl. The monovalent salt of (c) and (d) is KCl.

A.5.2 The effects of various monovalent salts on shifts of SSY transition temperatures (T_{NB}, T_{BI} and $T_{biphase}$) for fixed salts concentrations

Figure A.11 presents the shift of the transition temperature, ΔT_{NB}, and the shift of the biphase temperature range, $\Delta T_{biphase}$, at different SSY concentrations and fixed salts concentrations (1.16 M and 1.74 M). The effects of monovalent salts with different cations and anions were studied. The dependences of ΔT_{NB} and $\Delta T_{biphase}$ on the SSY concentration, salt cations, and salt anions are similar for different salts concentrations of 0.58 M (Figure 6.4), 1.16 M (Figure A.11a, b), and 1.74 M (Figure A.11c, d).

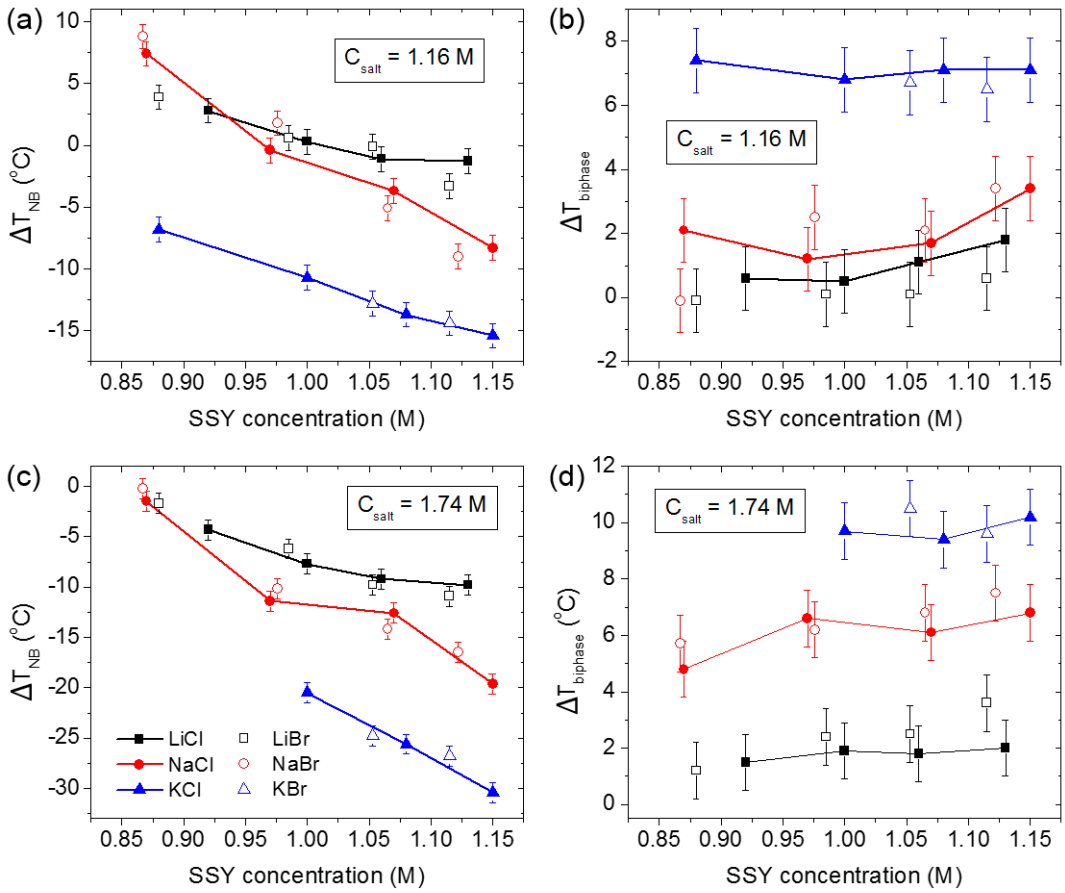

Figure A.11 The dependence of ΔT_{NB} and $\Delta T_{biphase}$ on SSY concentration and monovalent salts with different cations and anions. The salts concentrations are fixed at (a, b) 1.16 M and (c, d) 1.74 M.

A.6 Supporting information for Chapter 7

A.6.1 The effects of monovalent salts on SSY order parameters.

Figure A.12 presents the temperature dependence of the order parameters of SSY + LiCl for a fixed SSY concentration (1.06 M) when LiCl concentration is varied, and a fixed LiCl concentration (1.45 M) when SSY concentration is varied. Figure A.13 and Figure A.14 show the order parameters of SSY + NaCl and SSY + KCl, respectively. These data indicate that the effects of LiCl, NaCl, and KCl on SSY order parameters are similar as described in Chapter 7.3.2.

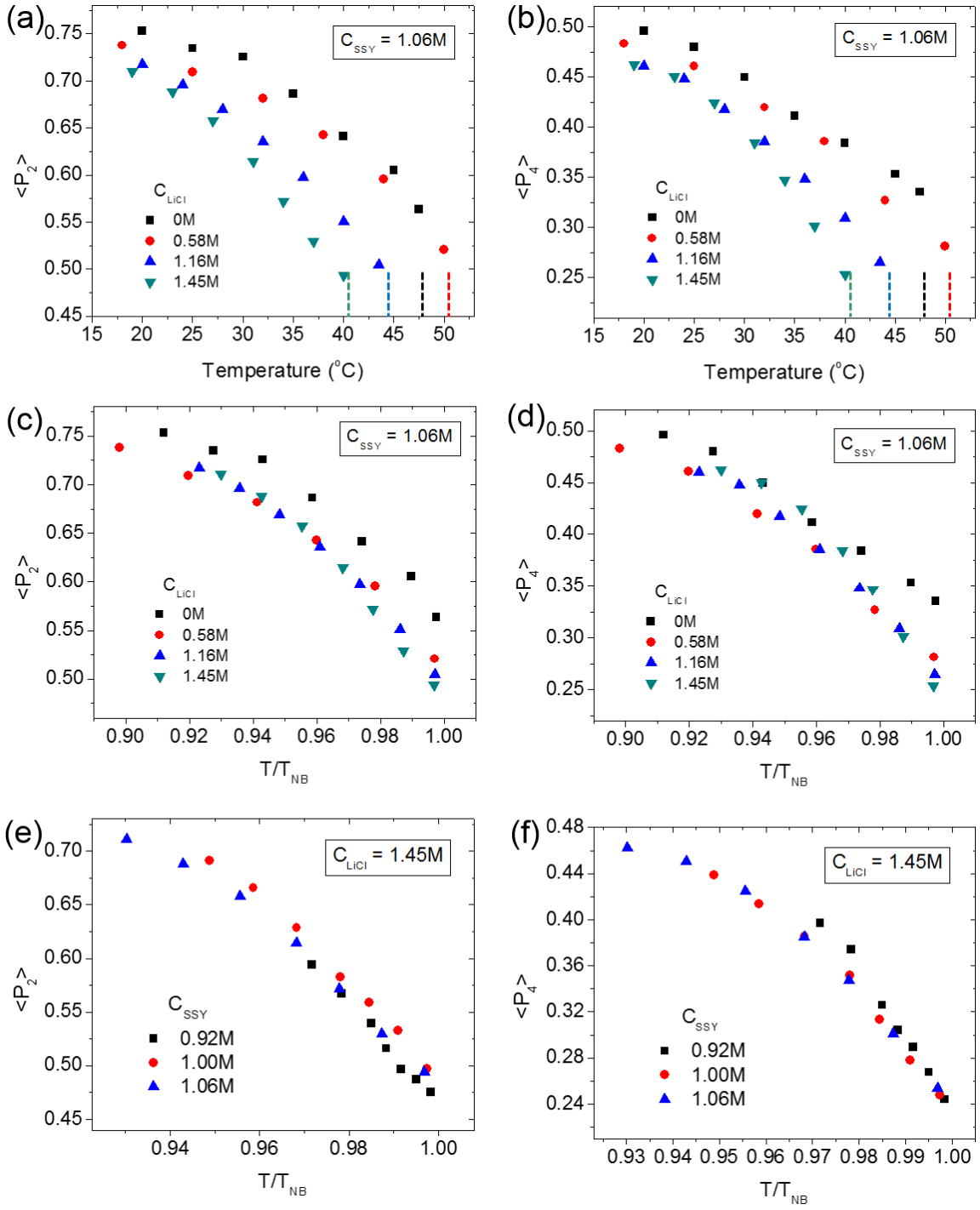

Figure A.12 (a, b) The 2nd and 4th order parameters of SSY + LiCl solutions for different LiCl concentrations as a function of temperature. The SSY concentration is fixed at 1.06 M. The dashed lines represent the transition temperature, T_{NB}. (c, d) The 2nd and 4th order parameters of SSY + LiCl solutions for different LiCl concentrations as a function of reduced temperature, T/T_{NB}. The SSY concentration is fixed at 1.06 M. (e, f) The 2nd and 4th order parameters of SSY + LiCl solutions for different SSY concentrations as a function of reduced temperature, T/T_{NB}. The LiCl concentration is fixed at 1.45 M.

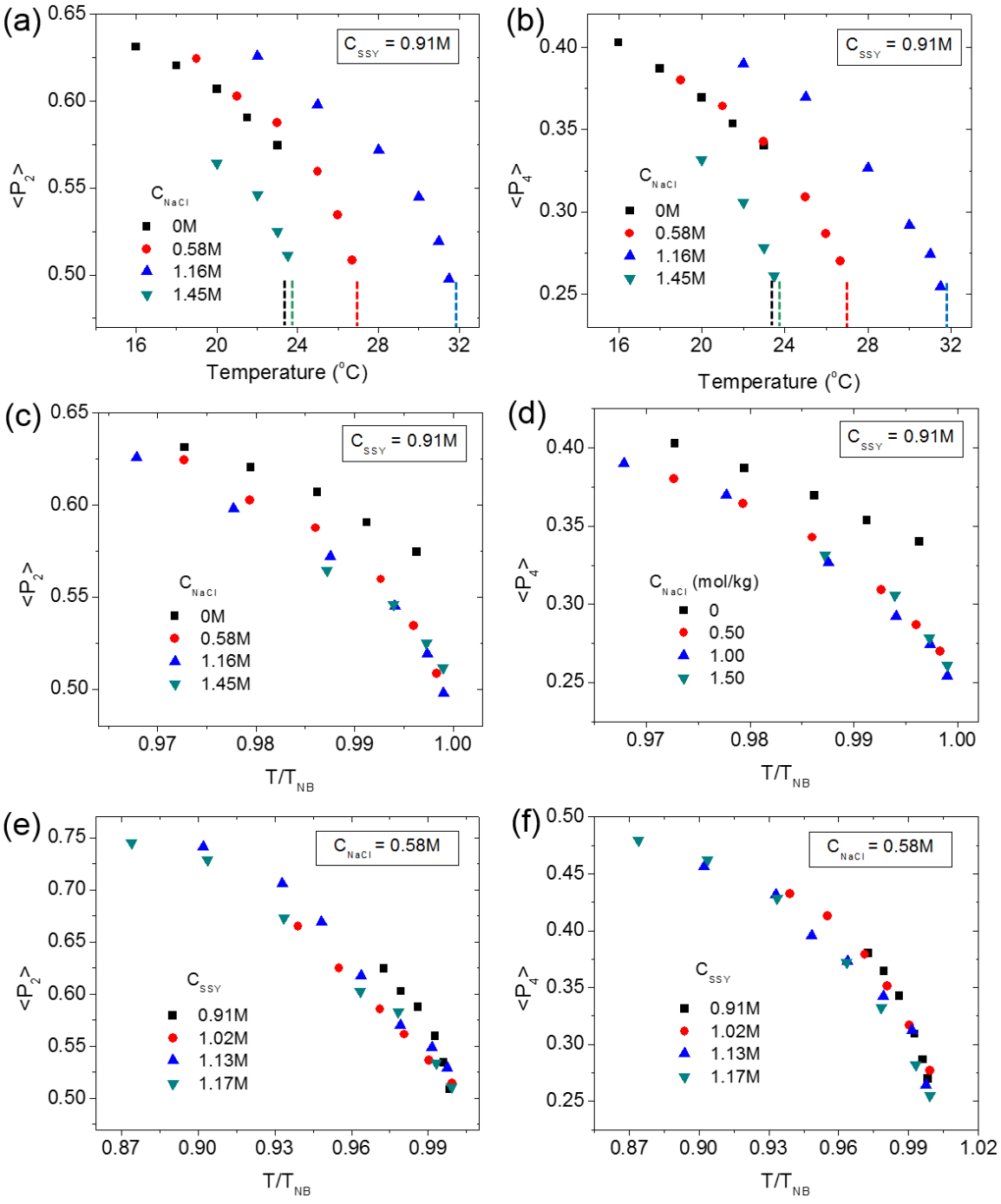

Figure A.13 (a, b) The 2nd and 4th order parameters of SSY + NaCl solutions for different NaCl concentrations as a function of temperature. The SSY concentration is fixed at 0.91 M. The dashed lines represent the transition temperature, T_{NB}. (c, d) The 2nd and 4th order parameters of SSY + NaCl solutions for different NaCl concentrations as a function of reduced temperature, T/T_{NB}. The SSY concentration is fixed at 0.91 M. (e, f) The 2nd and 4th order parameters of SSY + NaCl solutions for different SSY concentrations as a function of reduced temperature, T/T_{NB}. The NaCl concentration is fixed at 0.58 M.

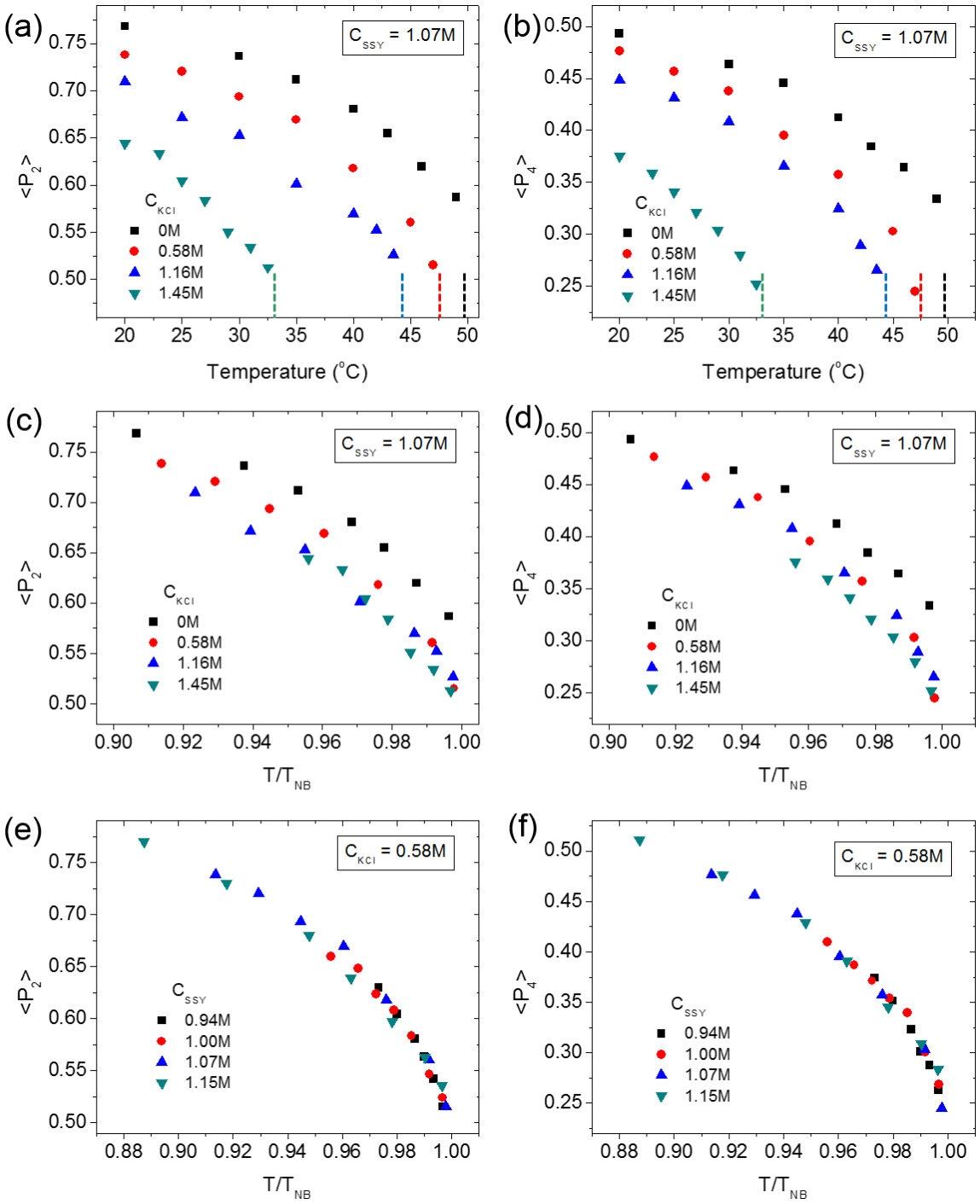

Figure A.14 (a, b) The 2nd and 4th order parameters of SSY + KCl solutions for different KCl concentrations as a function of temperature. The SSY concentration is fixed at 1.07 M. The dashed lines represent the transition temperature, T_{NB}. (c, d) The 2nd and 4th order parameters of SSY + KCl solutions for different KCl concentrations as a function of reduced temperature, T/T_{NB}. The SSY concentration is fixed at 1.07 M. (e, f) The 2nd and 4th order parameters of SSY + KCl solutions for different SSY concentrations as a function of reduced temperature, T/T_{NB}. The KCl concentration is fixed at 0.58 M.

A.7 Materials and methods

A.7.1 Materials

SSY was purchased from Sigma Aldrich with a purity of 90.0 wt% and was further purified by the twice-precipitation method before use, following the method in the literature[138,255]. The purified SSY powder was dissolved in deionized water to make solutions of different concentrations. DSCG was purchased from Sigma Aldrich with a purity > 99.0 % and used without any further purification. 5CB was purchased from Heibei Maison Chemical Co. with a purity > 99.7% and was used without any further purification.

N, N-dimethyl-*N*-octadecyl-3-aminopropyl trimethoxysilyl chloride (DMOAP) was purchased from Sigma Aldrich to induce the homeotropic anchoring for DSCG[143]. DMOAP is dissolved in methanol with the concentration of 42 wt% as received. In the dip coating, DMOAP solution was diluted by methanol to the concentration of 0.1 wt%. Lecithin (granular) was purchased from Acros Organics to induce the homeotropic anchoring for 5CB[256]. In the dip coating, lecithin was dissolved in hexane (98.5 wt% purity, BDH) with the concentration of 0.1 wt%.

The two PBG enantiomers, Poly-γ-benzyl-L-glutamate and Poly-γ-benzyl-D-glutamate, were purchased from Sigma Chemical Co. To make racemic solutions, the two enantiomers were mixed by 50:50 wt% and dissolved in a solvent mixture of 18% 1,4-dioxane, 82% dichloromethane, and a few drops of N,N-dimethylformamide[118]. 1,4-dioxane was purchased from Fisher Scientific with the purity of 99.9%. Dichloromethane and N,N-dimethylformamide were purchased from Sigma-Aldrich with the purities of 99.8% and 99.0 %, respectively. All the materials were used without further purification.

PEG was purchased from Sigma Aldrich with average molecular weight of M_w = 1500. LiCl was purchased from EMD Millipore. NaCl, LiBr, NaBr, and KBr were purchased from Sigma Aldrich. KCl was purchased from Alfa Aesar. All the salts have the purity > 99.0% and were used without further purification.

A.7.2 Sample preparations

The borosilicate cylindrical, square, and rectangular capillaries were purchased from Vitrocom. Nematic solutions were sucked into capillaries by a syringe. The two ends of capillaries were sealed with silicone grease and epoxy to prevent solvent evaporation. The nematic aqueous solutions of SSY and DSCG sealed in the capillaries are stable for at least one month until the phase transition occurs due to the slow water evaporation. PBG solutions sealed in the capillaries are stable for at least 5 days due to the use of volatile organic solvents.

Flat cells of liquid crystals were prepared by sandwiching the nematic solutions between two glass slides. The distance between the two slides was controlled by the glass capillaries or glass coverslips as spacers. The edges of the slides also were sealed by silicone grease and epoxy to prevent solvent evaporation.

Degenerate planar anchoring is achieved in the borosilicate glass capillaries/cells free of any coating for SSY, DSCG, and 5CB. PBG on borosilicate surface exhibits homeotropic anchoring. The planar anchoring of PBG and the homeotropic anchoring of SSY can be induced by the parylene-N film coated on both the outer and inner walls of capillaries by chemical vapor deposition[134]. The coating process ran in a commercial SCS parylene coater (PDS 2010) at room temperature of 22 ^{o}C under the vacuum of 55 mTorr.

The homeotropic anchoring of 5CB is achieved by dip coating the glass capillaries with lecithin[256]. The homeotropic anchoring of DSCG can be induced by *N, N*-dimethyl-*N*-octadecyl-3-aminopropyl trimethoxysilyl chloride (DMOAP)[143]. But after around 24 hrs, the anchoring transition occurs from homeotropic anchoring to planar anchoring.

A.7.3 Polarized Optical Microscopy

The birefringent patterns of liquid crystal samples were observed between a polarizer and an analyzer by Leica DMRX microscope. The Leica objectives with 100x (NA = 0.75), 20x (NA = 0.4), 10x (NA = 0.3) and 4x (NA = 0.15) were used to capture polarized optical microscopy images. The temperature of the samples is controlled by Linkam T95-PE heat stage with an accuracy of 0.1 ^{o}C mounted on the 360^{o} rotation stage. Conoscopy patterns were captured using a Bertrand lens with the objective of 100x (NA = 0.75) and the light source of Helium-Neon laser at 632.8 nm, 400 Hz.

A.7.4 Raman Spectroscopy

For Raman scattering measurements, a Kaiser Raman RXN1-785 system was used, equipped with a 785 nm diode laser, a microscope with two polarizers and a 50× objective attached to the fiber optic probe head. The sample temperature was controlled by a Linkam T95-PE heat stage with an accuracy of 0.1 ^{o}C mounted on the 360^{o} rotation stage.

A.7.5 Jones Matrix Simulation

Jones matrix simulation was applied in our work to investigate the birefringent patterns of uniaxial nematic liquid crystals under polarized light. The polarization of the light transmitting through the birefringent material is described by Jones calculus as

discovered by R. C. Jones in 1941 [257]. The polarization state of the light is represented by a Jones vector with two components, and the effect of each optical element is represented by a 2 × 2 Jones matrix.

The polarization state of the incident light can be expressed by Jones vector[257] as $\boldsymbol{V} = \begin{pmatrix} V_x \\ V_y \end{pmatrix}$, where V_x and V_y are two complex numbers, *x* and *y* are the fixed axes of the experimental system. For instance, the linearly polarized incident light can be expressed as[37] $\begin{pmatrix} cos\phi \\ sin\phi \end{pmatrix}$, where ϕ is the angle between polarization direction and *x* axis. To determine the polarization state of the light transmitting through the birefringent material, we need to decompose the light into two components along the slow axis and the fast axis of the nematic liquid crystals. The decomposition is accomplished by coordinate transformation from the *x*-*y* coordinate to the *s*-*f* coordinate[37]: $\begin{pmatrix} V_s \\ V_f \end{pmatrix} = \begin{pmatrix} cos\psi & sin\psi \\ -sin\psi & cos\psi \end{pmatrix} \begin{pmatrix} V_x \\ V_y \end{pmatrix} = R(\phi) \begin{pmatrix} V_x \\ V_y \end{pmatrix}$, where ψ is the angle between *x*-*y* coordinate and the *s*-*f* coordinate. Due to the birefringence of nematic phase, the decomposed beams along the slow axis and the fast axis experience different refractive indices, leading to phase retardation of the two beams. The polarization state of the light transmitting through a nematic plate is expressed as[37]:

$$\begin{pmatrix} V_s' \\ V_f' \end{pmatrix} = \begin{pmatrix} exp\left(-in_s \frac{2\pi}{\lambda} d\right) & 0 \\ 0 & exp\left(-in_f \frac{2\pi}{\lambda} d\right) \end{pmatrix} \begin{pmatrix} V_s \\ V_f \end{pmatrix}$$

where n_s and n_f are the refractive indices along the slow axis and the fast axis, respectively. *d* is the thickness of the nematic plate. λ is the wavelength of the beam.

For a non-uniform nematic director configurations in our study, the polarization of the light transmitting through the configuration can be calculated by considering the director field as the stacking of multiple nematic slices. The incident beam is assumed normal to the nematic planes. The polarization state of the light propagating through each nematic slice is calculated until the light exits the director configuration. Then the coordinate of the transmitted light is transformed from the *s-f* coordinate back to the *x-y* coordinate before transmitting through the analyzer. The director fields used in the simulation were calculated by the minimization of elastic free energy as described in Chapter 2. The simulation code was written in MATLAB.

REFERENCES

1 Sharma, V., Crne, M., Park, J. O. & Srinivasarao, M. Structural origin of circularly polarized iridescence in jeweled beetles. *Science* **325**, 449-451 (2009).

2 Bonner, W. A. *Physical origin of homochirality in life*. (AIP Conference Proceedings, 1996).

3 Cline, D. B. On the determination of the physical origin of homochirality in life. *Comments Nucl. Part. Phys.* **22**, 131-154 (1995).

4 Pasteur, L. *C. R. Acad. Sci* **26** (1848).

5 Kondepudi, D. K., Kaufman, R. J. & Singh, N. Chiral symmetry breaking in sodium chlorate crystallizaton. *Science* **250**, 975-976 (1990).

6 Saito, Y. & Hyuga, H. Colloquium: Homochirality: Symmetry breaking in systems driven far from equilibrium. *Reviews of Modern Physics* **85**, 603-621 (2013).

7 Nayani, K., Chang, R., Fu, J., Ellis, P. W., Fernandez-Nieves, A., Park, J. O. & Srinivasarao, M. Spontaneous emergence of chirality in achiral lyotropic chromonic liquid crystals confined to cylinders. *Nature communications* **6** (2015).

8 Davidson, Z. S., Kang, L., Jeong, J., Still, T., Collings, P. J., Lubensky, T. C. & Yodh, A. G. Chiral structures and defects of lyotropic chromonic liquid crystals induced by saddle-splay elasticity. *Physical Review E* **91**, 050501 (2015).

9 Jeong, J., Kang, L., Davidson, Z. S., Collings, P. J., Lubensky, T. C. & Yodh, A. G. Chiral structures from achiral liquid crystals in cylindrical capillaries. *Proceedings of the National Academy of Sciences* **112**, 1837-1844 (2015).

10 Chang, R., Nayani, K., Fu, J., Reichmanis, E., Park, J. O. & Srinivasarao, M. Double helix configuration of lyotropic chromonic liquid crystals in cylindrical capillaries with homeotropic anchoring. *APS March Meeting Abstract* (2015).

11 Nayani, K., Fu, J., Chang, R., Park, J. O. & Srinivasarao, M. Using chiral tactoids as optical probes to study the aggregation behavior of chromonics. *Proceedings of the National Academy of Sciences* 201614620 (2017).

12 Drzaic, P. S. *Liquid crystal dispersions*. Vol. 1 (World Scientific, 1995).

13 Perez-Garcia, L. & Amabilino, D. B. Spontaneous resolution, whence and whither: from enantiomorphic solids to chiral liquid crystals, monolayers and macro- and supra-molecular polymers and assemblies. *Chemical Society reviews* **36**, 941-967 (2007).

14 Blackmond, D. G. The origin of biological homochirality. *Cold Spring Harbor perspectives in biology* **2**, a002147 (2010).

15 Meierhenrich, U. J. Amino acids and the asymmetry of life. *European Review* **21**, 190-199 (2013).

16 Schilthuizen, M. & Davison, A. The convoluted evolution of snail chirality. *Naturwissenschaften* **92**, 504-515 (2005).

17 Srinivasarao, M. Chirality and polymers. *Current Opinion in Colloid & Interface Science* **4**, 370-376 (1999).

18 Eliel, E. L., Wilen, S. H. & Mander, L. N. in *Stereochemistry of Organic Compounds (1st ed.)*, Ch. 14, (Wiley & Sons., 1994).

19 Ruble, J. C., Latham, H. A. & Fu., G. C. Effective kinetic resolution of secondary alcohols with a planar-chiral analogue of 4-(dimethylamino) pyridine. Use of the Fe (C_5Ph_5) group in asymmetric catalysis. *J. Am. Chem. Soc.* **119**, 1492-1493 (1997).
20 Kipping, F. S. & Pope, W. J. LXIII.-Enantiomorphism. *Journal of the Chemical Society* **73**, 606-617 (1898).
21 Adlem, K., Copic, M., Luckhurst, G. R., Mertelj, A., Parri, O., Richardson, R. M., Snow, B. D., Timimi, B. A., Tuffin, R. P. & Wilkes, D. Chemically induced twist-bend nematic liquid crystals, liquid crystal dimers, and negative elastic constants. *Physical review. E,* **88**, 022503 (2013).
22 Chen, D., Nakata, M., Shao, R., Tuchband, M. R., Shuai, M., Baumeister, U., Weissflog, W., Walba, D. M., Glaser, M. A., Maclennan, J. E. & Clark, N. A. Twist-bend heliconical chiral nematic liquid crystal phase of an achiral rigid bent-core mesogen. *Physical Review E* **89** (2014).
23 Dietrich, C. F., Rudquist, P., Lorenz, K. & Giesselmann, F. Chiral structures from achiral micellar lyotropic liquid crystals under capillary confinement. *Langmuir : the ACS journal of surfaces and colloids* **33**, 5852-5862 (2017).
24 Kim, K.-N., Yoon, T.-H. & Lee, J.-H. Spontaneous chiral transition of a polymer-stabilised achiral nematic liquid crystal with cylindrical geometry. *Liq. Cryst.* **38**, 1111-1116 (2011).
25 Niori, T., Sekine, T., Watanabe, J., Furukawa, T. & Takezoe, H. Distinct ferroelectric smectic liquid crystals consisting of banana shaped achiral molecules. *J. Mater. Chem.* **6**, 1231-1233 (1996).
26 Goodby, J. W. Chirality in liquid crystals. *Journal of Materials Chemistry* **1**, 307-318 (1991).
27 Jeong, J., Davidson, Z. S., Collings, P. J., Lubensky, T. C. & Yodh, A. G. Chiral symmetry breaking and surface faceting in chromonic liquid crystal droplets with giant elastic anisotropy. *Proceedings of the National Academy of Sciences* **111**, 1742-1747 (2014).
28 Xu, F. & Crooker, P. P. Chiral nematic droplets with parallel surface anchoring. *Physical Review E* **56**, 6853-6860 (1997).
29 Koning, V., van Zuiden, B. C., Kamien, R. D. & Vitelli, V. Saddle-splay screening and chiral symmetry breaking in toroidal nematics. *Soft Matter* **10**, 4192-4198 (2014).
30 Pairam, E., Vallamkondu, J., Koning, V., van Zuiden, B. C., Ellis, P. W., Bates, M. A., Vitelli, V. & Fernandez-Nieves, A. Stable nematic droplets with handles. *Proceedings of the National Academy of Sciences* **110**, 9295-9300 (2013).
31 Ohzono, T. & Fukuda, J. Zigzag line defects and manipulation of colloids in a nematic liquid crystal in microwrinkle grooves. *Nature communications* **3**, 701 (2012).
32 Ohzono, T., Yamamoto, T. & Fukuda, J. A liquid crystalline chirality balance for vapours. *Nature communications* **5**, 3735 (2014).
33 Link, D. R., Natale, G., Shao, R., Maclennan, J. E., Clark, N. A., Eva Korblova & Walba, D. M. Spontaneous formation of macroscopic chiral domains in a fluid smectic phase of achiral molecules. *Science* **278**, 1924-1927 (1997).

34 Jákli, A. Electro-optical properties and possible applications of bent-core liquid crystals. *Liquid Crystals XIV, International Society for Optics and Photonics* **7775**, 77750R (2010).
35 Reddy, R. A. & Tschierske, C. Bent-core liquid crystals: polar order, superstructural chirality and spontaneous desymmetrisation in soft matter systems. *J. Mater. Chem.* **16**, 907-961 (2006).
36 Tortora, L. & Lavrentovich, O. D. Chiral symmetry breaking by spatial confinement in tactoidal droplets of lyotropic chromonic liquid crystals. *Proceedings of the National Academy of Sciences* **108**, 5163-5168 (2011).
37 Yeh, P. & Gu, C. *Optics of liquid crystal displays*. (John Wiley & Sons, 2009).
38 Bahadur, B. *Liquid crystals: applications and uses. Vol. 1.* (World Scientific Publishing Co. Pte. Ltd. , 1990).
39 Jaffe, M. Applications of Liquid Crystal Polymers. *Journal of Statistical Physics* **62** (1991).
40 Kikuchi, H., Haseba, Y., Yamamoto, S.-i., Iwata, T. & Higuchi, H. Invited paper: optically isotropic nano-structured liquid crystal composites for display applications. *SID Symposium Digest of Technical Papers. Blackwell Publishing Ltd.* **40**, 578-581 (2009).
41 Lagerwall, J. P. F. & Scalia, G. A new era for liquid crystal research: Applications of liquid crystals in soft matter nano-, bio- and microtechnology. *Current Applied Physics* **12**, 1387-1412 (2012).
42 Li, Q. *Liquid crystals beyond displays: chemistry, physics, and applications*. (John Wiley & Sons, 2012).
43 Martínez, J. L., García-Martínez, P., Sánchez-López, M. d. M. & Moreno, I. Accurate color predictability based on a spectral retardance model of a twisted-nematic liquid-crystal display. *Optics Communications* **284**, 2441-2447 (2011).
44 Bae, Y.-J., Yang, H.-J., Shin, S.-H., Jeong, K.-U. & Lee, M.-H. A novel thin film polarizer from photocurable non-aqueous lyotropic chromonic liquid crystal solutions. *Journal of Materials Chemistry* **21**, 2074-2077 (2011).
45 Yeh, P. A., Gunning, W. J., Eblen, J. P. J. & Khoshnevisan, M. Compensator for liquid crystal display, having two types of layers with different refractive indices alternating. U.S. patent No. 5 (1993).
46 Shiyanovskii, S., Schneider, T., Smalyukh, I., Ishikawa, T., Niehaus, G., Doane, K., Woolverton, C. & Lavrentovich, O. Real-time microbe detection based on director distortions around growing immune complexes in lyotropic chromonic liquid crystals. *Physical Review E* **71** (2005).
47 Pisula, W., Zorn, M., Chang, J. Y., Mullen, K. & Zentel, R. Liquid crystalline ordering and charge transport in semiconducting materials. *Macromolecular rapid communications* **30**, 1179-1202 (2009).
48 Laschat, S., Baro, A., Steinke, N., Giesselmann, F., Hagele, C., Scalia, G., Judele, R., Kapatsina, E., Sauer, S., Schreivogel, A. & Tosoni, M. Discotic liquid crystals: from tailor-made synthesis to plastic electronics. *Angewandte Chemie* **46**, 4832-4887 (2007).
49 Guo, F., Mukhopadhyay, A., Sheldon, B. W. & Hurt, R. H. Vertically aligned graphene layer arrays from chromonic liquid crystal precursors. *Advanced materials* **23**, 508-513 (2011).

50 Matus Rivas, O. M. & Rey, A. D. Molecular dynamics on the self-assembly of mesogenic graphene precursors. *Carbon* **110**, 189-199 (2016).
51 https://www.slideshare.net/pasi9192/liquid-crystal-display.
52 Gennes, P. G. d. & Prost, J. *The physics of liquid crystals, second edition*. (Oxford University Press, 1993).
53 Shiyanovskii, S. V., Lavrentovich, O. D., Schneider, T., Ishikawa, T., Smalyukh, I. I., Woolverton, C. J., Niehaus, G. D. & Doane, K. J. Lyotropic chromonic liquid crystals for biological sensing applications. *Molecular Crystals and Liquid Crystals* **434**, 259/[587]-270/[598] (2005).
54 Boiko, O. P., Vasyuta, R. M., Nazarenko, V. G., Pergamenshchik, V. M., Nastishin, Y. A. & Lavrentovich, O. D. Polarizing properties of functional optical films based on lyotropic chromonic liquid crystals. *Mol. Cryst. Liq. Cryst.* **467**, 181-194 (2007).
55 Alexander, G. P., Chen, B. G.-g., Matsumoto, E. A. & Kamien, R. D. Colloquium: Disclination loops, point defects, and all that in nematic liquid crystals. *Reviews of Modern Physics* **84**, 497-514, (2012).
56 Erlangung, H. z. *Physics of Inhomogeneous Nematic Liquid Crystals: Colloidal Dispersions and Multiple Scattering of Light*, (1999).
57 Kleman, M. & Levrentovich, O. D. *Soft matter physics: An introduction*. (Springer, 2003).
58 Lagerwall, J. P. & Giesselmann, F. Current topics in smectic liquid crystal research. *Chemphyschem : a European journal of chemical physics and physical chemistry* **7**, 20-45, (2006).
59 Neto, A., Figueiredo, M. & Salinas, S. R. A. *The physics of lyotropic liquid crystals: phase transitions and structural properties.*, Vol. 62 (OUP Oxford, 2005).
60 Zakharov, A. V., Tsvetkova, M. N. & Korsakov, V. G. Elastic Properties of Liquid Crystals. *Physics of the Solid State* **44**, 1795-1801 (2002).
61 Collings, P. J., Fisch, M. R. & Mooney, M. A. *Liquid crystals: nature's delicate phase of matter*. (Princeton University Press, 1992).
62 Andrienko, D. Introduction to liquid crystals. (2006).
63 Lavrentovich, O. D. & Kleman, M. in *Chirality in Liquid Crystals*, 115-158 (Springer, 2001).
64 Oseen, C. W. The theory of liquid crystals. *Transactions of the Faraday Society* **29**, 883-899 (1933).
65 Frank, F. C. I. Liquid crystals. On the theory of liquid crystals. *Discussions of the Faraday Society* **25**, 19-28 (1958).
66 Nehring, J. & Saupe, A. On the elastic theory of uniaxial liquid crystals. *The Journal of Chemical Physics* **54**, 337-343 (1971).
67 Fernandez, J. R. & Dupre, D. B. Measurements of the bend and splay elastic constants of a polymer liquid crystal by the Frederiks' distortion. *Molecular Crystals and Liquid Crystals* **72** (1981).
68 Gerber, P. R. & Schadt, M. On the Measurement of Elastic Constants in Nematic Liquid Crystals: Comparison of Different Methods. *Z. Naturforsch* **35**, 1036-1044 (1980).
69 Joshi, A. A., Whitmer, J. K., Guzman, O., Abbott, N. L. & de Pablo, J. J. Measuring liquid crystal elastic constants with free energy perturbations. *Soft Matter* **10**, 882-893 (2014).

70 Miraldi, E., Trossi, L., Valabrega, P. T. & Oldano., C. Absolute measurements of the elastic constants of nematic liquid crystals by light scattering. *Il Nuovo Cimento B (1971-1996)* **66**, 179-186 (1981).
71 Ericksen, J. L. Nilpotent energies in liquid crystal theory. *Archive for Rational Mechanics and Analysis* **10**, 189-196 (1962).
72 M.Somoza, A. & Tarazona, P. Density functional theory of the elastic constants of a nematic liquid crystal. *Molecular Physics* **72**, 911-926 (1991).
73 Yokoyama, H. Density-functional theory of surfacelike elasticity of nematic liquid crystals. *Physical Review E* **55** (1997).
74 Prinsen, P. & van der Schoot, P. Shape and director-field transformation of tactoids. *Physical Review E* **68**, 021701 (2003).
75 Kos, Z. & Ravnik, M. Relevance of saddle-splay elasticity in complex nematic geometries. *Soft Matter* **12** (2016).
76 Kralj, S., Rosso, R. & Virga, E. G. Periodic saddle-splay Freedericksz transition in nematic liquid crystals. *The European physical journal. E, Soft matter* **17**, 37-44 (2005).
77 Kralj, S. & Žumer, S. Saddle-splay elasticity of nematic structures confined to a cylindrical capillary. *Physical Review E* **51**, 366-379 (1995).
78 Polak, R. D., Crawford, G. P., Kostival, B. C., Doane, J. W. & Žumer, S. Optical determination of the saddle-splay elastic constant K_{24} in nematic liquid crystals. *Physical Review E* **49**, 978-981 (1994).
79 Crawford, G. P., Allender, D. W. & Doane, J. W. Surface elastic and molecular-anchoring properties of nematic liquid crystals confined to cylindrical cavities. *Physical Review A* **45**, 8693-8708 (1992).
80 Nayani, K. *Role of surface-like elastic constants in the phenomenology of confined nematics* Doctor of Philosophy thesis, Georgia Institute of Technology, (2017).
81 Lebovka, N., Melnyk, V., Mamunya, Y., Klishevich, G., Goncharuk, A. & Pivovarova, N. Low-temperature phase transformations in 4-cyano-4'-pentyl-biphenyl (5CB) filled by multiwalled carbon nanotubes. *Physica E: Low-Dimensional Systems and Nanostructures* **52**, 65-69 (2013).
82 Friberg, S. Lyotropic liquid crystals. *Naturwissenschaften* **64**, 612-618 (1977).
83 Petrov, A. G. *The lyotropic state of matter: molecular physics and living matter physics*. (CRC Press, 1999).
84 Lydon, J. Chromonic liquid crystalline phases. *Liq. Cryst.* **38**, 1663-1681 (2011).
85 Odijk, T. Theory of lyotropic polymer liquid crystals. *Macromolecules* **19**, 2313-2329 (1986).
86 Sonin, A. S. Inorganic lyotropic liquid crystals. *Journal of Materials Chemistry* **8**, 2557-2574. (1998).
87 Ciferri, A., Krigbaum, W. R. & Meyer, R. B. *Polymer liquid crystals*. (Academic Press. Inc. , 1982).
88 Meyer, R. B. *6 - Macroscopic phenomena in nematic polymers. In: polymer liquid crystals*. (Elsevier, 1982).
89 Noel, C. & Navard, P. Liquid crystal polymers. *Prog. Polym. Sci.* **16**, 55-110 (1991).
90 Vasilevskaya, A. S., Generalova, E. V. & Sonin, A. S. Chromonic mesophases. *Russian Chemical Reviews* **58**, 1575-1596 (1989).

91 Lydon, J. Chromonic mesophases. *Current Opinion in Colloid & Interface Science* **8**, 480-490 (2004).
92 Lydon, J. Chromonic review. *Journal of Materials Chemistry* **20**, 10071–10099 (2010).
93 Nastishin, Y. A., Neupane, K., Baldwin, A. R., Lavrentovich, O. D. & Sprunt, S. Elasticity and viscosity of a lyotropic chromonic nematic studied with dynamic light scattering. *arXiv preprint* arXiv:0807.2669 (2008).
94 Zhou, S., Nastishin, Y. A., Omelchenko, M. M., Tortora, L., Nazarenko, V. G., Boiko, O. P., Ostapenko, T., Hu, T., Almasan, C. C., Sprunt, S. N., Gleeson, J. T. & Lavrentovich, O. D. Elasticity of lyotropic chromonic liquid crystals probed by director reorientation in a magnetic field. *Physical Review Letters* **109**, 037801 (2012).
95 Zhou, S., Neupane, K., Nastishin, Y. A., Baldwin, A. R., Shiyanovskii, S. V., Lavrentovich, O. D. & Sprunt, S. Elasticity, viscosity, and orientational fluctuations of a lyotropic chromonic nematic liquid crystal disodium cromoglycate. *Soft Matter* **10**, 6571-6581 (2014).
96 Onsager, L. The effects of shape on the interaction of colloidal particles. *Annals of the New York Academy of Sciences* **51**, 627-659 (1949).
97 Collings, P. J., Dickinson, A. J. & Smith, E. C. Molecular aggregation and chromonic liquid crystals. *Liq. Cryst.* **37**, 701-710 (2010).
98 Luoma, R. J. *X-Ray scattering and magnetic birefringence studies of aqueous solutions of chromonic molecular aggregates.* Doctor of philosophy thesis, Brandeis University, (1995).
99 Kaznacheev, A. V., Bogdanov, M. M. & Taraskin, S. A. The nature of prolate shape of tactoids in lyotropic inorganic liquid crystals. *Journal of Experimental and Theoretical Physics* **95**, 57-63 (2002).
100 Verhoeff, A. A., Bakelaar, I. A., Otten, R. H., van der Schoot, P. & Lekkerkerker, H. N. Tactoids of plate-like particles: size, shape, and director field. *Langmuir : the ACS journal of surfaces and colloids* **27**, 116-125 (2011).
101 Bradac, Z., Kralj, S. & Zumer, S. Molecular dynamics study of nematic structures confined to a cylindrical cavity. *Physical Review E* **58** (1998).
102 Burylov, S. V. Equilibrium configuration of a nematic liquid crystal confined to a cylindrical cavity. *JETP* **85**, 873-886 (1997).
103 Crawford, G. P., Vilfan, M., Doane, J. W. & Vilfan, I. Escaped-radial nematic configuration in submicrometer-size cylindrical cavities: Deuterium nuclear-magnetic-resonance study. *Physical Review A* **43**, 835-842 (1991).
104 Pershin, V. K. & Klebanov, I. I. Helical disclinations in a cylindrical capillary with nematic liquid crystal. *Crystallogr. Rep.* **45**, 307-309 (2000).
105 Zhang, R. *Complex Liquid Crystal Phases in Cylindrical Confinement* Ph.D. thesis, The University of Sheffield, (2012).
106 Vilfan, I., Vilfan, M. & Žumer, S. Defect structures of nematic liquid crystals in cylindrical cavities. *Physical Review A* **43**, 6875-6880 (1991).
107 Williams, C. E., Cladis, P. E. & Kleman, M. Screw disclinations in nematic samples with cylindrical symmetry. *Molecular Crystals and Liquid Crystals* **21**, 355-373 (1973).

108 Lin, S.-Y. & Luskin, M. Relaxation methods for liquid crystal problems. *SIAM Journal on Numerical Analysis* **26**, 1310-1324. (1989).
109 Press, W. H., Teukolsky, S. A., Vetterling, W. T. & Flannery, B. P. *Numerical recipes in Fortran 90.*, (Cambridge university press, 1996).
110 De Jeu, W. H., Claassen, W. A. P. & Spruijt, A. M. J. The determination of the elastic constants of nematic liquid crystals. *Molecular Crystals and Liquid Crystals* **37**, 269-280 (1976).
111 Fréedericksz, V. & Repiewa, A. Theoretisches und Experimentelles zur Frage nach der Natur der anisotropen Flüssigkeiten. *Zeitschrift für Physik* **42**, 532-546 (1927).
112 Taratuta, V. G., Hurd, A. J. & Meyer, R. B. Light-scattering study of a polymer nematic liquid crystal. *Physical Review Letters* **55**, 246-249 (1985).
113 Allender, D., Crawford, G. & Doane, J. Determination of the liquid-crystal surface elastic constant K_{24}. *Physical Review Letters* **67**, 1442-1445 (1991).
114 Mauguin, M. C. Sur les cristaux liquides de Lehmann. *Bull. Soc. Fr. Min.* **34**, 71-117 (1911).
115 Odijk, T. Elastic constants of nematic solutions of rod-like and semi-flexible polymers. *Liq. Cryst.* **1**, 553-559 (1986).
116 Grosberg, A. Y. & Zhestkov, A. V. The dependence of the elasticity coefficients of a nematic liquid crystal polymer on macromolecular rigidity. *Polymer Science U.S.S.R.* **28**, 97-104 (1986).
117 Taratuta, V. G., Lonberg, F. & Meyer, R. B. Anisotropic mechanical properties of a polymer nematic liquid crystal. *Physical Review A* **37**, 1831 (1988).
118 Lee, S.-D. & Meyer, R. B. Crossover behavior of the elastic coefficients and viscosities of a polymer nematic liquid crystal. *Physical Review Letters* **61**, 2217-2220 (1988).
119 Fumeron, S., Moraes, F. & Pereira, E. Retrieving the saddle-splay elastic constant K_{24} of nematic liquid crystals from an algebraic approach. *The European physical journal. E, Soft matter* **39**, 83 (2016).
120 Zumer, S., Kralj, S. & Bezic, J. Freedericksz transition in nematic and cholesteric liquid crystal droplets: determination of K24 elastic constant. *Mol. Cryst. Liq. Cryst.* **212**, 163-172 (1992).
121 Israelachvili, J. N. *19 - Thermodynamic principles of self-assembly. In: intermolecular and surface forces (third edition)*. (Academic Press, 2011).
122 Kuriabova, T., Betterton, M. D. & Glaser, M. A. Linear aggregation and liquid-crystalline order: comparison of Monte Carlo simulation and analytic theory. *Journal of Materials Chemistry* **20**, 10287–10554, doi:10.1039/c0jm02355h (2010).
123 Park, H.-S., Kang, S.-W., Tortora, L., Kumar, S. & Lavrentovich, O. D. Condensation of self-assembled lyotropic chromonic liquid crystal sunset yellow in aqueous solutions crowded with polyethylene glycol and doped with salt. *Langmuir : the ACS journal of surfaces and colloids* **27**, 4164–4175 (2011).
124 Tortora, L., Park, H.-S., Kang, S.-W., Savaryn, V., Hong, S.-H., Kaznatcheev, K., Finotello, D., Sprunt, S., Kumar, S. & Lavrentovich, O. D. Self-assembly, condensation, and order in aqueous lyotropic chromonic liquid crystals crowded with additives. *Soft Matter* **6**, 4157-4176 (2010).

125 Simon, K. A., Sejwal, P., Gerecht, R. B. & Luk, Y.-Y. Water-in-water emulsions stabilized by non-amphiphilic interactions: polymer-dispersed lyotropic liquid crystals. *Langmuir* **23**, 1453-1458 (2007).
126 Schmidt, M. Combined integrated and dynamic light scattering by poly(y-benzyl glutamate) in a helicogenic solvent. *Macromolecules* **17**, 553-560 (1984).
127 K.Kubota & Chu, B. Laser light scattering of PBLG in DMF. *Biopolymers* **22**, 1461-1487 (1983).
128 Manning, G. S. The persistence length of DNA is reached from the persistence length of its null isomer through an internal electrostatic stretching force. *Biophysical journal* **91**, 3607-3616 (2006).
129 Dzyaloshinskii, I. E. Theory of disinclinations in liquid crystals. *Soviet Journal of Experimental and Theoretical Plysics* **31**, 773 (1970).
130 Cladis, P. E. & Kléman, M. Non-singular disclinations of strength S = + 1 in nematics. *Journal de Physique* **33**, 591-598 (1972).
131 Williams, C., Pierański, P. & Cladis, P. Nonsingular S=+1 screw disclination lines in nematics. *Physical Review Letters* **29**, 90-92 (1972).
132 Meyer, R. B. On the existence of even indexed disclinations in nematic liquid crystals. *Philosophical Magazine* **27**, 405-424 (1973).
133 Kleman, M. & Lavrentovich, O. D. Topological point defects in nematic liquid crystals. (2006).
134 Jeong, J., Han, G., Johnson, A. T. C., Collings, P. J., Lubensky, T. C. & Yodh, A. G. Homeotropic alignment of lyotropic chromonic liquid crystals using noncovalent interactions. *Langmuir : the ACS journal of surfaces and colloids* **30**, 2914-2920 (2014).
135 Nehring, J. & Saupe, A. On the schlieren texture in nematic and smectic liquid crystals. *Journal of the Chemical Society, Faraday Transactions 2: Molecular and Chemical Physics* **68**, 1-15 (1972).
136 Crawford, G. P., Mitcheltree, J. A., Boyko, E. P., Fritz, W., Zumer, S. & Doane, J. W. K_{33}/K_{11} determination in nematic liquid crystals: An optical birefringence technique. *Applied Physics Letters* **60**, 3226-3228 (1992).
137 Scharkowski, A., Crawford, G. P., Žumer, S. & Doane, J. W. A method for the determination of the elastic constant ratio K_{33}/K_{11} in nematic liquid crystals. *Journal of Applied Physics* **73**, 7280-7287 (1993).
138 Horowitz, V. R., Janowitz, L. A., Modic, A. L., Heiney, P. A. & Collings, P. J. Aggregation behavior and chromonic liquid crystal properties of an anionic monoazo dye. *Physical Review E* **72**, 041710 (2005).
139 Park, H.-S., Kang, S.-W., Tortora, L., Nastishin, Y., Finotello, D., Kumar, S. & Lavrentovich, O. D. Self-assembly of lyotropic chromonic liquid crystal sunset yellow and effects of ionic additives. *The Journal of Physical Chemistry B* **112**, 16307-16319 (2008).
140 Dickinson, A. J., LaRacuente, N. D., McKitterick, C. B. & Collings, P. J. Aggregate structure and free energy changes in chromonic liquid crystals. *Molecular Crystals and Liquid Crystals* **509**, 9/[751]-720/[762] (2009).
141 Rapini, A. & Papoular, M. Distorsion d'une lamelle nematique sous champ magnetique conditions d'ancrage aux parois. *Le Journal de Physique Colloques* **30**, C4-54-C54-56 (1969).

142 Lavrentovich, O. D. Transport of particles in liquid crystals. *Soft Matter* **10**, 1264-1283 (2014).
143 Nazarenko, V. G., Boiko, O. P., Park, H. S., Brodyn, O. M., Omelchenko, M. M., Tortora, L., Nastishin, Y. A. & Lavrentovich, O. D. Surface alignment and anchoring transitions in nematic lyotropic chromonic liquid crystal. *Physical Review Letters* **105**, 017801 (2010).
144 Jerome, B. Surface effects and anchoring in liquid crystals. *Rep. Prog. Phys.* **54**, 391-451 (1991).
145 Nazarenko, V. G. & Lavrentovich, O. D. Anchoring transition in a nematic liquid crystal composed of centrosymmetric molecules. *Physical Review E* **49**, R990-R993 (1994).
146 Senkevich, J. J. Thermal Oxidation of Parylene X. *Chemical Vapor Deposition* **17**, 204-210 (2011).
147 Collings, P. J., van der Asdonk, P., Martinez, A., Tortora, L. & Kouwer, P. H. J. Anchoring strength measurements of a lyotropic chromonic liquid crystal on rubbed polyimide surfaces. *Liq. Cryst.*, 1-8 (2016).
148 McGinn, C. K., Laderman, L. I., Zimmermann, N., Kitzerow, H. S. & Collings, P. J. Planar anchoring strength and pitch measurements in achiral and chiral chromonic liquid crystals using 90-degree twist cells. *Physical review. E,* **88**, 062513 (2013).
149 Stanley, W. M. Isolation of a crystalline protein possessing the properties of tobacco-mosaic virus. *Science* **81**, 644-645 (1935).
150 Bawden, F. C., Pirie, N. W., Bernal, J. D. & Fankuchen, I. Liquid crystalline substances from virus-infected plants. *Nature* **138**, 1051-1052 (1936).
151 Diao, B. & Berry, G. C. Studies on the texture of nematic solutions of a rod-like polymer 1. Distortion of the director field in a magnetic field. *Liq. Cryst.* **22**, 225-238 (1997).
152 Lonberg, F. & Meyer, R. New ground state for the splay-fréedericksz transition in a polymer nematic liquid crystal. *Physical Review Letters* **55**, 718-721 (1985).
153 Robinson, C. Liquid-crystalline structures in polypeptide solutions. *Tetrahedron* **13** (1961).
154 Robinson, C., Ward, J. C. & Beever, R. B. Liquid crystallines structure in polypeptide solutions. Part 2. *Disc. Faraday Soc.* **29** (1958).
155 DuPré, D. B. Temperature, concentration, and molecular weight dependence of the twist elastic constant of cholesteric poly-γ-benzyl-L-glutamate. *The Journal of Chemical Physics* **63**, 143 (1975).
156 Patel, D. L. & DuPré, D. B. Viscoelastic properties of mixtures of optical isomers of polybenzylglutamate in liquid crystal solution in tetrahydrofuran. *Rheol. Acta* **18**, 662-666 (1979).
157 Dupre, D. B. & Lin, F.-M. Measurement of the anisotropic refractive indices of polybenzylglutamate liquid crystals. Molecular factors and dispersions. *Mol. Cryst. Liq. Cryst.* **75**, 217-224 (1981).
158 Berride, F., Troche, E., Feio, G., Cabrita, E., Sierra, T., Navarro Vazquez, A. & Cid, M. Chiral amplification of disodium cromoglycate chromonics induced by a codeine derivative. *Soft Matter* **13**, 6810-6815 (2017).

159 Peng, C. & Lavrentovich, O. D. Chirality amplification and detection by tactoids of lyotropic chromonic liquid crystals. *Soft Matter* **11**, 7257-7263 (2015).
160 Ryschenkow, G. & Kleman, M. Surface defects and structural transitions in very low anchoring energy nematic thin films. *The Journal of Chemical Physics* **64**, 404-412 (1976).
161 Miller, D. S., Carlton, R. J., Mushenheim, P. C. & Abbott, N. L. Introduction to optical methods for characterizing liquid crystals at interfaces. *Langmuir* **29**, 3154-3169 (2013).
162 Chang, N. J. & Kaler, E. W. The Structure of Sodium Dodecyl Sulfate Micelles In Solutions of H_2O and D_2O. *The Journal of Physical Chemistry* **89** (1985).
163 Kaznacheev, A. V., Bogdanov, M. M. & Sonin, A. S. The influence of anchoring energy on the prolate shape of tactoids in lyotropic inorganic liquid crystals. . *Journal of Experimental and Theoretical Physics* **97**, 1159-1167 (2003).
164 Prinsen, P. & van der Schoot, P. Continuous director-field transformation of nematic tactoids. *The European physical journal. E, Soft matter* **13**, 35-41 (2004).
165 Prinsen, P. & Schoot, P. v. d. Parity breaking in nematic tactoids. *Journal of Physics: Condensed Matter* **16**, 8835-8850 (2004).
166 Zhang, C., Acharya, A., Walkington, N. J. & Lavrentovich, O. D. Computational modeling of tactoid dynamics in chromonic liquid crystals. *Liq. Cryst.*, 1-17 (2017).
167 Wang, P. X., Hamad, W. Y. & MacLachlan, M. J. Structure and transformation of tactoids in cellulose nanocrystal suspensions. *Nature communications* **7**, 11515 (2016).
168 Zocher, H. Spontaneous structure formation in sols; a new kind of anisotropic liquid media. *Z Anorg Allg Chem* **147**, 91-110 (1925).
169 Drzaic, P. S. A case of mistaken identity: spontaneous formation of twisted bipolar droplets from achiral nematic materials. *Liq. Cryst.* **26**, 623-627 (1999).
170 Williams, R. D. Two transitions in tangentially anchored nematic droplets. *Journal of physics A: mathematical and general* **19**, 3211 (1986).
171 Fernandez-Nieves, A., Link, D. R., Marquez, M. & Weitz, D. A. Topological Changes in Bipolar Nematic Droplets under Flow. (2007).
172 Kostko, A. F., Cipriano, B. H., Pinchuk, O. A., Ziserman, L., Anisimov, M. A., Danino, D. & Raghavan, S. R. Salt effects on the phase behavior, structure, and rheology of chromonic liquid crystals. *J. Phys. Chem. B* **109**, 19126-19133 (2005).
173 Tuinier, R., Rieger, J. & de Kruif, C. G. Depletion-induced phase separation in colloid–polymer mixtures. *Advances in Colloid and Interface Science* **103**, 1-31 (2003).
174 Asakura, S. & Fumio, O. Interaction between particles suspended in solutions of macromolecules. *Journal of Polymer Science* **33**, 183-192 (1958).
175 Madden, T. L. & Herzfeld, J. Exclusion of spherical particles from the nematic phase of reversibly assembled rod-like particles. *MRS Online Proceedings Library Archive* **248** (1991).
176 Xu, F., Kitzerow, H. S. & Crooker, P. Director configurations of nematic-liquid-crystal droplets: Negative dielectric anisotropy and parallel surface anchoring. *Physical Review E* **49**, 3061-3068 (1994).
177 Ding, J. & Yang, Y. Birefringence patterns of nematic droplets. *Jpn. J. Appl. Phys* **31**, 2837-2845 (1992).

178 Fick, A. Ueber diffusion. *Annalen der Physik* **170**, 59-86 (1855).
179 Fick, A. *Philos. Mag.* **10**, 30 (1855).
180 Renshaw, M. P. & Day, I. J. NMR characterization of the aggregation state of the azo dye sunset yellow in the isotropic phase. *J. Phys. Chem. B* **114**, 10032–10038 (2010).
181 Filas, R. W. Tactoidal shell defects in poly (γ-benzyl-D-glutamate) liquid crystals. *Journal de Physique* **39**, 49-55, (1978).
182 Yu, L. J. & Saupe, A. Deuteron resonance of D_2O of nematic disodium cromoglycate-water systems. *Mol. Cryst. Liq. Cryst.* **80**, 129-143 (1982).
183 Jones, J. W., Lue, L., Ormerod, A. P. & Tiddy, G. J. T. The influence of sodium chloride on the self-association and chromonic mesophase formation of Edicol Sunset Yellow. *Liq. Cryst.* **37**, 711-722 (2010).
184 Prasad, S. K., Nair, G. G., Hegde, G. & Jayalakshmi, V. Evidence of wormlike micellar behavior in chromonic liquid crystals: rheological, X-ray, and dielectric studies. *J. Phys. Chem. B* **111**, 9741-9746 (2007).
185 Mackintosh, F. C., Safran, S. A. & Pinus, P. A. Self-assembly of linear aggregates: the effect of electrostatics on growth. *Europhys. Lett.* **12**, 697-702 (1990).
186 Odijk, T. Ionic strength dependence of the length of charged linear micelles. *J. Phys. Chem.* **93**, 3888-3889 (1989).
187 Tomasik, M. R. & Collings, P. J. Aggregation behavior and chromonic liquid crystal phase of a dye derived from naphthalenecarboxylic acid. *J. Phys. Chem. B* **112**, 9883-9889 (2008).
188 Goldfarb, D., Luz, Z., Spielberg, N. & Zimmermann, H. Structural and orientational characteristics of the disodium/cromoglycate-water mesophases by deuterium NMR and X-ray diffraction. *Molecular Crystals and Liquid Crystals* **126**, 225-246 (1985).
189 Joshi, L., Kang, S.-W., Agra-Kooijman, D. M. & Kumar, S. Concentration, temperature, and pH dependence of sunset-yellow aggregates in aqueous solutions: An x-ray investigation. *Physical Review E* **80**, 041703 (2009).
190 Shannon, R. D. & Prewitt, C. T. Effective ionic radii in oxides and fluorides. *Acta Crystallographica Section B Structural Crystallography and Crystal Chemistry* **25**, 925-946 (1969).
191 Shannon, R. D. & Prewitt, C. T. Revised values of effective ionic radii. *Acta Crystallographica Section B: Structural Crystallography and Crystal Chemistry* **26**, 1046-1048 (1970).
192 Shannon, R. D. Revised effective ionic radii and systematic studies of interatomic distances in halides and chalcogenides. *Acta crystallographica section A: crystal physics, diffraction, theoretical and general crystallography* **32**, 751-767 (1976).
193 Buhler, E. & Boue, F. Persistence length for a model semirigid polyelectrolyte as seen by small angle neutron scattering: a relevant variation of the lower bound with ionic strength. *The European physical journal. E, Soft matter* **10**, 89-92 (2003).
194 Crowley, T. L., Bottrill, C., Mateer, D., Harrison, W. J. & Tiddy, G. J. T. Lyotropic chromonic liquid crystals: neutron scattering studies of shear-induced orientation and reorientation. *Colloids and Surfaces A: Physicochemical and Engineering Aspects* **129-130**, 95-115 (1997).

195 Gupta, A. K., Cotton, J. P., Marchal, E., Burchard, W. & Benoit, H. Persistence length of cellulose tricarbanilate by small-angle neutron scattering. *Polymer* **17**, 363-366 (1976).
196 Stieger, M., Richtering, W., Pedersen, J. S. & Lindner, P. Small-angle neutron scattering study of structural changes in temperature sensitive microgel colloids. *J Chem Phys* **120**, 6197-6206, (2004).
197 Kuczyński, W., Żywucki, B. & Małecki, J. Determination of orientational order parameter in various liquid-crystalline phases. *Molecular Crystals and Liquid Crystals* **381**, 1-19 (2010).
198 Fakruddin, K., Jeevan Kumar, R., Datta Prasad, P. V. & Pisipati, V. G. K. M. Orientational order parameter – 1 A birefringence study. *Molecular Crystals and Liquid Crystals* **511**, 133/[1603]-1145/[1615] (2009).
199 Hagemeyer, A., Tarroni, R. & Zannoni, C. Determination of orientational order parameters in liquid crystals from temperature-dependent 13C NMR experiments. *Journal of the Chemical Society, Faraday Transactions* **90**, 3433-3442 (1994).
200 Abe, A. & Flory, P. J. Statistical thermodynamics of mixtures of rodlike particles. 2. Ternary systems. *Macromolecules* **11**, 1122-1126 (1978).
201 Southern, C. D. & Gleeson, H. F. Using the full Raman depolarisation in the determination of the order parameters in liquid crystal systems. *European Physical Journal E* **24**, 119-127 (2007).
202 Jones, W. J., Thomas, D. K., Thomas, D. W. & Williams, G. Raman scattering studies of homogeneous and twisted-nematic liquid crystal cells and the determination of $\langle P_2 \rangle$ and $\langle P_4 \rangle$ order parameters. *Journal of Molecular Structure* **614**, 75-85 (2002).
203 Jen, S., Clark, N. A., Pershan, P. S. & Priestley, E. B. Polarized Raman scattering studies of orientational order in uniaxial liquid crystalline phases. *The Journal of Chemical Physics* **66**, 4635-4661 (1977).
204 Yao, X., Nayani, K., Park, J. O. & Srinivasarao, M. Orientational order of a lyotropic chromonic liquid crystal measured by polarized Raman spectroscopy. *The journal of physical chemistry. B* **120**, 4508-4512 (2016).
205 Steele, D. *Theory of vibrational spectroscopy*. . (Saunders: Philadelphia, , 1971).
206 Raman, C. V. & Krishnan, K. S. A new type of secondary radiation. *Nature* **121**, 501-502 (1928).
207 Tanaka, M. & Young, R. J. Review: Polarized Raman spectroscopy for the study of molecular orientation distributions in polymers. *Journal of Materials Science* **41**, 963-991 (2006).
208 Laserna, J. J. *Modern techniques in Raman spectroscopy*. (John Wiley & Sons 1996).
209 Banwell, C. N. & Mccash, E. M. *Fundamentals of molecular spectroscopy*. (McGraw-Hill, 1994).
210 Park, M. S. *Application of polarized raman spectroscopy for analysis of phase transitions and anisotropic behavior of soft condensed matter*. Doctor of Philosophy thesis, Georgia Institute of Technology, (2012).
211 Fu, J., Nayani, K., Park, J. O. & Srinivasarao, M. Spontaneous emergence of twist and the formation of a monodomain in lyotropic chromonic liquid crystals confined to capillaries. *NPG Asia Materials* **9**, e393 (2017).

212 Yao, X. *Studies on lyotropic chromonic liquid crystals in nematic and biphasic regions* Doctor of Philosophy thesis, Georgia Institute of Technology, (2011).
213 Shams, A., Yao, X., Park, J. O., Srinivasarao, M. & Rey, A. D. Theory and modeling of nematic disclination branching under capillary confinement. *Soft Matter* **8**, 11135 (2012).
214 Shams, A., Yao, X., Park, J. O., Srinivasarao, M. & Rey, A. D. Mechanisms and shape predictions of nematic disclination branching under conical confinement. *Soft Matter* **10**, 3245-3258 (2014).
215 Shams, A., Yao, X., Park, J. O., Srinivasarao, M. & Rey, A. D. Disclination Shape Analysis for Nematic Liquid Crystals under Micron-range Capillary Confinement. *Mater. Res. Soc. Symp. Proc* **1526** (2013).
216 Lekkerkerker, H. N. W., Coulon, P., Van Der Haegen, R. & Deblieck, R. On the isotropic-liquid crystal phase separation in a solution of rodlike particles of different lengths. *The Journal of chemical physics* **80**, 3427-3433 (1984).
217 Sanchez-Castillo, A., Osipov, M. A. & Giesselmann, F. Orientational order parameters in liquid crystals: A comparative study of x-ray diffraction and polarized Raman spectroscopy results. *Physical Review E* **81**, doi:10.1103/PhysRevE.81.021707 (2010).
218 Nastishin, Y. A., Liu, H., Schneider, T., Nazarenko, V., Vasyuta, R., Shiyanovskii, S. V. & Lavrentovich, O. D. Optical characterization of the nematic lyotropic chromonic liquid crystals: Light absorption, birefringence, and scalar order parameter. *Physical Review E* **72** (2005).
219 Khokhlov, A. R. & Semenov, A. N. Liquid-crystalline ordering in the solution of long persistent chains. *Physica A: Statistical Mechanics and its Applications* **108**, 546-556 (1981).
220 Chen, Z. Y. Effect of polydispersity on the isotropic-nematic phase transition of rigid rods. *Physical Review E* **50**, 2849-2855 (1994).
221 Chen, Z. Y. Nematic ordering in semiflexible polymer chains. *Macromolecules* **26**, 3419-3423 (1993).
222 Chen, Z. Y. Configuration of semiflexible polymer chains in the nematic phase. *Macromolecules* **27**, 2073-2078 (1994).
223 Maier, W. & Saupe, A. A simple molecular theory of the nematic crystallineliquid state. *Zeitschrift fuer Naturforschung* **13a**, 564-566 (1958).
224 Haller, I. Thermodynamic and static properties of liquid crystals. *Progress in Solid State Chemistry* **10**, 103-118 (1975).
225 Pieraccini, S., Masiero, S., Ferrarini, A. & Piero Spada, G. Chirality transfer across length-scales in nematic liquid crystals: fundamentals and applications. *Chemical Society reviews* **40**, 258-271, (2011).
226 Lee, S., Chang, R., Reichmanis, E., Park, J. O. & Srinivasarao, M. Amplification of chirality of lyotropic chromic liquid crystals confined to capillaries. *APS March Meeting Abstract* (2018).
227 Zhao, Y., Askarpour, A. N., Sun, L., Shi, J., Li, X. & Alu, A. Chirality detection of enantiomers using twisted optical metamaterials. *Nature communications* **14180** (2017).
228 A. J. Hutt, A. J. & Tan, S. C. Drug chirality and its clinical significance. *Drugs* **52**, 1-12 (1996).

229 Kelly, S. M., Jess, T. J. & Price, N. C. How to study proteins by circular dichroism. *Biochim. Biophys. Acta* **1751**, 119–139 (2005).
230 Kleman, M. Defects in liquid crystals. *Rep. Prog. Phys.* **52**, 555-654 (1989).
231 Wang, Y.-S., Yuan, B.-H. & Yang, G.-H. Effect of saddle-splay elasticity on stability of disclination rings in nematic liquid crystals. *Communications in Theoretical Physics* **50**, 847 (2008).
232 Lavrentovich, O. D., Ishikawa, T. & Terentjev, E. M. Disclination loop in Mori-Nakanishi ansatz: role of the divergence elasticity. *Molecular Crystals and Liquid Crystals Science and Technology. Section A. Molecular Crystals and Liquid Crystals* **299**, 301-306 (1997).
233 Mori, H. & Nakanishi, H. On the stability of topologically non-trivial point defects. *Journal of Physical Society of Japan* **57**, 1281-1286 (1988).
234 Frenkel, J. *Kinetic theory of Liquids*. (Dover, 1955).
235 Ericksen, J. L. Conservation laws for liquid crystals. *Transactions of the Society of Rheology* **5**, 23-34 (1961).
236 Leslie, F. M. Some constitutive equations for anisotropic fluids. *Quarterly Journal of Mechanics and Applied Mathematics* **19**, 357-370 (1966).
237 Leslie, F. M. Some thermal effects in cholesteric liquid crystals. *Proceedings of the Royal Society of London, Series A: Mathematical, Physical and Engineering Sciences* **307**, 359-372 (1968).
238 Leslie, F. M. Theory of flow phenomena in liquid crystals. *Advances in Liquid Crystals* **4**, 1-81 (1979).
239 Leslie, F. M. Viscometry of nematic liquid crystals. . *Molecular Crystals and Liquid Crystals* **63**, 111-127 (1981).
240 Kröger, M. & Sellers, S. On the signs of the Leslie viscosities α2 and α3 for nematics and discotic nematics. *Molecular Crystals and Liquid Crystals* **293**, 17-27 (1997).
241 Larson, R. G. *The Structure and Rheology of Complex Fluids*. (Oxford University Press, 1999).
242 Kuzuu, N. & Doi, M. Constitutive equation for nematic liquid crystals under weak velocity gradient derived from a molecular kinetic equation. *Journal of the Physical Society of Japan* **52**, 3486-3494 (1983).
243 Kuzuu, N. & Doi, M. Constitutive equation for nematic liquid crystals under weak velocity gradient derived from a molecular kinetic equation. II. Leslie coefficients for rodlike polymers. *Journal of the Physical Society of Japan* **53**, 1031-1038 (1984).
244 Archer, L. A. & Larson, R. G. A molecular theory of flow alignment and tumbling in sheared nematic liquid crystals. *Journal of Chemical Physics* **103**, 3108-3111 (1995).
245 Zannoni, C. Order parameters and orientational distributions in liquid crystals. *Polarized Spectroscopy of Ordered Systems*, 57-83 (1988).
246 Srinivasarao, M. & Berry, G. C. Rheo-optical studies on aligned nematic solutions of a rodlike polymer. *Journal of Rheology* **35**, 379-397 (1991).
247 Burghardt, W. R. & Fuller, G. G. Role of director tumbling in the rheology of polymer liquid crystal solutions. *Macromolecules* **24**, 2546-2555 (1991).

248 Magda, J. J., Baek, S.-G. & DeVries, K. L. Shear flows of liquid crystal polymers: measurements of the second normal stress difference and the Doi molecular theory. *Macromolecules* **24**, 4460-4468 (1991).
249 Srinivasarao, M. *Rheo-optical studies on a polymer liquid crystal under the influence of flow or magnetic fields.* Doctor of philosophy thesis, Carnegie Mellon University, (1990).
250 Carlton, R. A. in *Pharmaceutical microscopy*, 7-64 (Springer, 2011).
251 Horowitz, V. R. *Fundamental Measurements on an Aggregated Dye Liquid Crystal* B. A. thesis, Swarthmore College, (2005).
252 Joesten, B. L. Thermogravimetry and differential scanning calorimetry of some poly-p-xylylenes containing halogen atoms. *J. Appl. Polym. Sci.* **18**, 439-448 (1974).
253 Yokoyama, H., Kobayashi, S. & Kamei, H. Temperature dependence of the anchoring strength at a nematic liquid crystal-evaporated SiO interface. *Journal of Applied Physics* **61**, 4501-4518 (1987).
254 Rosenblatt, C. Temperature dependence of the anchoring strength coefficient at a nematic liquid crystal-wall interface. *Journal de Physique* **45**, 1087-1091 (1984).
255 Edwards, D. J., Jones, J. W., Lozman, O., Ormerod, A. P., Sintyureva, M. & Tiddy, G. J. T. Chromonic Liquid Crystal Formation by Edicol Sunset Yellow. *J. Phys. Chem. B* **112**, 14628–14636 (2008).
256 Cognard, J. Alignment of nematic liquid crystals and their mixtures. *Routledge* **1** (1982).
257 Jones, R. C. A new calculus for the treatment of optical systemsi. description and discussion of the calculus. *JOSA* **31**, 488-493 (1941).
258 Rubinson, K. A. & Krueger, S. Poly(ethylene glycol)s 2000–8000 in water may be planar: A small-angle neutron scattering (SANS) structure study. *Polymer* **50**, 4852-4858 (2009).